Photophysical Investigation of Composite Systems of Metal Complexes and Nanostructured Substrates

Robert Groarke

A Thesis presented to Dublin City University for the degree of Doctor of Philosophy

2008

Photophysical Investigation of Composite Systems of Metal Complexes and Nanostructured Substrates

By

Robert Groarke, BSc. (Hons), AMRSC

A Thesis presented to Dublin City University for the degree of Doctor of Philosophy

Supervisors: Professor Johannes G. Vos

School of Chemical Sciences

Dublin City University

Dr. Enda McGlynn

School of Physical Sciences

Dublin City University

I hereby certify that this material, which I now submit for assessment on the programme of study leading to the award of Doctor of Philosophy by research and thesis, is entirely my own work, and has not been taken from work of others, save and to the extent that such work has been cited within the text of my work.

Signed:_____

Robert Groarke

I.D. Number: 50034053

Date:_____

Abstract

This thesis is concerned primarily with the modification of nanostructured systems with ruthenium polypyridyl complexes and the investigation of these composite systems using UV, fluorescence spectroscopy, SEM, and AFM. The nanostructured systems are of two types, ZnO nanorods, grown on a Silicon substrate, and carbon nanotubes (CNT), in an organic solvent.

Chapter 2 gives an overview of the experimental techniques and instruments used in this thesis. Where necessary, the theory behind these techniques is also discussed.

Chapter 3 presents the ZnO / Ru system. The emissive and morphological properties of ZnO nanorods have been well studied over the years, and the studies presented in Chapter 3 deal with the effect of the modification of the ZnO nanorods with a Ru complex on the emission and morphological properties of the ZnO. It is well known that nanowires and nanorods have high surface areas, and can therefore be sensitized with a greater number of dye molecules than nanocrystalline surfaces. Nanowires also, by virtue of their morphology, tend to allow for a more direct path for the electron to the substrate. A critical tool in this investigation has been AFM, and this has been used on both the unmodified and modified ZnO nanorod samples. The effect of temperature on the emission of the system has also been investigated.

Chapters 4 and 5 deal with the CNT / Ru polymer composite system. The efficient exfoliation of carbon nanotubes in a solvent is a critical step in the process of realizing their potential applications. Chapter 4 deals with the exfoliation of Single Walled Nanotubes (SWNT's) using the Ruthenium PVP polymer, and the subsequent investigation of the system on a solid substrate using AFM.

Chapter 5 presents the data obtained in the exfoliation of both Multi Walled Nanotubes (MWNT'S) and amino functionalized Multi Walled Nanotubes (MWNT-NH_2) with the same ruthenium PVP polymer used in Chapter 4, $[Ru(bpy)_2(PVP)_{10}Cl]Cl$.

Chapter 6 presents the data obtained in the investigation of the excited state lifetimes of various Ruthenium complexes, some are tris bpy analogues, other complexes have

phenanthroline ligands. The phenanthroline ligands are in some cases, brominated, and in other cases, have extended aromatic structures.

Chapter 7 gives general conclusions regarding the work carried out, and outlines potential avenues for future work in the various systems presented in this thesis. Appendix A contains the publications which have been contributed to. Appendix B presents data in support of the AFM images in Chapter 4 and Chapter 5, while Appendix C contains data in support of the lifetime measurements presented in Chapter 6.

Acknowledgements

First of all, I would like to thank my parents and my two brothers James and John for being a constant and much appreciated support for me throughout my entire life, but particularly during my PhD. I could never have done this without you, and I dedicate this thesis to you all. I would also like to thank my supervisors Prof. Han Vos, and Dr. Enda McGlynn for their invaluable help and guidance throughout the work, and for enduring my rather puzzled looks during the progress meetings. My sincere thanks to Prof. Philip Moriarty of Nottingham University for allowing me to work in his group during my second year, and to Dr. Tony Cafolla of DCU for continuing my training in AFM.

There are so many other people I have to thank for making my time as a postgraduate enjoyable, even in the bad times (and there were a few), Ill have a go at naming them all though. Dr. Fadi "I have 3 reactions and 4 columns done today, and I'm working on my thesis now, and later Ill have to go to work in another lab" Hatoum for being my best mate, 3rd brother and comrade-in-arms throughout my 8 years (god, 8 years?) in DCU, and for keeping me sane and mindful of what busy truly means. Thanks to my other best mates Catherine "nano-technician" Keogh and Mick "Go On Carlow" Ryan for all the laughs and help you've given me. Thanks to Dr. Eric "Eddie" Engeldinger for help in the early days of my PhD, and for understanding my love of heavy metal and the mighty Iron Maiden. It was an honour to work (and headbang) with you. May your neck never weaken. Sincere thanks as well to Dr. Claire "Captain Blunder" Hanson for your incredible friendship and for all the laughs and coffee breaks while we both should have been working. Thanks also to the members of the Han Vos Research Group, past and present, particularly Dr. Stefania Tasca, Dr. Fiona Frehill, Dr. Wesley Browne, Laura "Go Team Chemistry!!" Cleary for the laughs and your support and kind words in the bad times, Yvonne "Navan is *not* the wilderness, Rob" Halpin, (I hereby declare in writing that you *can* headbang), Hamid, Jane, and of course, Dr. Danilo Dini for your invaluable help. Id like to thank two other members of the HVRG, Dr. Bill "don't call me William" Henry for all your help and advice, particularly for the SPC, Id have blown it up long ago only for you, and Nadia "Princess Shortie Cupcake" Coburn, for your

friendship and help and for the non stop laughs, you made the lab a very pleasant place for me to be. I hope the dictionary I bought you will help you when you write your thesis, because I'm not going to answer 1800 spelling-related emails every day. Anymore. Id like to also thank my bandmates Steve Finn and Dr. Michele Kelly, and the "groupies" Saibh "Saibheenee" Morrissey, and Ewa Kowalska for the laughs and encouragement. Thanks also to Sonia "Duchess of Donegal" Gallagher for the laughs and smiles, (and for putting me in my place now and then, I deserved it most of the time in fairness), Dr. Grainne Sheerin, Dr. Justina Grabowska, Dr. Cedric Volcke for the assistance in the final AFM measurements, Gavin Sewell, Dr. Emmet O Reilly, Dr. Jonathon Rochford, Jamie, Sharon, Anita V, Kyriaki, Rachel, Claudio, Yann, Dr. Giselle Fontes, Chris Martin, Will, Andy, Debbie, Michal, Patrick Ryan, Drs. Alex Yavorskyy, Silvija Abele, and Aaron Santana, and others that I am probably forgetting (old age is a terrible thing).

Time now to thank all the Chemistry Dept. Technical Staff, particularly Veronica Dobbyn, Damien "I love Star Wars and drumming" McGuirk, Vinny, Ambrose "Have you got a COSHH form for that?" May, Maurice Burke, John McLoughlin for performing open hard drive surgery on my laptop, and Mary Ross. Oh, and Susanna "nano-technician no.2" Farrell, you were brilliant craic.

Id like to thank myself, but I won't. Instead, Id like to thank my heroes, Steve Harris, Jon Schaffer, Chuck Norris, Sylvester Stallone (well, Rocky and Rambo), Dave Mustaine, James Hetfield, John Bardeen, and I suppose Id better thank Albert Einstein for figuring out that the universe is crazy before I had a chance to look into the issue. At least now I know a PhD is just one of the crazier parts of the universe. Id like to take this opportunity to thank the numerous Yorkie bars and burgers that have given their lives to the cause of my PhD, its true what the bearded one once said, "Man does not live on bread alone". Chocolate and beef are immensely important also.

And finally, to all the people I've annoyed with my table drumming over the years: "I've had my fun, and that's all that matters…."

Table of Contents

Structures of Complexes used or cited within the work.

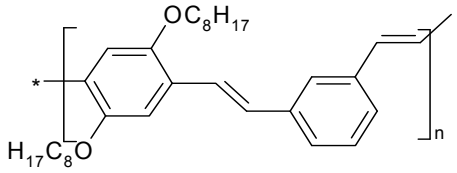

PmPV (Poly(m-phenylenevinylene-co-2,5-dioctoxy-p-phenylenevinylene)

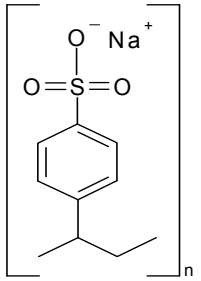

Poly (Sodium 4-Styrenesulfonate) (PSS)

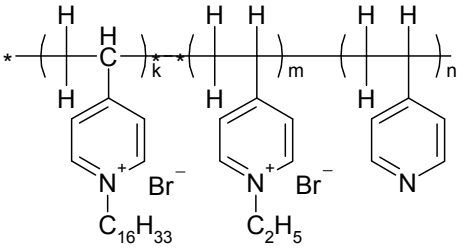

Poly(N-cetyl-4-vinylpyridinium bromide-co-N-ethyl-4-vinylpyridinium bromide-co- 4-vinylpyridin

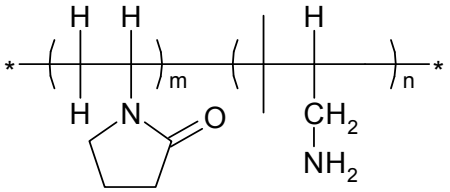

Poly(vinylpyrrolidone-co-allylamine)

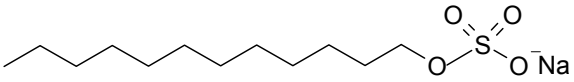

Sodium Dodecyl Sulphate (SDS)

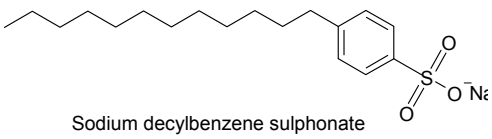

Sodium decylbenzene sulphonate

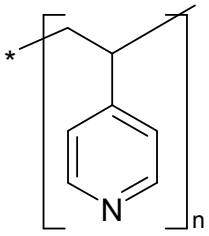

Poly (4-vinylpyridine) (PVP)

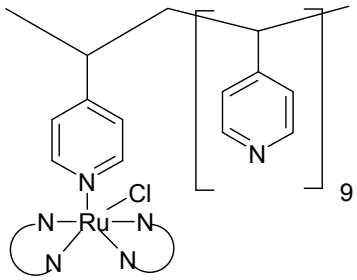

$[Ru(bpy)_2(PVP)_{10}Cl]Cl$

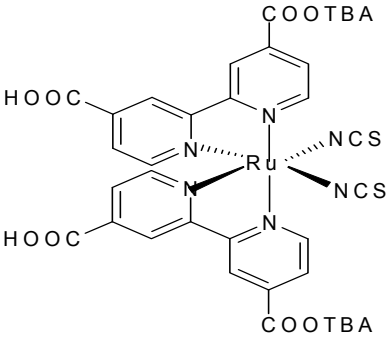

N719

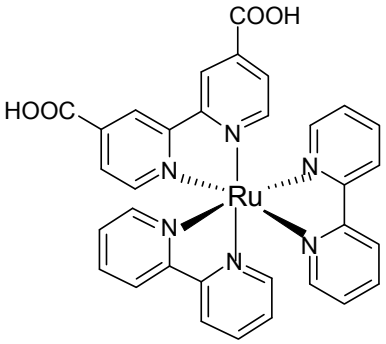

$[Ru(bpy)_2(dcbpy)]\ PF_6$

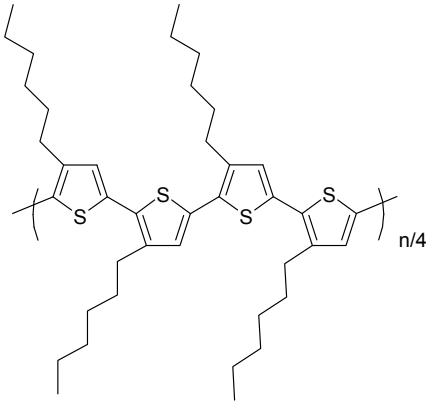

P3HT

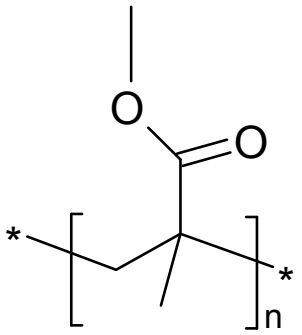

PMMA

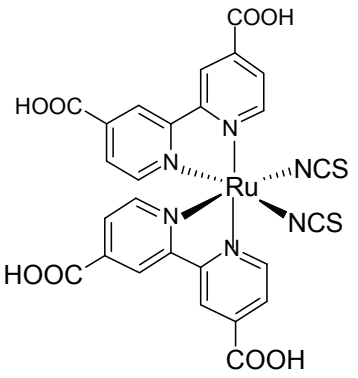

$[Ru(dcbpy)_2(NCS)_2]2H_2O$

$[Ru(NH_3)_5(N\text{-dodecyl 4,4'-bpy})](PF_6)_3]$

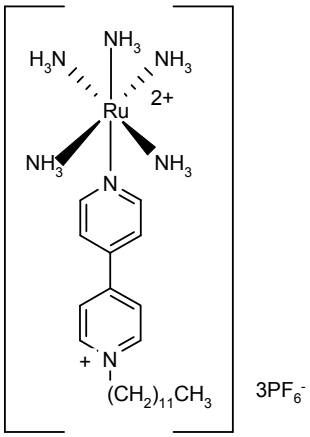

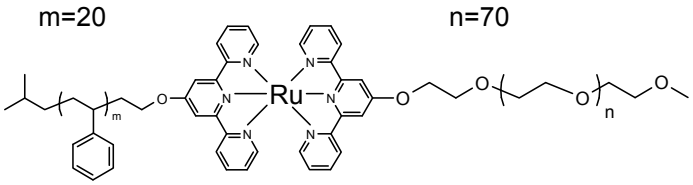

PS_{20}-[Ru]-PEO_{70}

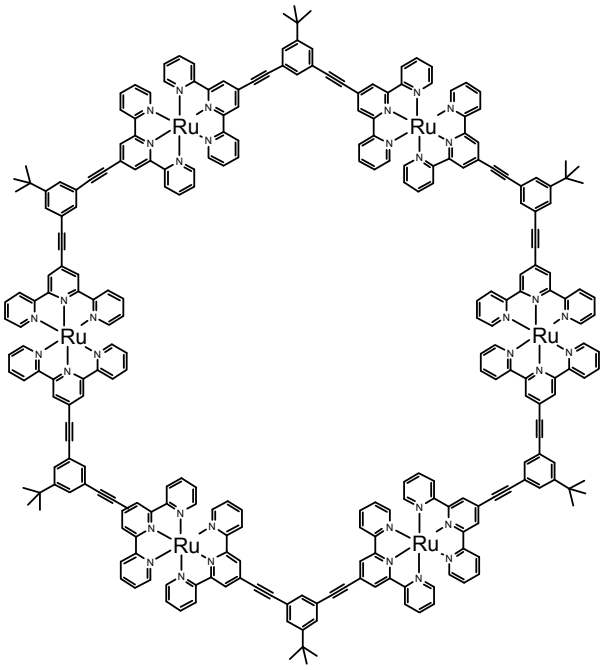

[{1,3-bis(2,2':6,2"-terpyridin-4-ylethynyl)-5-tert-butylbenzene}$_6$$Ru_6$$(PF_6)_{12}$]

Chapter 1 Introduction

In this chapter, the basic properties of ZnO, Ru polypyridyl- based polymers and carbon nanotubes, the three principle materials used in this work, will be discussed together with an overview of the potential applications of these materials. Particular emphasis will be paid to the properties of ZnO nanorods, as they are the material of interest in this work. This leads to a discussion of ZnO - based solar cells, using ruthenium complexes as the sensitizing agent, with regard to the photophysical properties of such systems. In this section the analysis of such systems by other groups using surface probes such as Atomic Force Microscopy AFM and Scanning Electron Microscopy (SEM) is discussed.

The second section is concerned with carbon nanotubes, an introduction to the properties of these fascinating materials is given, along with an overview of literature reports concerned with the exfoliation and dissolution of carbon nanotubes in various solvents, particularly where ruthenium polypyridyl based complexes have been utilized. This is the primary aim of the work done in this section of the thesis.

In order to appreciate and understand the photophysical data obtained for the ruthenium component of the two composite systems discussed in this thesis, an introduction to the excited state properties and photochemistry of ruthenium polypyridyl complexes is also presented. Finally, the scope and aims of this thesis are also outlined.

1.1 ZnO

1.1.1 History and Introduction

Zinc oxide is a unique material which exhibits piezoelectric, semiconducting and pyroelectric properties. One of the first studies relating to ZnO in the literature is in 1940 by Copeland and Short[1], where they investigated the phase diagrams of ZnO, as part of the ternary system ZnO-SO_3-H_2O. In 1944, a report by Fuller[2(a)] was one of the first instances of the investigation of semiconductor metal oxides with well defined nanostructural topologies. Fuller reported "nanoneedles" of ZnO, and established this morphology through stereoscopic electron micrographs. It is thought that this is one of the first reports of ZnO nanorod-type structures in the literature. In the period between this report [2(a)], and the 1990's, when the present surge in ZnO research began, there were periods of great activity in the 1960's, however between 1970 and 1990, there was very little progress made in the area, due to a greater interest in III-V semiconductors. From the 1990's to the present day, however, there has been a huge surge in the investigation of ZnO nanostructures. This has been due to discovery of the room temperature lasing properties of ZnO nanostructures[2(b,c)], and a healthy competition between ZnO and Gallium Nitride (GaN). In 2001, ZnO nanorods were reported in the literature, and is representative of much of the work reported since then in this area. The work reported in ref [3] was carried out by Li and co workers[3], and focused on the preparation and characterization of the nanorods by X-Ray Diffraction (XRD), Field - Effect Scanning Electron Microscopy (FE-SEM), Energy Dispersive X-Ray Spectroscopy (EDX), and TEM.

Over the last number of years, many other different types of ZnO nanostructures have been reported, such as and nanoneedles[4(a,b)] and nanocombs[4(c)] **,** nanorings[5], quantum dots[6], nanoflowers and nanoshuttles[7], and nanodumbells[8], amongst others.

ZnO has been used in solar cells, as a substrate such as a thin film[9], and, to a lesser extent, a well defined nanostructured[10] substrate, and has been sensitized with ruthenium complexes in these reports [9,10].

An illustration of some of the different possible morphologies of ZnO nanostructures is shown in FIGURE 1.1, below.

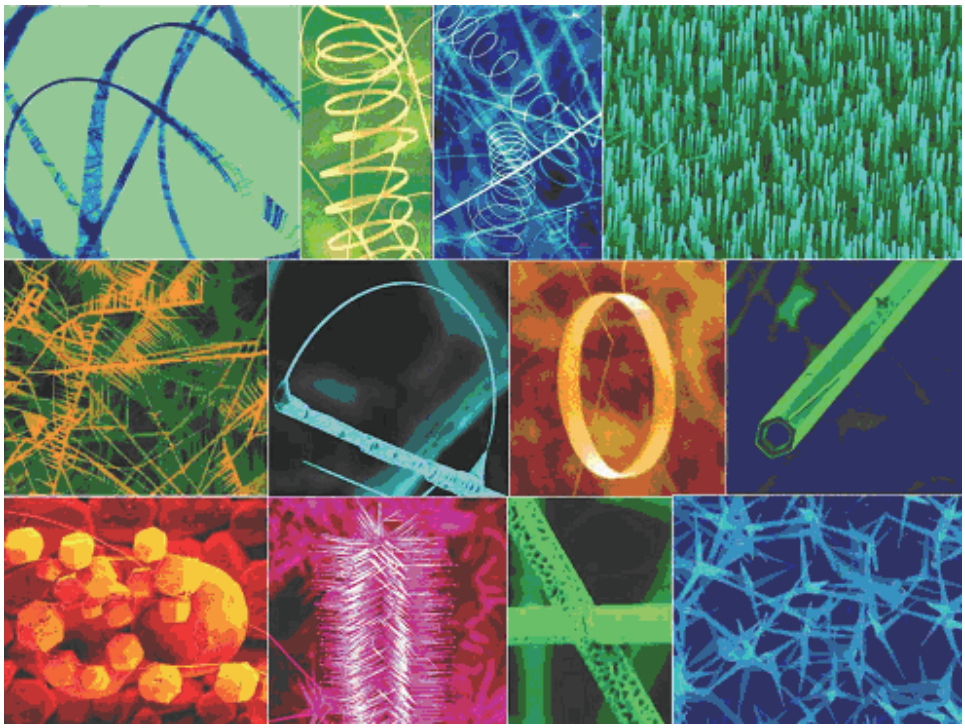

FIGURE 1.1: VARIOUS ZnO NANOSTRUCTURES, INCLUDING NANORODS, NANOBELTS, NANOCOILS AND SPRINGS, NANOCOMBS, AND NANOCAGES[20].

A number of excellent reviews of ZnO can be found in refs [20, 21] and the references therein.

1.1.2 Crystal and Electronic Structure of ZnO

1.1.2.1 Crystal Structure of ZnO

It is known that at room temperature and atmospheric pressure, ZnO crystallizes in a hexagonal crystal, known as wurtzite. As seen in FIGURE 1.2 (see below), wurtzite ZnO has a hexagonal structure, with a C6mc space group. It is composed of alternating planes of tetrahedrally coordinated O^{2-} and Zn^{2+} ions, stacked alternately along the c-axis. The ±(0001) polar surfaces are atomically flat, stable, and do not undergo surface reconstruction[21(a)]. The bonding arrangement closely resembles CH_4, in that the Zn-O

bond is predominantly sp^3 hybridised, and is considered to be partially ionic, and partially covalent in character, with the ionicity parameter reported to be 0.616[22]. The tetrahedral arrangement of the Zn and O atoms leads to the possibility of polar and non polar facets. For example, (±0001) are polar faces and {11-20} and {01-10} are considered non-polar faces. It is this mixture of polar and non-polar facets that endow ZnO with some of its rather interesting properties, such as piezoelectricity, and its tendency to grow along certain, preferential directions in the crystal lattice.

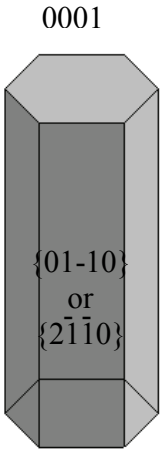

FIGURE 1.2: GROWTH DIRECTIONS AND FACETS OF A ZnO NANOROD, (ADAPTED FROM REF[21(A)]).

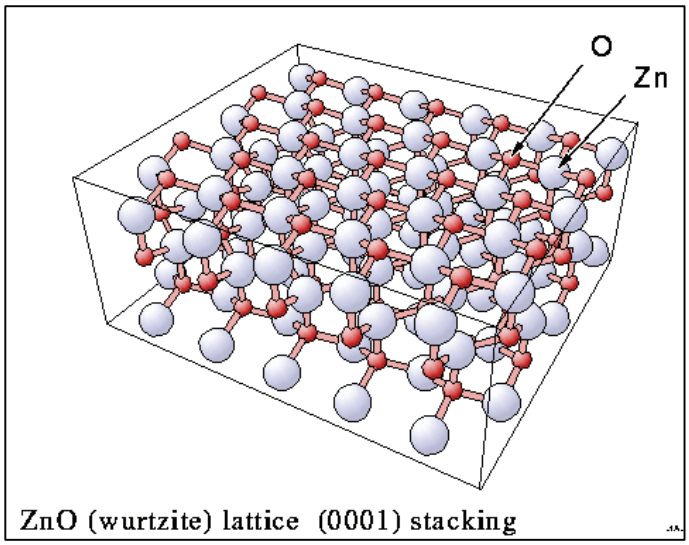

FIGURE 1.3: CRYSTAL STRUCTURE[28] OF WURTZITE TYPE ZnO

The wurtzite structure of ZnO as mentioned at the beginning of this section is shown in FIGURE 1.3, on the previous page. The unit cell of ZnO consists of four atoms. This unit cell means that there are nine optical phonon modes (3n-3, where n=4, as this is the number of atoms), and 3 acoustic phonon modes. A phonon is defined as a quantized mode of vibration in a crystal lattice. An acoustic phonon is a phonon that has a very small frequency at long wavelengths, while optical phonons are phonons that always have a minimum frequency, even at long wavelengths, and are easily excited by light.

1.1.2.2 Electronic Structure of ZnO

ZnO is considered to be a wide, direct band gap semiconductor, with a band gap energy of 3.37eV. It is defined as a *direct* band gap semiconductor the highest energy of the valance band, (VB) in FIGURE 1.4 below, can overlap with the lowest energy of the conduction band, (CB). This allows recombination of electrons with holes, with the conservation of momentum, and is therefore an allowed process. This is not the case with indirect band gap materials, where this overlap of the VB with CB does not occur, and such recombination processes are formally forbidden.

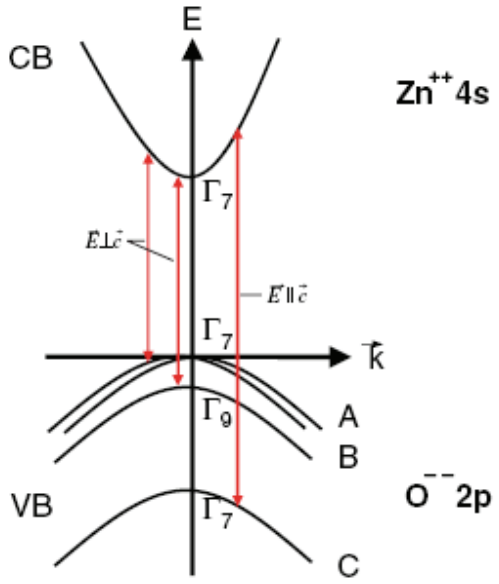

FIGURE 1.4: ELECTRONIC BAND STRUCTURE OF ZnO, TAKEN FROM REF [21(B)].

It is seen from FIGURE 1.4 that there are three degenerate "Kramers doublets" in the valance band, labeled, with decreasing energy, "A", "B and "C". The conduction band is considered to be non-degenerate. It is also seen that the valance bands reside predominantly on the O^{2-} 2p levels, while the conduction band is formed from the Zn^{2+} 4s levels.

1.1.3 Optical Properties of ZnO

As has been shown in many reports, ZnO exhibits strong absorption and emission properties predominantly in the near UV and blue regions of the spectrum. The processes observed in this region of the spectrum are due to excitonic processes with the electronic structure of ZnO. An exciton is a bound state, composed of an excited electron, and the hole resulting from the excitation. The excitons result from the excitation of the material with light, and the binding energy of the electron and the hole is of the order of 60meV, and this value is more or less indifferent to the origin of the electron, whether it is from the "A", "B" or "C" levels in the valance band. Other emission bands are observed, depending on the sample, defect related bands are observed in the green region, usually from 450nm-550nm. Representative examples of the emission bands observed from various groups are discussed in this section. Particular attention has been paid to systems of ZnO nanorods, on silicon substrates, since this is the system investigated in this thesis. It is important to note however, that ZnO emission has been observed from thin films and on many other substrates.
It is important to note that the preparation method for the nanowire systems varies widely, as does the substrate on which the nanowires have been grown. In each case, the growth method is mentioned along with the substrate, since these are important factors which may influence the emission properties of the system.

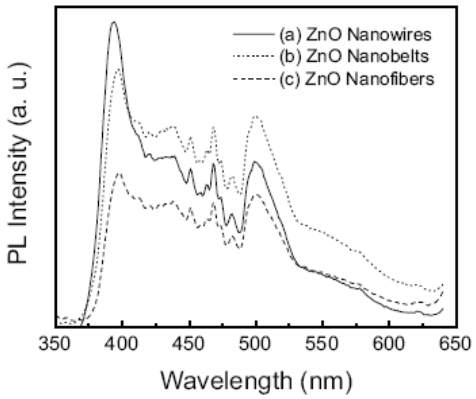

FIGURE 1.5: PL SPECTRUM AT ROOM TEMPERATURE OF THE ZnO NANOWIRES[23]

In FIGURE 1.5, above, a Photoluminescence (PL) spectrum of ZnO nanorods grown on Si(100) by Chen and co-workers[23], is shown. The ZnO emission is reported as a narrow band at 395 nm, a broad blue band, between 425 nm and 481 nm, and a broad green band at 500 nm.The excitation wavelength is stated as 325nm, using a Xenon lamp as the excitation source. The UV band at 395nm is the most intense relative to the green band and is attributed to the near band edge transition of the wide band gap of ZnO. The green band is explained by the recombination of the photo-generated hole with an electron from the ionized oxygen vacancy at the surface of the ZnO crystal. Oxygen vacancies can arise from the growth process, particularly in processes that use higher concentrations of catalyst, such as gold, as this factor has been shown to affect the diameter of the nanorods[36]. The diameter of the nanorods in turn affects the level of oxygen vacancies in the nanorods, which therefore results in a greater possibility of hole – electron recombination processes. The blue band is attributed by the authors to impurities in the dopants, such as the gold used in the growth process.
Room temperature PL spectra of ZnO nanotips grown on amorphous SiO_2 deposited on r-sapphire have also been reported[24]. The ZnO emission spectrum of this system is shown in FIGURE 1.6, on the next page.

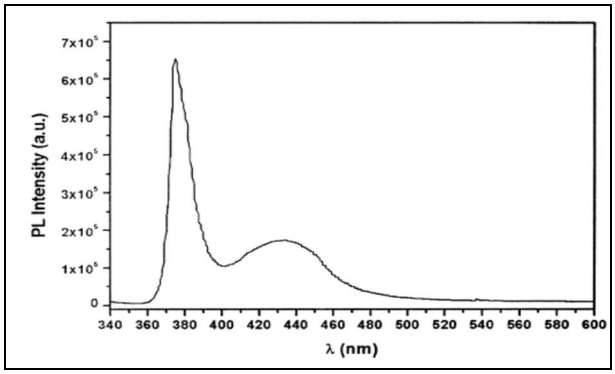

FIGURE 1.6: EMISSION OF ZnO NANOWIRES GROWN ON AMORPHOUS SiO_2 DEPOSITED ON R-SAPPHIRE[24]

There is a narrow emission band at approximately 375nm and a broad blue band from 410nm to 470nm. The narrow band is again due to free exciton recombination and the broad peak is attributed to deep level induced emission. This has also been reported by Reynolds *et al*[35].

Conley *et al*[25] reported the assembly and photoluminescence of ZnO nanowires grown on Si (100), without a metal catalyst, but by using a seed layer of ZnO patterned onto the silicon substrate. The nanowires were found to be well aligned vertically, and the PL spectrum is shown in FIGURE 1.7, below.

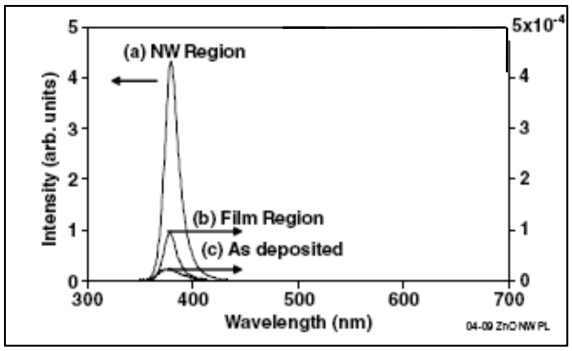

FIGURE 1.7: EMISSION SPECTRA OF ZnO NANOWIRES (A) GROWN ON A ZnO SEED LAYER. THE EMISSION OF THE SEED LAYER IS SHOWN IN COMPARISON, (B),[25].

The emission appears to be quite good, with no defect emission peaks observed. In comparison, the emission from the ZnO seed layer is far weaker in intensity, indicating the advantages in emission characteristics that nanowires have over thin films. This is possibly due to the higher crystal quality of the nanowires, compared with the thin films. Hsu and co-workers[26] prepared ZnO nanowires on porous silicon substrates and investigated the emission properties of theses nanowires at room temperature and at 7K.

It was found that the nanowires were better aligned on the porous silicon than on plain silicon. The PL spectra of the nanowires measured from 300K to 7K is given in FIGURE 1.8, on below.

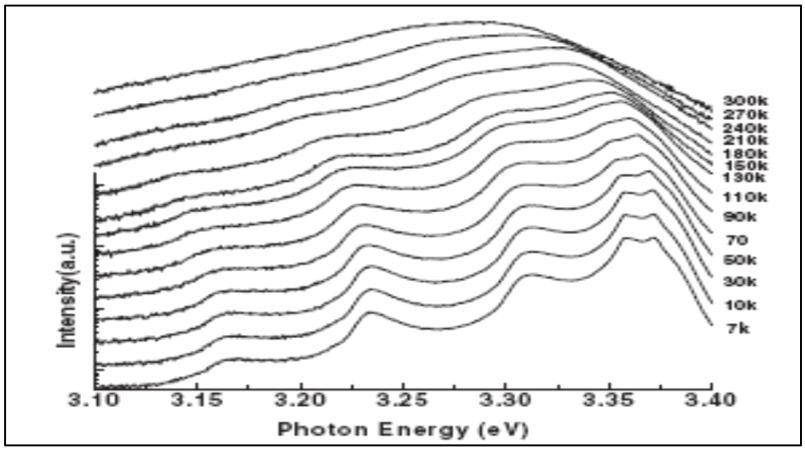

FIGURE 1.8: PL SPECTRA OF THE ZnO NANOWIRES ON POROUS SILICON, TEMPERATURE RANGE 300K-7K[26]

ZnO nanowires and nanorods were also fabricated on silicon substrates by Xu *et al*[27], using a vapour-phase transport method. One of the advantages of this method is that it is carried out at relatively low temperatures. Distinct PL spectra were obtained for the ZnO nanowires catalysed by copper and those catalysed by gold. These spectra were recorded using a 350nm excitation source and are shown in FIGURE 1.9, below. The copper catalysed nanowires exhibit a stronger green emission at around 450nm-550nm than do the gold catalysed nanowires. This green band is attributed to the electron transfer from the oxygen vacancy to the photo-excited hole in the valance band. This suggests that the nanowires grown on the copper have more defects than those grown on the gold catalyst. The UV emission band is strong in both types of nanowires, and is assigned to the band edge excitonic recombination.

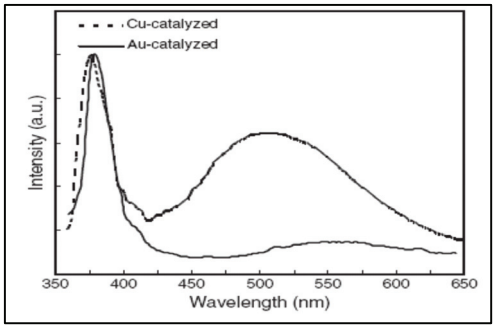

FIGURE 1.9: ROOM TEMPERATURE PL SPECTRA OF ZnO GROWN ON Si USING A VAPOUR PHASE TRANSPORT METHOD[27].

Wang *et al*[36] reported the fabrication of well aligned ZnO nanorod arrays on Si (100), and measured the room temperature PL. The PL spectra are shown in FIGURE 1.10, below.

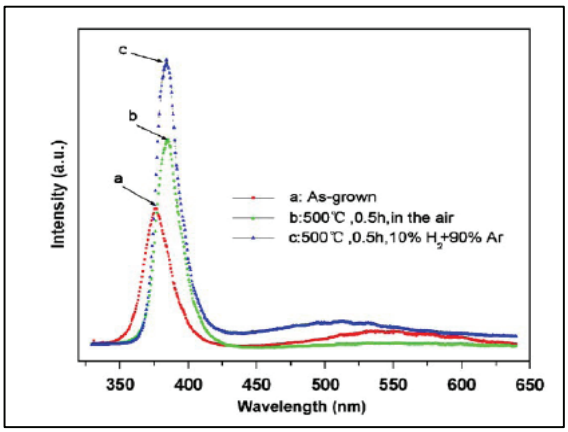

FIGURE 1.10: PL OF THE ZnO NANORODS, AS GROWN AND NANORODS ANNEALED POST FABRICATION[36].

It was found that annealing improved the crystal quality of the nanorods, as seen by the absence of a defect peak (green trace, FIGURE 1.13) compared with the defect peak seen in the other two traces, at around 450 nm – 550 nm.

Cao and co-workers prepared ZnO nanoneedle arrays via an electrochemical deposition method[37] on Si (100), and measured the emission spectra at 13K and 300K. The results are shown in FIGURE 1.11, below.

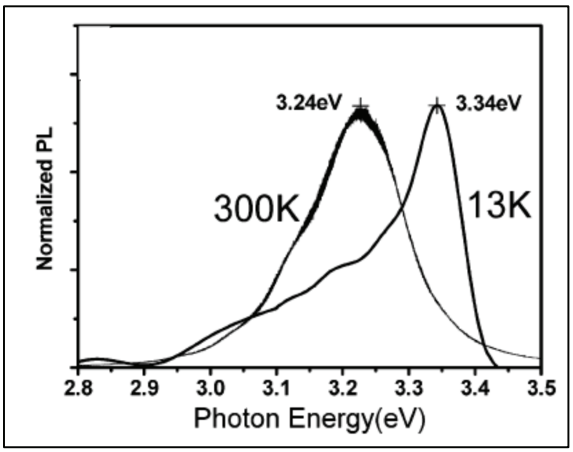

FIGURE 1.11: ROOM TEMPERATURE PL VS LOW TEMPERATURE PL OF ZnO NANONEEDLES ON Si[37].

The shift to higher energy (lower wavelength) is seen when the temperature is decreased from 300K to 13K. The emission peak at low temperatures is narrower than the peak of the 300K emission.

Hsu *et al*[26] also investigated the PL of the ZnO nanowires on porous silicon substrates at low temperatures such as 7K. The PL data obtained from their work is shown in FIGURE 1.12, below.

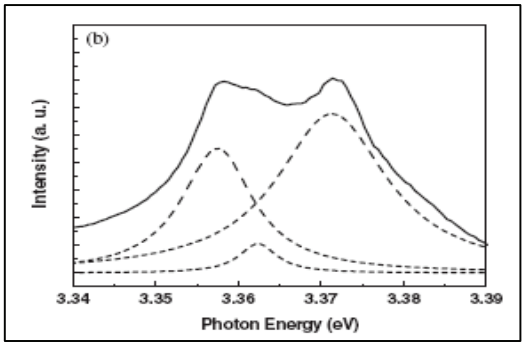

FIGURE 1.12: LOW TEMPERATURE (7K) PL SPECTUM FOR THE ZnO NANOWIRES GROWN ON POROUS Si SUBSTRATES, AND THE FITTING CURVES FOR THE SPECTRUM[26]

The two peaks at 3.358eV and 3.363eV shown in the spectrum in FIGURE 1.12 are attributed by the group to two exciton bound to defect emissions and the third peak at 3.372eV is assigned to a free exciton emission.

Zhao and co-workers[38] investigated exciton recombination in ZnO nanorods on Si. The spectra in FIGURE 1.13, below is the PL spectra of the ZnO nanorods, measured at 80K.

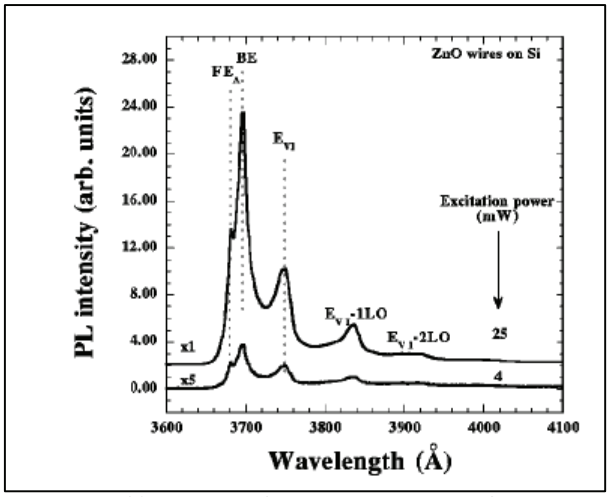

FIGURE 1.13: PL SPECTRA, MEASURED AT 80K OF THE ZnO NANORODS GROWN ON Si[38].

In FIGURE 1.13, above, FE_A refers to the free exciton emission, and BE is attributed to the impurity-bound exciton. E_{VI} is a transition that has the same characteristics as a free to bound exciton transition.

In conclusion, the emission properties of ZnO nanostructures have been extensively studied on silicon, and modified silicon surfaces, using a number of fabrication methods. It has been found that the initial starting conditions of the growth process can affect the emission characteristics of the nanostructures, as can post fabrication processes, such as annealing. Room temperature photoluminescence has been the most commonly reported technique in the characterization of the optical properties of the nanostructures, and in some cases, the photoluminescence of ZnO nanowires/nanorods has been investigated at low temperatures, 80K, 13K, and below. The peaks tend to be sharper at lower temperatures, and can often split into two or more peaks. Shifting of the peak relative to its room temperature position is commonly observed, as is the narrowing of the peak, particularly in the case of the UV emission. The spectra obtained can be used as an indication of the quality of the nanowires, and the presence of oxygen vacancies and defect states can be determined. Defect related peaks can also be observed in the emission spectra, and these generally are of two types, "shallow" defects, where the emission peaks are sharp, while deep level defects tend to result in broad, featureless emission peaks.

1.1.4 Synthesis of ZnO Nanorods

As mentioned in section 1.1.1, there are many different types of ZnO nanostructures. It follows therefore, that there are many different synthesis methods to prepare these different morphologies, and there many methods even for the preparation of ZnO nanorods, which are the nanostructure used in this work. The synthesis of the myriad of morphologies depends on the manipulation of the axes of growth in the crystal structure. ZnO is known to have three fast growth directions, $<2\bar{1}\bar{1}0>$ ($\pm[2\bar{1}\bar{1}0]$, $\pm[\bar{1}2\bar{1}0]$, $\pm[\bar{1}\bar{1}20]$); $<01\bar{1}0>$ ($\pm[01\bar{1}0]$,$\pm$ $[10\bar{1}0]$,$\pm[1\bar{1}00]$), and $\pm$ [0001].

Differing growth rates along these directions are the reason for the many different structures. The structures can be prepared by controlling the growth rates along these directions. The type of morphology obtained under a given set of conditions is also dependant on the relative surface activity of the different growth facets[21]. For example, for a nanorod-type structure will result when the $\{2\bar{1}\bar{1}0\}$ and $\{01\bar{1}0\}$ facet areas are maximized, due to these facets being more energetically favourable. This is shown in FIGURE 1.2, (see above).

ZnO nanorods have been prepared by various methods such as Vapour Phase Transport (VPT) using the Vapour Liquid Solid (VLS) method[11,12(a)], molecular beam epitaxy[13,14], metal-organic vapor phase epitaxy[15], and Pulse Laser Deposition (PLD)[16,17,18,19], being very common. The method used to prepare the ZnO nanorods used in this work is the VPT-VLS process, illustrated in SCHEME 1.1, below.

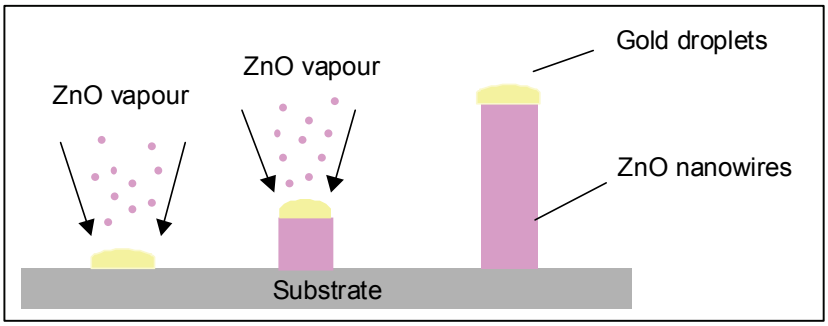

SCHEME 1.1: SCHEMATIC DIAGRAM OF THE VLS GROWTH PROCESS.

The ZnO nanorods in the experiments in this thesis are grown on silicon substrates using a vapour phase transport process with Au as a catalyst. The details of this process are given in Ref [12(b)]. In this process, Au (in thin film form) was first deposited on a substrate, and ZnO powder was vaporized and condensed on the particles, resulting in catalysed epitaxial growth of the ZnO nanowires as shown in SCHEME 1.1, above. The diameter of the nanowires can be tuned by controlling the size of the Au particles which are formed when the Au film is heated, whereas the length of the wires can be controlled by the growth time. The model to explain the growth mechanism of conventional whisker involves the participation of vapour, liquid, and solid phase (VLS) in the growth process. The central idea of the VLS growth concerns the existence of a liquid – forming agent, and the whole growth process of a VLS mechanism can be divided into two

stages:1- the nucleation and growth of eutectic alloy droplets and 2- the growth of whiskers (or nanowires) from the liquid droplets due to supersaturation (SCHEME 1.1). The growth of ZnO nanorods on silicon has been reported by many groups[23,24,25,26,27]. Chen *et al*[23] prepared ZnO nanowires on a gold coated silicon (100) substrate. This report focuses primarily on explaining the growth mechanism, that of vapour transport deposition. FIGURE 1.14, below shows an SEM image of the prepared, densely arrayed ZnO nanorods.

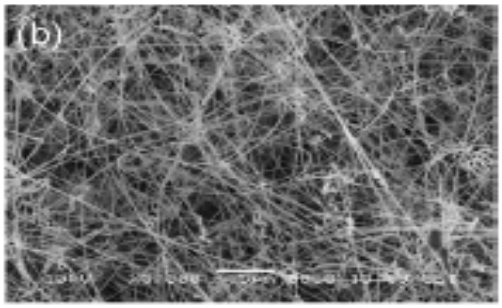

FIGURE 1.14: SEM IMAGE OF THE DENSE ZnO NANORODS, PREPARED ON Si(100), USING AN Au CATALYST[23].

Muthukumar *et al*[24] studied the growth of what they referred to as ZnO nanotips on Silicon dioxide, via the metal-organic chemical vapour deposition (MOCVD) method. The nanotips grown on the SiO_2/Si substrate were investigated by FE-SEM, and the one of the images reported is shown in FIGURE 1.15, below.

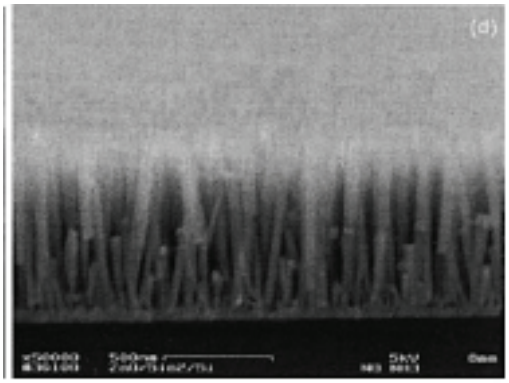

FIGURE 1.15: FIELD EFFECT SEM IMAGE OF THE ZnO NANOTIP ARRAY ON SiO_2/Si SUBSTRATE[24].

The nanotips shown in FIGURE 1.15, above appear well aligned and of approximately uniform size (~40 nm diameter). The ZnO nanotips were also prepared on other substrates such as c-plane Al_2O_3, GaN deposited on Al_2O_3, and also on fused Silica[24].

Conley *et al*[25] reported the assembly and photoluminescence of ZnO nanowires grown on Si (100), without a metal catalyst, but by using a seed layer of ZnO patterned onto the silicon substrate. The nanowires were found to be well aligned vertically, and the SEM image is shown in FIGURE 1.16, below.

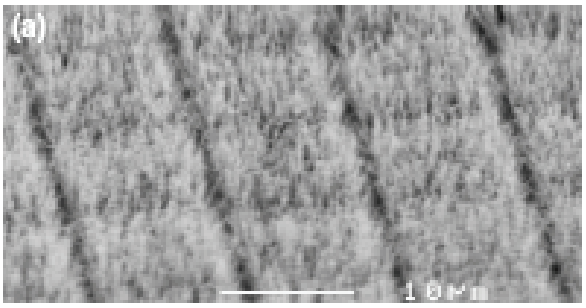

FIGURE 1.16: SEM IMAGE OF THE ZnO NANOWIRES PREPARED ON Si(100), USING AN ALD (ATOMIC LAYER DEPOSITION) OF ZnO[25].

The ZnO nanorods in the above image appear to be well aligned with respect to each other, and to the substrate. Separate arrays can be clearly observed and this was attributed to the seeding layer and substrate. It was also found that changing the seeding layer produced changes in the morphologies of the nanowires and it will be seen in section 1.1.3 that the method of preparation of the ZnO nanostructure also affects the nature of the emission to a certain extent.

Silicon and Silicon Dioxide (SiO_2) are not the only substrates that ZnO nanostructures have been grown or deposited on, many others have also been used, for example, GaAs[39(a)], α-plane sapphire[39(b)], amongst many others. It has been seen in these reports and others, that the different substrates result in slightly different emission spectra and morphologies of the nanorods/nanowires.

1.1.5 Topological Analysis of ZnO Nanostructures

Atomic Force Microscopy has been used to investigate the topology and uniformity of nanostructured ZnO samples. Xu and co-workers[29] used Contact Mode AFM to analyse the surface topography of the ZnO nanorod arrays prepared on Zn foil by a low temperature aqueous solution method. The image obtained appears to show an array of nanowire tips, however the image is not of great quality and could equally well be a

nanoparticulate surface. This result reflects the difficulty in obtaining good quality AFM data on well aligned ZnO nanowire surfaces. Mari *et al*[30] used AFM to determine the average height of ZnO nanocolumns on conducting glass substrates and obtained values ranging form 100 nm to 900 nm. This is quite a significant range, and again highlights the difficulty in obtaining accurate values for the ZnO nanorod dimensions, using this technique.

An example of the ability of Atomic Force Microscopy to measure the elastic modulus of ZnO nanowires was reported by Song and co-workers[31]. The ZnO nanowires were grown on an α- Al_2O_3 substrate using a Vapour Liquid Solid (VLS) process, and the array was prepared such that the nanowires were shorter and less dense, and therefore addressing a single nanowire with the AFM tip was possible, and via Hook's Law and other calculations, the elastic modulus of the nanowires was determined. ZnO nanowires capped with Au tips were also grown on Al_2O_3 by Park *et al*[32], and were analysed by AFM. When compared with the SEM data obtained for the same samples, it is seen that the features defined as the tips of the nanostructures are larger in the AFM image than they are in the SEM. This indicates that while using AFM in the determination of the dimensions of nanostructures is useful, care should be taken not to take the values as definitive values, rather, the technique should be used alongside other techniques such as SEM and TEM, in order for a more accurate picture of the system to be obtained.

Zhou and Li reported the solution based method[33] of the preparation of nanowires, nanorods, and eventually nanoparticles of ZnO on mica, and used AFM to analyse the various systems, some very nice images were obtained, particularly of the sparser networks of nanowires. An AFM image of the denser nanorod network is shown in FIGURE 1.17.

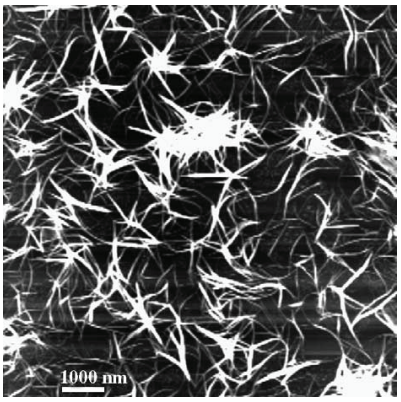

FIGURE 1.17: AFM IMAGE OF THE ZnO NANORODS GROWN ON A MICA SUBSTRATE[33].

Gupta *et al*[34] investigated phonon modes in ZnO nanorods prepared by pulsed laser deposition on Si, and used AFM to again measure the determine the dimensions of the nanorods. The images obtained indicate good uniform, well aligned and well isolated coverage of the substrate with the nanorods. They reported that the data obtained via AFM analysis agreed well with the SEM data.

1.1.6 ZnO Modified with Ruthenium Polypyridyl Complexes

The design of dye sensitized solar cells has advanced rapidly since the first report of the Grätzel cell[40]. In this system, the solar cell is composed of nanocrystalline TiO_2, with a photosensitizer bound to the surface. This photosensitizer often takes the form of a ruthenium polypyridyl complex, and in this report, the complex used was $RuL_2(\mu\text{-}(CN)Ru(CN)L'_2)_2$, where L= 2,2' bipyridine-4,4'-dicarboxylic acid, and L'= 2,2' bipyridine. Other complexes used have modified bipyridine ligands, and all are thought to bind to the surface via the COOH moieties on one or more of the bipyridyl ligands[41,42,43]. Over the years several important features of dye sensitized solar cells have been identified. An efficient dye sensitized solar cell should have a sensitizer that is panchromatic, that is, it should absorb efficiently in a broad spectrum of the wavelengths of visible light and, it should, once excited, inject electrons into the substrate efficiently. The energy levels of the sensitizer should be well matched to the lower level of the conduction band of the oxide substrate. This is so as to minimize energy losses during

the electron transfer step. A schematic diagram of a typical dye sensitized solar cell is shown in SCHEME 1.2, below. The first step involves absorption of light by the ruthenium dye, (Step 1) and subsequent injection of an electron from the dye molecule into the conduction band of the semiconductor (Step 2). Step 3 in the diagram refers to the back reaction which competes with the injection process, however this is generally much slower than the injection process. Step 4 is the reduction of the triiodide electrolyte by conduction band electrons from the semiconductor substrate, another important recombination route for the cell.

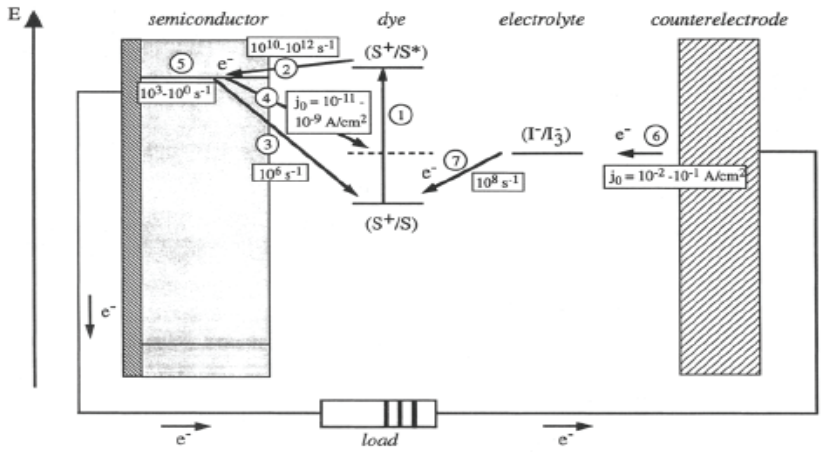

SCHEME 1.2: DIAGRAM OF A DYE SENSITIZED SOLAR (DSSC), SHOWING THE COUNTER ELECTRODE, AND THE RELATIVE ENERGY LEVELS OF THE RUTHENIUM DYE AND SEMICONDUCTOR SURFACE, SUCH AS TiO_2 OR ZnO.[42]

After the electron injection process, any electrons that do not take part in Steps 3 or 4 move through the semiconductor electrode and then to the external electrical circuit, and finally the couterelectrode, where they are used to reduce the triiodide electrolyte (Step 6). This then in turn reduces the oxidized dye in Step 7.

The surface area of a solar cell substrate is also an important factor. If the surface area can be increased, then it follows that a greater number of dye molecules can be deposited on the surface while still maintaining a monolayer coverage.

ZnO nanowire-based dye sensitized solar cells have been not been investigated as thoroughly as those based on nanocrystalline substrates. In particular, solar cells composed of ZnO nanowires and ruthenium complexes have not, to the authors

knowledge, been widely studied at all, with only a handful of references in the literature pertaining to this type of system[10,44,45].

The relative sparseness of reports in the literature can be attributed to several factors, possibly one of the most important being the contention[46], that one of the more promising and well studied ruthenium complexes, $[Ru(dcbpy)_2(SCN)_2]\cdot 2H_2O$, has the ability to lose the carboxylic acid moiety protons. This process makes the dye solution acidic which can dissolve the ZnO, to give Zn^{2+} and dye aggregates.

Importantly, the preparation of reproducible, well aligned ZnO nanowires in a scaleable manner for industrial applications is still in its infancy, in comparison to the well established science of nanocrystalline surfaces. The problem with the treatment process is that the dye molecules can attach to the nanowire, or can go into the spaces between the nanowires, called interstitial spaces. However, as will be seen later[44], this can be used to increase the efficiency in some cases. The concentration of the dye solution becomes very important. If the concentration of the dye loading solution is too high, then a monolayer will definitely not be formed and the ZnO nanowires can become saturated with the ruthenium dye. As reported by Anderson and co workers [48], this can result in lowering the efficiency of the cell.

Law *et al*[10], propose a ZnO nanowire based system where the dye sensitizer is $(Bu_4N)_2[Ru(dcbpyH)_2(NCS)_2]$, shown in FIGURE 1.19, and the system is illustrated in FIGURE 1.18, below.

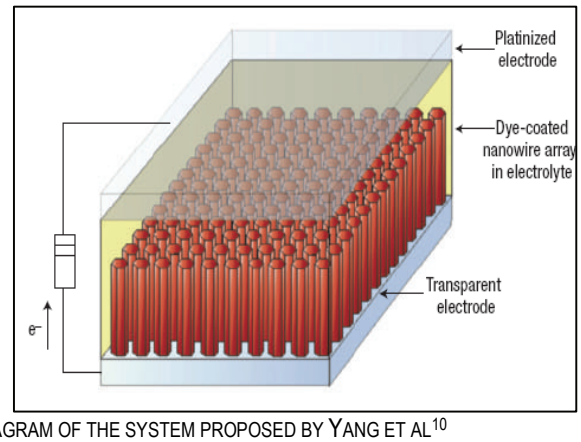

FIGURE 1.18: SCHEMATIC DIAGRAM OF THE SYSTEM PROPOSED BY YANG ET AL[10]

This system exhibits fast electron injection and the injection kinetics were compared for ZnO nanoparticle films and nanowire morphologies, both of which were dye sensitized. The nanoparticulate based system exhibited tri-exponential kinetics, and the time constants were of the order of <250fs, 20ps, 200ps, which are quite similar to the data obtained for sensitized nanoparticulate ZnO films investigated by Asbury et al[47]. The nanowire system exhibited bi-exponential kinetics, with time constants for the electron injection of <250fs and approximately 3ps. Asbury found that by increasing the dye loading concentration, the injection times remained the same, but the injection yield decreased. This leads to the conclusion that multilayers of dye molecules leads to a reduction in the injection efficiency due to aggregation of the nanoparticles, which can lead to particles of non-uniform size. Nanoparticle size is very important, as quantum confinement effects come into play. Non-uniform size distributions lead to a distribution of the density of states of electrons, and affect electron transfer rates. It is thought, however that the injection occurs from the first adsorbed layer of the dye.

The kinetics of the electron transfer process are affected by the morphology of the ZnO substrate, it is thought that nanoparticles have numerous different surfaces upon which the dye molecules can bind, while the dye molecules bind to the ZnO nanowires predominantly through the {100} crystal plane. It is also postulated in the same report[10], that the ZnO nanowires possess an internal electric field, which tends to force the injected electrons into the centre core of the nanowires, and therefore provides an efficient conduit for the electron transfer to the external circuit.

Baxter and co workers[45] have reported a ZnO nanowire based DSSC in which the sensitizer is N719, (structure shown in FIGURE 1.19, below). The nanowires were prepared via MOCVD and then immersed in oxygen plasma for 10 minutes before being immersed in the ruthenium complex solution. The overall energy conversion efficiency for the cell was reported as 0.5%. The Incident Photon to Current Efficiency (IPCE) maximum for the system was 6% at 525nm.

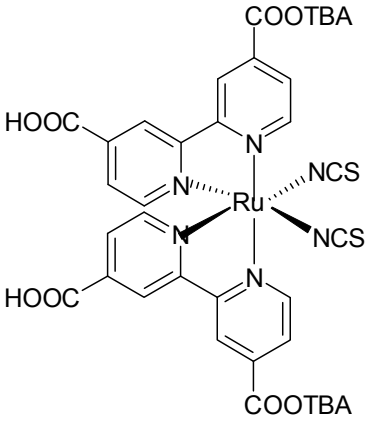

FIGURE 1.19: MOLECULAR STRUCTURE OF N719, $(Bu_4N)_2[Ru(dcbpyH)_2(NCS)_2]$

The idea presented by Baxter and co workers[44] utilizes a different type of system, it is a nanoparticle – nanowire system, sensitized with the ruthenium complex N719 (FIGURE 1.19), however, the nanoparticles in this case are not just the ruthenium complex, but ZnO nanoparticles. In this system, three potential arrangements are discussed. The first is where the concentration of zinc oxide nanoparticles is kept relatively low, in order to sparsely cover the edges of the nanowires. The second arrangement is where a higher concentration of ZnO nanoparticles is used, to not only cover the zinc oxide nanowires, but to fill in the interstitial spaces.

It was found that with this arrangement, the open circuit voltage, V_{oc}, is the same as that of the ZnO nanowire only system, but higher than the system utilizing just ZnO nanoparticles. It is suggested that the nanowires are more efficient electron transport pathways, for the electrons that arise from the excitation of the nanoparticles surrounding the nanowires. It is also inferred that the nanoparticles that harvest the electrons and inject into the nanowires also aid in the recombination process, by providing a larger surface area for recombination to occur.

The third arrangement discussed involves the nanoparticles sitting on top of the nanowires. In this case, the interstitial spaces are not filled in, due to the absence of the surfactant and binder.

It was found that this third arrangement was unfavourable as the nanowires were in fact slowing down electron injection into the electrode, due to their narrower diameter and

less dense coverage in comparison to a relatively thick film of ZnO nanoparticles. An illustration of the three different arrangements is shown in FIGURE 1.20, below.

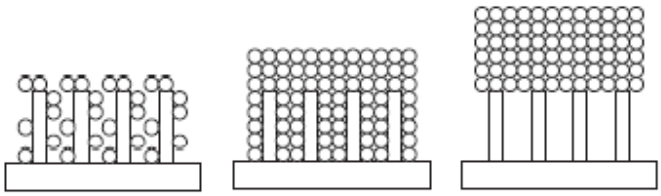

FIGURE 1.20: ARRANGEMENTS OF THE ZNO NANOPARTICLES (CIRCLES) AND ZNO NANORODS (VERTICAL RECTANGLES), IN SOLAR CELL DEVICES, (ADAPTED FROM REF [44]).

1.1.7 ZnO Conclusion

In conclusion, it has been seen that ZnO is an extremely versatile material, and ca be prepared in a wide variety of morphologies and nanostructures. In particular, ZnO nanorods have been the focus of a great deal of research over the years, with regard to their emissive properties at room and low temperature, and their morphologies. Their potential as a substrate in solar cells has also been investigated. The use of ruthenium complexes in solar cells has been extensively studied, and it has been found that they are a very promising candidate as a dye sensitizer. Some have been found to exhibit very fast electron injection into the ZnO substrate, however much of this work has been carried on nanocrystalline thin films of ZnO, as opposed to ZnO nanostructures with a defined morphology.

1.2 Carbon Nanotubes

1.2.1 History and Introduction

Carbon nanotubes are quite unique nanostructures with extremely interesting and fascinating electronic and mechanical properties. It is thought that they were first prepared in the 1970's by Morinobu Endo, and at this stage they were thought to be

filaments of carbon, of nanometer dimensions. Their structure was not elucidated until 1991 when Sumio Iijima used High Resolution Transmission Electron Microscopy (HR-TEM) to observe them.[49] It was found that these particular nanotubes were Multi Walled Nanotube (MWNT's). Such nanotubes consist of a central tubule, surrounded by layers of graphite, separated from each other by ~3.4Å. Around the same time, researchers in the Institute of Chemical Physics in Moscow independently discovered carbon nanotubes, but these had a greater diameter, but termed the tubes "barrelenes".
The interest in carbon nanotubes was reignited when a similar allotrope of carbon was discovered by Harold Kroto and Richard Smalley and co-workers. This new class of carbon-based molecules was called "fullerenes" and the best known of these is Buckminster-fullerene, a closed cage of 60 carbon atoms. It was found in 1990 by Kratschmer *et al*[50] that the soot formed from arcing graphite electrodes contained this C_{60} molecule. It was then possible to form large quantities of this fullerene in the laboratory, using this relatively simple process. This high yield process was the catalyst required for widespread and intensive investigation into this new class of compounds.
It was also because of this process that Iijima discovered the nanotubules on the negative electrode of the direct current arcing setup[49].
In 1993, another type of nanotube fullerene was synthesized for the first time[51], this consisted of the central nanotubule, without any of the surrounding graphitic outer layers, seen in the MWNT's. The tubules, called Single Walled Nanotubes (SWNT's) were later observed in bundles of aligned nanotubes, and it was seen that the nanotubes had a narrow distribution of diameters[52].

1.2.2 Synthesis Methods

1.2.2.1 Multi-Walled Nanotubes (MWNT's)

As mentioned in the previous section, MWNT's were first prepared by current arcing between two graphite electrodes, in 2/3atm (~500torr) of helium. An optimized arcing

method was reported by Ajayan *et al*, in 1992, such that most of the carbon anode is deposited on the cathode as carbon nanotubes and graphite nanoparticles[53].
Other methods have been employed in the synthesis of MWNT's, such as plasma arc jets[54], by controlling the quenching process in an arc between a graphite anode and a cooled copper cathode[55], and electrolysis of molten halide salts in an argon atmosphere, using carbon electrodes[56],
In addition to the various arcing techniques reported, carbon nanotubes have been prepared via the decomposition of hydrocarbons, such as acetylene under inert conditions over transition metal catalysts at 700°C[57-59], Similarly, they can be prepared using metallocene complexes[60].

1.2.2.2 Single-Walled Nanotubes (SWNT's)

Single Walled Nanotubes were first prepared by Iijima *et al*, and Bethune and co-workers and were reported in the same issue of Nature[51-52]. The method used was a metal-catalysed direct current arcing of graphite rods under a helium atmosphere. The anode was filled with metal powders (Fe, Co, Ni) while the cathode used was pure graphite. The SWNT's were found deposited behind the cathode. Over the years various metals have been used as catalysts in this process, Mo[61], Fe/Ni [62] and metal oxides[63].
Single Walled Nanotubes can also be prepared using the pyrolysis of metallocenes with acetylene. Amorphous carbon is also produced in this process, but this can be reduced by reducing the acetylene relative to the metallocene, and by adding hydrogen to the argon stream[64].
SWNT's can still contain many impurities, such as amorphous carbon and nanoparticles of the catalyst coated with carbon. These can be removed by heating in air at around 300°C, and by subsequent microfiltration[65].
Several review articles[66-68], have been written over the last decade on the numerous production and purification methods developed for carbon nanotubes, and the many investigations into the chemistry of carbon nanotubes[69-71]. It is beyond the scope of this work to provide an exhaustive investigation of these reports, as this work is not concerned with the comparison or development of production methods, but rather with

the formation of carbon nanotubes/polymer composites and the subsequent analysis of these composite systems.

1.2.3 Physical and Chemical Properties

1.2.3.1 Structural Features

The physical structure of carbon nanotubes has primarily been investigated using Transmission Electron Microscopy (TEM). It has been shown that the MWNT's contain a central microtubule surrounded by graphitic layers[49]. However, similar to the parent molecule, buckminsterfullerene, the layers themselves are composed of six membered rings of the carbon atoms, resulting in the lattice structure shown in FIGURE 1.20, below. The "caps" of the nanotubes have been shown to consist of pentagons of carbon atoms, to provide the necessary curvature[72].

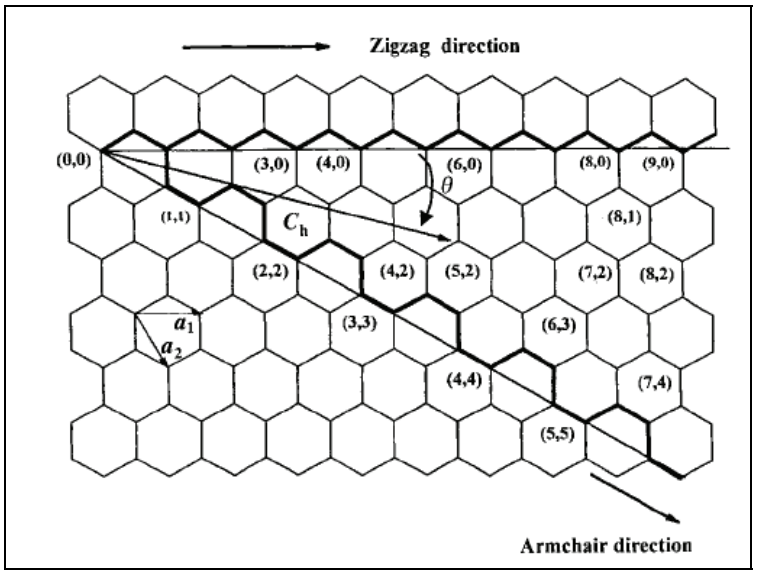

FIGURE 1.20: THE DIFFERENT ORIENTATIONS OF THE SIX MEMBERED RINGS AROUND THE HELICAL AXIS OF THE NANOTUBE. THE DIRECTION OF THIS AXIS DETERMINES TO A CERTAIN EXTENT, THE ELECTRONIC PROPERTIES OF THE NANOTUBE[73].

Structural investigations have also shown that the diameter of the tube is the same as the diameter of the parent fullerene molecule. This is evidence for the possibility of the nanotube being capped at either end. The lattice structure of the nanotube is the same as that which forms crystalline graphite, and this is how a tube can also be visualized as a two dimensional "sheet", as shown in FIGURE.1.20, above.

1.2.3.2 Electronic Properties

This somewhat unusual lattice structure means that carbon nanotubes can be either conducting or semiconducting, and the degree of conductivity depends on the degree of helicity of the tube and the number of six-membered rings per turn around the tube. This is illustrated in FIGURE 1.20, on the previous page. The degree of conductivity or semiconductivity is also due to the scattering of the electrons within the lattice. The electrons around the Fermi energy (E_F) are in most directions backscattered by the atoms in the lattice, and this leads to an energy band gap similar to a semiconductor. There are however, certain directions within the lattice where the electrons interfere destructively with each other, and this results in a suppression of the backscattering, and, consequently, metallic behaviour[74]. This only occurs in the line running through the length of the nanotube, *y*, and in directions 60°, 120°, 180°, and 240° away from *y*. The situation is shown more clearly in FIGURE 1.21, below.

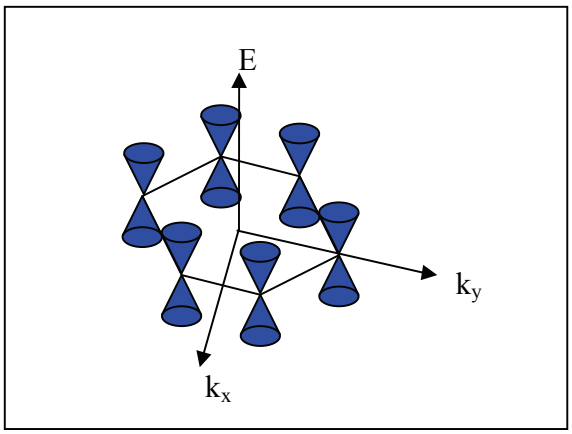

FIGURE 1.21: THE ENERGY OF THE CONDUCTING STATES IN GRAPHENE, AS A FUNCTION OF K, THE WAVEVECTOR OF THE ELECTRONS. THE MATERIAL DOES NOT CONDUCT, EXCEPT ALONG CERTAIN, SPECIAL DIRECTIONS WHERE "CONES" OF STATES EXIST. (ADAPTED FROM REF 74).

The electronic structure of graphene at low energies consists of a series of cones. This means that in the *y* and other "metallic" directions, the cones are sliced through the middle, and the energy as a function of k, the wavevector of the electrons, is also a slice through the centre of the cone, and results in a 1-D metal.

1.2.3.3 Chemical Modification of Carbon Nanotubes with Polymers and Surfactants.

1.2.3.3.1 Sodium Dodecyl Sulphate-Based Polymers

There have been many reports in the literature concerning the modification of carbon nanotubes with a wide variety of chemical moieties, such as cyclodextrins[75], fluorine[76], hydrogenation[77]. One of the most interesting modifications of carbon nanotubes was reported by Tour[78] involving aryldiazonium salts reacted with Single Walled Nanotubes coated along the walls with Sodium Dodecyl Sulphate (SDS). This functionalization and subsequent removal of the SDS from the nanotubes resulted in an efficient unbundling or exfoliation of the nanotubes in DMF. This surfactant, SDS has since been regarded as a standard in the exfoliation of nanotubes, due to its high efficiency, and has been used by many groups[79-82].

The modification of the Single Walled Nanotubes with the aryldiazonium salts reported by Tour in ref [78] was monitored using UV-vis spectroscopy (FIGURE 1.22, on the next page) and the spectrum of the reaction mixture (SDS-SWNT + aryldiazonium salt) was compared with that of SDS-SWNT, and the spectrum of the reaction mixture after the SDS was removed. There is little difference between the three spectra, the spectra of the reaction mixture before and after removal of the SDS are cleaner than that of the SDS-SWNT solution and there is a feature in the SDS-SWNT solution around 1100-1300cm^{-1} that is not observed in the other two spectra. These are thought to be the first van Hove singularities[83], E_{11}, of the nanotubes, and it is argued that the disappearance of these transitions is evidence for the removal of the SDS surfactant. It is interesting to note that these transitions are not really observed in the spectra of the reaction mixture, as the SDS is still present in the system at this point.

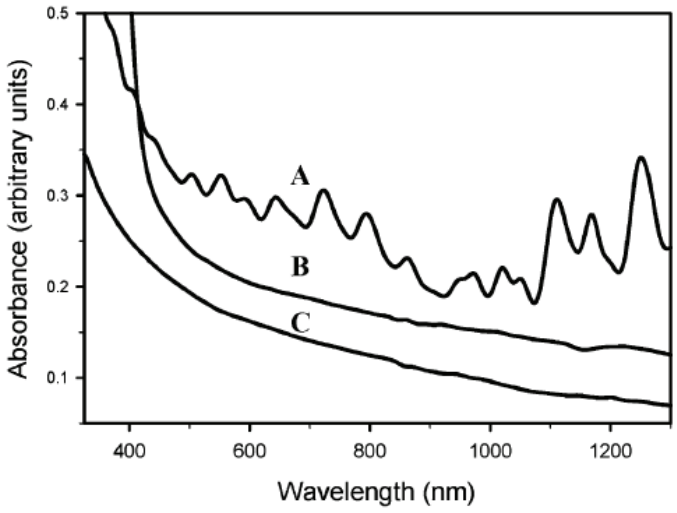

FIGURE 1.22: ABSORPTION SPECTRA OF (A) SDS-COATED SWNTS, (B) ALIQUOT OF THE REACTION MIXTURE (SWNT-(Ph-Cl)$_n$) AFTER 10MIN, AND (C) SWNT-(Ph-Cl)$_n$ AFTER ISOLATION, REMOVAL OF THE SDS, AND DISPERSION IN DMF[78].

Recently[84], the surface coverage of exfoliated carbon nanotubes was determined by four different methods, and the results were compared. The nanotubes used in the experiments were HiPCO SWNT's and the nanotubes were exfoliated or solubilized in water, using SDS as the surfactant. The exfoliation process involved sonication of the solution using an ultrasonic tip, and this process was monitored using UV-vis spectroscopy, surface tension measurements, thermogravimetric analysis, and a variant of Marons titration. The analysis of the solutions by UV-vis spectroscopy is the most relevant to the work described in this thesis, since this is the primary method of analysis used for the composite solutions prepared and described in this authors work. It was found in these experiments and in previous work by the same group[85] that the UV spectra of the SDS-SWNT solutions increased to a maximum of approximately 0.3 at 650nm, with increasing sonication, and it is thought that this is the point of maximum exfoliation. It is seen that the relationship between the plateau of the UV absorbance and the SDS concentration is linear, indicating that the surface coverage of the carbon nanotubes with SDS molecules is complete, and this is also suggested by results by Matarredona *et al*[86], which used a slightly different surfactant, sodium dodecylbenzenesulfonate, (NaDDBS).

Polyvinyl pyridine, (PVP) has also been used in the exfoliation of carbon nanotubes. Sinani and co-workers[87] used modified poly 4-vinyl pyridine (P4VP), such as poly(N-

cetyl-4-vinylpyridinium bromide-co-N-ethyl-4-vinylpyridinium bromide-co- 4-vinylpyridine) and poly(vinylpyrrolidone-co-allylamine), and analogues of these, to exfoliate SWNT's, and used AFM to investigate the degree of dispersion of NT's when stabilized by the various polymers. The structures of these polymers, and other relevant complexes can be found in the Appendices. It was found that the polymers used dispersed the nanotubes quite well. UV-vis data were reported and are shown in FIGURE 1.23, below.

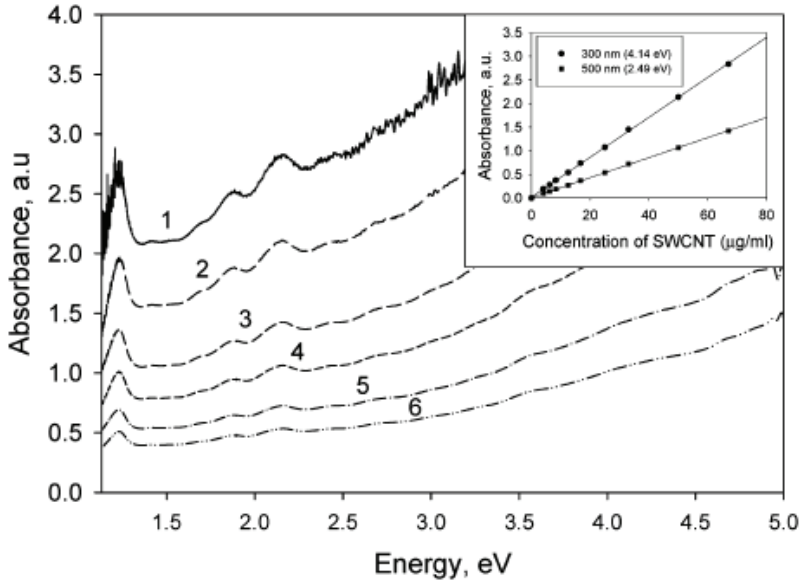

FIGURE 1.23: UV DATA OF THE SWNT-POLYMER COMPOSITES AT VARYING CONCENTRATIONS OF SWNT'S[87].

The van Hove singularities were still visible in the nanotubes which had been modified with polymer. It was suggested that the exfoliation of the polymer around these nanotubes did not appear to affect the overall morphology of the nanotubes, or the aromatic system responsible for the strength and conductivity properties This suggestion was further indicated by the AFM images reported. In addition, It is also interesting to note in FIGURE 1.23 that the UV spectra of the composite of one of the polymers, poly(N-cetyl-4-vinylpyridinium bromide-co-N-ethyl-4-vinylpyridinium bromide-co- 4-vinylpyridine), at varying concentrations of the nanotubes, shows non-zero baselines similar to those observed at 800 nm in the data to be presented in this work, indicating that the high baseline is not necessarily indicative of scatter, it may be an indication of exfoliation.

Rouse[88] dispersed SWNTs in an alcoholic solvent using sonication with P4VP and obtained good dispersions, 0.3g of SWNT's per litre of alcohol with 0.6g of PVP. They found that it was possible to disperse the SWNT's in a variety of alcoholic solvents, and that solutions were stable up to approximately 6 weeks after preparation.
Previous work[89] by the same group focused on the same system, dispersed in DMF, and then deposited on a silicon wafer, and analysed with AFM and SEM. It was found that with increased adsorption of the composite on the substrate, the AFM images showed a denser network of the composite nanotubes.

1.2.3.3.2 Metal Complex-Based Polymers And Complexes

There have not been, to the author's knowledge, many reports in the literature of carbon nanotubes modified or exfoliated in solution using polymers with pendant metal complex moieties. This has been due perhaps to the overwhelming interest in simpler polymers such as SDS, PVP and PmPV and derivatives, since they tend to be more easily obtained, being either commercially available, or reached through relatively facile synthetic routes. Polymers with metal complexes are more difficult to synthesise, and so have played a lesser part in the investigation of exfoliation methods. However, this does not mean that they do not have significant advantages over more traditional polymers. Ruthenium complex-based polymers, like standard ruthenium complexes have excellent photophysical and electrochemical properties, and the possibility exists for the tailoring of the ligands to improve the solvation of the complex in various solvents. This factor becomes important when the molecular weight of PVP is considered, if the additional moieties did not contribute to the salvation process of the polymer, then the exfoliation of the nanotubes would be far less efficient.
A report by Yonemura *et al*[90] described the use of a modified version of tris bpy, $[Ru(bpy)_3]^{2+}$-PSS, where the PSS is poly(sodium 4-styrenesulfonate) in wrapping around SWNT's.
The solutions were then deposited on an ITO electrode and photocurrent measurements were performed. They were also deposited on mica, and were analysed by AFM. The morphology of the composites on the surface was determined by cross sectional analyses

of the AFM images. It was found that the SWNT/PSS/Ru(bpy)$^{2+}_3$ composites were slightly bigger than the SWNT/PSS composites, which were also studied, and the SWNT/PSS/[Ru(bpy)$^{2+}_3$] composite was postulated adopt the arrangement as shown in FIGURE 1.24, below[90].

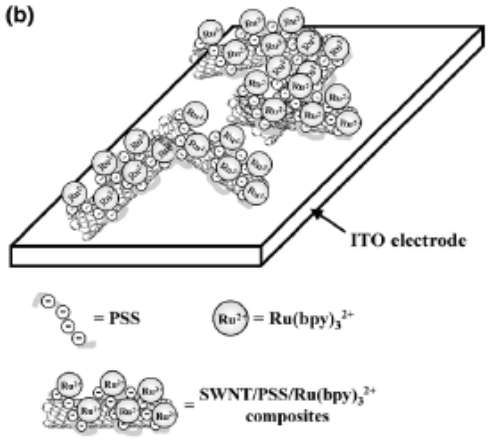

FIGURE 1.24: SCHEMATIC REPRESENTATION OF THE SWNT/PSS/Ru(BPY)$^{2+}_3$ COMPOSITE (TAKEN FROM REF [90]).

Jousselme and co-workers[91] have recently reported the electrochemical deposition of diazonium salts of ruthenium bpy and terpy complexes onto SWNT's. This was carried out by sweeping the potential 10 times between 0V and -2V or 1.2V to -2V. Cyclic Voltammetry (CV) measurements were then carried out on the system. The films of the ruthenium complex were electrochemical grafted, and showed an intense, but reversible oxidation wave. E$^{o'}_{ox}$ was found to be 0.97V. The films were also investigated using UV-vis spectroscopy, and it was observed that van Hove peaks of the nanotubes were absent after the electrografting of the ruthenium complex, indicating that the π network of bonds has been disrupted by the grafting.

Dendritic ruthenium polynuclear complexes have also been bound to carbon nanotubes, reported by Chaturvedi and Poler[92]. $[\Lambda_6\Delta_3\Lambda\text{-}Ru_{10}]^{20+}[PF_6^-]_{20}$, which was composed of 10 units of modified [Ru(phenanthroline)$_3$] $(PF_6^-)_2$, was found to bind strongly and efficiently to the SWNT's. The system was studied with AFM, SEM and UV-vis, and the morphology observed with AFM indicated that the nanotube ends bind with one of the endo- or exo-receptors of the ruthenium dendrimer.

Recent work done by our own group[93], involved the interconnection of carbon nanotubes using a ruthenium polypyridyl complex, ($[Ru(bpy)_2(H_2dcbpy)](PF_6)_2$) as the connecting

moiety. Various surface analysis and spectroscopic techniques were employed to investigate this rather novel system, such as STM, AFM and emission spectroscopy. Further from this work, Ru metallopolymers were used to solubilize SWNT's and MWNT's, using sonication in methanol[94]. The metallopolymer used was the same one used in the work to be presented in this thesis, $[Ru(bpy)_2(PVP)_{10}Cl]Cl$, where PVP is poly (4-vinyl-pyridine). The synthesis of this polymer and its analogues was reported by Clear and co-workers[95]. UV-vis spectroscopy, Tapping Mode AFM, Raman and TEM were used to probe the system used in Ref [94]. It was found that the structure of the metallopolymer was not significantly changed when wrapped around the nanotubes. TEM and AFM images obtained suggest an efficient wetting of the nanotubes with the polymers, and therefore an attractive force between the polymers and the nanotubes, therefore having the potential of being a stable composite material.

Finally, an interesting paper was published[96], in which a combination of two of the main substrates investigated in this thesis, ZnO and carbon nanotubes, was investigated as a peculiar kind of composite system. Multi-walled Carbon Nanotubes were heat treated with Zn and as a result of this process, ZnO nanowires were produced on the outer walls of the nanotubes. The system was probed with Field Emission Scanning Electron Microscopy (FE-SEM) and a representative image is shown in FIGURE 1.25, on the next page.

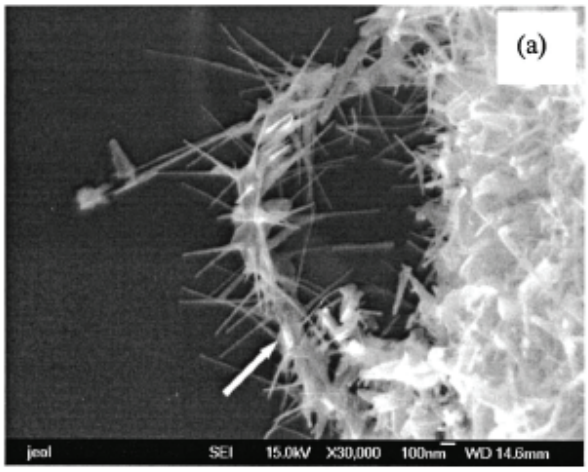

FIGURE 1.25: FIELD EFFECT SCANNING ELECTRON MICROSCOPY IMAGE OF ZnO NANOWIRES GROWING ON THE SURFACE OF A CARBON NANOTUBE[96].

In conclusion, much work has been carried out, both on investigating the properties of carbon nanotubes themselves and composite materials of carbon nanotubes and polymers. Particular emphasis has been placed on those composites with ruthenium based polymers. It has been found that carbon nanotubes can be solubilized or exfoliated using polymers such SDS and P4VP, however, exfoliation using metallopolymers is being reported, and these metallopolymers also have very interesting photophysical and electrochemical properties. This exfoliation process can be followed using UV-vis spectroscopy. The composite materials have also been deposited on various substrates, and have been probed by various surface analysis techniques, and in some cases, the nature of the "packing" of the polymer around the nanotube can be elucidated.

1.3 Introduction to the Photophysics of Metal Complexes

The study of the mechanisms and consequences of the interaction of light with matter is a vast subject area, and the concept itself is the scientific basis for many natural phenomena. This section will introduce some of the concepts and ideas of photophysics, which are important for this work, particularly the section dealing with the lifetimes of excited states of various ruthenium polypyridyl complexes, and also in the absorption/emission data, presented in the ZnO and carbon nanotubes chapters.

1.3.1 Absorption and Emission

The first step in the production of an excited state is the absorption of light by the material (black solid line, FIGURE 1.26(A), above). This process is considered to be instantaneous. Various excited states are possible and the one that is produced is dependant on the energy of the incident photon. The excited state that is formed from this initial excitation is usually one in which the positions of the nuclei are exactly the same as they are in the ground state, and therefore the molecule can be said to be vibrationally excited. This is because the time required for the absorption of a photon (and the initial excitation) is so short (generally 10^{-15}s) that the nuclei do not have

sufficient time to be appreciably displaced. This is known as the Franck-Condon principle.

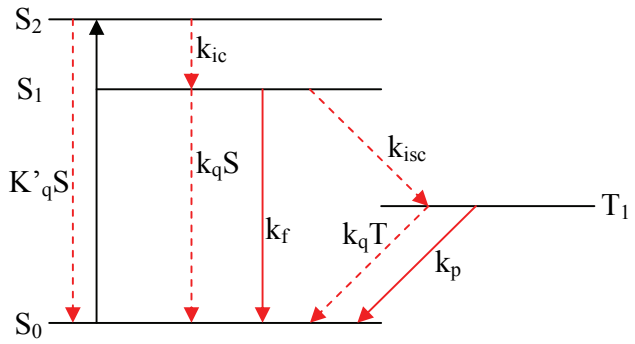

FIGURE 1.26(A): SCHEMATIC ENERGY LEVEL DIAGRAM SHOWING THE INITIAL EXCITATION (BLACK SOLID LINE——), AND THE POSSIBLE RADIATIVE DEGENERATION PATHWAYS (RED SOLID LINES——), WHICH OCCUR WITH THE EMISSION OF A PHOTON, AND NON RADIATIVE PATHWAYS (RED DASHED LINES ----). SINGLET STATES ARE DENOTED BY S'S AND TRIPLET STATES ARE DENOTED BY T'S. (ADAPTED FROM REF [97])

It is important to note however, that the positions of the nuclei in this "initial" excited state are not usually the equilibrium positions. This initial excited state is referred to as the Franck – Condon state. The energies of possible excited states relative to each other and the ground state are usually illustrated in a *Jablonski diagram*, such as that shown in FIGURE 1.26(A), and the Franck-Condon state would be denoted as S_2 in this diagram. The disparity between the structures of the ground and excited states results in a shift observed in the absorption and emission spectra. This is due to the fact that the vibrationally excited states lose some of their energy via non-radiative process, before an equilibrium is reached. This shift that is observed in the spectra is called Stokes Shift and is calculated from the difference in energy between the maxima of the absorption and emission bands. The Jablonski diagram for $Ru(bpy)_3$ or an analogue can also be represented as a potential energy surface, as illustrated in FIGURE 1.26(B), on the next page.

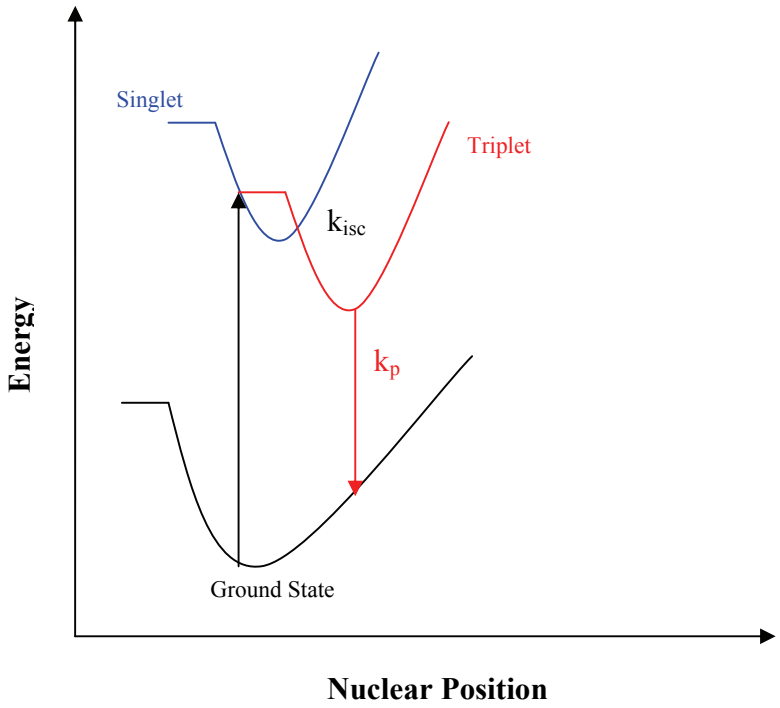

FIGURE 1.26(B): REPRESENTATION OF FIGURE 1.26(A) AS A POTENTIAL ENERGY SURFACE, SHOWING THE DISPLACEMENT OF THE NUCLEI IN THE EXCITED STATE WITH RESPECT TO THE GROUND STATE.

Once the molecule has undergone conversion to its lowest excited state and has reached its equilibrium position via vibrational relaxation, it is then considered to be in the Thermally Equilibrated Excited or THEXI state. The THEXI state can be considered as the "parent" state for the majority of the emissive processes that occur, for example, k_p, in FIGURE 1.26(A).

There are two broad possibilities regarding the nature of the emitting state, first it may be the initial excitation or THEXI state, or secondly, this THEXI state may be converted into the emitting state, by two possible processes. The first of these is radiationless conversion to a state of the same multiplicity (spin allowed, *internal conversion*, S_2 to S_1 in FIGURE 1.26(A)), or, to a state of different multiplicity (formally spin forbidden, *intersystem crossing*, S_1 to T_1 in FIGURE 1.26(A)).

There are two main types of emission, fluorescence, and phosphorescence. The former refers to radiative decay between two states of sharing the same multiplicity, while the latter indicates a radiative deactivation between two states of differing multiplicity.

In contrast to radiative decay processes, deactivation may also occur via non-radiative pathways, such as k_qT or k_qS in FIGURE 1.26, on the previous page, the "T" and "S" in the process names referring to the excited state which is being deactivated, "T" indicating that it is a triplet state, and "S" showing it is a singlet state. It is important to note that the nature of the deactivation process, energy and lifetime of the THEXI state are all influenced by the nature of the ground and excited state molecular orbitals. It is for this reason that the probing of the photophysics of molecules yields valuable information regarding the excited state properties.

A simple diagram illustrating the formation of the molecular orbitals for the metal complex is shown in FIGURE 1.27, below. The molecular orbitals for the metal complex are obtained from the orbitals for the metal on the left hand side of the diagram and those for the ligand, on the right hand side. It is seen that the ligand has three different orbitals, bonding σ_L and π_L orbitals, and an antibonding π^*_L orbital.

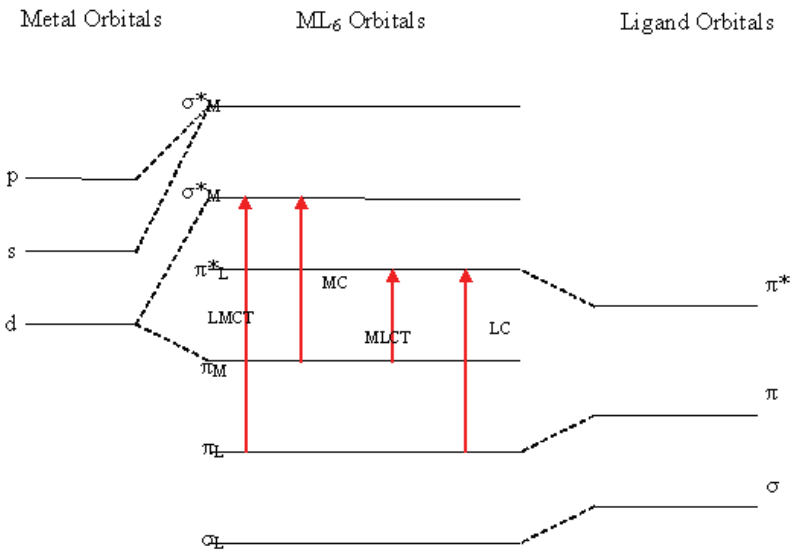

FIGURE 1.27: THE RELATIVE ENERGY LEVELS IN AN OCTAHEDRAL INORGANIC METAL COMPLEX, (ADAPTED FROM REF [99]).

The metal also has three orbitals, a non-bonding π_M orbital, and two antibonding orbitals, both are σ^*_M in nature, however one is in the e_g band. As expected, the

electronic structure of the complex is strongly dependant on the relative energies of the metal and ligand orbitals.

The transitions shown in FIGURE 1.27 are the possible absorption processes. From these we can identify the possible emission processes, by looking at the excited state that the emission originates from. These can be summarized as follows:

1. The transition $\pi_M \rightarrow \pi^*_L$ in FIGURE 1.27 above would be identified as an MLCT (Metal To Ligand Charge Transfer). Deactivation of this π^*_L state generally results in a quite intense emission at low temperatures, and at room temperature results in a luminescence which can be solvent dependant[100].
2. The transition $\pi_L \rightarrow \sigma^*_M$ in FIGURE 1.27 above would be identified as an LMCT (Ligand To Metal Charge Transfer). Deactivation from this metal based antibonding sigma orbital have rarely been observed in solution, and have not been well characterized.
3. The transition $\pi_M \rightarrow \sigma^*_M$ in FIGURE 1.27 above would be identified as an MCCT (Metal Centred Charge Transfer). The lifetime of the state resulting from this transition tends to be very short, and no emission tends to be observed, instead radiationless decay to the ground state occurs or a ligand dissociation reaction is observed[105(i)].
4. The transition $\pi_L \rightarrow \pi^*_L$ in FIGURE 1.27 above would be identified as an LCCT (Ligand Centred Charge Transfer). This emission from the excited state resulting from this transition is quite well structured at low temperature and tends to resemble the structure of the free ligand, which suggests the excited state is based solely on the ligand. This excited state tends to have a longer lifetime than the MLCT excited state, at low temperature[105(i)].

Emission of light is not the only possible process for the deactivation of an excited state in a metal complex. The excited state can be used in chemical reactions and this is the basis of the photochemical production of numerous compounds, an extremely fast

growing field within chemistry today. The various deactivation possibilities open to the excited state are shown in FIGURE 1.28, below.

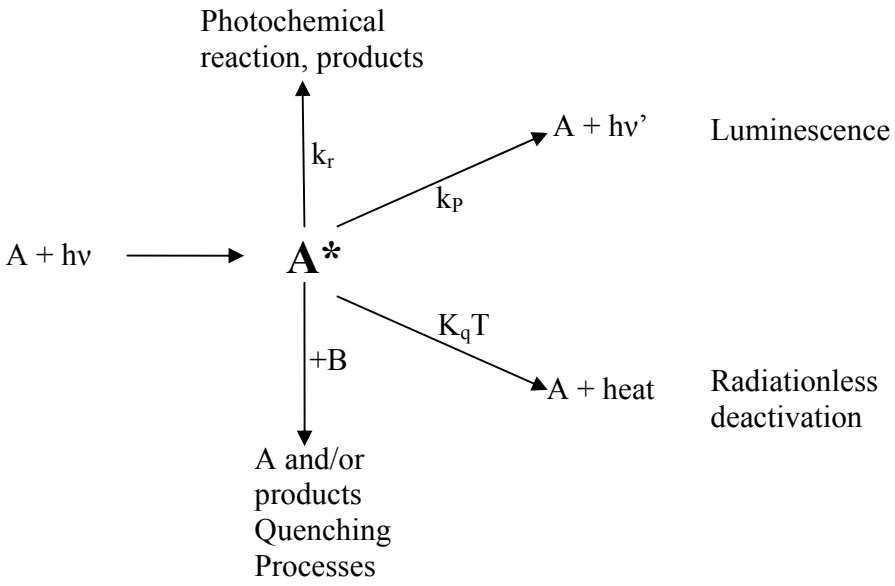

FIGURE 1.28: SCHEMATIC DIAGRAM OF THE POSSIBLE EXCITED STATE DEACTIVATION PATHWAYS FOR A METAL COMPLEX (ADAPTED FROM REF [102].

Bimolecular quenching is a common deactivation process in inorganic photophysics. In this process, the metal complex that has been excited transfers its energy to a second species, usually in solution. This energy transfer process can be of two varieties, the first is that of long range resonance based transfer, which is less common in solution, it is more prevalent in rigid media, and the second is collisional energy transfer[101]. This second process is more common with transition metal complexes in solution, and hence is more related to the work described in parts of this thesis. The quenching takes place between an excited donor molecule D*, and an acceptor, A, as described by EQUATION 1.1, below,

$$D^* + A \rightarrow D + A^* \qquad \text{EQN 1.1}$$

As seen in EQUATION 1.1, above, the transfer results in the molecule being excited, however it is also possible via intermolecular electronic to vibrational energy conversion for the following process[101] to occur, (EQUATION 1.2),

$$D^* + A \rightarrow D + A \qquad \text{EQN 1.2}$$

The molecule may also act as a sensitizer in photoreactions, providing synthetic pathways to products that are not possible or feasible to obtain using conventional synthetic methodologies.

Each of the deactivation processes shown in FIGURE 1.28, as with the excitation processes seen in FIGURE 1.26, has an associated rate constant, called "k". The excited state lifetime of the complex or species in solution is the sum total of these processes that actually occur, according to EQUATION 1.3.

$$\frac{1}{\tau} = \sum(k_r + k_{nr}) \qquad \text{EQN 1.3}$$

where k_r and k_{nr} are the rate constants for the radiative and non-radiative processes, respectively, and τ is the excited state lifetime.

The emission quantum yield of the complex can also be determined using the rate constants, in EQUATION 1.4, below,

$$\Phi_{em} = \frac{k_r}{\Sigma(k_r + k_{nr})} \qquad \text{EQN 1.4}$$

1.3.2 Ruthenium Polypyridyl Photophysics

The metal complexes of ruthenium and osmium, have been amongst the most heavily studied transition metals, with reports in the literature dealing with the syntheses[103] and photophysical properties[98,104] of $[Ru(bpy)_3]^{2+}$, the paradigm complex, and its numerous analogues numbering in the thousands, as well as being the subject of a large number of review articles[100,102,105].

The most intensively studied Ru(II) complex is $[Ru(bpy)_3]^{2+}$. This complex has certain desirable properties, among them a strong, room temperature emission, a long lived excited state, (of the order of hundreds of ns), and it is also easily prepared. As stated in

the previous paragraph, many analogues of this parent complex, $[Ru(bpy)_3]^{2+}$ have been prepared, however, the parent complex is still the standard complex for photophysical and most synthetic studies, as it remains the best understood complex of its type. Ruthenium (II) is a d^6, low spin system. This implies that the t_{2g} orbitals are filled. The orbitals in the uncoordinated 2,2'-bipyridine ligands show predominantly σ character on the nitrogen atoms, and exhibit π character in the orbitals on the aromatic rings, which tends to be delocalized on the rings themselves. The π orbitals are π donor and π* acceptor orbitals. Studies on the Ru-N bond lengths show significant back bonding into the π* ligand orbitals[113]. FIGURE 1.29, below shows the absorption spectrum of $[Ru(bpy)_3]^{2+}$ in aerated acetonitrile.

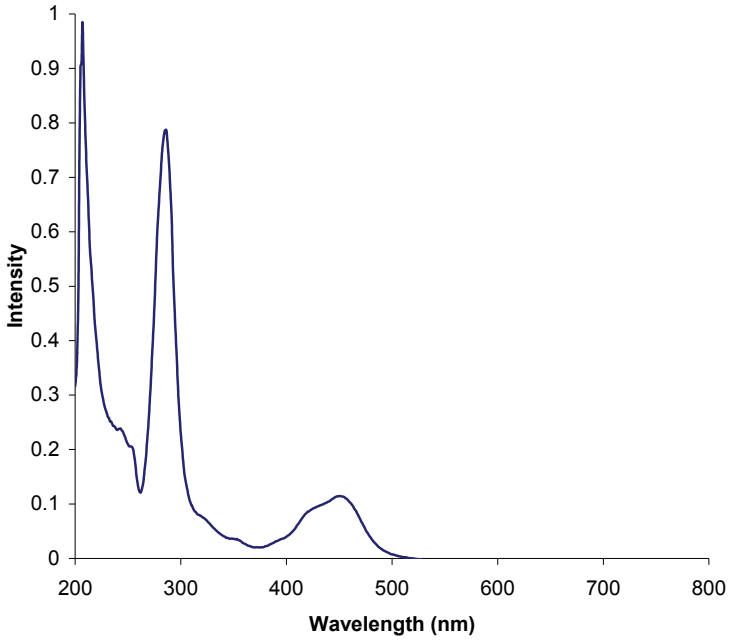

FIGURE 1.29: ABSORPTION SPECTRUM OF $[Ru(BPY)_3]^{2+}$ IN AERATED ACETONTRILE.

The intense band at 286nm is attributed to the Ligand Centred (LC) π → π* transition. The other main band observed at 455nm is assigned to the Metal - to - Ligand - Charge - Transfer (MLCT) transition, which is denoted as d → π*.

In general for most Ru(II) polypyridine complexes the initial excited state is the singlet MLCT state, as seen in FIGURE 1.26(B), however the lowest excited state is the ^{3}MLCT state, which is considered to be comprised of a cluster of MLCT states which are

predominantly triplet in character, which was postulated by Meyer and co-workers[104(d)], through low temperature studies, and also by Crosby and co-workers[106,114]. This state is reached from the ^{1}MLCT state via Inter System Crossing (ISC). This leads to the conclusion that this is the predominant emitting state, by virtue of Kasha's rule[115]. This rule states that only the lowest excited state, and the states that can be populated due to Boltzmann distribution, are responsible for the photochemistry and photophysics of the complex. FIGURE 1.30 shows a typical emission spectrum obtained for $[Ru(bpy)_3]^{2+}$ in aerated ACN, at room temperature. As seen in FIGURE 1.27, the metal centred (^{3}MC) state lies above the MLCT state. It can be populated thermally by the lowest ^{3}MLCT level. This population results in the ^{3}MC state becoming distorted with respect to the ^{3}MLCT state and this can lead to dissociation of ligands, due to the increased Ru-N bond lengths.

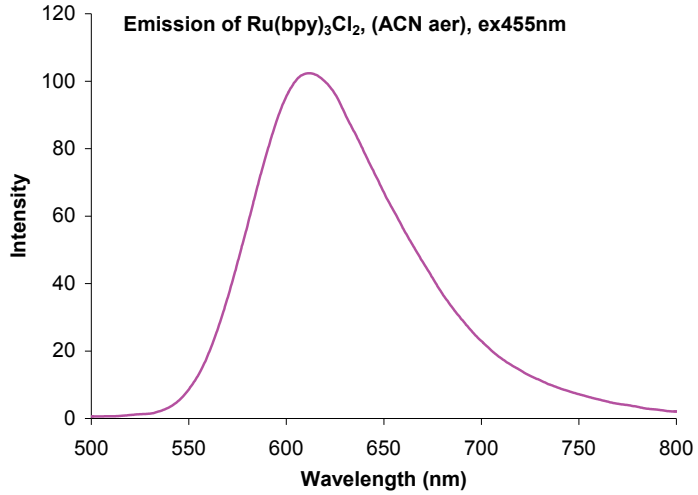

FIGURE 1.30: EMISSION SPECTRUM OF $[Ru(BPY)_3]^{2+}$, RECORDED IN AERATED ACN, AT ROOM TEMPERATURE, USING AN EXCITATION WAVELENGTH OF 455NM.

The excited state emission from Ru(II) tris bpy in aerated acetonitrile is observed at approximately 611nm, and this emission is blue or hypsochromically shifted to approximately 582nm, when it is measured in an ethanol:methanol (4:1) glass at 77K. This implies that the emission energy is higher at lower temperatures, and this is exmplained by the lack of stabilization of the excited state by the solvent sphere, as a result of the lack of solvent mobility.

The investigation of the nature of the excited state throughout the range of temperatures between 77K and room temperature is complicated by the effects of fluid to glass

transitions which occur at intervening temperatures. It has been observed by Balzani *et al*[107], amongst others, that there is a discontinuity in the emission profile of ruthenium polypyridyl complexes between the fluid and glassy states and have investigated to model the variations observed in the emission lifetimes empirically. They have postulated from this work that the source of this fluid to glass transition, and its consequences is the effect that changing viscosity has on the low frequency Ru-N stretching and bending vibrations. Other groups have put forward alternative theories, such as orientation of solvent dipoles[108], non-equilibrium salvation and dielectric friction.

At lower temperatures, the solvent loses its ability to stablise the excited state of the complex, via the method it adopts at room temperature, that of solvent sphere reorganization. This leads to a higher energy excited state at low temperatures, and consequently a blue shift in the emission λ_{max}. This is more pronounced in the MLCT bands, as these transitions require significant solvent reorganization to accommodate the charge distribution, and thus stabilize the excited state formed.

The investigation of Ruthenium polypyridyl complexes presented in this thesis is based on complexes synthesized by the group of Sven Rau, University of Jena, Germany. These complexes are based on a *bis* bpy ruthenium core, with the bpy ligand modified with methyl esters or butyl groups, and with the third ligand being a phenanthroline derivative, or another modified bpy. Excited state lifetimes of analogues of these complexes in various solvents have been investigated by the Vos group before[109-112].

It has been seen in the photophysical investigation that addition of bromine atoms on the phenanthroline ligands significantly alters the electron density of the phenanthroline ligands, and this is seen in the red shifts in the absorption and emission spectra of the bromo-modified complexes compared to those of the complex with the standard phenanthroline ligand. These bromo substituted phenanthroline ligands have been further modified[112] with aryl groups, and the complexes exhibit lower energy Ligand Centred transitions, and more intense $\pi \rightarrow \pi^*$ transitions, and red shifted MLCT bands. The complexes have been seen to be oxygen sensitive, and exhibit very long lifetimes. These shifts have been observed with other similar complexes[110], and it has been suggested by Rau and others that these red shifts and overlap of the $\pi \rightarrow \pi^*$ transition

with the MLCT band may result in more efficient sensitizers, with increased absorption in the visible region. Investigation of the nature and location of the excited state is a primary aim in this work.

1.4 Aims of Thesis

As discussed earlier in this chapter, the emission and morphology of ZnO nanorods modified with ruthenium complexes have not been studied as intensively as those of unmodified ZnO nanorods, or ruthenium complexes deposited on a thin film substrate. It is one of the aims of the work presented in this thesis to investigate these composite systems with regard to their photophysical and morphological properties. It was decided to investigate the low temperature and room temperature emission of the ZnO nanorod/Ru system, and to determine if electron injection is observed, upon excitation of the sample. In addition, AFM was used to elucidate the structure of the system, and to attempt to determine dimensions of the nanorods and ruthenium aggregates, if observed. It has been seen that much work remains to be done in the investigation of the exfoliation of carbon nanotubes using ruthenium polymers, and the work presented in chapters 4 and 5 represent a significant effort in this investigation, both in the analysis of the exfoliation process and in the investigation of thin films of the CNT/Ru polymer composite on a substrate using AFM.

Finally, the photophysics of a number of ruthenium complexes was investigated, in order to determine the lifetimes of the excited states, and the nature of the emitting state. Some of this work has been published, and the reader is directed to the Appendices for copies of the publications.

1.5 Bibliography

1 L. C. Copeland, O. A. Short, *J. Am. Chem. Soc.*, **1940**, *62*, 3285-3291

2 **(a)** M. L. Fuller, *J. Appl. Phys.*, **1944**, *15*, 164-170, **(b)** P. Zu, Z. K. Tang, G. K. L. Wong, M. Kawasaki, A. Ohtomo, H. Koinuma, Y. Segawa, *Solid State.*

Commun., **1997**, *103*, 459-463, **(c)** D.M. Bagnal, Y.F. Chen, M.Y. Shen, Z. Zhu, T. Goto, T. Yao, *J. Crys. Growth*, **1998**, *184-185*, 605-609

3 J.Y. Li, X.L. Chen, H. Li, M. He, Z.Y. Qiao, *J. Crystal Growth*, **2001**, *233*, 5-7

4 **(a)** D. Ledwith, S. C. Pillai, G. W. Watson and J. M. Kelly, *Chem. Commun.*, **2004**, 2294-2295, **(b)** R. A. McBride, J. M. Kelly, D. E. McCormack, *J. Mater. Chem.*, **2003**, *13*, 1196-1201 **(c)** S. Hashimoto, A. Yamaguchi, *J. Am. Ceramic Soc.*, **1996**, *79*, 1121-1123

5 X. Y. Kong, Z. L. Wang, *Nano Lett.*, **2003**, *3*, 1625-1631

6 H.Z. Wu, D.J. Qiu, Y.J. Cai, X.L. Xu, N.B. Chen, *J. Crystal Growth*, **2002**, *245*, 50-55

7 B. Wen, Y. Huang, J. J. Boland, *J. Phys. Chem. C*, **2008**, *112*, 106-111

8 Z. Zhang, S. Liu, S. Chow, and M.-Y. Han, *Langmuir*, **2006**, *22*, 6335-6340

9 **(a)** I. Bedja, P. V. Kamat, X. Hua, A. G. Lappin, S. Hotchandani, *Langmuir*, **1997**, *13*, 2398-2403, **(b)** R. Katoh, A. Furube, A. V. Barzykin, H. Arakawa, M. Tachiya, *Coord. Chem. Rev.*, **2005**, *248*, 1195-1213

10 M. Law, L. E. Greene, J. C. Johnson, R. Saykally, P. Yang, *Nat. Mater.*, **2005**, *4*, 455-459

11 W. I. Park, D. H. Kim, S.-W. Jung, Gyu-Chul Yi, *Appl. Phys. Lett*. **2002**, *80*, 4232-4234

12 **(a)** Y. C. Kong, D. P. Yu, B. Zhang, W. Fang, S. Q. Feng, *Appl. Phys. Lett*. **2001**, *78*, 407-409, **(b)** R. Groarke, J. Grabowska, E. McGlynn, J. G. Vos, SPIE Proceedings 5826, **2005**, 194-201

13 Y. W. Heo, V. Varadarajan, M. Kaufman, K. Kim, D. P. Norton, F. Ren, P. H. Fleming, *Appl. Phys. Lett.*, **2002,** *81*, 3046-3048

14 D. C. Look, D. C. Reynolds, C. W. Litton, R. L. Jones, D. B. Eason, G. Cantwell, *Appl. Phys. Lett.* **2002**, *81*, 1830-1832

15 W. I. Park, Y. H. Jun, S. W. Jung, G. C. Yi, *Appl. Phys. Lett.* **2003**, *82*, 964-966

16 Y. R. Ryu, S. Zhu, J. D. Budai, H. R. Chandrasekhar, P. F. Miceli, H. W. White, *J. Appl. Phys*. **2000**, *88*, 201-204

17 B.J. Jin, S. Im, S.Y. Lee, *Thin Solid Films,* **2000**, *366*, 107-110

18 M. Yan, H. T. Zhang, E. J. Widjaja, R. P. H. Chang, *J. Appl. Phys.* **2003**, *94*, 5240-5246

19 E.McGlynn, J. Fryar , G. Tobin , C. Roy , M. O. Henry , J. P. Mosnier , E.de Posada , J. G. Lunney, *Thin Solid Films*, **2004**, *458*, 330-335

20 Z. L. Wang, *Mater. Today,* June 2004, 26-33

21 **(a)** Z. L. Wang, *J. Phys.: Condens. Matter*, **2004**, *16*, R829-R858, **(b)** C. Klingshirn, *Phys. Stat. Sol. B*, **2007**, *244*, 3027-3073, **(c)** E. McGlynn, M. O. Henry, J.-P. Mosnier, ZnO Wide Bandgap Semiconductor Nanostructures: Growth, Characterization and Applications, Handbook of Nanoscience and Technology, Oxford University Press, UK, in press.

22 J. C. Phillips, *Rev. Modern Phys.*, **1970**, *42*, 317-356

23 B. J. Chen, X. W. Sun, C. X. Xu, *Ceramics International*, **2004**, *30*, 1725-1729

24 S. Muthukumar, H. Sheng, J. Zhong, N. W. Emanetoglu, *IEEE Trans. Nanotechnology*, **2003**, *2*, 50-53

25 J. F. Conley, L. Stecker, Y. Ono, *Nanotechnology*, **2005**, *16*, 292-296

26 H. C. Hsu, C. S. Cheng, C. C. Chang, S. Yang, C. S. Chang, W. F. Hsieh, *Nanotechnology*, **2005**, *16*, 297-301

27 http://www.fhi-berlin.mpg.de/th/personal/hermann/ZnO.gif

28 C. X. Xu, X. W. Sun, Z. L. Dong, M. B. Yu, T. D. My, X. H. Zhang, S. J. Chua, T. J. White, *Nanotechnology*, **2004**, *15*, 839-842

29 F. Xu, Z.-Y. Yuan, G.-H. Du, T.-Z. Ren, C. Volcke, P. Thiry, B.-L. Su, *J. Non-Crys. Solids*, **2006**, *352*, 2569-2574

30 B. Mari, M. Mollar, A. Mechkour, B. Hartiti, M. Perales, J. Cembrero, *Microelectronics Journal*, **2004**, *35*, 79-82

31 J. Song, X. Song, E. Riedo, Z. L. Wang, *Nano Lett.*, **2005**, *5*, 1954-1958

32 W. I. Park, G.-C. Yi, J.-W. Kim, S.-M. Park, *Appl. Phys. Lett.*, **2003**, *82*, 4358-4360

33 H. Zhou, Z. Li, *Mater. Chem. & Phys.*, **2005**, *89*, 326-331

34 V. Gupta, P. Bhattacharya, Y. I. Yuzuk, K. Sreenivas, R. S. Katiyar, *J. Crystal Growth*, **2006**, *287*, 39-43

35 D. C. Reynolds, D. C. Look, B. Jogai, H. Morkoc, *Solid State Comm*. **1997**, *101*, 643-646

36 M. Wang, C. H. Ye, Y. Zhang, G. M. Hua, H. X. Wang, M. G. Kong, L. D. Zhang, *J. Crystal Growth*, **2006**, *291*, 334-339

37 B. Cao, Y. Li, G. Duan, W. Cai, *Crystal Growth & Design*, **2006**, *6*, 1091-1095

38 Q. X. Zhao, M. Willander, R. E. Morjan, Q. H. Hu, E. E. B. Campbell, *Appl. Phys. Lett.* **2003**, *83*, 165-167

39 **(a)** W. Lee, M. C. Jeong, J. M. Myoung, *Acta Materialia*, **2004**, *52*, 3949-3957, **(b)** M. H. Huang, Y. Wu, H. Feick, N. Tran, E. Weber, P. Yang, *Adv. Mater.*, **2001**, *13*, 113-116

40 B. O Regan, M. Gratzel, *Nature*, **1991**, *353*, 737-740

41 A. Hagfeldt, M. Gratzel, *Acc. Chem. Res.*, **2000**, *33*, 269-277

42 A. Hagfeldt, M. Gratzel, *Chem. Rev.*, **1995**, *95*, 49-68

43 N. A. Anderson, T. Lian, *Coord. Chem. Rev.*, **2004**, *248*, 1231- 1246

44 J. B. Baxter, E. S. Aydil, *Sol. Energy Mat. & Sol. Cells*, **2006**, *90*, 607-622

45 J. B. Baxter, E. S. Aydil, *Appl. Phys. Lett.* **2005**, *86*, 053114-1 – 053114-3

46 K. Kakiuchi, E. Hosono, S. Fujihara, *J. Photochem. & Photobio. A: Chemistry*, **2006**, *179*, 81-86

47 J. B. Asbury, Y. Wang, T. Lian, *J. Phys. Chem. B.*, **1999**, *103*, 6643-6647

48 N. A. Anderson, X. Ai, T. Lian, *J. Phys. Chem. B.*, **2003**, *107*, 14414-14421

49 S. Iijima, *Nature*, **1991,** *354*, 56-58

50 W. Kratschmer, L. D. Lamb, K. Fostiropoulos, D. R. Huffman, *Nature,* **1990**, *347*, 354-358

51 S. Iijima, T. Ichihashi, *Nature*, **1993**, *363*, 603-605

52 D. S. Bethune, C. H. Kiang, M. S. de Vries, G. Gorman, R. Savoy, J. Vasquez, R. Bayers, *Nature,* **1993**, *363*, 605-607

53 T. W. Ebbesen, P. M. Ajayan, *Nature*, **1992**, *358*, 220-222

54 N. Hatta, K. Murata, *Chem. Phys. Lett*., **1994**, *217*, 398-402

55 D. T. Colbert, J. Zhang, S. M. McClure, P. Nikolaev, Z. Chen, J. H. Hafner, D. W. Owens, P. G. Kotula, C. B. Carter, J. H. Weaver, R. E. Smalley, *Science*, **1994**, *266*, 1218-1222

56 W. K. Hsu, M. Terrones, J. P. Hare, H. Terrones, H. W. Kroto, D. R. M. Walton, *Chem. Phys. Lett*., **1994**, *262*, 161-166

57 M. Jose-Yacaman, M. Miki-Yoshida, L. Rendon, T. G. Santiesteban, *Appl. Phys.. Lett.* **1993**, *62*, 202-204

58 V. Ivanov, J. B. Nagy, Ph. Lambin, A. Lucas, X. B. Zhang, X. F. Zhang, D. Bernaerts, G. Van Tendeloo, S. Amelinckx, J. Van Landuyt, *Chem. Phys. Lett*. **1994**, *223*, 329-335

59 K. Hernadi, A. Fonseca, J. B. Nagy, D. Bernaerts, J. Riga, A. Lucas, *Synth. Met.,* **1996**, *77*, 31-34

60 R. Sen, A. Govindaraj, C. N. R. Rao, *Chem. Phys. Lett*., **1997**, *267*, 276-280

61 H. Dai, A. Z. Rinzler, P. Nikolaev, A. Thess, D. T. Colbert, R. E. Smalley, *Chem. Phys. Lett.*, **1996**, *260*, 471-475

62 Y. Saito, M. Okuda, T. Koyama, *Surf. Rev. Lett.*, **1996**, *3*, 863-864

63 Y. Saito, K. Kawabata, M. Okuda, *J. Phys. Chem.,* **1995**, *99*, 16076-16079

64 B. C. Satishkumar, A. Govindaraj, R. Sen, C. N. R. Rao, *Chem. Phys. Lett.*, **1998**, *293*, 47-52

65 S. Bandow, A. M. Rao, K. A. Williams, A. Thess, R. E. Smalley, P. C. Eklund, *J. Phys. Chem. B*, **1997**, *101*, 8839-8842

66 **(a)** N. Grobert, *Mater. Today,* Jan/Feb **2007,** 28-35, **(b)** M. L. Terranova, V. Sessa, and M. Rossi, *Chem. Vap. Deposition*, **2006**, *12*, 315-325

67 M. Terrones, A. Jorio, M. Endo, A. M. Rao, Y. A. Kim, T. Hayashi, H. Terrones, J.-C. Charlier, G. Dresselhaus, and M. S. Dresselhaus, *Mat. Today,* Oct. 2004**,** 30-45

68 M. Terrones, *Annu. Rev. of Mater. Sci.,* **2003,** *33*, 419-501

69 **(a)** D. Tasis, N. Tagmatarchis, A. Bianco, M. Prato, *Chem. Rev.,* **2006,** *106*, 1105-1136, **(b)** C. T. White, J. W. Mintmire, *J. Phys. Chem. B.*, **2005**, *109*, 52-65

70 P. M. Ajayan, *Chem. Rev.,* **1999,** *99*, 1787-1799

71 Y. Ando, X. Zhao, T. Sugai, M. Kumar, *Mater. Today,* Oct. 2004**,** 22-29

72 P. M. Ajayan, T. Ichihashi, S. Iijima, *Chem. Phys. Lett.*, **1993**, *202*, 384-388

73 C. N. R. Rao, B. C. Satishkumar, A. Govindaraj, M. Nath, *Chem. Phys. Chem.*, **2001**, *2*, 78-105

74 P. L. McEuen, *Physics World*, June 2000, 31-36

75 G. Chambers, C. Carroll, G. F. Farrell, A. B. Dalton, M. McNamara, M. in het Panhuis, H. J. Byrne, *Nano Lett.*, **2003,** *3*, 843-846

76 A. Hamwi, H. Alvergnat, S, Bonnamy, F. Beguin, *Carbon*, **1997**, *35*, 723-728

77 S. Pekker, J.-P. Salvetat, E. Jakab, J.-M. Bonard, L. Forro, *J. Phys. Chem. B*, **2001**, *105*, 7938-7943

78 C. A. Dyke, J. M. Tour, *Nano Lett.*, **2003**, *3*, 1215-1218

79 L. Jiang, L. Gao, J. Sun, *J. Colloid & Interface Sci.*, **2003**, *260*, 89-94

80 X. Zhang, J. Zhang, Z. Liu, *Carbon*, **2005**, *43*, 2186-2191

81 J. Lu, *Carbon*, **2007**, *45*, 1599-1605

82 J. Yu, K. Lu, E. Sourty, N. Grossiord, C. E. Koning, J. Loos, *Carbon*, **2007**, *45*, 2897-2903

83 M. J. O'Connell, S. M. Bachilo, C. B. Huffman, V. C. Moore, M. S. Strano, E. H. Haroz, K. L. Rialon, P. J. Boul, W. H. Noon, C. Kittrell, J. Ma, R. H. Hauge, R. B. Weisman, R. E. Smalley, *Science*, **2002**, *297*, 593-596

84 N. Grossiord, P. van der Schoot, J. Meuldijk, C. E. Koning, *Langmuir*, **2007**, *23*, 3646-3653

85 N. Grossiord; O. Regev; J. Loos, J. Meuldijk, C. E. Koning, *Anal. Chem*., **2005**, *77*, 5135-5139.

86 O. Matarredona, H. Rhoads, Z. Li, J. H. Harwell, L. Balzano, D. E. Resasco, *J. Phys Chem. B*., **2003**, *107*, 13357-13367

87 V. A. Sinani, M. K. Gheith, A. A. Yaroslavov, A. A. Rakhnyanskaya, K. Sun, A. A. Mamedov, J. P. Wicksted, N. A. Kotov, *J. Am. Chem. Soc.*, **2005**, *127*, 3463-3472

88 J. H. Rouse, *Langmuir*, **2005**, *21*, 1055-1061

89 J. H. Rouse, P. T. Lillehei, J. Sanderson, E. J. Siochi, *Chem. Mater.*, **2004**, *16*, 3904-3910

90 H. Yonemura, Y. Yamamoto, S. Yamada, *Thin Solid Films*, **2008,** *516*, 2620-2625

91 B. Jousselme, G. Bidan, M. Billon, C. Goyer, Y. Kervella, S. Guillerez, E. A. Hamad, C. Goze-Bac, J-Y Mevellec, S. Lefrante, *Journal of Electroanalytical Chemistry,* In Press, **2008**

92 H. Chaturvedi, J. C. Poler, *J. Phys. Chem B.*, **2006**, *110*, 22387-22393

93 F. Frehill, J. G. Vos, S. Benrezzak,. A. A. Koós, Z. Kónya, M. G. Rüther, W. J. Blau, A. Fonseca, J. B. Nagy, L. P. Biró, A. I. Minett, M. in het Panhuis, *J. Am. Chem. Soc.*, **2002**, *124*, 13694-13695

94 F. Frehill, M. in het Panhuis, N. A. Young, W. Henry, J Hjelm, J. G. Vos, *J. Phys. Chem. B*, **2005**, *109*, 13205-13209

95 J. M. Clear, J. M. Kelly, C. M. O'Connell, J. G. Vos, *J. Chem. Res. Miniprint*, **1981**, 3039-3069

96 H. Kim, W. Sigmund, *Appl. Phys. Lett.*, **2002**, *81*, p2085-2087

97 J. N. Demas, *J. Chem. Ed.*, **1983**, *60*, 803-808

98 W. H. Elfring Jr., G. A. Crosby, *J. Am. Chem. Soc.*, **1981**, *103*, 2683-2687

99 William Henry, PhD Thesis, **2006**, Dublin City University

100 K. Kalyanasundaram, Photochemistry of Polypyridine and Porphyrin Complexes, Academic Press, London, **1996**.

101 A. W. Adamson, P. D. Fleischauer, Concepts of Inorganic Photochemistry, Wiley – Interscience, New York, **1975**.

102 A. Juris, V. Balzani, F. Barigelletti, S. Campagna, P. Belser, A. von Zelewsky, *Coord. Chem. Rev.* **1988**, *84*, 85-277

103 **(a)** D. P. Rillema, G. Allen, T. J. Meyer, D. Conrad, *Inorg. Chem.*, **1983**, *22,* 1617-1622, **(b)** S. J. Valenty, G. L. Gaines, Jr., *J. Am. Chem. Soc.,* **1977**, *99*, 1285-1287, **(c)** D. Kuang, S. Ito, Bernard Wenger, C. Klein, J.-E Moser, R. Humphry-Baker, S. M. Zakeeruddin, and Michael Gratzel, *J. Am. Chem. Soc.,* **2006**, *128*, 4146-4154, **(d)** R. Hage, A. H. J. Dijkhuis, J. G. Haasnoot, R. Prim, J. Reedijk, B. E. Buchanan, J. G. Vos, *Inorg. Chem.* **1988**, *27*, 2185-2189, **(e)** O. Kohle, S. Ruile, M. Grätzel, *Inorg. Chem.* **1996**, *35*, 4779-4787, **(f)** R. Ziessel, V. Grosshenny, M. Hissler, C. Stroh, *Inorg. Chem.* **2004**, *4*3, 4262-4271, **(g)** M. A. Halcrow, *Coord. Chem. Rev.*, **2005**, *249*, 2880-2908

104 **(a)** R. A. Palmer, T. S. Piper, *Inorg. Chem.* **1966**, *5,* 864-878 **(b)** E. M. Kober, T. J. Meyer, *Inorg. Chem.*, **1983**, *22,* 1614-1616, **(c)** W. R. Cherry, L. J. Henderson,

Jr., *Inorg. Chem.*, **1984**, *23,* 983-986, **(d)** E. M. Kober, T. J. Meyer, *Inorg. Chem.*, **1984**, *23,* 3877-3886, **(e)** J. P. Paris, W. W. Brandt, *J. Am. Chem. Soc.*, **1959**, *81*, 5001-5002, **(f)** C. M. Elliott, F. Pichot, C. J. Bloom, L. S. Rider, *J. Am. Chem. Soc.,* **1998**, *120*, 6781-6784, **(g)** F. E. Lytle, D. M. Hercules, *J. Am. Chem. Soc.,* **1969**, *91*, 253-257, **(h)** N. H. Damrauer, J. K. McCusker, *Inorg. Chem.* **1999**, *38*, 4268-4277, **(i)** L. Hammarström, F. Barigelletti, L. Flamigni, N. Armaroli, A. Sour, J.-P Collin, J.-P. Sauvage, *J. Am. Chem. Soc.,* **1996**, *118*, 11972-11973, **(j)** H. P. Hughes, D. Martin, S. Bell,: J. J. McGarvey, J. G. Vos, *Inorg. Chem.* **1993**, *32*, 4402-4408, **(k)** Y. Chen, T. J. Meyer, *Chem. Rev.*, **1998**, *98*, 1439-1477, **(k)** A. Webb, F. Knorr, J. McHale, *J. Raman Spectroscopy*, **2001**, *32*, 481-485

105 **(a)** J. G. Vos, J. M. Kelly, *Dalton Trans.*, **2006**, 4869-4883, **(b)** Md. K. Nazeeruddin, S.M. Zakeeruddin, R. Humphry-Baker, S.I. Gorelsky, A.B.P. Lever, M. Grätzel, *Coord. Chem. Rev.*, **2000**, *208*, 213-225, **(c)** V. Balzani, A. Juris, *Coord. Chem. Rev.,* **2001***, 211,* 97-115, **(d)** H. Yersin, C. Kratzer, *Coord. Chem. Rev.,* **2002***, 229,* 75-93, **(e)** J. A. Rard, *Chem. Rev.*, **1985**, *85*, 1-39, **(f)** V. Balzani, A. Juris, M. Venturi, S. Campagna, S. Serroni, *Chem. Rev.*, **1996**, *96*, 759-833, **(g)** K. D. Demadis, C. M. Hartshorn, T. J. Meyer, *Chem. Rev.*, **2001**, *101*, 2655-2685, **(h)** L. De Cola, P. Belser, *Coord. Chem. Rev.*, **1998**, *177*, 301-346, **(i)** S. Campagna, F. Puntoriero, F. Nastasi, G. Bergamini, V. Balzani, *Top. Curr. Chem.*, **2007**, *128*, 1-98

106 **(a)** G. D. Hager, G. A. Crosby, *J. Am. Chem. Soc.*, **1975**, *97*, 7031-7037, **(b)** G. D. Hager, R. J. Watts, G. A. Crosby, *J. Am. Chem. Soc.*, **1975**, *97*, 7037-7042

107 **(a)** A. Juris, F. Barigelletti, P. Belser, A. von Zelewski, V. Balzani, *Inorg. Chem.* **1985**, *24*, 202-206, **(b)** F. Barigelletti, A. Juris, V. Balzani, P. Belser, A. von Zelewski, *J. Phys. Chem.,* **1986**, *90*, 5190-5193, **(c)** F. Barigelletti, P. Belser, A. von Zelewski, V. Balzani, *J. Phys. Chem.,* **1985**, *89*, 3680-3684

108 E. Danielson, R. S. Lumpkin, T. J. Meyer, *J. Phys. Chem.*, **1987**, *91*, 1305-1306

109 S. Rau, B. Schäfer, D. Gleich, E. Anders, M. Rudolph, M. Friedrich, H. Görls, W. Henry, J. G. Vos, *Angew. Chemie Int. Ed.* **2006**, *45*, 6215-6218

110 B. Schäfer, H. Görls, M. Presselt, M. Schmitt, J. Popp, W. Henry, J. G. Vos, S. Rau, *Dalton Trans.*, **2006**, *18*, 2225-2231

111 S. Rau, R. Fischer, M. Jäger, B. Schäfer, S. Meyer, G. Kreisel, H. Görls, M. Rudolf, W. Henry, J. G. Vos, *Euro. J. Inorg. Chem,.* **2004**, *22*, 2001-2003

112 B. Schäfer, H. Görls, S. Meyer, W. Henry, J. G. Vos, S. Rau, *Euro. J. Inorg. Chem,.* **2007**, *25*, 4056-4063

113 D. P. Rillema, D. S. Jones, C. Woods, H. A. Levy, *Inorg. Chem.*, **1992**, *31*, 2935-2938

114 G. A. Crosby, *Acc. Chem. Res.*, **1975**, *8*, 231-238

115 M. Kasha, *Discuss. Faraday Soc.*, **1950**, *9*, 14-19

Chapter 2: Experimental

Chapter 2 deals with the experimental equipment and procedures employed in this work. The instrumental setups are discussed for each of the primary instruments used, UV spectrophometer, fluorimeter, atomic force microscope, sonic tip and cryostats. These techniques allow for the investigation of the systems from the steady state to the nanosecond timescale, and in - situ investigations of the surface morphologies. Synthesis of complexes and preparation of experimental carbon nanotube solutions will also be described.

2.1 Atomic Force Microscopy (AFM)

2.1.1 Introduction to AFM

Atomic Force Microscopy, was first developed in 1986, by Binnig et al[1], after their work in developing the parent surface scanning probe, the Scanning Tunnelling Microscope, (STM). Atomic Force Microscopy involves moving a very sharp tip, over the surface of interest. This technique is particularly useful, as it can be applied to surfaces that are conductive, insulating and also to semiconductor substrates. In some of the other scanning probe microscopies, for example, STM, non-conductive surfaces cannot be investigated because of the contact forces which are repulsive in nature, and non contact forces, which have both repulsive and attractive components, between the tip and the sample.

An illustrative diagram of the Atomic Force Microscope is shown in FIGURE 2.1, on the next page.

There are 3 main modes of operating an atomic force microscope, Contact Mode, Non Contact Mode, and Tapping Mode. In this work, Tapping Mode was used. However, the three modes of operation all have certain principles in common.

- A very sharp tip at the end of a cantilever is used to interact with the surface of the sample
- The interaction of the tip with the surface is very sensitive to changes in the distance between the sample and the tip.
- A piezoelectric crystal is used to control the displacement of the tip or the sample in the x, y, or z planes. This displacement can be controlled to a very high degree of precision, in modern systems to less than an Angstrom.
- A feedback loop controls the distance between the tip and the sample.

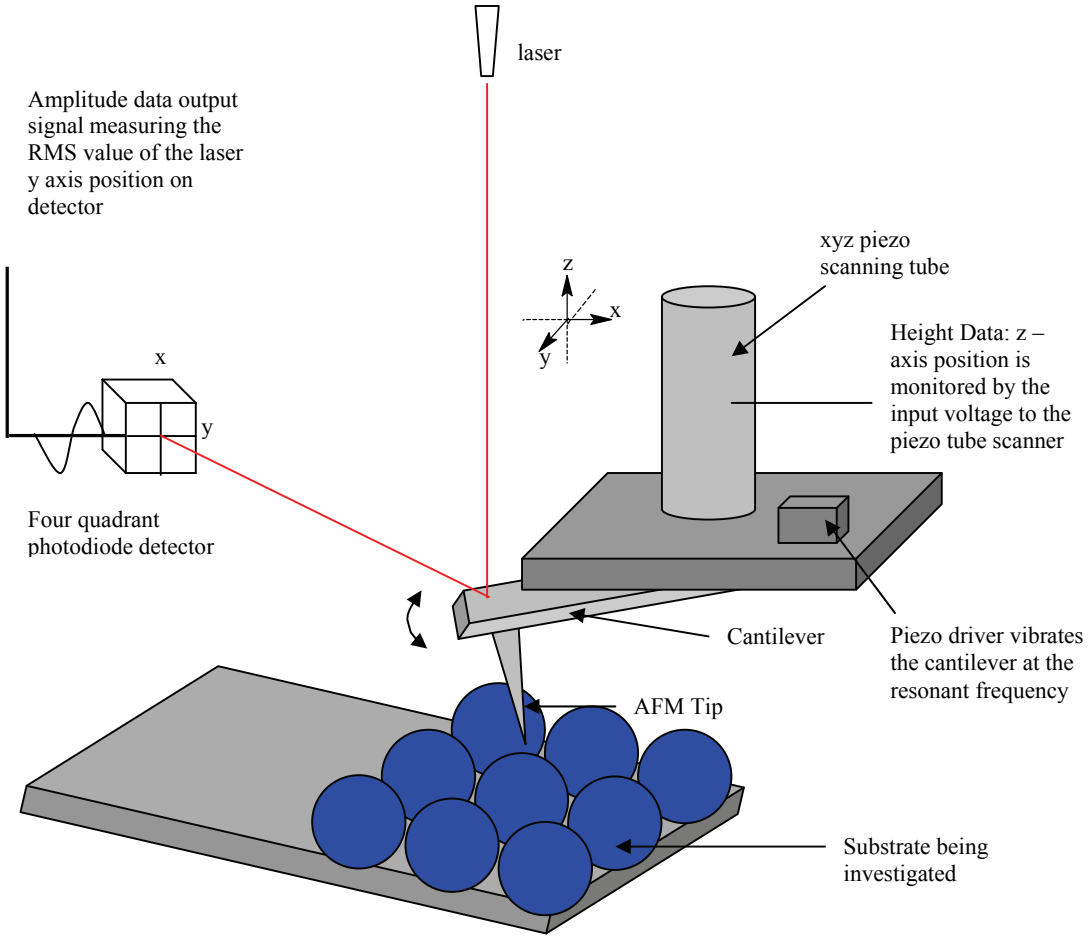

FIGURE 2.1: ILLUSTRATIVE DIAGRAM OF THE AFM INSTRUMENT INVESTIGATING A SUBSTRATE.

AFM analysis of zinc oxide has been primarily limited to analysing thin films of the metal oxide, on Silicon[2,4,5,7,9], as its own substrate[3,6] and on other substrates such as soda lime glass[8], and Indium Phosphide[9], with only a few references in the literature dealing specifically with nanorods[10,11,12], none of which used Si as the substrate.

The AFM instrument used in this work is shown in FIGURE 2.2(A) and (B), on the next page.

The AFM work on the ZnO nanorods was carried out in the Department of Physics and Astronomy, Nottingham University.

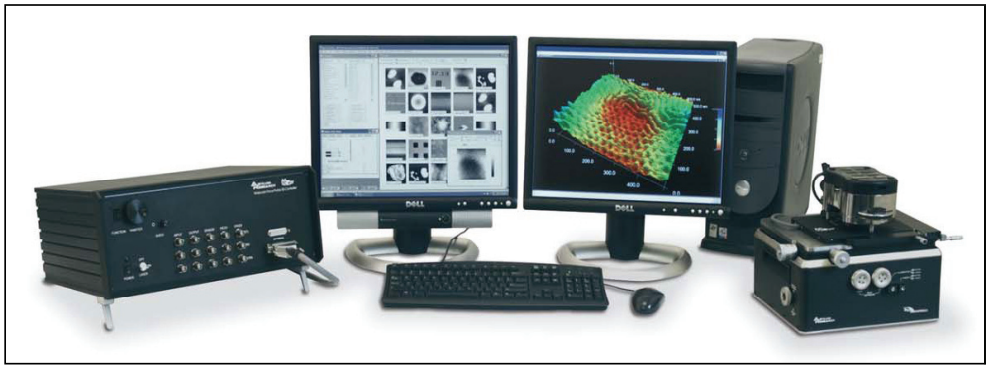

FIGURE 2.2(A): ASYLUM RESEARCH MFP3D ATOMIC FORCE MICROSCOPE[13].

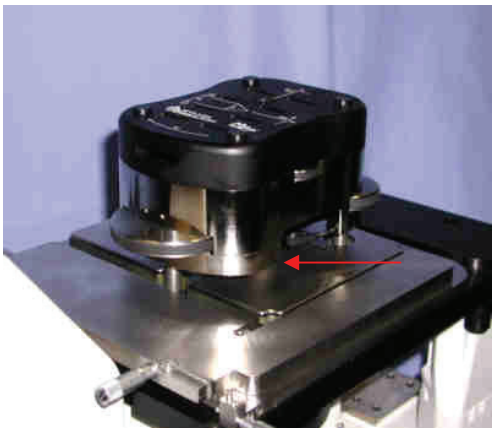

FIGURE 2.2(B): AFM MOUNT ASSEMBLY. THE SAMPLE IS PLACED APPROXIMATELY WHERE THE RED ARROW INDICATES[13].

AFM has also been used to investigate carbon nanotubes[14], and their polymer based composites[15-20].

2.1.2 Method of Operation

The sample to be investigated was placed on a glass slide, underneath the AFM mount. The mount is shown in FIGURE 2.2(B), and the tip is located on the underside of the assembly. The mount is lowered down to the sample by means of a function in the controller software called "simple engage". A microscope is used to show the tip, cantilever and sample on the PC screen. Initially, the sample is out of focus, while the tip is in focus. The laser is aligned on the tip until the sum value is reasonably high, and the deflection is as close to zero as possible. The sample is moved until the area of interest is

under the tip, this is done using the microscope image as a guide. All AFM imaging was performed in air, but the instrument was in a large closed "box", with special walls to minimize vibrations.

The mount is then lowered manually until the sample comes into focus, and the amplitude and z-voltage decrease. The amplitude is approximately 1V in air and is lowered until the z-voltage is around 70mV.

The scan size is then selected, and the scan started. The amplitude setpoint is usually lowered initially, and the integral gain increased to provide better feedback from the tip, and to sharpen the images. In general, the tips used were Silicon Nitride (SiN) tapping mode tips. These tips had an operating oscillating frequency of around 280kHz, this was found to be the optimum frequency, however generally a frequency scan was performed each time from 0-500kHz. The mode of operation used was always tapping mode.

The AFM instrument used to image the carbon nanotube / ruthenium polymer samples was a atomic force microscopy was a Digital Instruments Nanoscope IIIa. Laser alignment was performed manually, and cantilever tuning and drive frequency selection was automatically performed by the DI software. The Si substrates used were Si(100) and were first cleaned by sonicating the slides in acetone and methanol, both for 5mins. The slides were then immersed overnight in a basic piranha solution, NH_4OH: H_2O_2: H_2O (1:1:5). The composite solution was deposited on the cleaned Si(100) substrates via the drop cast method, and allowed to dry in a beaker, purged with Argon, over a period of 3 days.

2.2 Emission Spectroscopy

Emission spectroscopy is the investigation of the radiative relaxation processes which a complex may undergo during the transition between its excited state and its ground state. The excited state is formed via the absorption of light, followed by the relaxation to the thermally equilibrated (THEXI) state. The lifetime of the THEXI state can range from ns to ms, and its formation occurs on the sub-nanosecond time scale[27]. Steady state emission spectroscopy is used to investigate this steady state, via the intensity and energy of the emitted light.

It is important to note that sample preparation and concentration are just as important in emission spectroscopy as they are in UV-vis absorption spectroscopy. Samples that are too highly concentrated have been observed to re-absorb the emitted light, leading to an overall decrease in the intensity of the emission. This is known as the inner filter effect. The other possibility is that samples that are too weakly concentrated have such low signal intensity that the signal to noise ratio becomes a major issue, and the error in the measurement becomes more apparent.

Throughout the work to be presented, regarding lifetime and emission measurements, temperature dependence of emission and lifetimes has been investigated. Most of the low temperature work has been performed at 77K, and sometimes out of necessity. Some of the samples analysed were found to be extremely air sensitive, and therefore the measurements done on these samples in deaerated ACN or DCM yielded inconsistent results, as the samples exhibited signs of "re-aeration" during the recording of the measurements. In order to obtain lifetime values for these air sensitive samples in these deaerated conditions, it was necessary to use a 4:1 ethanol : methanol solution, and measure the lifetime at 77K. In general, this 4:1 E:M solvent forms a really well defined glass, and is a more desirable choice at low temperatures than ACN or DCM, so it was used in all low temperature measurements.

Most of the samples for which lifetime data was obtained were measured in two solvents, usually ACN and DCM. The reason for the use of two solvents was to investigate effect of solvent on the emission energy and intensity. The solvent can sometimes play a key part in the stabilization of the excited state of the complex, and this can affect the energy of the emission. The solvent generally affects the charge transfer states such as MLCT and LMCT to a greater degree than it affects the metal and ligand centred states. This is due to the large change in dipole upon the formation of the excited state[21], which does not occur to the same amount in the MC and LC states, as the electron is not displaced as much.

All emission spectra were recorded using a Perkin Elmer LS50B Luminescence spectrophotometer, which was interfaced with an Elonex-466 PC via Windows 3.1 based fluorescence data manager software, FLWinlab, and a Varian UV Fluorimeter, using

Cary UV software. Excitation and emission slit widths were usually set to 10nm and 15nm, but 5nm slits were also used, depending on the conditions required.
For low temperature measurements the solid state and solution based samples were mounted in an Oxford Instruments Liquid Nitrogen PE1704 cryostat. The solid state samples were mounted on a flat paddle attached to a long steel rod passing through the center of the cryostat and sealed at the top of the cryostat with parafilm. The solution based samples were placed in a pyrex tube, placed inside the cryostat.
Great care was taken, particularly with the solid state samples, to ensure the correct alignment of the solid sample with respect to the incident beam and the detector, to reduce scatter and to obtain the strongest possible signal. An Oxford Instruments Intelligent Temperature Controller ITC 601 was used to adjust the temperature of the sample to the desired value.
The excitation wavelength was 280nm generally for both the room temperature and low temperature measurements of the solid state samples using these instruments. Room temperature measurements were performed at 293K, and the low temperature measurements were carried out from 77K to 280K.
The excitation wavelengths for the solution based samples varied with each sample, as required. Other very low temperature emission studies were carried out using a one metre grating spectrometer (SPEX 1704) and detected with a photomultiplier tube (Hamamatsu model R3310-02) in photon counting mode. Controllable temperatures down to 5 K were achieved using a closed cycle cryostat (Janis SHI-950-5). The excitation wavelength was 325nm and the actual measurement temperature was 10K.

2.3 Time Correlated Emission

Time resolved emission measurements were also performed on various Ruthenium polypyridyl based complexes, bearing various conjugated polycyclic moieties, and modified pyridine ligands. These measurements were performed to complement steady state measurements such as quantum yields and fluorescence, discussed in more detail in chapter 6. These measurements are closely related and this relationship is described in EQUATION 2.1, below.

$$I_{SS} = \int_0^\infty I_0 e^{-t/\tau} dt = I_0 \tau \qquad \text{EQN 2.1}$$

where I_0 is the illumination intensity, τ is the lifetime of the excited state, and I_{SS} is the intensity of the steady state emission.

It can be seen from the above equation that the steady state measurement of the emission of a complex is an average of the time-resolved phenomena over the intensity decay of the sample. It is therefore possible to extract further information regarding the excited state processes of the system using time resolved emission techniques, as the lifetime and number of decays are both valuable pieces of information.

2.3.1 NanoSecond Time Resolved Single Photon Counting

The lifetime measurements were carried out in air, using an Edinburgh Instruments Single Photon Counter, with nF900 flash lamp. The apparatus is shown in FIGURES 2.3(A) and (B), below.

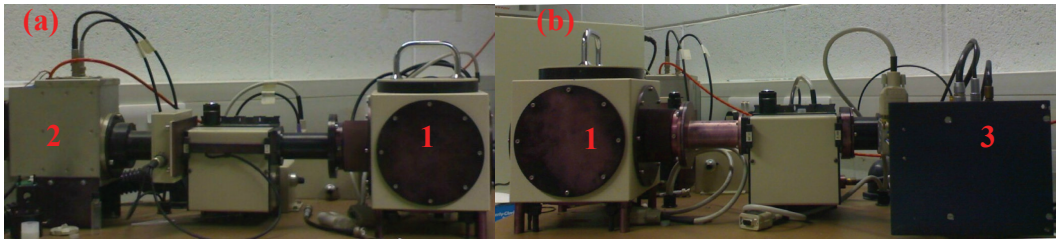

FIGURE 2.3: (A) EMISSION ARM OF SINGLE PHOTON COUNTER, SAMPLE CHAMBER (1) ON RIGHT HAND SIDE OF IMAGE, AND DETECTOR (2) ON LEFT SIDE OF IMAGE, **(B)** EXCITATION ARM OF SINGLE PHOTON COUNTER, SHOWING THE SAMPLE CHAMBER (1) AGAIN ON THE LEFT HAND SIDE OF THE IMAGE, AND THE LAMP CHAMBER (3) ON THE RIGHT HAND SIDE.

A schematic diagram of the SPC system is shown in FIGURE 2.4 and FIGURE 2.5, on the next page. The system is comprised of two main components, the excitation source and the detection system. The excitation source is an nF900 nanoflash lamp, using N_2 as the filler gas within the lamp chamber. The lamp itself is two tungsten/thorium electrodes, one flat and one pointed.

FIGURE 2.4 on the following page shows the electrical circuit diagram of the flashlamp. A highly positive charge is applied to the anode of the spark gap by charging resistors R_1 and R_2. The cathode of the spark gap is connected to the anode of the thyratron and has a

similar potential due to resistor R_3. The thyratron uses hydrogen gas as its switching medium. A gating pulse is sent to the grid of the thyratron which causes it to switch to its conducting state. The cathode of the spark gap is therefore grounded, causing a large intergap voltage, which leads to a spark discharge. When the capacitance is discharged, the anode current falls below its minimum holding value and the thyratron returns to its non-conducting state. The repetition rate is dependant on the time required for the thyratron and the spark gap to recover after conduction. As the intergap resistance increases the energy per flash and the flash duration increase, therefore this capacitance is kept at a minimum to ensure a high repetition rate. The typical pulse width (Full Width Half Maximum - FWHM) possible using N_2 as the filler gas is 1ns, therefore it is possible to measure lifetimes as short as 100ps, after the lamp profile has been deconvoluted from the decay profile.

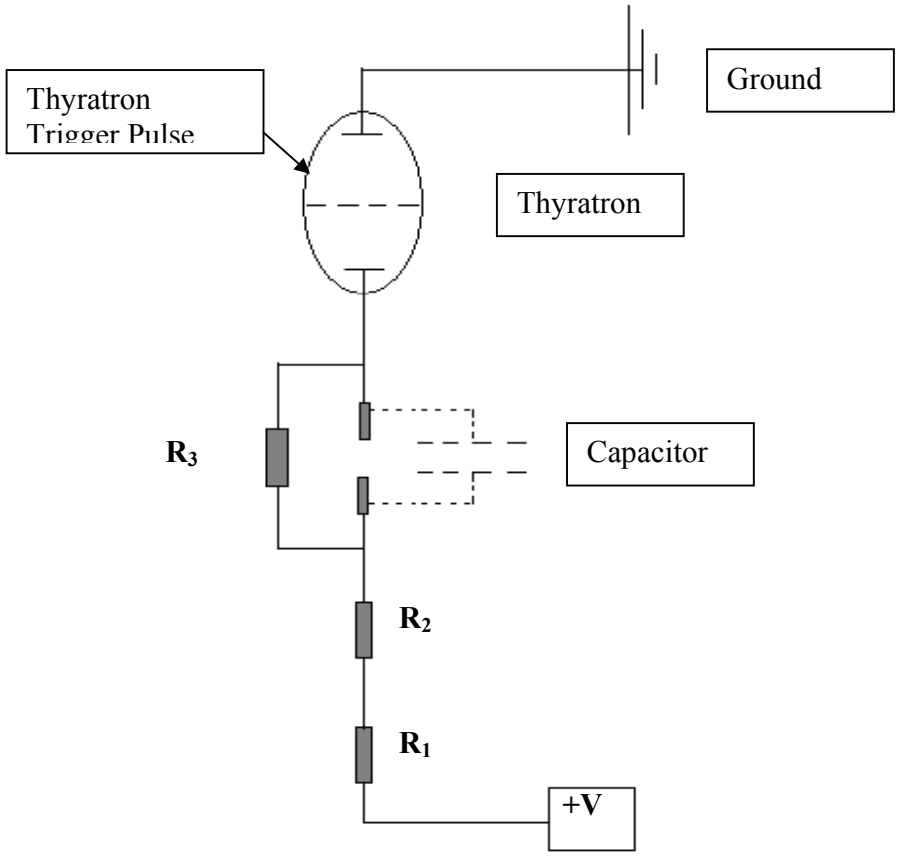

FIGURE 2.4: ELECTRICAL CIRCUIT OF THE SPC NANOSECOND FLASHLAMP(ADAPTED FROM REF [26]).

The method of operation of the Single Photon Counter is described below and in FIGURE 2.5. A photon of light is emitted from the nanoflash lamp and travels via an optical cable to the START detector. When this photon is detected by the START detector, the TAC (Time to Analogue Converter) initiates a voltage ramp. Simultaneously, another photon passes through the excitation monochromator, which is set to the appropriate excitation wavelength. This photon is then absorbed by the sample. The re-emitted photon passes through a filter and also through an emission monochromator, which has been set to the desired emission wavelength of the sample.

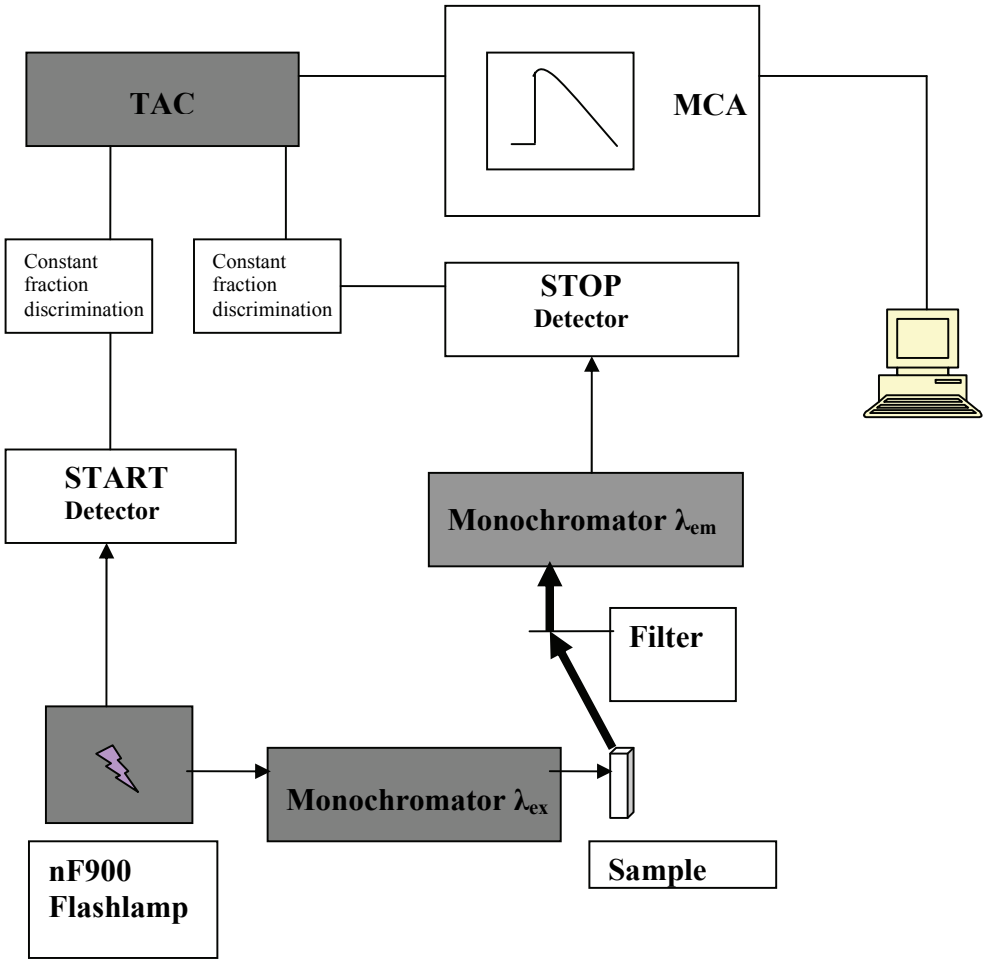

FIGURE 2.5: NANO SECOND TIME CORRELATED SINGLE PHOTON COUNTING SETUP. (ADAPTED FROM REF [26]).

The voltage ramp is stopped when the STOP detector receives a photon of light from the sample. Both the START and STOP detectors contain signal amplifiers, which may be

varied to adjust the sensitivity of the instrument. The signal amplifiers are related to the potential bias applied to the photomultiplier tubes, and therefore the lifetime of the tubes may be reduced if too high a voltage is applied. The time range is split into 1024, 2048, or 4096 channels, depending on the settings chosen by the operator. Each of these channels is assigned a range of voltages corresponding to a certain time range. The Multi Channel Analyser (MCA) records the number of times a specific voltage is obtained in each of the channels. A spectrum of voltages, and therefore time differences, is produced by the MCA memory and the experiment is terminated when a sufficient number of counts are collected. The number of counts collected depends on a number of factors:

- The signal to noise ratio.
- The number of decays in the sample.
- The presence of scatter from the sample.

It is sufficient in most experiments to obtain 1000 counts in order to get a good quality fit after data analysis, a process which will be discussed later.
The detector contains a red sensitive S900-R photomultiplier. It has a working range of 160-870nm, due to the quartz glass in its side window. This detector is generally operated within a peltier element – cooled housing at 50K below ambient temperature, so as to reduce of dark counts. It is still necessary to perform some measurements in the dark, if the emission arm filters are removed. The spectrum of the nanoflash lamp is shown in FIGURE 2.6, below.

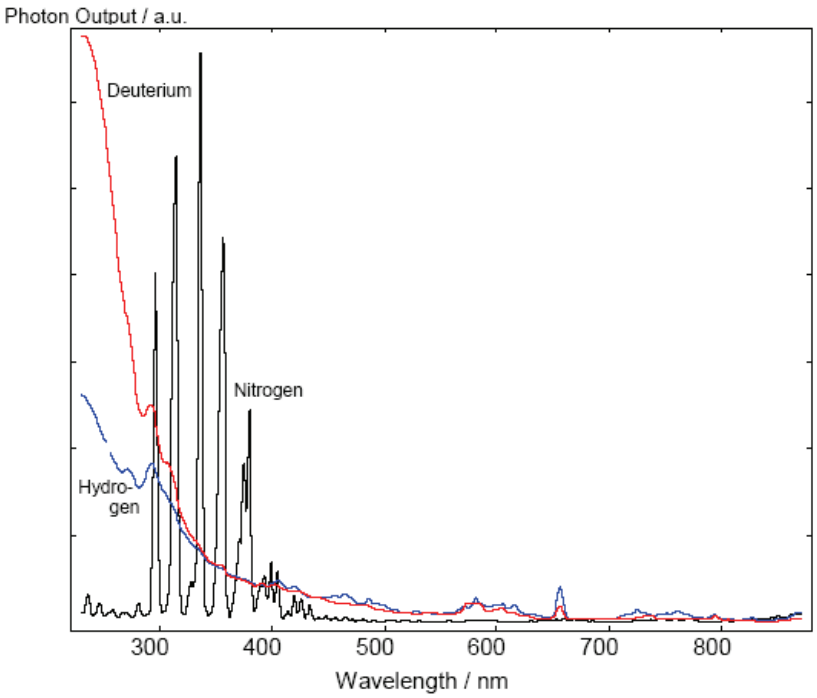

FIGURE 2.6: SPECTRAL OUTPUT OF THE N_2 FILLER GAS, COMPARED WITH SPECTRA OF H_2 AND D_2.[22]

2.3.2 Analysis of TCSPC Data

There are two methods by which the decay data obtained from the lifetime measurement can be analysed using the F900 program Version 6.24, Reconvolution Fit, and Tail Fit. Reconvolution Fit takes into account the finite nature of the excitation pulse, and the possibility that the sample decay is convoluted with the excitation pulse. The convolution integral (EQUATION 2.2) shows the mathematical relationship between the sample response function (X(t)), the instrument response function (E(t)) and the sample decay model (R(t)):[26]

$$X(t)=\int_0^t E(t')R(t-t')dt' \qquad \text{EQN. 2.2}$$

Reconvolution fit can be used to completely describe the data, apart from noise. It will fit the rise of the signal, the initial part of the decay, and the tail.

The second data analysis method within the software is the tail fit. In this method, X(t) is considered to be equal to R(t), and the instrument response is considered negligible. Since this is the case with most of the measurements described in this work, this is method of analysis used unless otherwise stated.

Once the method of fit has been chosen, the lifetime value is calculated by fitting the experimental decay to the equation;

$$R(t)= A + B_i e^{-(t/\tau i)} \qquad \text{EQN 2.3}$$

where R(t) is the the sample decay model, B_i is the pre-exponential factor, τ_i is the characteristic lifetime and A is an additional background. The Marquardt-Levenberg algorithm is used to search for the best values of B_i and τ_i.

The quality of the lifetime data is assessed by two criteria, the reduced Chi-squared, χ^2, and the nature of the residuals data. The χ^2 value is obtained by dividing the goodness of fit χ_g^2, which itself is ultimately found by the Marquardt-Levenberg algorithm, by the number of free parameters, n, (which is approximately the number of fitted points divided by the number of lifetime parameters used in the fit) and is shown in EQUATION 2.4, below. The data follows a Poisson distribution, and therefore χ^2 has a theoretical limit of 1.0. Values above this indicate a bad fit of the data, and values below 1.0 are the result of poor choice of the fitting range.[21,26] The F900 program also displays the residuals in a graph of residual value vs time (ns). This is inspected visually to ensure that the residuals are more or less random in nature, and to ensure the absence of peaks or tails of peaks at the beginning of the trace. These peaks would suggest the presence of a very short lifetime, in addition to a longer decay, and can also indicate other processes such as energy transfer.

$$\chi^2= \Sigma W_k^2 \frac{[X_k - F_k]^2}{n} \qquad \text{EQN. 2.4}$$

2.4 UV-Spectroscopy

Absorption spectroscopy measures the transition of atoms and molecules between different electronic states. As the name suggests, the technique relates to the absorption by atomic or molecular species of light of the visible or ultraviolet (and sometimes both) regions of the spectrum. It is generally assumed that radiation in the infra-red and microwave regions of the radiative spectrum are too low in energy to causes significant perturbations of the electronic structure of the species.

The most important equation in absorption spectroscopy is the Beer-Lambert Law, defined in EQUATION 2.5, below[23]. It relates Abs (the intensity of the light absorbed) to the path length of the light, l, and the concentration of the species in the solution, c.

$$Abs = \log_{10}(I_0/I_t) = \varepsilon cl \qquad \text{EQN 2.5}$$

I_0 and I_t are the incident and transmitted light intensities, respectively. ε is referred to the molar extinction coefficient, and is a measure of the strength of the transition between the ground state and the excited state. A large value for ε indicates that the transition is almost fully allowed, such as the Metal to Ligand Charge Transfer (MLCT) process in $[Co(NH_3)Br]^{2+}$, where ε_{max} at 250nm = 20,000M^{-1} cm^{-1}. In order to put this value in perspective, the ε_{max} of the ligand field transition for the same complex at 550nm is just 50 M^{-1} cm^{-1} and is termed a Laporte (Spin) forbidden process[23]. The transition metal can sometimes affect the electronic structure, in such a way that certain transitions that are formally forbidden actually occur, with reasonably high molar extinction coefficients. In order for the measurements to be accurate, the absorbance should not be too low, as this may make it difficult to distinguish the actual peaks from the baseline noise. However, if the absorbance value is too high, this indicates that all the light has been absorbed by the sample and therefore the amount of light available for measurement is not enough for a statistically accurate measurement to be made.

The UV measurements presented throughout this work were recorded on a Varian Cary 50 Scan UV spectrometer interfaced with a Dell Optiplex GX1 PC, via the Win UV

Scan Application 2.00. Samples were measured inside quartz cuvettes with a 1.0cm pathlength. The instrument employs a Xenon flash lamp as the light source, which allows for very fast scan rates, however in all the measurements presented in this work, the scan speed used was 600nm/min.

2.5 Carbon Nanotube/Polymer Sample Preparation

The carbon nanotubes used throughout this work were of two main types, Single Walled, (SWNT's) and Multi Walled (MWNT's). The latter can be further differentiated by virtue of the fact that some samples consisted of simple Multi Walled Nanotubes, while others were comprised of MWNT's functionalized with amino moieties, these samples have been designated throughout the work as MWNT-NH_2, while the unfunctionalized nanotubes are designated as MWNT.

The polymer used as the exfoliating agent in some of the experiments was $[Ru(bpy)_2(PVP)_{10}Cl]Cl$, shown in FIGURE 2.7, below. Poly (4-vinyl pyridine) or PVP was also used as a control, because, as discussed in Chapter 1, it has been reported as an efficient exfoliation agent of carbon nanotubes.[15,24]

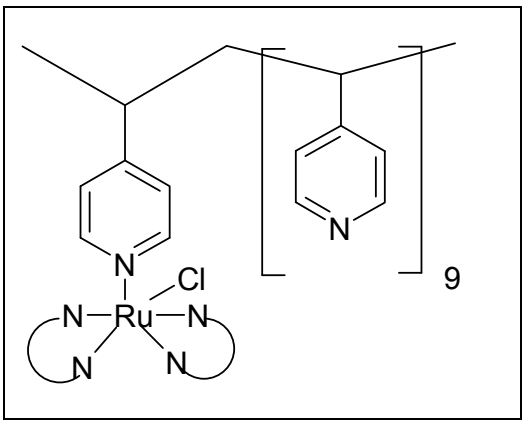

FIGURE 2.7: STRUCTURE OF $[Ru(bpy)_2(PVP)_{10}Cl]Cl$. N____N INDICATES A 2, 2' - BIPYRIDINE LIGAND.

The nanotubes and Ruthenium polymer were both weighed out using glass Pasteur pipettes, into plastic sample tubes. In every experiment, 10ml of Methanol was added to the nanotubes. 100μL of this solution was transferred into a cuvette, and diluted with

1000 µL of Methanol. This absorbance of this solution was measured, and designated as "NT at 0mins". The Ruthenium polymer was added to the parent NT solution by diluting it with a small amount of the methanol used in the parent NT solution. A 100µL aliquot of this "mix" solution was then diluted with 1000µL of Methanol in a cuvette, and its absorbance was then measured. This was designated "NT+polymer at 0mins". This solution was then sonicated, in some cases using an ultrasonic bath, but in most of the experiments, an ultrasonic tip was used. This was a Hielscher UP50H ultrasonic probe, shown in FIGURE 2.18, below[25]. used at 40% amplitude and 0.5 cycles.

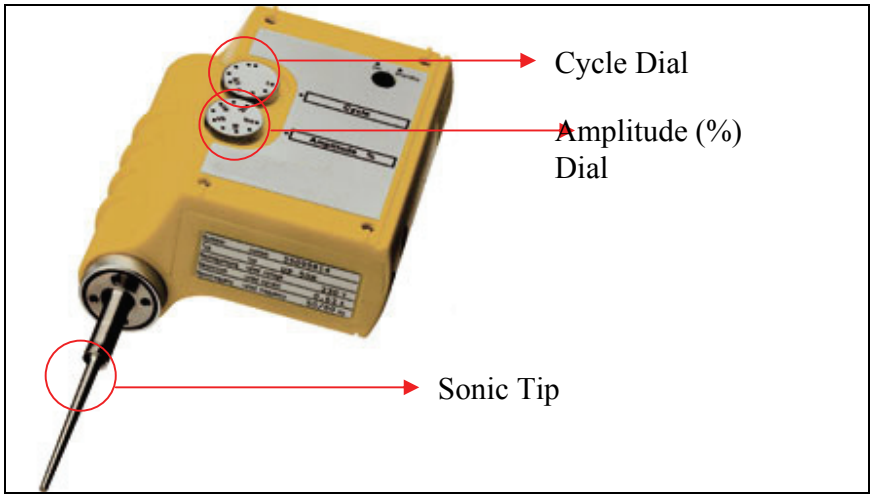

FIGURE 2.8: HIELSCHER UP50H ULTRASONIC TIP USED IN THE CARBON NANOTUBE EXFOLIATION EXPERIMENTS[25].

The sonic tip was mounted on a retort stand and kept at a constant height, to ensure consistent distance of the tip in the solution, as this could affect the efficiency of the sonication process from experiment to experiment. The sonication times were usually 6-7 hours, with periods ranging from 10mins of constant sonication to 90 minutes. The time periods were carefully noted. The solutions were placed in an ice bath throughout the entire sonication period, as the methanol was observed to evaporate if the solution was not kept cool throughout the experiment. The depth of the tip in the solution was monitored, and following the advice of the instrument operating manual, the tip was never submerged more than 3cm into the solution. The absorbance data obtained were plotted as a function of wavelength (nm). The absorbances at 300nm, 350nm, 600nm and 800nm were also plotted as a function of sonication time.

2.6 Bibiliography

1 G. Binnig, C. F. Quate, Ch. Gerber, *Phys. Rev. Lett.,* **1986**, *56*, 930-934
2 T.W. Kim, K.H. Lee, H.S. Lee, J.Y. Lee, S.G. Kang, D.W. Kim, W.J. Cho, *J. Crys. Growth*, **2004**, *262*, 72-77
3 J. Fryar, E. McGlynn, M.O. Henry, A.A. Cafolla, C.J. Hanson, *Physica B*, **2003**, *340-342*, 210-215
4 H. W. Kim, N.H. Kim, *Mat. Sci. & Eng. B*, **2003**, *103,* 297-302
5 X. Xu, C. Guo, Z. Qi, H. Liu, J. Xu, C. Shi, C. Chong, W. Huang, Y. Zhou, C. Xu, *Chem. Phys. Lett.*, **2002**, *364,* 57-63
6 X. Sun, Z. Fu, Z. Wu, *Physica A*, 2002, *311,* 327-338
7 W. Water, S. Y. Chu, *Materials Letters*, **2002**, *55*, 67-72
8 G. Gordillo, C. Calderón, *Sol. Energ. Mat. & Sol. Cells*, **2001**, *69,* 251-260
9 M. Purica, E. Budianu, E. Rusu, *Microelec. Eng.*, **2000**, *51-52*, 425-431
10 W. I. Park, G.-C. Yi J.-W. Kim, S.-M. Park, *App. Phys. Lett.*, **2003**, *82*, 4358-4360
11 J. Song, X. Wang, E. Riedo, Z. L. Wang, *Nano Lett*., **2005**, *5*, 1954-1958
12 B. Marı, M. Mollar, A. Mechkour, B. Hartiti, M. Perales, J. Cembrero, *Microelectronics Journal,* **2004**, *35*, 79-82
13 www.asylumresearch.com/Products/Mfp3D/Mfp3D.pdf - Brochure of the AFM instrument.
14 P. T. Lillehei, C. Park, J. H. Rouse, E. J. Siochi, *Nano Letters*, **2002**, *2*, 827-829
15 J. H. Rouse, P. T. Lillehei, J. Sanderson, E. J. Siochi, *Chemistry of Materials*, **2004**, *16*, 3904-3910
16 H. Yonemura, Y. Yamamoto, S. Yamada, *Thin Solid Films*, **2008**, *516*, 2620-2625
17 H. Chaturvedi, J. C. Poler, *J. Phys. Chem B.*, **2006**, *110*, 22387-22393
18 F. Frehill, J. G. Vos, S. Benrezzak, A. A. Koós, Z. Kónya, M. G. Rüther, W. J. Blau, A. Fonseca, J. B. Nagy, L. P. Biró, A. I. Minett, M. in het Panhuis, *Journal of the American Society*, **2002**, *124*, 13694-13695
19 F. Frehill, M. in het Panhuis, N. A. Young, W. Henry, J Hjelm, J. G. Vos, *J. Phys. Chem. B*, **2005**, *109*, 13205-13209
20 I. Y. Phang, T. Liu, W.-D. Zhang, H. Schönherr, G. J. Vancso, *European Polymer Journal*, **2007**, *43*, 4136–4142
21 Edinburgh Instruments, nF900 Nanosecond Flashlamp Operating Manual Issue 1, 2000
22 Edinburgh Instruments, nF900 Nanosecond Flashlamp Operating Manual Issue 2, 2000.
23 G. B. Porter, *J. Chem. Ed*., **1983**, *60*, 785-790
24 J. H. Rouse, *Langmuir*, **2005**, *21*, 1055-1061
25 http://www.hielscher.com/ultrasonics/50h_p.htm
26 William Henry, PhD Thesis, Dublin City University, **2006**
27 A.W. Adamson, *J. Chem. Ed.*, **1983**, *60*, 797-802

Chapter 3 Preparation of the ZnO / Ru (II) Dye Hybrid System and Analysis by Surface Probing and Spectroscopic Techniques

Chapter 3 discusses the preparation of the transition metal complex/metal oxide nanostructured system. The ruthenium complex used to modify the Zinc Oxide nanorods will be described briefly. The reader is directed to Chapter 2 for the experimental procedures used in this work.

The results from the analysis of the system in both its unmodified and modified forms using the surface probing and microscopy techniques (AFM, SEM) and spectroscopic techniques such as photoluminescence (PL) described in Chapters 1 and 2, are presented.

Finally, conclusions are made as to the nature of the system of interest, with regard to morphology and attempts are made to account for the observations in the systems by the various surface sensitive analytical tools employed. This represents an important step in the analysis of the emission of the ruthenium moiety in the system, as this is an area which has not received great attention in some of the work done by other researchers.

3.0 Introduction

The modification of metal oxide nanostructures such as TiO_2 with photoactive molecules, especially transition metal complexes such as Ruthenium polypyridyl complexes, has resulted in a vast area of research, with significant applications to molecular electronics, solar cells and many other areas of science. This is due to the extremely versatile and efficient photophysical, photochemical, and redox properties of both the substrate, particularly TiO_2 and Ruthenium polypyridyl complexes which act as sensitizing agents in many of the systems that have been investigated. However, the area of ZnO nanostructured substrates modified with ruthenium complexes has not been investigated as thoroughly, to the authors' knowledge. In terms of designing devices based on ZnO nanostructured substrates, modified with photoactive components, the surface topology of the ZnO is of great importance, as it can affect the efficiency of the electron transfer from the sensitizer to the electrode, through the ZnO substrate. As discussed in Chapter 1, ZnO systems have been studied in great detail, both as nanostructured films, or nanostructures of a more definite topology, for example nanorods[1,25,27] and nanosprings[2]. The reader is also referred to refs [21,22] for further reviews of the various ZnO nanostructures that have been prepared.

Both of the factors mentioned in the previous paragraph, namely the surface topology of the ZnO, and the optical emission properties of the ZnO and the Ruthenium complex, are investigated in this work, using AFM (Atomic Force Microscopy), SEM (Scanning Electron Microscopy) and fluorescence spectroscopy. The latter was carried out on both the unmodified ZnO nanorods and the ZnO/Ru composite system, at temperatures ranging from 77K-293K.

The emission properties of both ZnO nanostructures and Ru(II)-based complexes have been extensively studied over the years by many groups. Since this has been discussed in detail in Chapter 1, it is not necessary to tread the same ground here. However, since some of this work is quite relevant to the work discussed in this chapter, and will be referred to in light of the results obtained in the course of this author's work, it is thus useful to discuss the work done by other groups on the ZnO / Ru complex *composite* system, with regard to both the AFM investigations, and the emission studies. It is

important to note however that the AFM studies reported by other groups were performed on the ZnO nanorod / Ru system deposited on a substrate other than Silicon, which was the substrate used in this thesis. This is important as the substrate used can affect nucleation and, to a certain extent, the ZnO nanostructures obtained. This usually affects the degree of alignment of the ZnO nanorods, with respect to the substrate, and also to the other nanorods in the sample[3,4]. There have been, to the best of the author's knowledge, no reports of AFM investigations of ZnO nanorods grown on a Silicon substrate *and* modified with a ruthenium complex. Therefore, we will briefly review some previous studies on ZnO nanorod growth on silicon and ruthenium complex thin films separately as a background to our studies of the combined system**.**

3.0.1 Surface Analysis of ZnO Nanorods + Ru Polypyridyl Complex Composite System

3.0.1.1 AFM of ZnO Nanorods

It will be necessary to consider the studies done by other groups on the morphology of both ZnO nanorods and ruthenium complexes separately using Atomic Force Microscopy (AFM) in order to understand the data presented in much of this chapter. ZnO nanorods will be first considered, followed by an overview of the reports of the deposition of films of ruthenium complexes on various substrates, and the analysis of these films by AFM.

Blackledge and co-workers[5] prepared ZnO nanorods on a quartz substrate by a microsphere lithography process and investigated the nanostructures using AFM, this tool was also used to estimate the dimensions of the nanorods, it was found that the nanorods were approximately 30nm in diameter. That is narrower than the nanorods used in this chapter, judging by the values obtained from the AFM analysis presented later in this chapter. This is more than likely a result of using a different growth procedure (microsphere lithography) for the ZnO nanorods, compared with the Vapour Liquid Solid (VLS) process used in this thesis. A representative AFM image of the ZnO nanorods in spheres grown in ref [5] is shown in FIGURE 3.1, below. This image is of

unusually high resolution, for an AFM image, the diameters of the nanorods are estimated to be approximately 30nm, this would be quite difficult to image using AFM. Unfortunately, no experimental details were reported in the paper regarding the acquisition of the AFM images. It is the authors belief that this is actually an SEM image, as the gold tips of the nanorods are seen to be brighter in the image than the nanorods. There is no reason for this to be the case if this is an AFM image, in addition, no height scale is given.

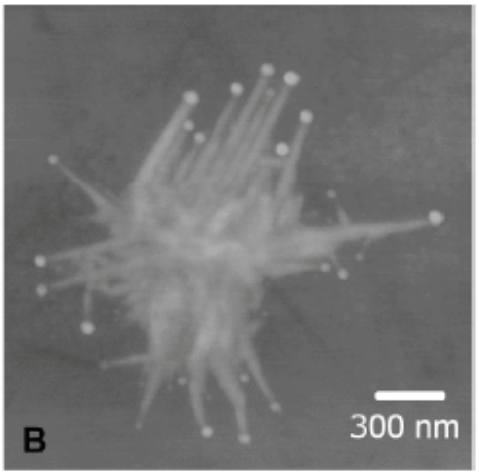

FIGURE 3.1: AFM IMAGE OF ZnO NANORODS GROWN IN SPHERES, NANORODS ARE APPROXIMATELY 30NM IN DIAMETER[5].

AFM has also been utilized by Hari *et al*[6] to investigate the surface roughness of ZnO nanorods samples prepared on glass coated with ITO (Indium Tin Oxide), using a chemical bath method. It was found that the surface roughness increased with increasing the heating time of the ZnO in the chemical bath. It was suggested that the ZnO nanorods prepared using shorter heating times, bundled or coalesced together during longer heating times, forming larger nanorods, and this is accounted for in the slightly larger surface roughness values observed. An AFM image reported in the article[6] is shown in FIGURE 3.2, on the next page.

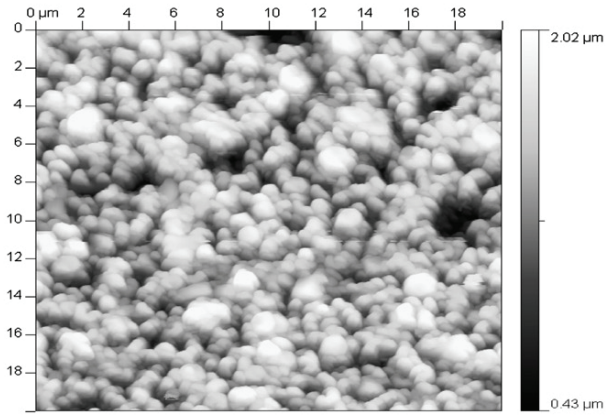

FIGURE 3.2: AFM IMAGE OF THE ZnO NANORODS AFTER 26 HOURS OF HEATING IN THE CHEMICAL BATH.[6]

It is observed in FIGURE 3.2 that the nanorods are quite closely packed, and therefore the AFM tip is really only imaging the tips of the nanorods. A similar situation is observed in some of the AFM images obtained in the work of this thesis, and some of these will be presented later in this chapter. It is also seen that the coverage of the substrate with the nanorods is reasonably uniform, at least over the 20µm x 20µm scan size used in FIGURE 3.2.

Cheng and co-workers[7] also prepared ZnO nanorods on an ITO substrate and used a modified version of AFM called PhotoConductive-Atomic Force Microscopy (PC-AFM) to probe the Current – Voltage (*I-V*) characteristics of the ZnO nanorods. However, AFM (or DFM, as it is termed in the report) was also used to study the morphology of the nanorods. One of the images reported is shown in FIGURE 3.3, below.

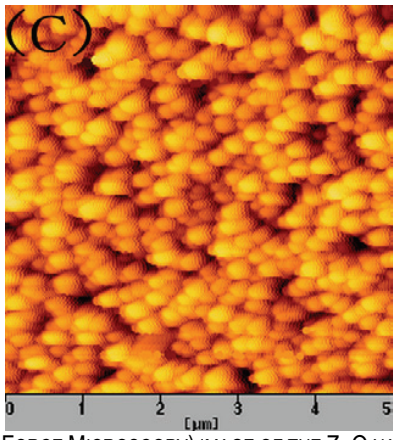

FIGURE 3.3: 5µM X 5µM DFM (DYNAMIC FORCE MICROSCOPY) IMAGE OF THE ZnO NANORODS.[7]

It was observed that the dimensions of the nanorods calculated from the AFM images were greater than those calculated using the SEM images also reported. This was attributed to the tip convolution, and this is considered to be a result of the high aspect ratio of the nanorods themselves.

Park *et al*[8] investigated a similar system, namely a Shottky nanocontact between the ZnO nanorod tips and the AFM tip. They used AFM to image the nanorod arrays prepared on an Al_2O_3 (00$^{\cdot}$1) (sapphire) substrate. One of the images reported is shown in FIGURE 3.4, below.

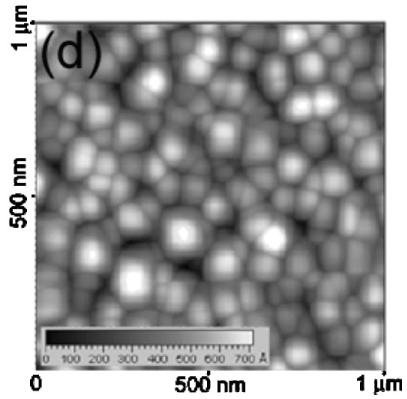

FIGURE 3.4: CONTACT MODE AFM IMAGE OF ZnO NANORODS ON A SAPPHIRE SUBSTRATE. [8]

It is difficult to accurately ascertain the diameters of the nanorods from the above image, however, they are of the order of 100nm. It is again observed in this system that only the tips of the nanorods themselves are imaged by the AFM tip, and this can be attributed to AFM tip convolution, and also the densely packed nature of the nanorod arrays.

Song and co workers[9] reported the growth of ZnO nanorods on a sapphire surface and the measurement of the elastic modulus of these nanorods, using an AFM tip. The topographic AFM image reported in the article is shown in FIGURE 3.5, below. Again, only the tops of the nanorods appear to be imaged by the AFM tip.

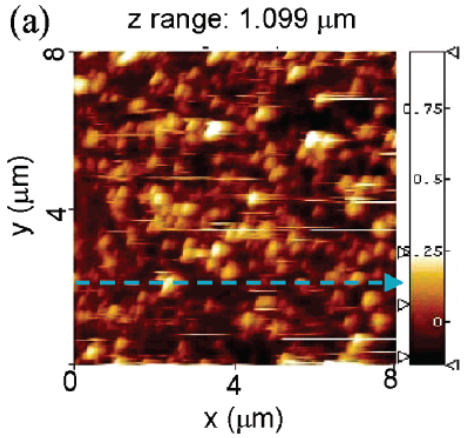

FIGURE 3.5: CONTACT MODE AFM IMAGE OF ZNO NANORODS GROWN ON A SAPPHIRE SUBSTRATE.[9]

The image is not as sharp or as well defined as the others presented so far, this can be probably be attributed to the use of a different tip, or different post-imaging digital treatment of the image.

Marí *et al*[10] prepared ZnO nanocolumns on a conducting glass substrate, and used AFM to measure the heights of the nanocolumns. An AFM image was reported, and is shown in FIGURE 3.6. Height data for the nanocolumns was also reported and the heights were found to range between 110nm and approximately 900nm, depending on the growth conditions used.

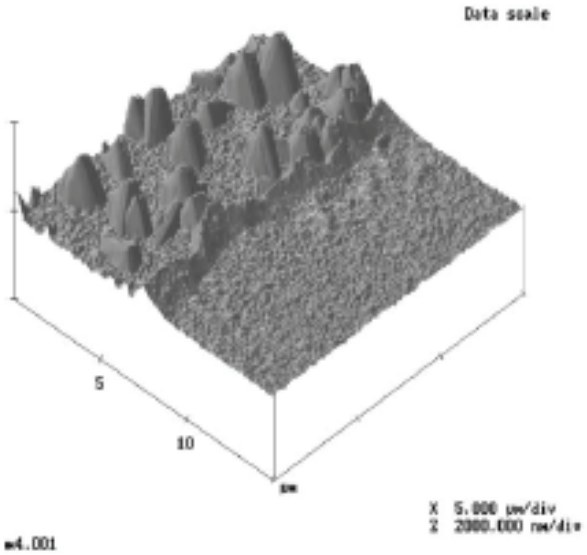

FIGURE 3.6: 3-DIMENSIONAL REPRESENTATION OF AN AFM IMAGE OF ZNO NANOCOLUMNS PREPARED ON GLASS. [10]

The image size in FIGURE 3.6 is 15µm x 15µm.

3.0.1.2 AFM of Ruthenium Complex films

Atomic Force Microscopy has also been used to study the morphology of thin films of ruthenium complexes that have deposited on a substrate. Di Bella *et al*[11] reported the deposition of a ruthenium complex on a hydrophobic quartz slide, via a Langmuir-Blodgett method. This deposition was then investigated by AFM. The images reported in ref [11] are shown in FIGURE 3.7, below.

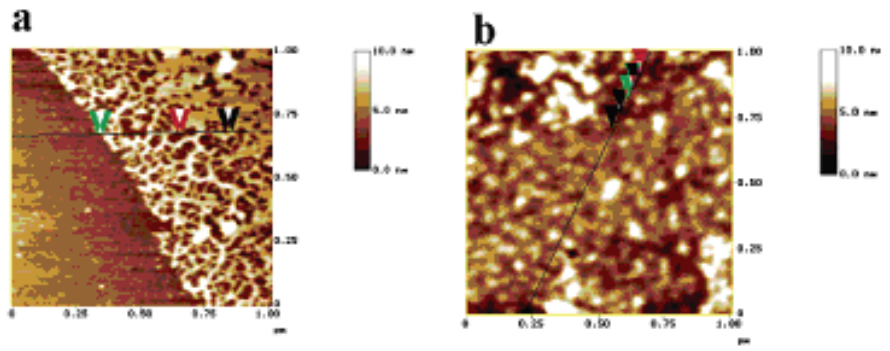

FIGURE 3.7: AFM IMAGES OF THE RUTHENIUM FILM ON A QUARTZ SLIDE. (ADAPTED FROM REF [11])

It is seen in the "**a**" image in FIGURE 3.7 that aggregates have formed (5nm in height, white ridges), and are surrounded by a network of nanowires, (2nm in height, brown patches). This image refers to one Langmuir Blodgett deposition, the "**b**" image shows the film after five depositions. This film is more uniform and more homogenous than the film obtained after a single deposition, and shows densely packed aggregates of the ruthenium complex. It is important to note that while the deposition technique used in this report (ref [11]) is different from that used in this thesis for the modification of the ZnO nanorods, the images seen in FIGURE 3.7 can still used as a guide as to what to expect from the system investigated in this chapter. In the images shown in FIGURE 3.7, the height scale bar is 0nm – 10nm, and the image size is 1μm x 1μm, in each case. Gohy *et al*[12] used a drop cast method to deposit a film of ruthenium block co-polymer micelles on a mica surface. This was then investigated by AFM, and it was found that some aggregation of the micelles occurred; however no mechanism for this aggregation was proposed. Ma *et al*[13] created thin films of a mixture of a ruthenium phenanthroline

complex, $[Ru(phen)_3]Cl_2$ and a polyoxo-metalate, on quartz, silicon and ITO substrates. It was found from AFM studies that the films prepared on a silica substrate were relatively uniform and smooth. One of the AFM images reported is shown in FIGURE 3.8, below. This type of system has also been investigated by Cheng and Cox[15], and more recently again by Ma *et al*[16].

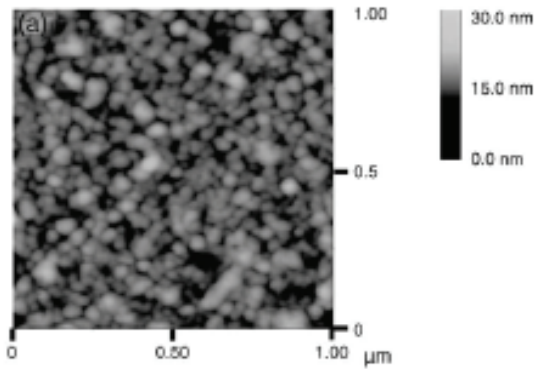

FIGURE 3.8: AFM IMAGE OF PEI/$[P_2Mo_{18}/Ru(phen)_3]_4$ P_2Mo_{18} DEPOSITED ON A SILICA SUBSTRATE.[13]

He and co-workers[14] prepared films on a mica substrate, using an amphiphilic ruthenium complex, $[Ru(CN)_4L]$ where L was a bipyridine ligand with n-dodecylaminoyl moieties in the 4,4' positions. Aggregates described as "string-like" were observed, and it was found that much of the mica substrate was unoccupied after the Langmuir Blodgett deposition. The above discussion serves as an overview of the results obtained by other groups, using slightly different systems (ZnO nanorods, and films of ruthenium complexes) to that used in this thesis. Therefore, it should be noted that the above discussion will not provide a definitive guide to what is to be expected in the AFM analysis of the ZnO nanorods / ruthenium complex system investigated in this chapter. However it should give a general idea of the types of features which are observed in the images in the following sections of this chapter.

3.0.2 Emission of ZnO Nanorods + Ru Polypyridyl Complex Composite System

Hsu *et al*[17] have investigated the emission properties of ZnO nanorods modified with a similar ruthenium complex to that used in this work, N719. The chemical structure of this complex is shown in FIGURE 3.9, below.

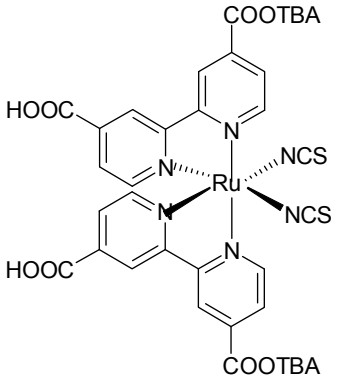

FIGURE 3.9: MOLECULAR STRUCTURE OF N719, $(Bu_4N)_2[Ru(DCBPYH)_2(NCS)_2]$

A system exhibiting dual emission is described, with both ZnO and ruthenium based emissions being observed. The emission spectra given are shown in FIGURE 3.10 on the next page.

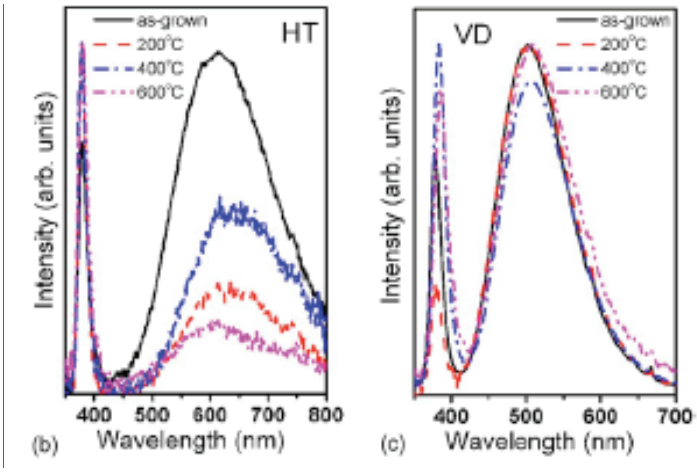

FIGURE 3.10: EMISSION SPECTRA OF THE ZnO NANORODS ANNEALED AT VARIOUS TEMPERATURES. HT AND VD REFER TO THE GROWTH METHODS USED, HYDROTHERMAL AND VAPOUR DEPOSITION.[17]

It is not clear however from the report whether the spectra shown in FIGURE 3.10 refer to the modified ZnO nanorods, or to the unmodified nanorods, as the peaks seen at

approximately 600nm in the HT spectra and 500nm in the VD spectra could be a ruthenium based emission originating from the MLCT excitation, or it could attributed to oxygen or other defects in the ZnO itself, this has been observed by other groups before[18,19]. Given that there is a shift in the λ_{max}, and also considering that the samples are annealed at 200ºC, 400ºC, and 600ºC, it is more likely that the peak in question is due to defects in the ZnO peaks, and therefore it is not is easy to compare this data to that obtained in the course of this thesis.

Taratula *et al*[20] studied the binding of $[Ru(bpy)_2(dcbpy)]^{2+}$ and another complex, shown in FIGURE 3.11, to ZnO nanotip films, and in particular investigated the emission properties of this composite system. The emission data presented in the report (an example of which is shown in FIGURE 3.12) suggests quenching of the ruthenium MLCT based emission upon binding with the ZnO film. This is not what is found in this chapter, emission is still observed from both the ZnO and the ruthenium components. The concentrations of the ruthenium dye used by Taratula *et al*[20] are very slightly higher than that used in this work, however, the differences in the emissions observed can best be explained by differences in the procedures used to create the films, removal of solvent and excess dye material is a large feature of Taratulas process, while only simple evaporation of the solvent is used in this work.

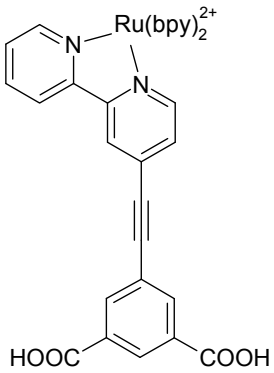

FIGURE 3.11: STRUCTURE OF RUTHENIUM COMPLEX USED IN BINDING STUDY IN REF [20].

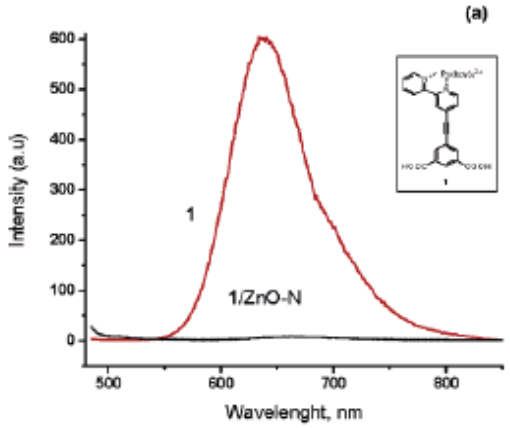

FIGURE 3.12: EMISSION DATA FOR RUTHENIUM COMPLEX ON ZnO NANOTIPS FILM (BLACK LINE) COMPARED WITH THE EMISSION SPECTRA OF THE COMPLEX IN SOLUTION (RED LINE), FROM REF [20].

3.0.3 Aims of Work and Outline of Chapter

A central aim of the work is to investigate the effect of modifying ZnO nanorods with a photoactive ruthenium complex. Changes in ZnO emission and morphology will be investigated, as will the ruthenium emission. It is thought that the ruthenium complex will inject electrons into the ZnO nanorods, as this has been demonstrated with ZnO films modified with ruthenium complexes[32]. It is anticipated that the investigation of the morphological and photophysical properties of the composite ZnO/Ru system will enable a greater understanding of the parameters which affect the efficiency and design of such systems, with a view to more efficient solar cell type devices. The use of AFM to analyse such systems is unusual, however it can be done, and the work presented in this chapter demonstrates both the experimental difficulties involved, and also the type of information that can be obtained from such a method. Many ZnO samples have been investigated throughout the investigation of the emission properties of this ZnO/Ru system. Results from one representative sample will be presented for the fluorescence data. This sample was called ZnO [RU2]. This sample was scribed into two pieces prior to modification with the ruthenium complex, and these two pieces will be referred to as A and B. A refers to the ZnO sample left unmodified, while B refers to the ZnO sample modified with the ruthenium complex. The results focus on two aspects of the system, the ZnO emission, and the ruthenium based emission.

AFM was carried out in the Department of Physics and Astronomy, University of Nottingham, and focused on the topology of the unmodified and modified ZnO nanorods, and whether the modification of the ZnO nanorods with the Ruthenium complexes produced in any obvious morphological change in the nanorods. Using the AFM controller software, MFP3D, an attempt was made to calculate the dimensions of various features observed in the AFM images obtained.

Auger Electron Spectroscopy (AES) was also carried out on some of the ZnO samples, again this was done in University of Nottingham. This technique focused on the presence or absence of Ruthenium peaks in the spectra of modified and unmodified ZnO nanorod samples.

Scanning Electron Microscopy (SEM) data will be presented for a sample used in the initial stages of this project. SEM images of both the unmodified ZnO nanorods and ZnO nanorods will be presented and discussed.

3.1 Preparation of the ZnO Nanorod/Metal Complex System

The ZnO nanorods were grown on a silicon surface using a Vapour Liquid Solid process as referenced previously in Section 1.1.2. Gold was used as a catalyst. The hybrid system was prepared by immersing the ZnO sample in a 1mM methanol solution of the ruthenium complex (FIGURE 3.13 below), taking care to use a dry solvent and to keep water from the air away from the sample. This complex was synthesized according to a previously published procedure[33]. The ZnO was immersed overnight in this solution and then removed and allowed to dry in air. Care was taken to ensure that no significant deposition of the ruthenium complex had occurred on the silicon surface where ZnO deposition had not occurred (i.e. the region not coated with Au catalyst) as this would interfere with the emission measurements.

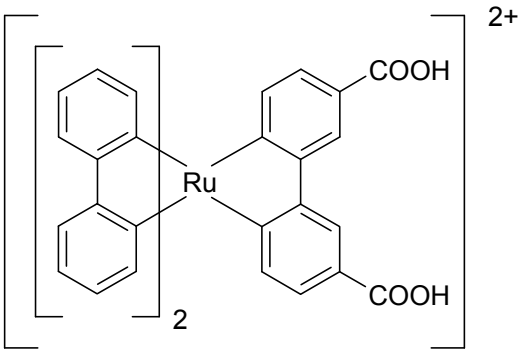

FIGURE 3.13: STRUCTURE OF [RU(2,2'-BPY)2(4,4'-DICARBOXY - 2,2'-BPY)], THE COMPLEX USED IN THE SENSITIZATION OF THE ZNO NANORODS, DISCUSSED IN THIS CHAPTER.

AFM measurements were performed as described later in this chapter, and the experimental setup used is discussed in Chapter 2.

3.2 Results and Discussion

3.2.1 Scanning Electron Microscopy (SEM)

The unmodified and modified ZnO samples were also briefly investigated using High Resolution Scanning Electron Microscopy. These were some of the earliest ZnO samples to be investigated, and some interesting results were observed. The SEM images for the unmodified sample are shown in FIGURE 3.14, below.

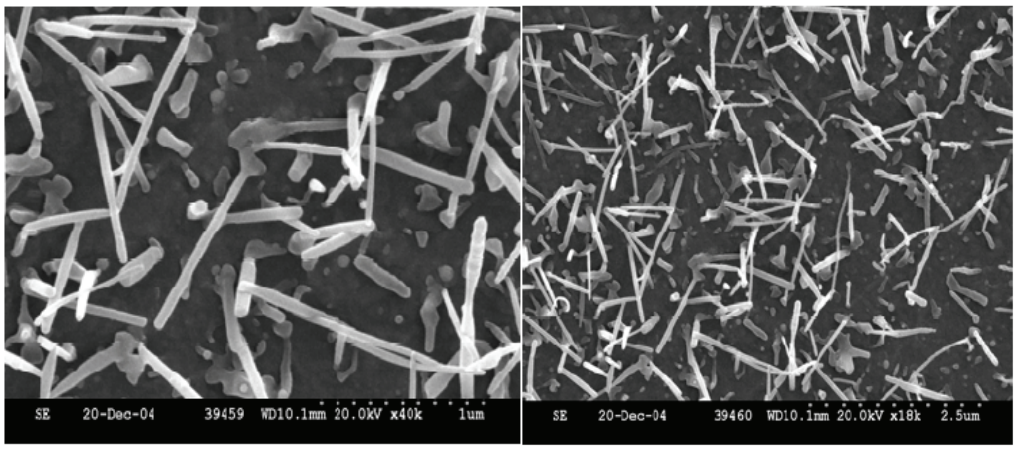

FIGURE 3.14: HR-SEM IMAGES OF THE UNMODIFIED ZNO NANORODS. MAGNIFICATION IS 40K, AND 10K, LEFT AND RIGHT IMAGES RESPECTIVELY.

In FIGURE 3.14, above, the unmodified ZnO nanorods are seen to be smooth, narrow and they appear to be separate from each other. The surface coverage of the ZnO nanorods is quite low, at least in the area of the image above. These images differ quite significantly from the images obtained of the modified ZnO nanorods. These are shown in FIGURE 3.15, below.

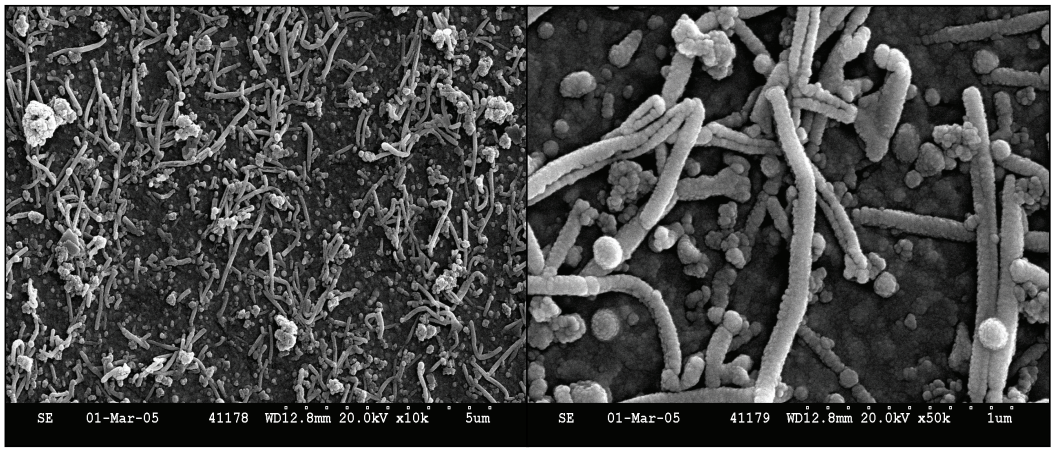

FIGURE 3.15: HR-SEM IMAGES OF THE ZnO NANORODS MODIFIED WITH THE Ru POLYPYRIDYL COMPLEX.

The morphology of the nanorods seen in FIGURE 3.15, above is markedly different from that of the unmodified nanorods in FIGURE 3.14. The morphology observed can best be described as "fuzzy". There also appears to be some deformation of the nanorods, some are no longer straight, as they were in FIGURE 3.14. It is difficult to say if this the ruthenium complex layer on the nanorods, or whether the nanorods have been decomposed by water in the solution containing the ruthenium complex. Given that the general ZnO nanorod morphology has been preserved to a certain extent, it is hoped that the decomposition is minimal, or that the added mass of the ruthenium complex particles has caused the nanorods to buckle in the fashion observed in FIGURE 3.15. An interesting point with regard to some of the analysis work done using the AFM is the determination of the dimensions of the nanorods. From the above figures, it is estimated that the unmodified nanorods have a diameter of approximately 60-70nm, and the modified nanorods have a diameter of approximately 100nm. These do not concur with the values for the diameters of the unmodified and modified nanorods obtained AFM analysis. These AFM determined values were considerably higher than the estimates from the SEM images. This suggests that in the case of this system, AFM is good for determining

overall sample uniformity, and morphology, but may not be able to provide the same level of accuracy as SEM in determining the dimensions of features on the surface. It is important to note, however, that the AFM tip used to scan the samples in this study was a fairly standard tip. Using a higher resolution tip may increase the level of detail and accuracy in the sectional analysis measurements. It is also extremely important to bear in mind that different samples were used for the AFM analysis than were used studied using SEM. It is well known that all samples will have slight differences, and it may be that in the case of the samples investigated with AFM, these samples may have been composed of nanorods with greater diameters than those samples in the SEM images, perhaps due to different growth parameters.

3.2.2 Atomic Force Microscopy (AFM)

3.2.2.1 AFM Data and Preliminary Analysis

It was decided to examine various aspects of the ZnO sample growth and subsequent modification using AFM, and the work presented in this section is ordered as follows:

- Uniformity of substrate coverage
- Uniformity of nanostructure dimensions
- Modification of nanorods, and analysis using AFM.

The AFM images obtained and the analysis of these images are shown in FIGURES 3.16-3.31. FIGURES 3.16-3.23 show AFM images of sample Au14, not modified with the ruthenium complex, while FIGURES 3.24-3.28 show AFM images of sample Au14, modified with ruthenium complex. FIGURES 3.29-3.31 show AFM images of a single unmodified ZnO nanorod, from a different ZnO sample Au15.

3.2.2.2 Uniformity of Substrate Coverage-Unmodified Sample

It was decided to first investigate the uniformity of the sample over a reasonably large area, 20µm x 20µm. This would give a idea of the extent of the coverage of the sample with the ZnO nanorods, and serve as a general guide as to what sort of features to expect in smaller scan sizes. FIGURE 3.14 is indicative of the type of scan obtained over this scan size for a ZnO nanorod sample, prior to any modification with the ruthenium complex.

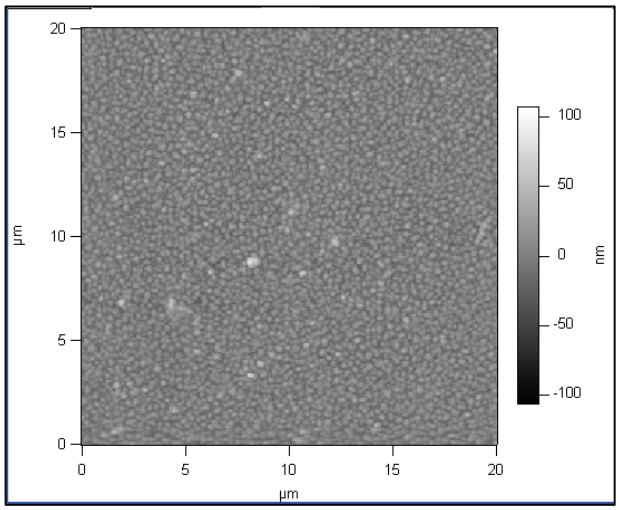

FIGURE 3.16: 20µM AFM IMAGE OF THE UNMODIFIED ZnO SAMPLE. THIS IMAGE SUGGESTS THE SAMPLE IS QUITE UNIFORM.

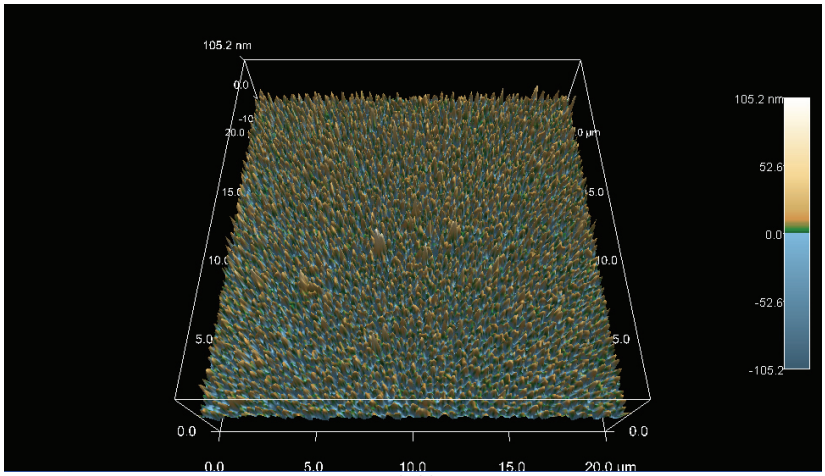

FIGURE 3.17: 3D REPRESENTATION OF THE IMAGE IN FIGURE 3.16, ABOVE.

The images in FIGURES 3.16 and 3.17 show the relative uniformity of the sample, at least over the area of 20µm. This is inferred from the distribution of the features, shown in yellow in FIGURE 3.17 above. This indicates that the growth of the ZnO is relatively

uniform in this area, and more importantly, shows that the AFM tip is able to track across the features. This image was recorded using 256 scan points and a scan rate of 1Hz. It was decided to scan the sample over a smaller area, to investigate more fully the features seen in FIGURE 3.16.

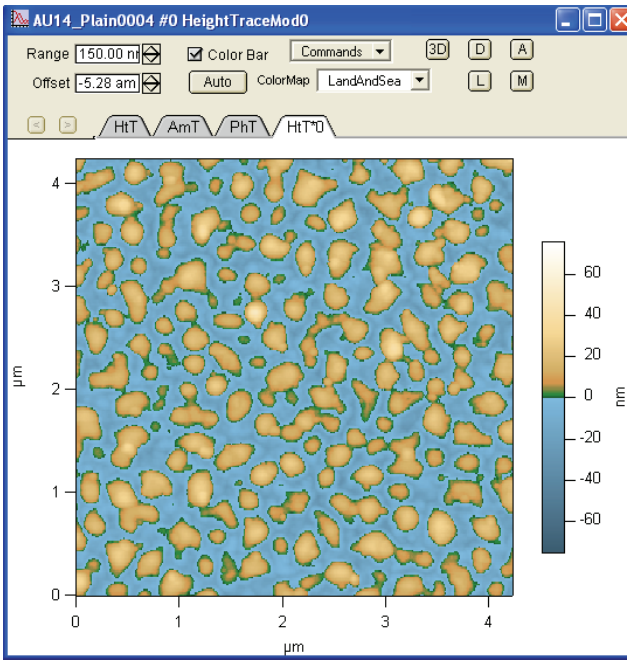

FIGURE 3.18: AFM IMAGE OF THE UNMODIFIED ZnO SAMPLE. THE SAMPLE APPEARS TO BE AGAIN REASONABLY WELL ORDERED. THIS IS ALSO OBSERVED IN FIGURE 3.17, BELOW.

In FIGURE 3.18, above, the sample appears to show the tops of rod-like structures. This indicates that the growth mechanism is producing good quality samples, with the sample uniformity being evident over at least an area of the scan size (20µm). The important observation to note with regard to the images shown in FIGURE 3.16 and FIGURE 3.18 is that they agree with the images reported by other groups[6,7]. Overall, the features appear quite similar, the only minor difference being that the nanorods shown in FIGURE 3.18 do not appear to be as densely packed as those reported by Hari[6] and Cheng[7].

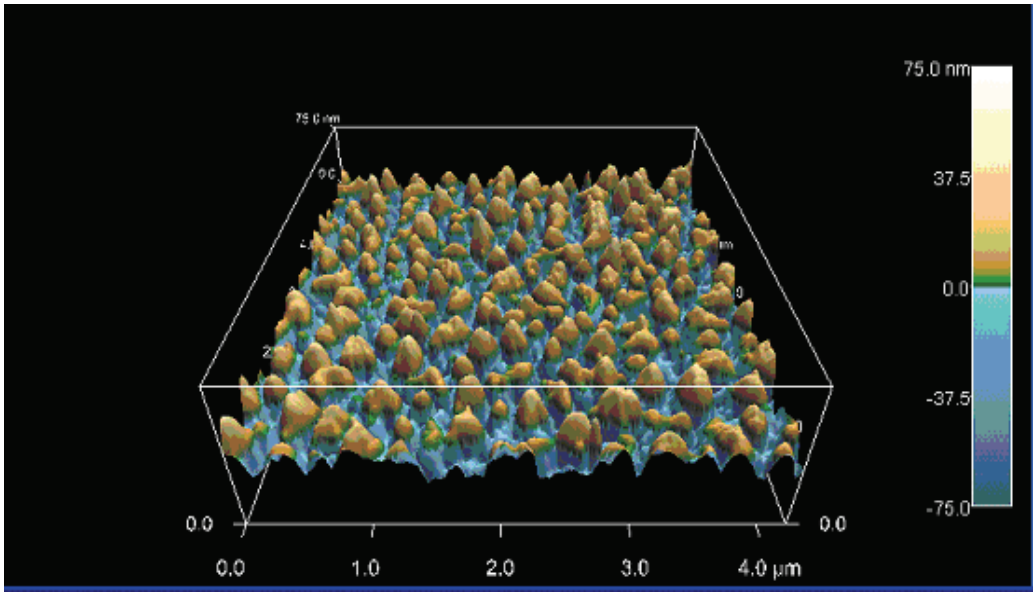

FIGURE 3.19: 3 DIMENSIONAL REPRESENTATION OF THE IMAGE SHOWN IN FIGURE 3.18, ABOVE. THIS IMAGE APPEARS TO SHOW THE TOPS OF THE NANORODS, AND SUGGESTS THAT THEY ARE REASONABLY WELL ALIGNED WITH RESPECT TO EACH OTHER. THE FEATURES SEEN ALSO APPEAR TO BE OF A SIMILAR HEIGHT.

The images in FIGURE 3.18 and Figure3.19, on the previous page and above, respectively, show a scan size of just over 4µm, and show the relative uniformity of the individual feature sizes and heights, a fact that the sectional analysis presented later in this chapter confirms. It is also observed, particularly in FIGURE 3.19, above, that only the tips of the nanorods have been imaged by the AFM tip. This is possibly due to the scan rate of the tip being set too high, thus preventing the AFM tip from having enough time to oscillate in "between" the nanorods. However, given that the tips of the nanorods themselves have been adequately imaged, this possibility seems unlikely. Alternatively, it may be that the nanorods are relatively well "packed". This would mean therefore, that the interstitial spaces are very small, and this, combined with the high aspect ratios for nanorods may result in the AFM tip only imaging the tops of the nanorods adequately. This has been reported by other groups[7-9].

The scan size was again reduced in an attempt to image more closely the features observed in FIGURE 3.18 and FIGURE 3.19, and the images obtained are shown in FIGURE 3.20.

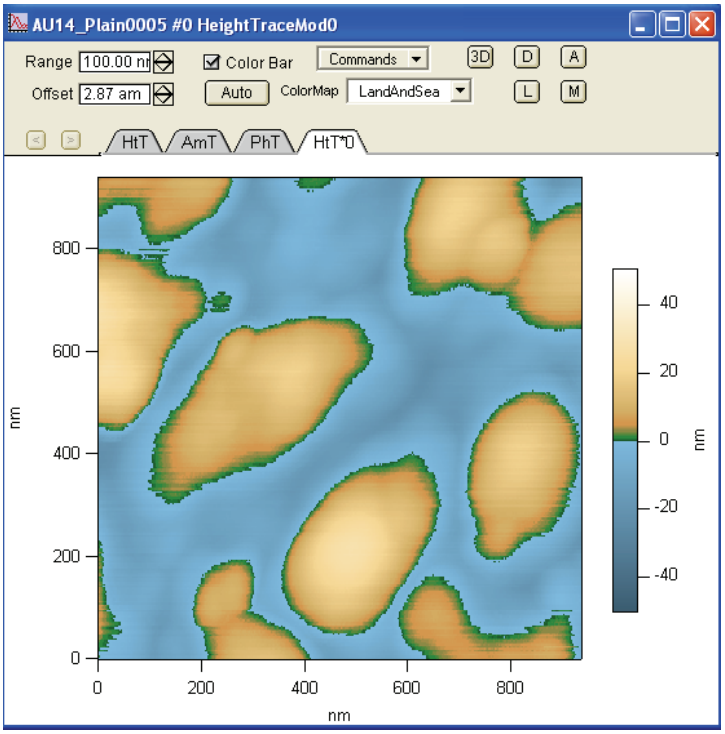

FIGURE 3.20: AFM IMAGE OF WHAT APPEAR TO BE TIPS OF THE NANORODS SHOWN IN THE PREVIOUS IMAGES, FIGURES 3.18 AND 3.19.

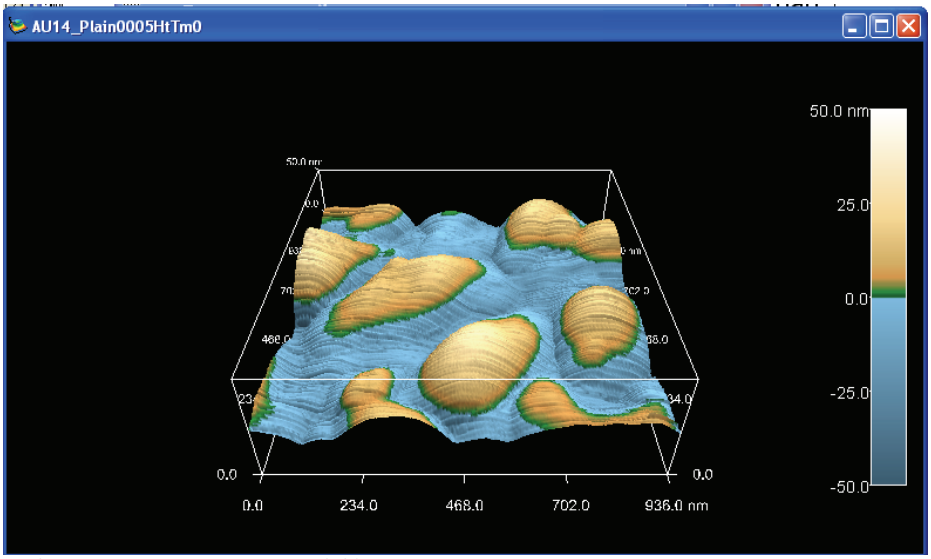

FIGURE 3.21: 3 DIMENSIONAL VIEW OF FIGURE 3.20, ABOVE.

The images in FIGURE 3.20 and FIGURE 3.21 above were obtained by increasing the number of data points to 512, instead of 256, and by decreasing the scan speed to 0.2Hz, in order for the AFM tip to track properly over the very small sample area. Previously, when similar images were obtained, it was found that using a higher scan rate resulted in the tip and piezo being unable to react in time to the rapid change in the height of the

features, and consequently the features observed in the image were badly "skewed". The above AFM images appear to show nanorod like structures, as expected. The images appear to show the tops of the nanorods, and show the uniformity of the sample. The sample appears to be quite clean, and it was found that the tip tracked the surface quite well in each case. The nanorods also appear to be fairly smooth, and this property can be contrasted with the decidedly "clumpier" morphologies observed in the modified samples, presented in the images to follow. A sectional analysis of the images was carried out in the case of the second sample, and the results of this analysis are shown in FIGURES 3.22-3.23.

3.2.2.3 Determination and Uniformity of Nanostructure Dimensions of unmodified ZnO sample

In this section, the AFM Igor software was used to make sectional images of the overall AFM image, along a user-defined line. In the images in this section, the red line is the line defined as the section line. FIGURE 3.22(A) shows the sectional analysis of the feature just below the centre of the image, while FIGURE 3.22(B) shows the analysis of the feature to the left of the centre of the image.

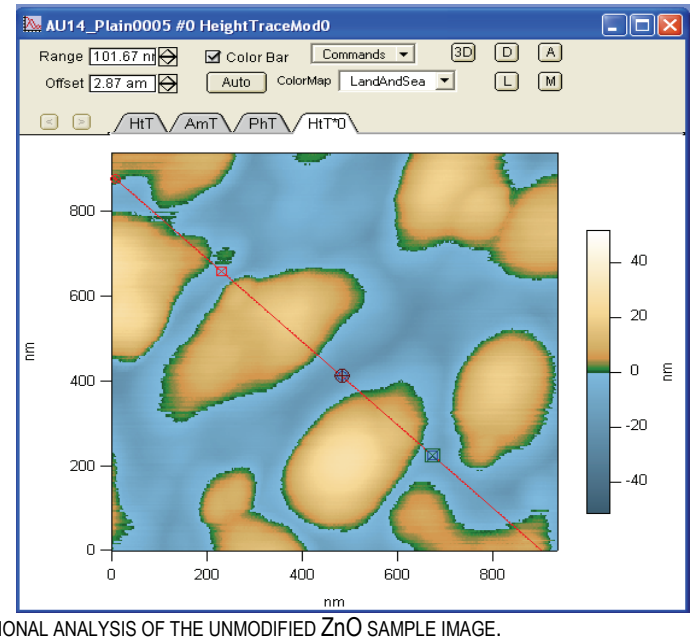

FIGURE 3.22(A): SECTIONAL ANALYSIS OF THE UNMODIFIED ZnO SAMPLE IMAGE.

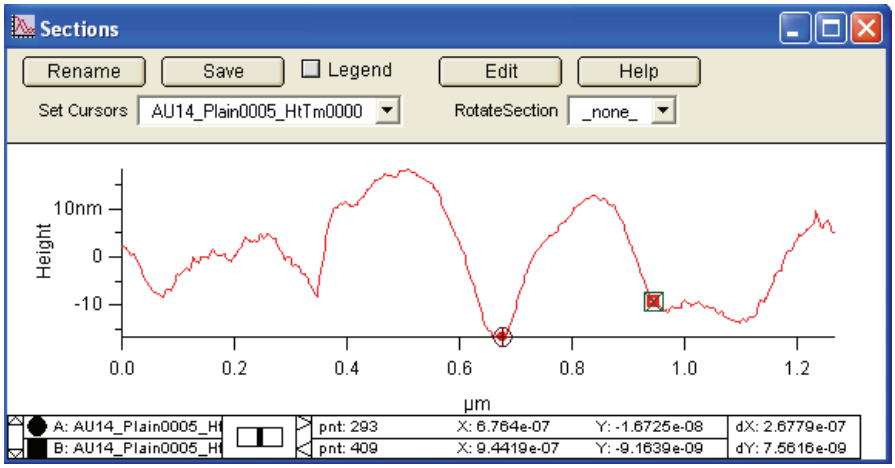

FIGURE 3.22(B): SECTIONAL ANALYSIS OF THE SELECTED FEATURE INDICATES THAT ITS WIDTH IS APPROXIMATELY 270NM

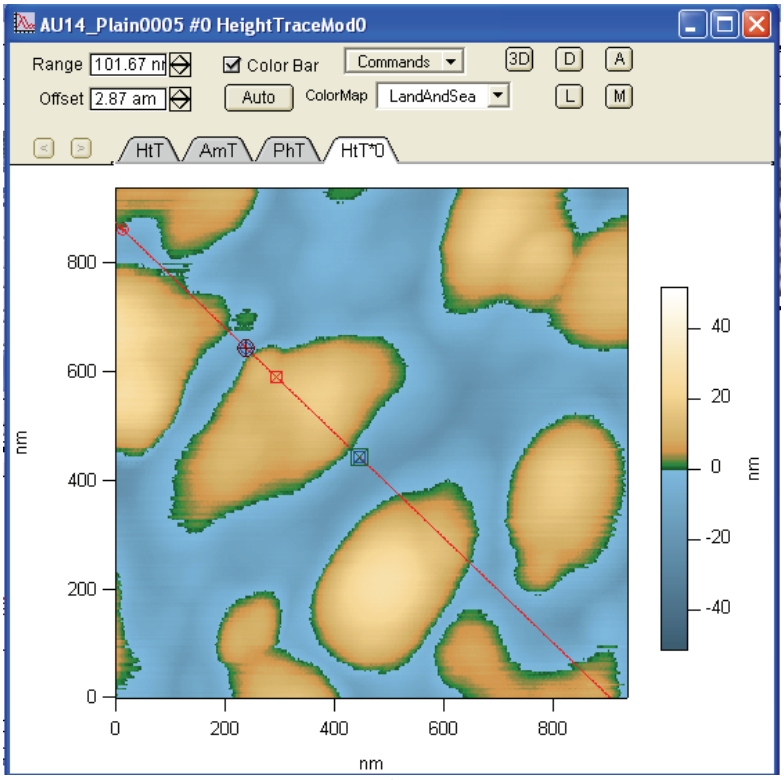

FIGURE 3.23(A): SECTIONAL ANALYSIS OF THE UNMODIFIED ZNO SAMPLE IMAGE.

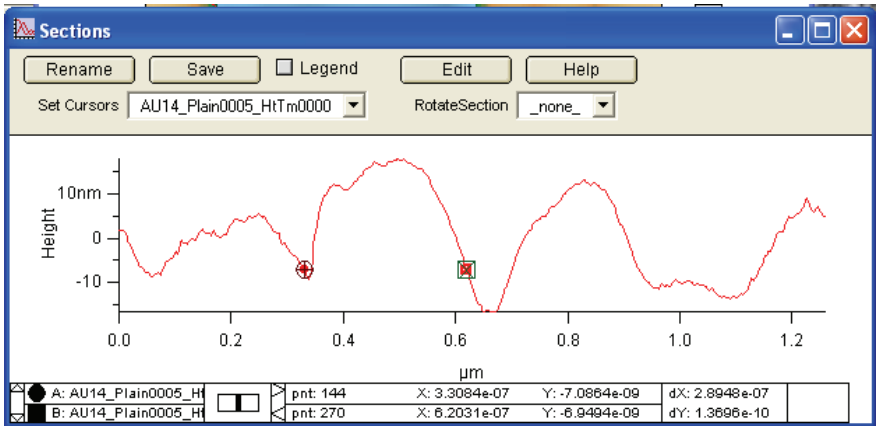

FIGURE 3.23(B): SECTIONAL ANALYSIS SUGGESTS THE WIDTH OF THE FEATURE IS APPROXIMATELY 290NM

The sectional analysis of the sample area indicates that the features analyzed, which are not an exhaustive representation of the sample as a whole, have widths of the order of 280nm. This still shows some uniformity of the sizes of the features, thought to be the tips of the nanorods. The width of the nanorod feature found in FIGURE 3.23(B) is of the same order as that found for ZnO nanorods grown by solution prepared nanoparticles which were used as a seeding layer for nanorods[7] and metalorganic vapour phase epitaxy[8].

3.2.2.4 Uniformity of Surface Coverage-Modified Sample

The same methodical scanning approach for the AFM investigation of the unmodified sample discussed in the previous section, section 3.3.3, was used for the investigation of the ZnO nanorods modified with the ruthenium complex. The reason and purpose for this are the same as that outlined in section 3.3.3, namely to probe the uniformity of the sample after modification, and then investigate the dimensions observed in the images. FIGURE 3.24(A) shows the surface topography over a reasonably large area, 20µm x 20µm, and again serves as a guide to the acquisition of the subsequent images.

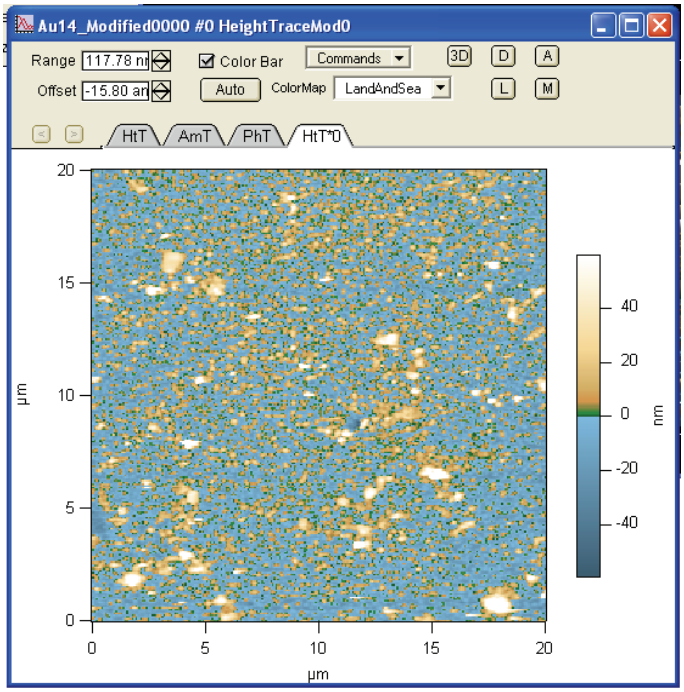

FIGURE 3.24(A): 20µM IMAGE OF THE MODIFIED SAMPLE, THIS SHOWS SOME AREAS OF DIRT, BUT OVERALL, THE SAMPLE APPEARS TO BE FAIRLY UNIFORM, AND INDEED FAIRLY SIMILAR TO THE 20µM SCAN OF THE UNMODIFIED SAMPLE.

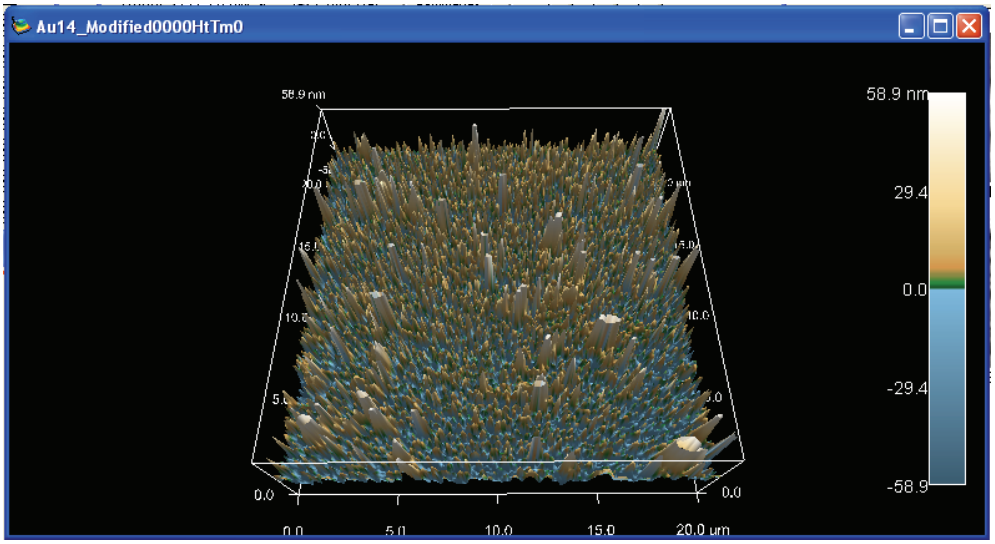

FIGURE 3.24(B): 3D REPRESENTATION OF THE IMAGE IN FIGURE 3.24(A), ABOVE. THE SAMPLE IS REASONABLY UNIFORM WITH SOME CLUMPING OBSERVED, PARTICULARLY IN THE CENTER OF THE IMAGE.

There appear to be particles of dirt on the sample, in the area imaged in FIGURE 3.24(A) and FIGURE 3.24(B). They are most evident in the bottom right hand corner, and in a few areas right of the centre of the image, where the height is greatest. These features are unlikely to be nanorods, or ruthenium moieties given the lateral size and heights (values of around 60nm, compared with 40nm at most for the nanorod features).

It was decided to decrease the scan size to better image the different features, and to look at a relatively "clean" area of the sample. The results of this investigation are shown in FIGURE 3.25(A) and FIGURE 3.25(B).

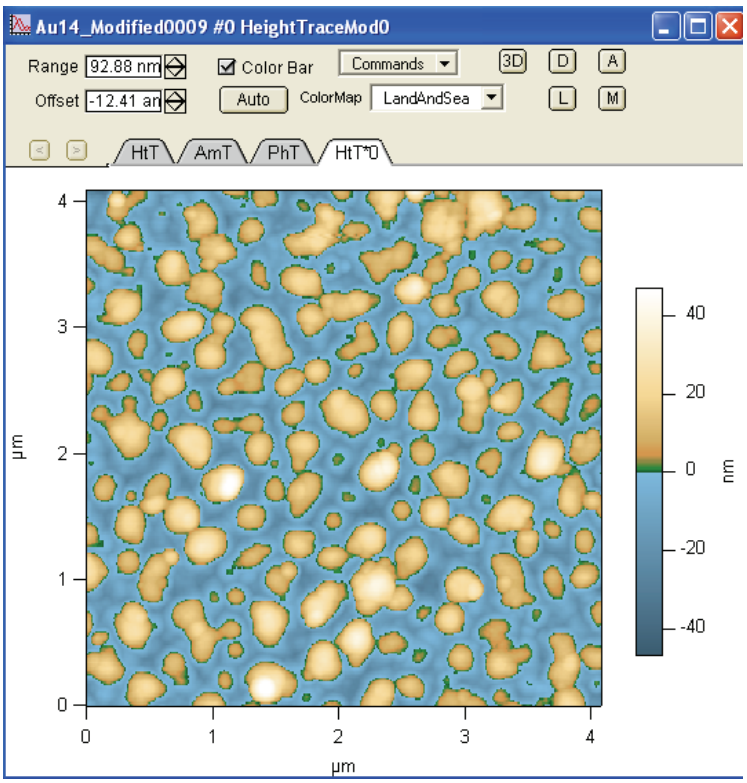

FIGURE 3.25(A): 4.08µM X 4.08µM IMAGE OF THE MODIFIED ZnO SAMPLE

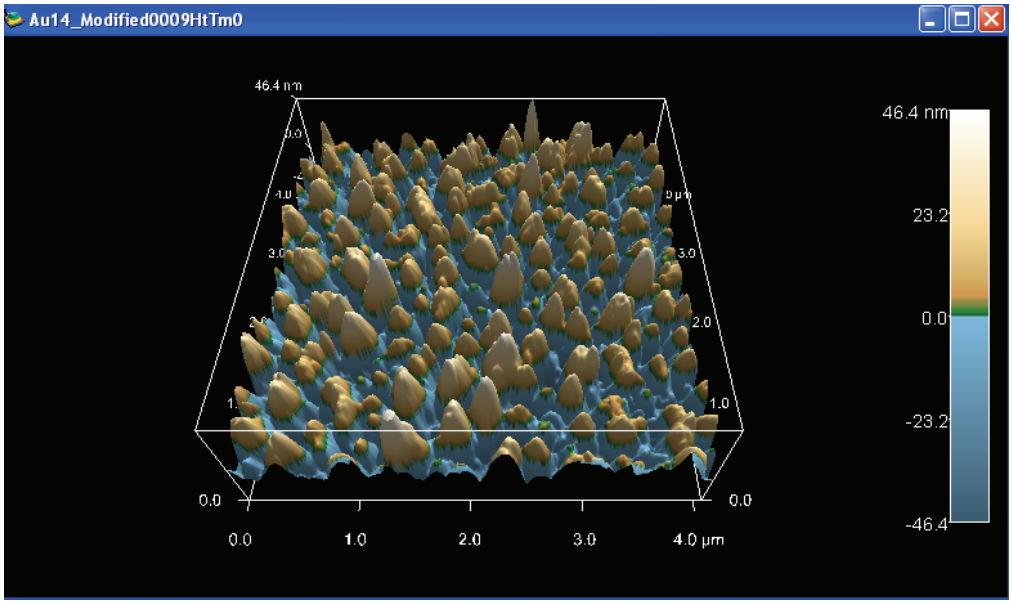

FIGURE 3.25(B): 3D VIEW OF THE IMAGE IN FIGURE 3.25(A), ABOVE.

In FIGURE 3.24 and FIGURE 3.25 above, the presence of what appear to be two types of features is observed, and in FIGURE 3.26 below, which is a smaller scan size, the two types of features are more clearly seen. One is quite similar to the tips of the nanorods seen in the unmodified samples, and the other is smaller, almost spherical features. It may be that what is being observed is simply a film of the complex solution over the nanorods, but the distribution seen in the 20µm scan in FIGURE 3.24(B), above seems to suggest that this is not the case.

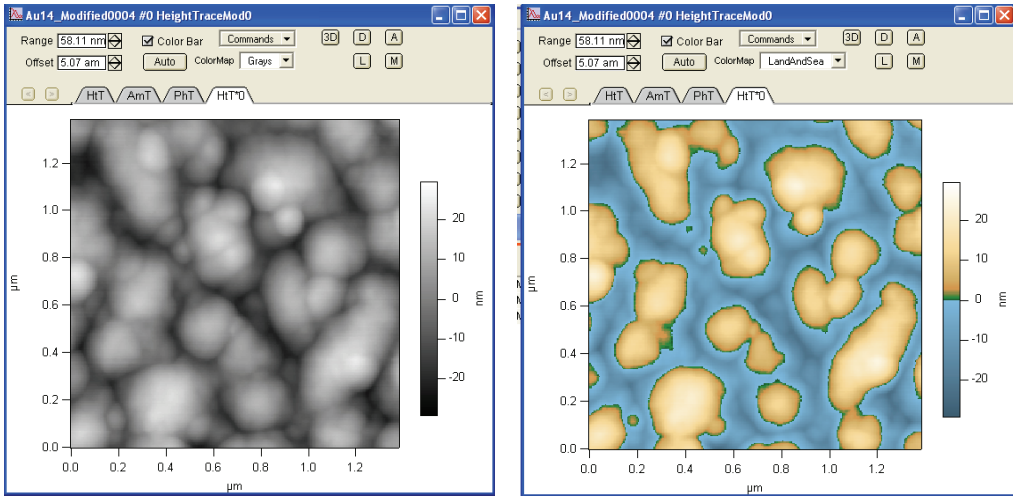

FIGURE 3.26(A): 1.4µM X 1.4µM SCANS OF THE MODIFIED SAMPLE IN TWO COLOUR SCHEMES. THIS IMAGE, DUE TO THE SMALLER SCALE SHOWS THE CLUMPING AND THE PRESENCE OF WHAT APPEAR TO BE TWO TYPES OF FEATURES.

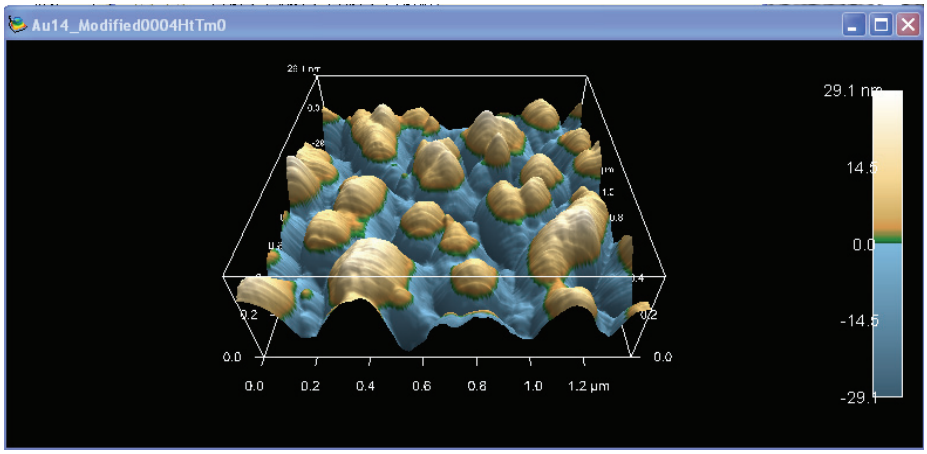

FIGURE 3.26(B): 3D REPRESENTATION OF THE IMAGE IN FIGURE 3.26(A) ABOVE.

A sectional analysis was also carried out on the "height" images taken from this sample. Both types of features were analysed. The results of the analysis are shown in FIGURES 3.27-3.28, in the following pages.

3.2.2.5 Uniformity of Dimensions of Modified Nanostructures

It was decided to investigate the sizes of the features observed in the modified sample, again using the sectional analysis tool in the AFM controller and analysis software. The results of this analysis are presented in the images which follow.

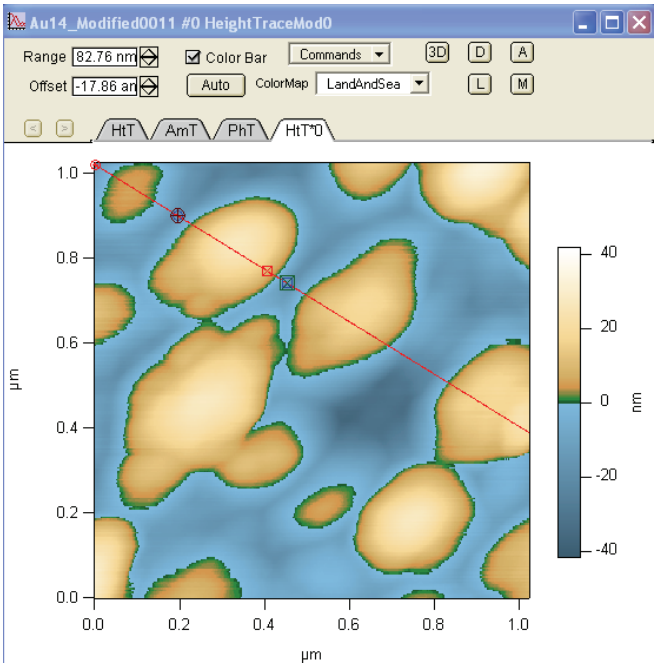

FIGURE 3.27(A): SECTIONAL ANALYSIS OF THE MODIFIED ZnO SAMPLE.

FIGURE 3.27(B): SECTIONAL ANALYSIS OF THIS FEATURE SUGGESTS THAT THE WIDTH IS APPROXIMATELY 300NM AND THE FEATURE IMMEDIATELY TO ITS RIGHT (RED TRACE) IS APPROXIMATELY 319NM.

In FIGURE 3.27(A) and FIGURE 3.27(B), the features examined are determined to be approximately 300nm in width, this is seen to be wider than the features in the unmodified sample which were determined to be approximately 290nm. Whether these

are the modified nanorods in the image is difficult to say for certain. The other, somewhat spherical feature, is measured in FIGURE 3.28(A) and FIGURE 3.28 (B), below.

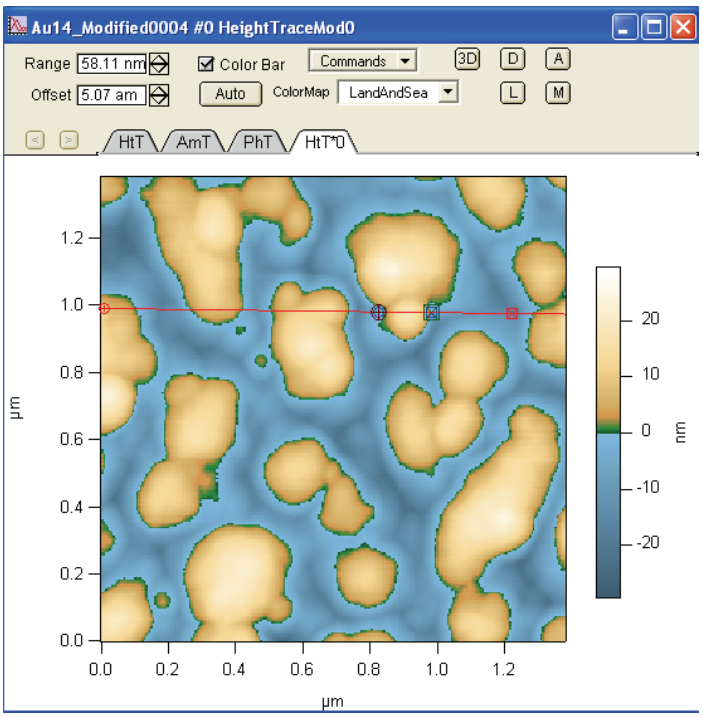

FIGURE 3.28(A): SECTIONAL ANALYSIS OF SMALL SPHERICAL FEATURE IN THE MODIFIED ZnO SAMPLE.

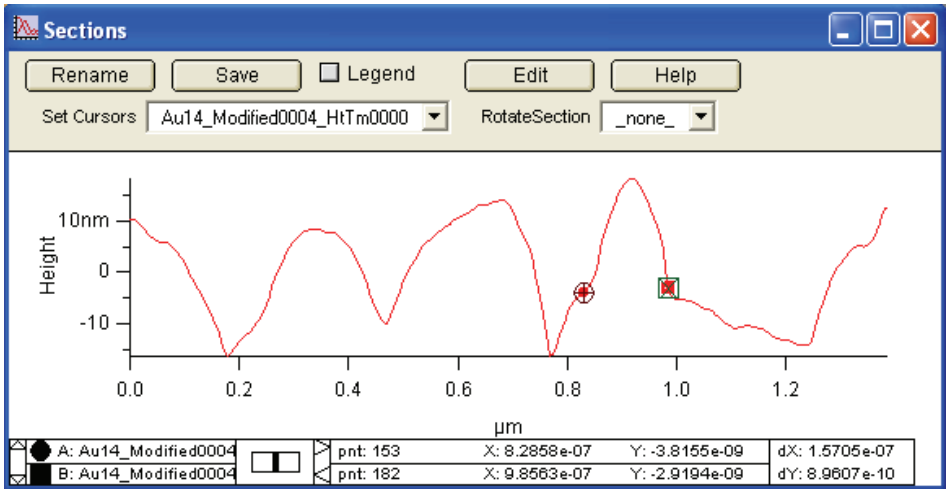

FIGURE 3.28(B): SECTIONAL ANALYSIS OF THE FEATURE INDICATES ITS WIDTH IS APPROXIMATELY 140NM

As seen from the dimensional analysis, it appears that the modified features are approximately 10nm - 20nm wider in diameter than the unmodified features. This would almost certainly mean a greater than a monolayer coverage of ruthenium complex. This

result concurs with the findings of the emission studies and also the SEM data and this will be discussed in the ZnO emission section of this chapter.

3.2.2.6 Imaging a Single ZnO Nanorod

The images presented in this section are of a different sample to the one that was presented in the previous sections of this chapter, but prepared in the same way as the others used in this work. The process of obtaining the images presented in this section is the same as that used to obtain all the other images in this chapter, namely scanning a 20μm x 20μm area (FIGURE 3.29) and zooming in on a promising area, and then scanning that area (FIGURE 3.30). This second scan was generally of the order of 5μm x 5μm, and was obtained by reducing the scan rate to 0.5Hz usually.

In the case of the image of the single nanorod, (FIGURE 3.31 (A) and (B)) the scan rate was set even lower still, to 0.2Hz.

In general, the amplitude set point was lowered from its initial value, until the tip began to track reasonably well, and the integral gain increased to 13 or 14 usually, in order to get better image clarity and to sharpen the features.

The images in the sequence are presented in the order they were obtained. The red square indicates approximately where the next image in the sequence was taken from.

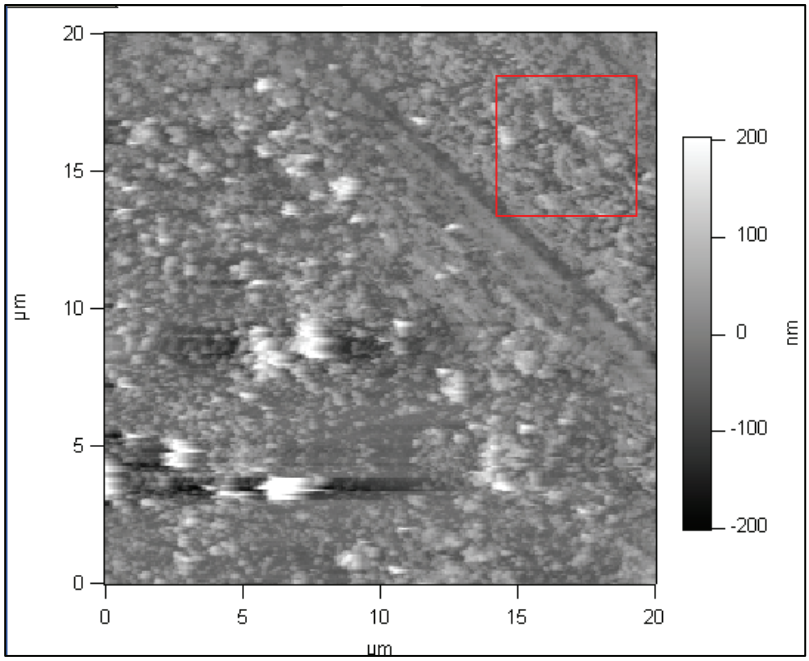

FIGURE 3.29: 20µM X 20µM SCAN OF THE ZnO SAMPLE. RED SQUARE INDICATES APPROXIMATELY WHERE THE NEXT IMAGE WAS TAKEN, SHOWN IN FIGURE 3.30.

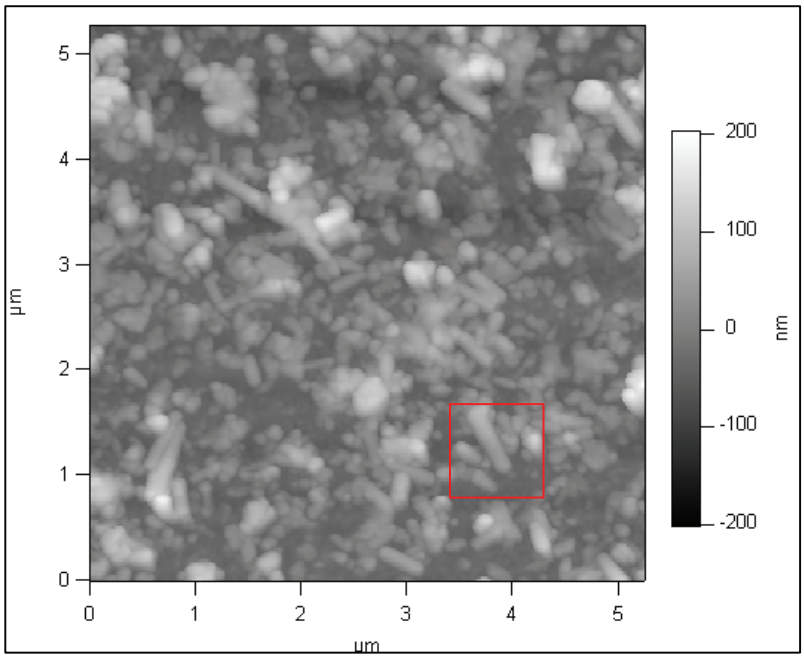

FIGURE 3.30: 5.25µM X 5.25µM SCAN OF THE PREVIOUS IMAGE. AGAIN, THE RED SQUARE INDICATES THE SCAN AREA OF THE NEXT SCAN IN THE SEQUENCE.

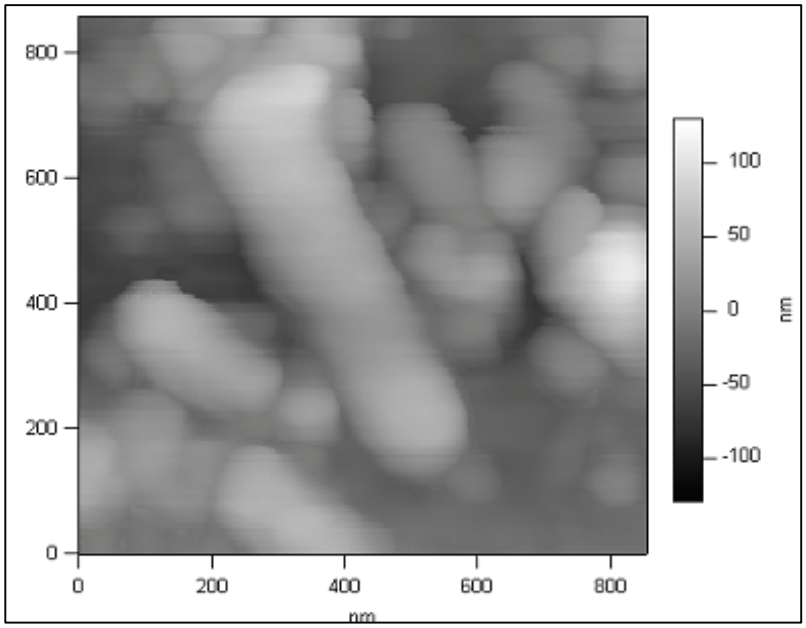

FIGURE 3.31(A): AFM IMAGE OF A WHAT APPEARS TO BE A SINGLE NANOROD. THE SCAN RATE WAS REDUCED TO 0.2HZ AND THE SCAN AREA IS 855NM X 855NM

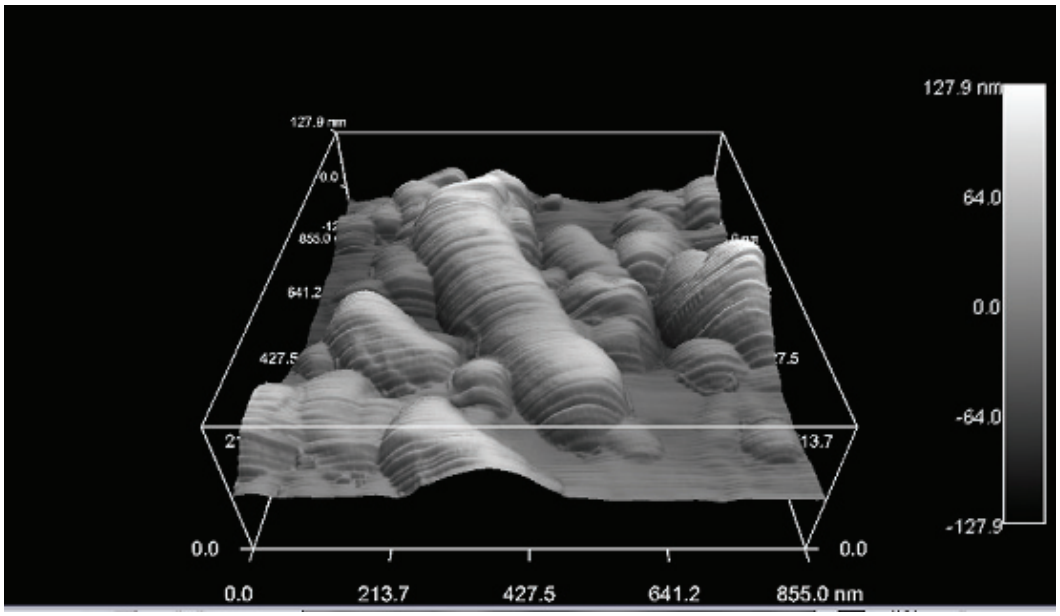

FIGURE 3.31(B): 3D REPRESENTATION OF THE IMAGE OF THE SINGLE NANOROD IN FIGURE 3.31(A), ABOVE. THE IMAGES IN FIGURES 3.30 AND 3.31(A), ABOVE SHOW WHAT APPEARS TO BE A SINGLE NANOROD ON THE SURFACE, AMONGST OTHER FEATURES. THE NANOROD APPEARS TO BE APPROXIMATELY 600NM-800NM LONG.

The image in FIGURE 3.31(A) on the previous page shows what appears to be a single ZnO nanorod, in amongst many others in the sample. From the 3-dimensional representation in FIGURE 3.31(B), above, it is observed that the feature appears to a complete nanorod,

and it was decided that this feature would be appropriate for dimensional analysis. As stated in the caption of FIGURE 3.31(B), the length of the feature has been measured using the IGOR software to be between 600 and 800nm. This, combined with the widths of the various unmodified nanorods measured in the previous sections of this chapter suggests that the nanorods appear to be relatively "stubby", as opposed to the long slender nanorods presented by other groups, at least judging by the surface images they have presented (SEM, TEM). It is important to note that in the report by Marí *et al*[10] the ZnO nanocolumns were found to be between 110nm and 900nm in length, so this is of the same order as the values observed in the system investigated in this thesis. Whether this observation is as a result of the AFM tip used, or the nature of the AFM instrument, or whether the nanorods in this system are actually quite wide relative to their length is quite difficult to say. The SEM images shown in section 3.2.1 are of different, much earlier ZnO samples. No SEM images were performed on the samples investigated in this AFM analysis. It does appear, however from FIGURE 3.30 that the ZnO nanorod investigated is quite similar to the others observed in the image. This would lead to the conclusion that either the nanorods are relatively stubby, or the AFM tip is distorting them equally, however it is difficult to see in the images presented any obvious distortion or skewing.

3.2.3 Auger Electron Spectroscopy (AES)

Auger Electron Spectroscopy was performed on both an unmodified and modified ZnO sample. The purpose was to attempt to observe a ruthenium peak in the modified sample, and also an increased carbon peak in the modified, due to the presence of carbon atoms in the polypyridyl ligands of the complex. This second peak is less reliable, since a carbon signal may also arise from dirt on the sample. Another peak of interest is the oxygen peak, since there are oxygens in the COOH linkers on one of the bipyridyl ligands. This peak may be shifted slightly relative to the peak observed for normal O_2, due to the fact that it is thought that the complex binds through these oxygen atoms. Whether this shift will be observed or not is questionable. The Auger spectra obtained for the unmodified ZnO sample is shown in FIGURE 3.32, and the spectra of the modified sample is shown in FIGURE 3.33. The interpretations of these spectra are aided by

references [23] and [24]. In FIGURE 3.32, The spectrum was obtained using a beam energy of 3kV. The peak at approximately 950eV can be attributed to Zn, and there is a large oxygen peak at 500eV, which is to be expected, since there is always oxygen present. .In FIGURE 3.33, the Auger spectrum of the modified ZnO surface is shown. While no clear Ru peak is seen due to the strong carbon peak always present at ~270eV, a possible N peak is seen at 367eV. This is tentatively assigned to the nitrogen heteroatoms in the bipyridine ligands. Crucially, this peak is not observed in FIGURE 3.32.

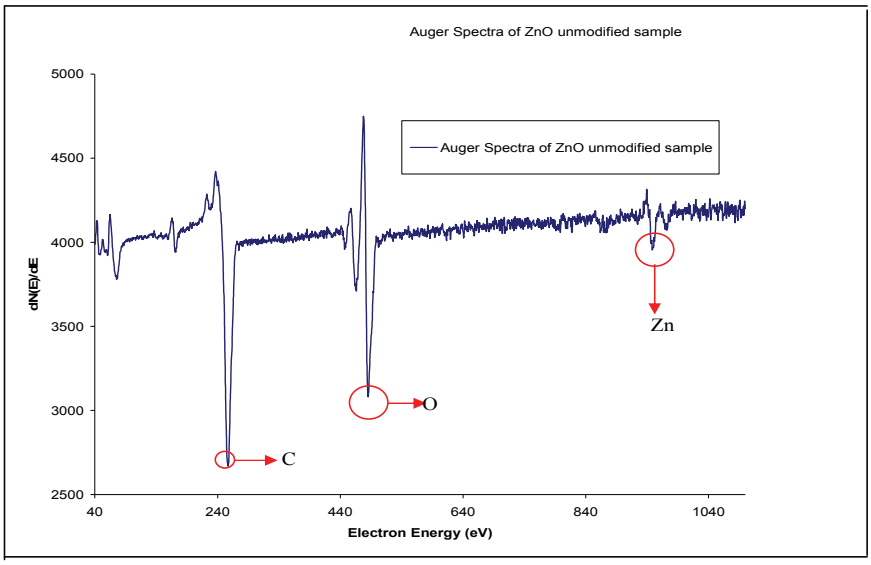

FIGURE 3.32: AUGER SPECTRA OF THE UNMODIFIED ZnO SAMPLE.

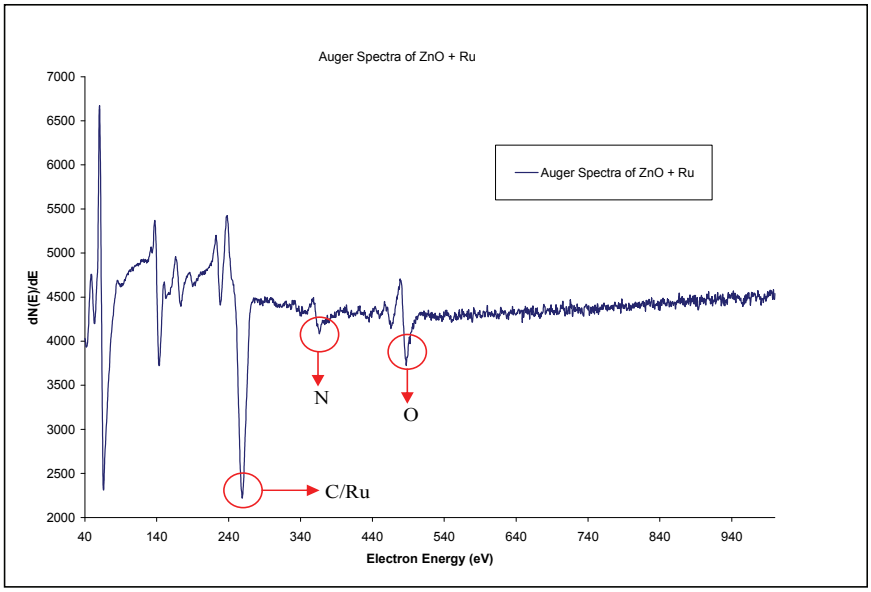

FIGURE 3.33: AUGER SPECTRA OF THE ZnO SAMPLE MODIFIED WITH THE RUTHENIUM COMPLEX

From these Auger spectra, it is tentatively concluded that the ruthenium complex is present on the surface, however the manner of binding and orientation of the dye molecules has not been established. It is anticipated that using XPS to investigate the system would give more information on the ruthenium peak, since the carbon and ruthenium peaks would be sufficiently separated in energy in the XPS spectra, while it is seen here in the Auger spectra that they overlap. It is thought that the more intense peak at 270eV in the spectrum of the modified sample suggests the presence of ruthenium, and this along with the absence of the Zn peak and the possible N peaks indicates the presence of the ruthenium complex in a high enough concentration that the ZnO is not detected, this would agree with the AFM data, and the photoluminescence data. Since the surface sensitivity of AES is high, it is reasonable to assume that only a small amount of ruthenium would need to be present for it to mask the ZnO signal.

3.2.4 Fluorescence Emission of ZnO Nanorods with and without Ru Complex

This section presents the photoluminescence measurements performed on the ZnO nanorods, in both their unmodified, and modified state. The samples were excited at 280nm, and also 460nm. The reason 280nm has been chosen as the excitation wavelength is because using this wavelength, it is then possible to observe the emission of the ruthenium complex at the same time as the emission of the ZnO nanorods, ruthenium still absorbs reasonably well at this wavelength, as well as when it is excited at 460nm. If an excitation wavelength of 325nm is used, the overtone from this excitation will cover the ruthenium-based emission. Unfortunately, due to a problem with the filter, it was not possible to observe both emissions simultaneously, but it was obviously possible for them to be observed separately. This issue is important for the comparison of the emission intensities of the two components of the modified system, as long as certain important factors are recognised. One of these factors is the disparity in the strength of the emission signals of the two components, it has become necessary to use different slit widths in the experiments, which makes the comparison of intensities difficult. The ZnO signals were generally recorded using slit widths of 5nm or 10nm,

while the ruthenium-based emission was recorded using slits of 15nm and 20nm, and using an excitation wavelength of 460nm.

3.2.4.1 ZnO Sample A, Unmodified Sample

The emission spectra for the unmodified ZnO nanorods (Sample A) is shown in FIGURE 3.34(A), below. The excitation wavelength used for the recording of the ZnO emission was 280nm, unless otherwise stated. We see a shift in the emission λ_{max} as the temperature is lowered from 293K to 77K.

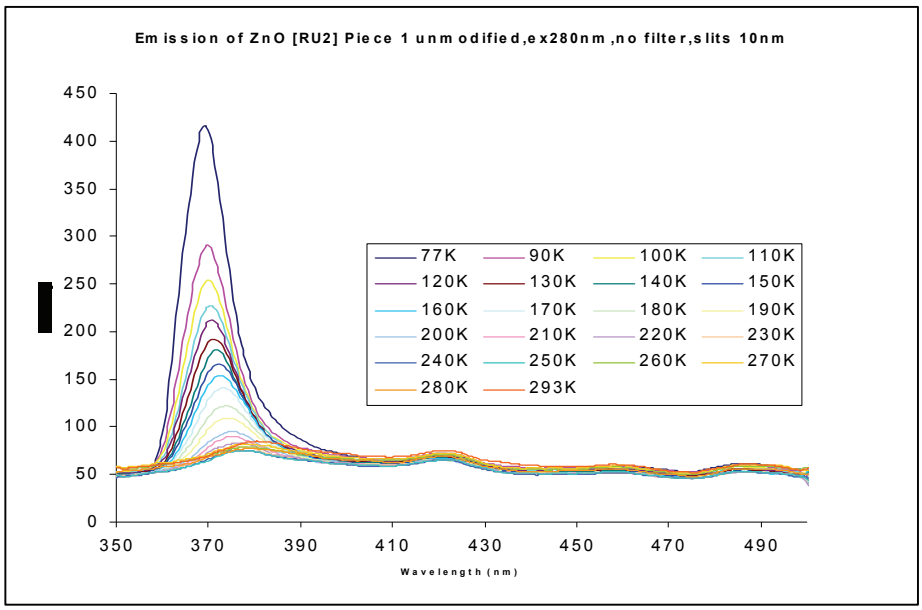

FIGURE 3.34(A): EMISSION OF UNMODIFIED ZNO NANORODS, (SAMPLE A), OVER A TEMPERATURE RANGE OF 77K-293K.

In FIGURE 3.34 (A), above, it is seen that the ZnO emission peak at approximately 380nm, is relatively weak and indistinct at 260K-293K. It is unclear as to why the spectra should be this shape, however it has been observed in this sample in other measurements. The spectra were normalized and the baseline modified. The normalized spectra are shown in FIGURE 3.34(B), on the next page. The variation of the λ_{max} with temperature is shown in FIGURE 3.35, on the following page. The room temperature peak seen at 380nm in FIGURE 3.34(A) is generally assigned to a free exciton emission, however it has been noted by Wang *et al*[29] that this peak is a combination due to the overlap of the free exciton emission with first- and second-order phonon replicas of the free exciton emission.

At 77K, this shifts to a possible combination of the free and bound exciton emissions, again, suggested in ref [29]. However, it should be noted that at 77K, the phonon replicas remain convoluted with the excitonic peaks, which may explain the broad peaks observed in the spectrum.

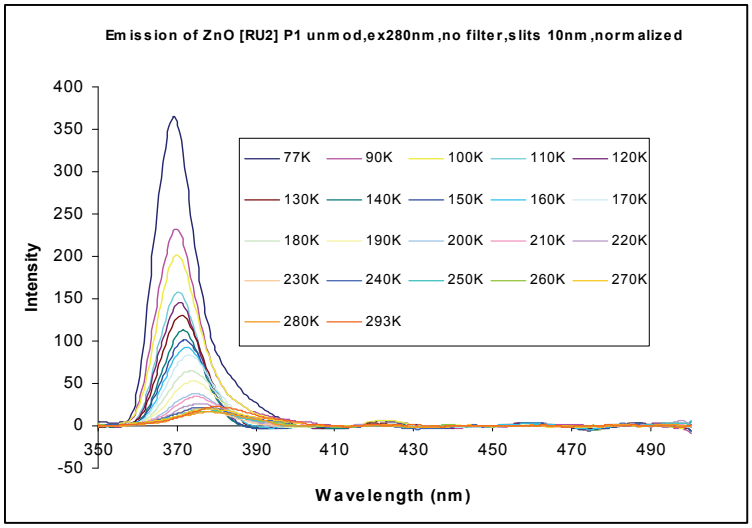

FIGURE 3.34(B): SPECTRA IN FIGURE 3.22(A) NORMALIZED AND THE BASELINE HAS BEEN MODIFIED IN THE REGION 410NM-500NM.

In the modification of the baseline, Microcal Origin 6.0 was used. The baseline was modified in the region of 410nm-500nm on the x-axis, and this was subtracted from the curve.

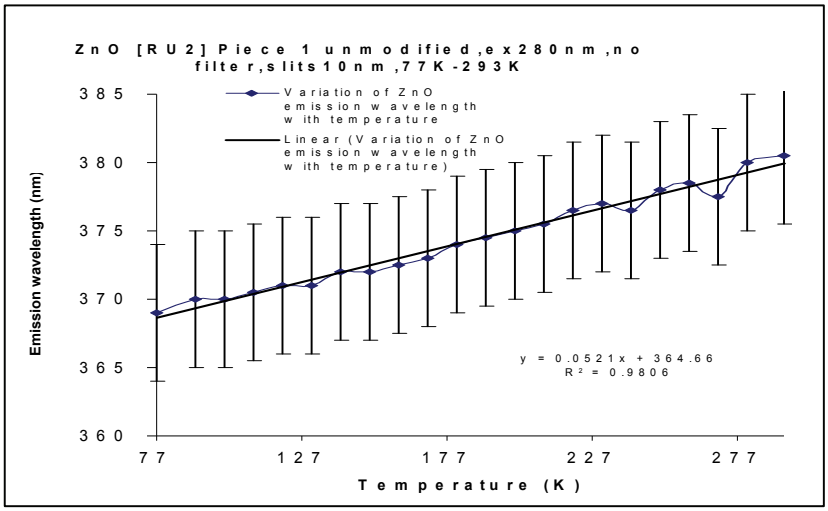

FIGURE 3.35(A): VARIATION OF λ_{MAX} (NM) OF ZNO SAMPLE A EMISSION WITH TEMPERATURE (K), SHOWN WITH ±5NM Y-AXIS ERROR BARS.

In FIGURE 3.35(A), above it is seen that the relationship between the λ_{max} and temperature is approximately linear across the temperature range. It is observed that the emission shifts to lower energies with increasing temperature due to shrinking of the semiconductor bandgap as discussed in chapter 1. It is also observed that the intensity of the emission signal increases with decreasing temperature and this data is shown in FIGURE 3.36, below. This appears to be a trend for this sample, and has been observed in other data obtained that not shown in this chapter. The shift of emission λ_{max} with temperature has been observed for ZnO nanorods by other groups[27,30,31]. The relationship can be visualized in another way by converting the emission wavelength to photon energy, in electron-volts(eV), as shown in FIGURE 3.35(B), below. Using the Cody approach, outlined in ref [29], the following expression was used to analyse the data.

$$E_g(T) = E_g(0) - k/[e^{(\theta/T)} - 1] \qquad \text{EQN 3.1}$$

E_g is the band gap energy, and k is a constant. θ is related to the average phonon frequency.

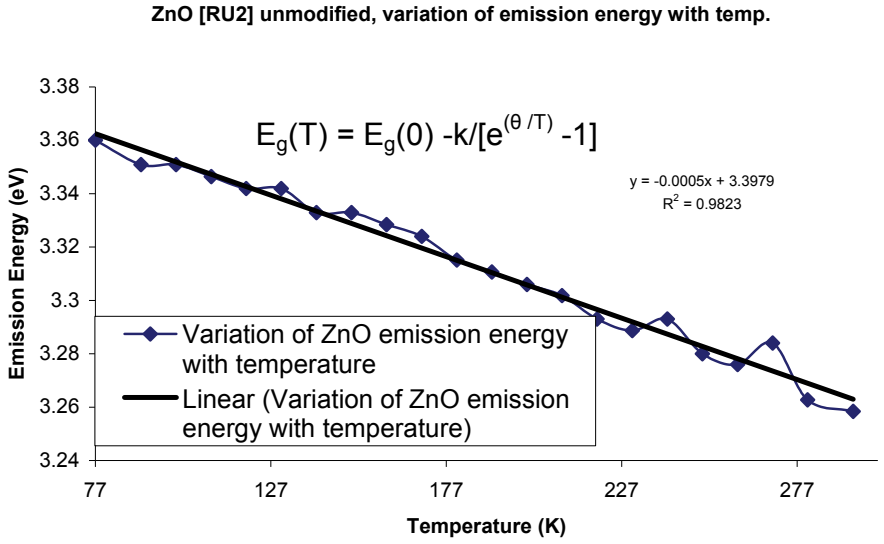

FIGURE 3.35(B): VARIATION OF ZNO SAMPLE A EMISSION ENERGY OF UNMODIFIED SAMPLE WITH TEMPERATURE.

EQUATION 3.1 is then used to fit the data in FIGURE 3.35(B). The fitted curves and the experimental data for the ZnO emission of both the unmodified and modified samples are shown in FIGURE 3.35(C), below.

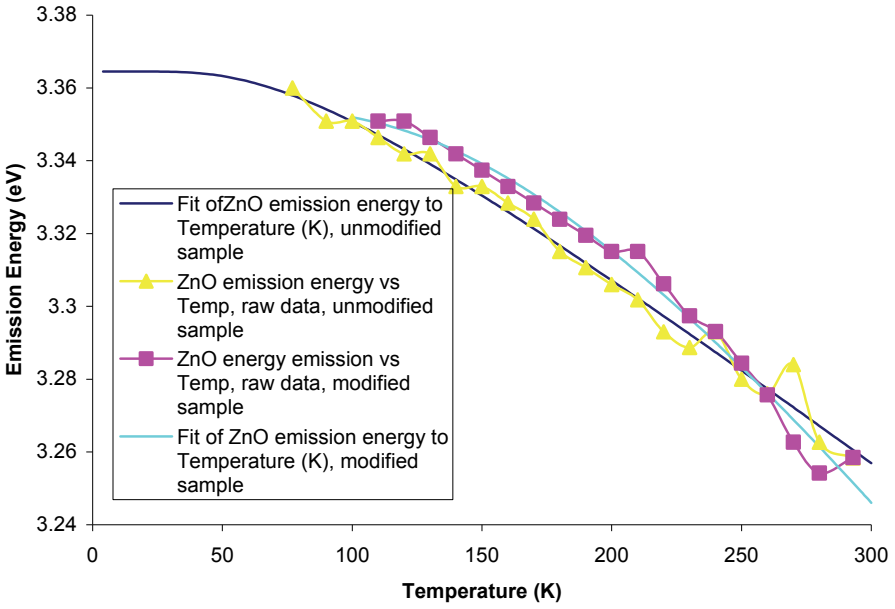

FIGURE 3.35(C): COMPARISON OF ZnO EMISSION ENERGIES FOR BOTH UNMODIFIED AND MODIFIED ZnO SAMPLES, WITH THE FITTED TRENDLINES BASED ON THE CODY EQUATION.

The fitted trendlines give values for $E_g(0)$, k, and θ for both the unmodified ZnO and the modified ZnO. For the unmodified sample, these values are found to be: Eg(0) = 3.365eV, k = 0.125eV, and θ = 231K. The fitted trendline for the modified sample gives values of Eg(0) = 3.35eV, k = 0.555eV, and θ = 544K. The values for the unmodified sample are in close approximation to those reported by Wang *et al*[29], Eg(0) = 3.38eV, k = 0.09eV, and θ = 240K. It is seen that the values for the modified sample deviate from these values, this is likely due to the range of temperatures that the data was fitted over, it is a much shorter range than that used by Wang in ref [29], and also the range used in the uunmodified data. The relationship of the emission intensity at λ_{max} with temperature is more complicated and approximates a cubic expression. It is unlikely that this is a result of discrepancies in the data, as this cubic type curve is seen in other results obtained using similar parameters on a different day, with the same sample. The only significant difference between the results presented here and the other data is the use of

larger slits widths in the other data than those used in the experiment presented here. The data was obtained using slit widths of ex15nm and em20nm, as opposed to ex10nm, and em10nm in the data shown in this report. The R^2 value of 0.9692 does indicate a reasonably high level of correlation between the trend line and the plotted data. The physical reason for the reduction in intensity with increasing temperature is due to exciton thermal dissociation as discussed in chapter 1 and while this can be modelled using an Arhennius – type thermally-activated quenching, we have not undertaken such a model and have simply fit the data with a cubic fit to enable us to compare results from day to day and sample to sample in a semi-quantitative way.

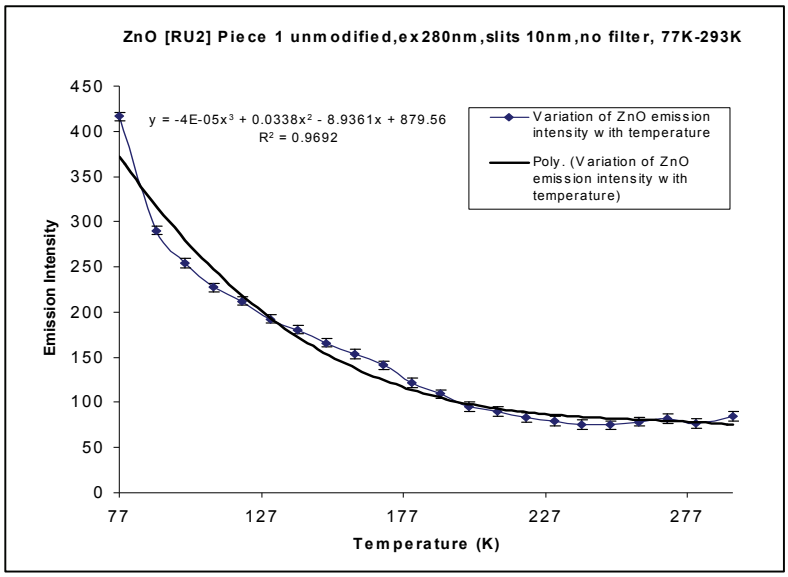

FIGURE 3.36: VARIATION OF THE ZNO SAMPLE A EMISSION INTENSITY WITH TEMPERATURE OVER THE RANGE OF 77K-293K

In FIGURE 3.36, above, the intensity of the ZnO emission is plotted across the entire temperature range (77K-293K). The relationship is again approximated using a cubic expression. This is primarily due to the broader temperature range plotted. It is important to note that these expressions have been observed at least twice for this sample. The error bars are also overlaid on the traces, and are based on approximate errors in the curves of the emission signals around room temperature and slightly below.

In the ruthenium region of the spectra, (600nm-800nm), there is a peak around 600-620nm for the unmodified sample when the sample is excited at 460nm. There should

not be a ruthenium based emission peak for this sample, as the ZnO has not been modified with the ruthenium complex. It is thought though, that this peak is the tail of the excitation peak, as it shifts when the excitation wavelength is changed to 480nm. FIGURE 3.37 shows the spectrum obtained for the unmodified sample when excited at 460nm over a temperature range of 77K-293K, and FIGURE 3.38 shows the spectrum of the same sample excited at 460nm and 480nm, at 293K.

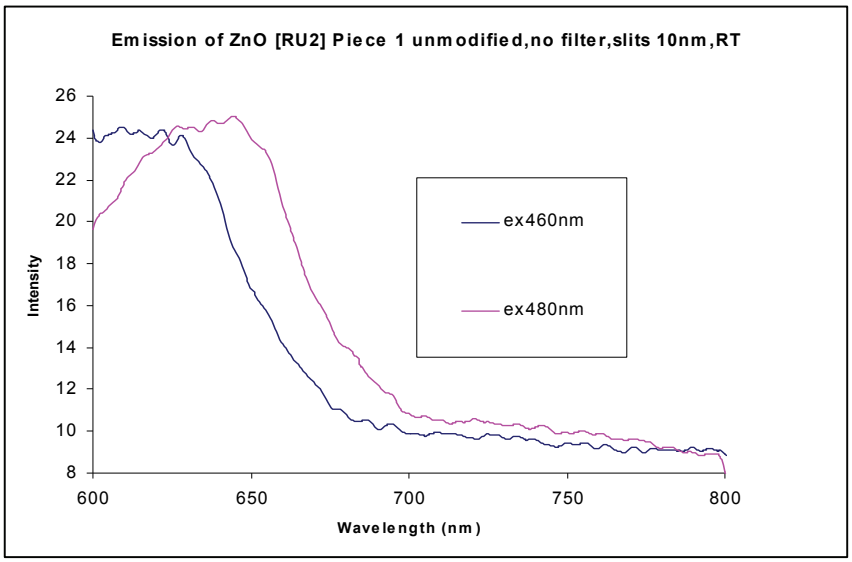

FIGURE 3.37: COMPARISON OF EMISSION SPECTRA OF UNMODIFIED ZnO OBTAINED WHEN SAMPLE WAS EXCITED AT 460NM AND 480NM, AT ROOM TEMPERATURE.

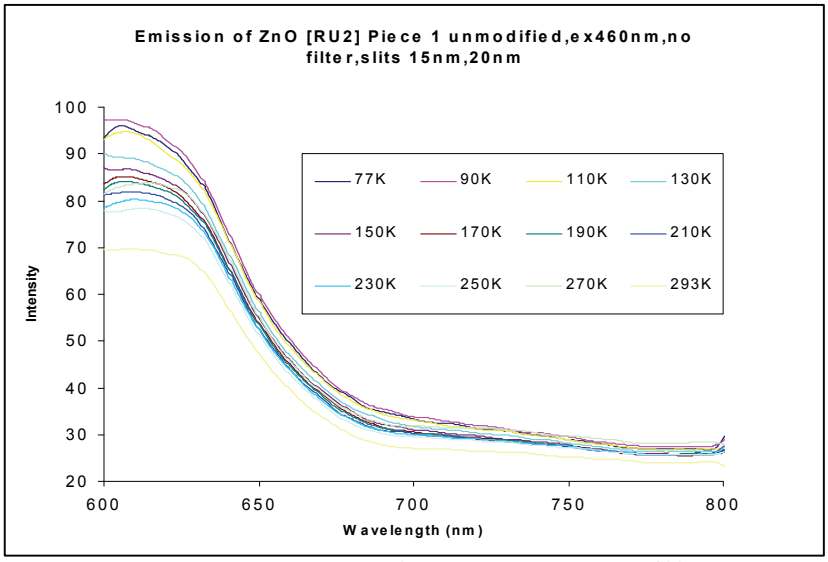

FIGURE 3.38: EMISSION SPECTRUM OF UNMODIFIED ZnO SAMPLE WHEN EXCITED AT 460NM AT VARIOUS TEMPERATURES BETWEEN 77K AND 293K.

In FIGURE 3.38, it is seen that the intensity of the peak does not appear to vary significantly or in any obvious manner with varying temperature. In FIGURE 3.37, it is seen that the emitted signal shifts in a similar manner and magnitude to the shifting excitation wavelength. This suggests, along with the evidence in FIGURE 3.38, that the signal observed in both spectra is indeed the tail of the excitation peak. This is to be expected for the unmodified sample, since no ruthenium dye is present in this sample, and the ZnO nanorods are not known to emit strongly in this region.
In order to investigate the reproducibility of these results, it was decided to examine another unmodified ZnO nanorod sample in the same way, and compare the results obtained with those presented above. This conclusion was confirmed by performing similar tests on another unmodified ZnO nanorod sample, and similar results were obtained.

3.2.4.2 ZnO [RU2] B-Modified Sample

This modified sample was mounted in the cryostat and analysed in the same manner as the unmodified sample. The data presented in this section was carried out using the same sample but on different days, and the sample was re-modified between sets of experiments. In addition, different fluorimeters were used on different occasions. In each case, the fluorimeter is specified, (1) Varian UV, and (2) Perkin Elmer LS50B.

3.2.4.2.1 ZnO emission

In FIGURE 3.44, below, the ZnO emission spectra of the modified ZnO nanorods are shown. The temperature range is 110K-293K, and the slits used are 15nm and 20nm. The slightly smaller temperature range used compared to the unmodified sample is due to the fact that the emission intensity saturated the detector at 77K, 90K, and 100K and the values were thus discarded. Again a shift in the λ_{max} of the ZnO emission peak is observed as the temperature is varied, as for the unmodified sample. This wavelength shift is analysed in more detail in FIGURE 3.40(A), on the next page, where the variation in ZnO emission wavelength with temperature is plotted.

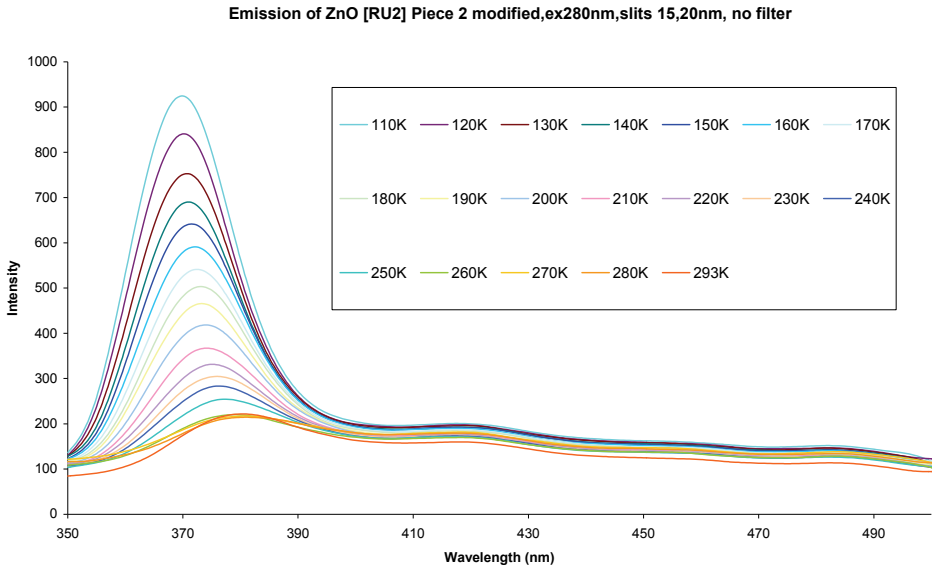

FIGURE 3.39: ZnO EMISSION ACROSS A TEMPERATURE RANGE OF 77K-293K, FLUORIMETER (2)

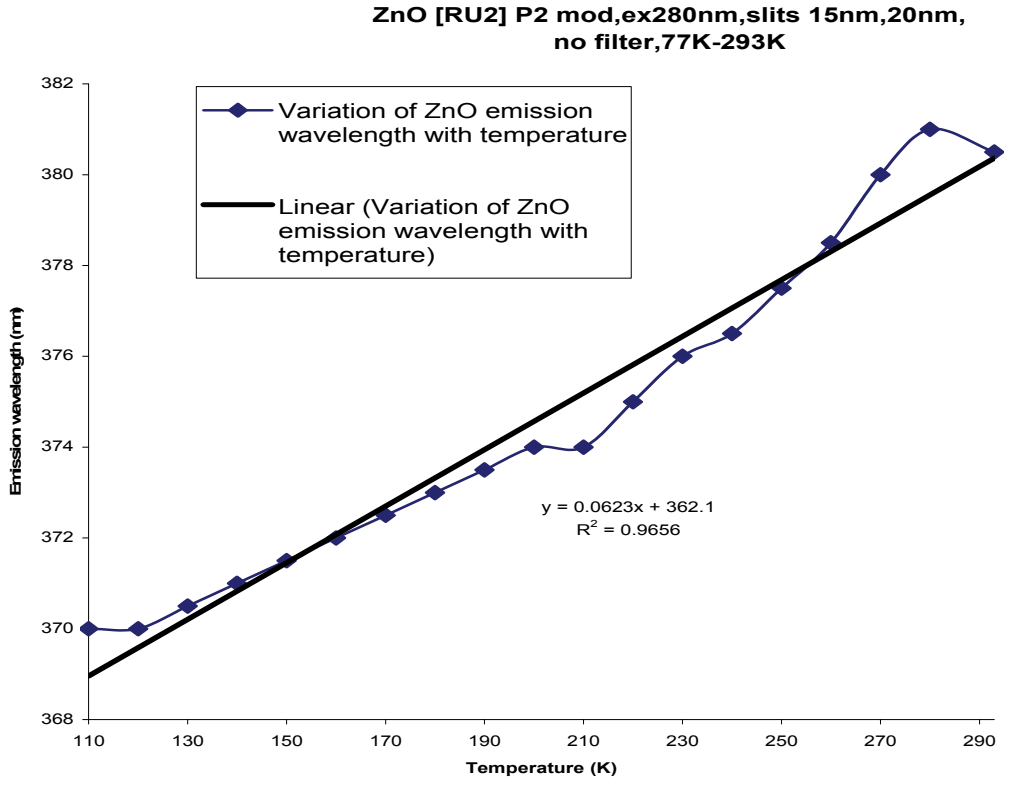

FIGURE 3.40(A): VARIATION OF ZnO EMISSION Λ_{MAX} WITH TEMPERATURE (77K-293K), FLUORIMETER (2)

It is seen in FIGURE 3.40(A) that the relationship between these two parameters is approximately linear, as was the case for the unmodified sample. Again, the emission *energy* can be plotted as a function of temperature, as was done with the unmodified ZnO sample. This is shown in FIGURE 3.40(B), on the next page. Again, EQUATION 3.1 can be used to find the $E_g(0)$. The temperature dependence of the ZnO emission intensity is illustrated in FIGURE 3.41 on the next page.

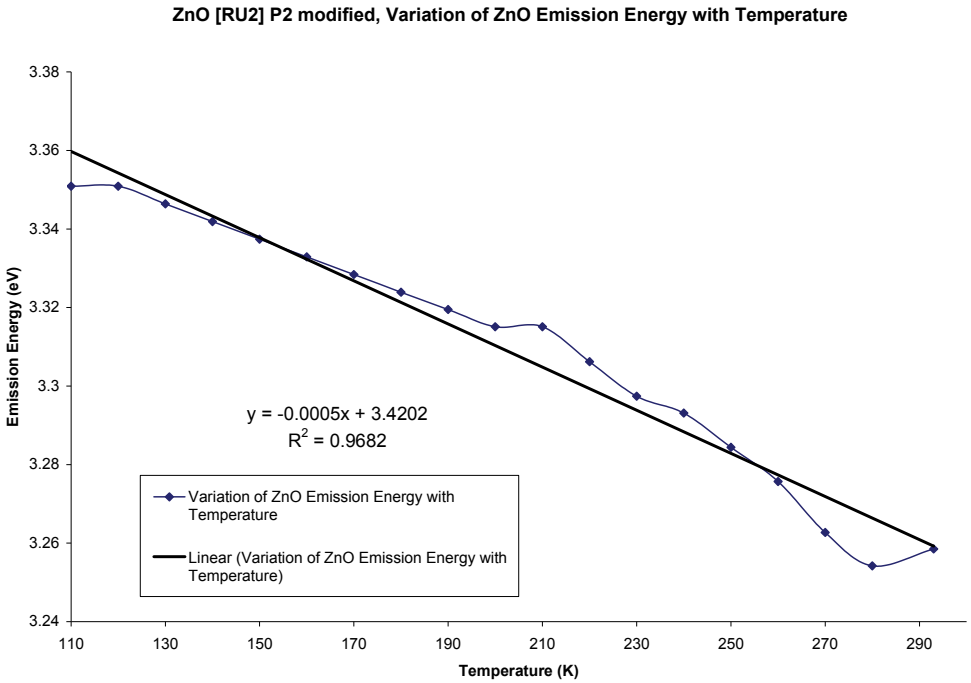

FIGURE 3.40(B): VARIATION OF ZnO EMISSION ENERGY WITH TEMPERATURE, FOR THE ZnO SAMPLE MODIFIED WITH THE RUTHENIUM COMPLEX.

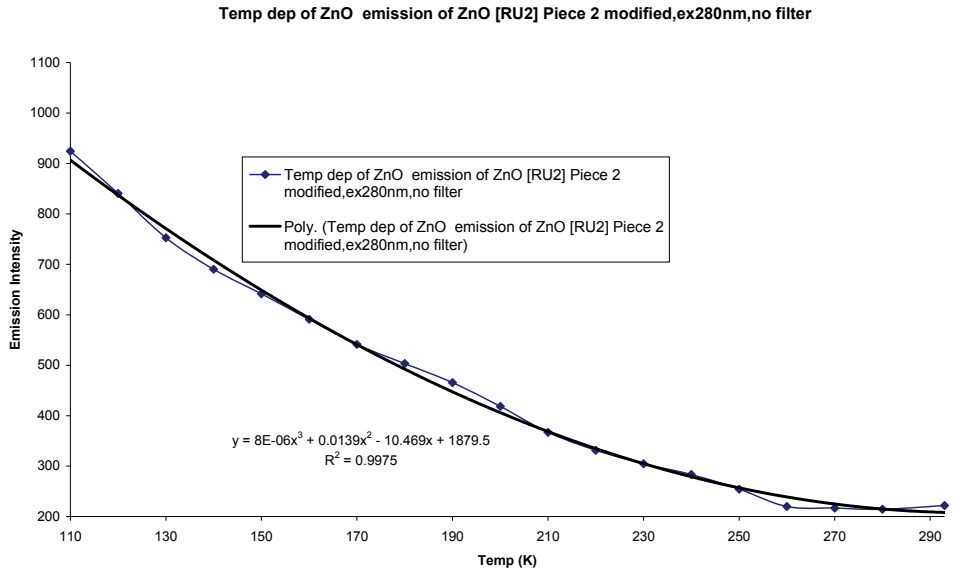

FIGURE 3.41: TEMPERATURE DEPENDENCE OF THE EMISSION INTENSITY OVER THE RANGE 77K-293K, FLUORIMETER (2).

It is seen that the intensity of the bandedge fluorescence emission again approximates a cubic relationship with temperature, for this slightly truncated temperature range, relative to that shown for the unmodified sample. The coefficient of the cubic term for the unmodified sample is very slightly less than that for the modified sample, ($-4x10^{-5}$ vs $8x10^{-6}$), however both trendlines are seen to be decreasing over the temperature range. Overall the fits exhibit a high degree of correlation with the experimental data, as evidenced by the R^2 values.

3.2.4.2.2 Ruthenium - Based Emission

The ruthenium based emission of the modified sample was investigated with two excitation wavelengths, 280nm, and 460nm were used. The emission was investigated across the temperature range 77K-293K. The emission wavelength of the ruthenium peak was not observed to shift significantly with changing temperature, as was the case with the ZnO emission. The ruthenium emission spectra are shown in FIGURE 3.42.

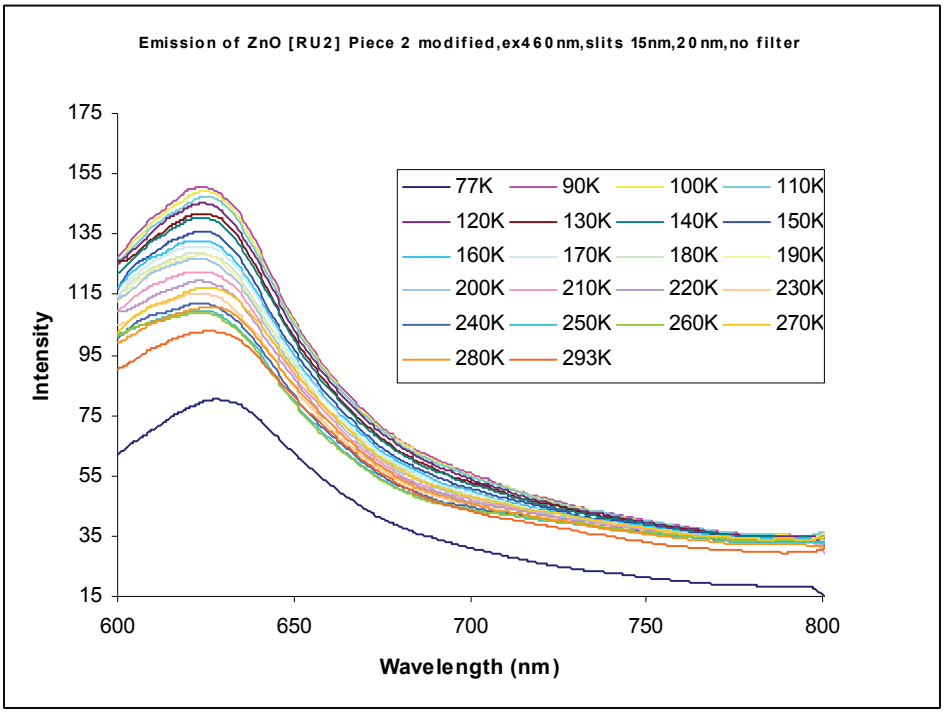

FIGURE 3.42: TEMPERATURE DEPENDENCE OF THE INTENSITY OF THE RUTHENIUM BASED EMISSION, 77K-293K, FLUORIMETER (2).

It is also seen that the intensity of the emission is only weakly dependant on the temperature, and the variation in intensity is quite small, as seen in FIGURE 3.42 above. It is in fact a relatively weak ruthenium emission, considering that the slit widths were at their widest possible setting for this instrument. There does appear to be Ruthenium present on the sample however, as indicated by FIGURE 3.43, on the next page. This is an excitation spectrum, with the emission wavelength setting at 630nm. This was performed at 77K, to investigate the ruthenium signal at this temperature.

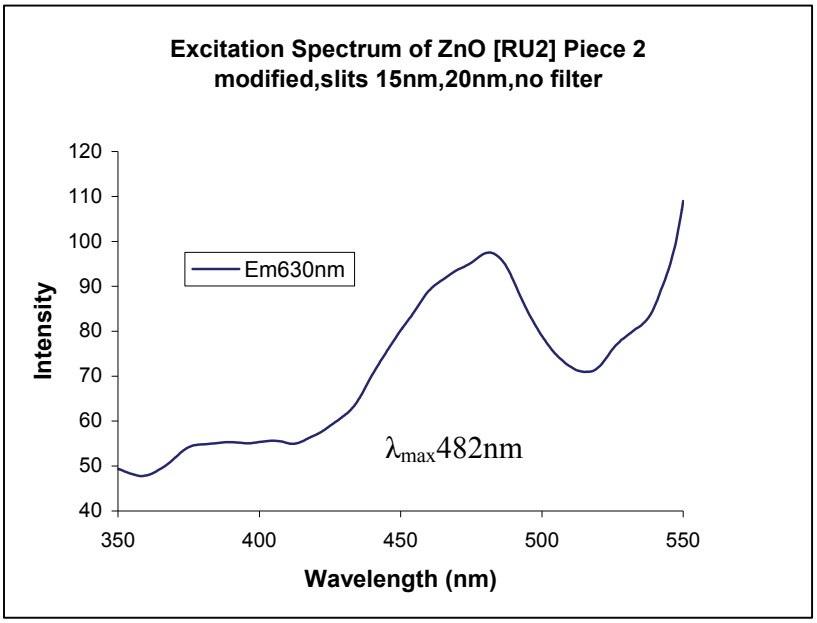

FIGURE 3.43: EXCITATION SPECTRUM OF THE MODIFIED ZnO SAMPLE, 77K, FLUORIMETER (2).

A peak at 482nm is seen in FIGURE 3.43, above, and this may be attributed to the ruthenium complex in its excited ^{3}MLCT state. Further indication that the ruthenium signal is a true emission and not scattered light is seen in FIGURE 3.44, on the next page. This figure is a comparison of the emission spectra obtained when the sample is excited at 460nm and 480nm.

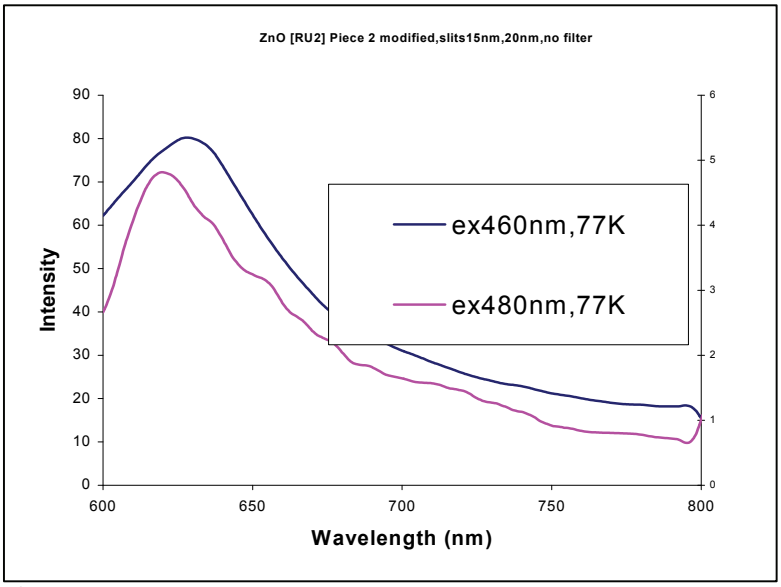

FIGURE 3.44: COMPARISON OF THE EMISSION SPECTRA OBTAINED WHEN THE MODIFIED SAMPLE WAS EXCITED AT 460NM AND 480NM, FLUORIMETER (2).

The emission signal from the sample when excited at 480nm, although weak, is very similar in terms of λ_{max} to the emission peak observed when excited at 460nm. This suggests that the signal is not scattered light, and that this is a true ruthenium emission, which is in contrast to the discussion for the 600 nm emission seen in the unmodified sample above. In comparison to the spectrum from the unmodified sample excited at 460nm (FIGURE 3.38), no shift in the emitted peak is observed, while a noticeable shift was observed in the emission spectra for the unmodified ZnO nanorods, in this wavelength region. It also indicates that in this case at least, the excitation efficiency of the ruthenium complex is quite dependant on the excitation wavelength used. This is seen in the absorption spectrum of the ruthenium complex in ethanol, the intensity drops by approximately 25% going from 460nm, to 480nm. It is not clear why electron injection is not occurring in the modified sample, but may be due to the possibility of more than a monolayer of the ruthenium complex present on the nanorods, providing the possibility of quenching of the signal due to energy transfer between neighbouring molecules. It is also possible that very little of the ruthenium complex bound to the ZnO nanostructures. This would explain the fact that the ZnO emission intensity in the modified sample is very similar to that in the unmodified sample, and also the low ruthenium emission intensity.

3.3 Conclusions and Future Work

It has been seen from the AFM images presented that it is possible to image ZnO nanorods effectively using AFM. Using a suitable scan size and by setting the scan rate and data points to appropriate values, the uniformity of a sample can be assessed, and in the smaller scan size images, what appear to be individual nanorods can be observed,. However, the image can sometimes be a distorted version of what is expected. For example, some of the values obtained through section analysis were larger than those measured from SEM images of similar samples.

The AFM images of the ZnO nanorods modified with the Ruthenium complex show two distinct features, the nanorod-type feature, and a second, spherical feature. The second feature may be a result of aggregation of the Ru complex molecules, which may go some way towards the explanation of two separate emissions, and the fact that the ZnO

emission does not change appreciably with the modification of the Ruthenium complex. It may be that the Ruthenium complex does not coat the nanorods in this system but may in fact sit on top of them in spherical aggregations, which. **THERE SHOULD BE A REF FOR THIS SORT OF FEATURE, FIND AND INSERT.**

Determining the dimensions of individual features can also be accomplished, although as discussed above, the use of these values as absolute values is questionable. A more appropriate use of the data is as a guide.

Using a sample in which the nanorods are lying reasonably parallel to the plane of the substrate, and are not particularly well aligned with respect to each other, may provide an opportunity to obtain images of the entire nanorod. An example of such an image obtained on a different sample to that discussed thus far in this report is presented in section 3.2.2.6, above. The modification of such a sample with the ruthenium complex will be investigated using AFM in the future, and the images obtained will also be compared with the SEM images in Section 3.2.1.

In FIGURE 3.32, above, it can be seen that peaks attributed to the presence of C, O, and Zn are marked. C and O are expected to be observed in every sample, since there is always the possibility of organic compounds on the surface and oxygen is also expected to be present due to the fact that the sample has been in air. However, it appears that there is a Zn peak, albeit a weak one. This is to be expected, given the sample, however it was expected to be more intense and the oxygen peak observed may also be due at least in part,to the oxygen in the ZnO.

In FIGURE 3.33, the spectrum of the modified sample is shown. Unfortunately, the C peak, which is always strong obscures the Ru peak, at approximately 270eV. It is also observed that this C / Ru peak is more intense in FIGURE 3.33 than in FIGURE 3.32. This may be due to the presence of ruthenium, or it may be the result of the carbons in the ligands of the ruthenium complex. The oxygen peak at approximately 500eV is less intense in the modified sample. The reason for this observation is not clear. It may be from the oxygen atoms in the COOH groups on the ligands, though the signal has not been shifted appreciably. It is possible that some of the organic compounds which may have been present in the unmodified sample were removed with the addition of the methanolic solution of the Ruthenium complex.

An interesting point to note is the presence of a peak at approximately 367eV in FIGURE 3.33, which has been assigned to N. N is present in the bipyridine ligands in the ruthenium complex. This peak is not observed in the unmodified sample. This may be evidence to suggest that the ruthenium complex has indeed bound to the ZnO substrate. The lack of a Zn peak in the spectrum of the modified sample supports this assertion.

The images obtained from SEM provide information on the uniformity of the sample and the dimensions of the features observed. It is slightly more difficult to ascertain the dimension of the features using the scale bar as opposed to the AFM analysis, however this latter method is only accurate if the image has been obtained and processed carefully and the tip is in good condition. This is because the image quality is inherently dependant on the tip. In addition, a higher quality tip may have provided more accurate dimensions.

The calculated value for $E_g(0)$ and the fitting of the peak energy versus temperature for the unmodified ZnO nanorods is quite close to the literature value and is also consistent with the data for the modified nanorods. The ZnO sample presented in this chapter is representative of the other samples, however it should be said that differences have been noted between the samples, and in particular when a cryostat is used, this adds to the complexity of the system, and compounds the difficulty in getting accurate reproducible data.

The ruthenium signal from the modified sample is relatively weak, considering that it is quite a strong emitter. However, it is a true ruthenium emission signal, given the different peak shape obtained from the unmodified sample (FIGURE 3.38), and the modified sample (FIGURE 3.42).

It is clear that in the case of the [RU2] sample, both the unmodified and modified ZnO nanorods exhibit a very strong ZnO emission, FIGURE 3.34(A) and FIGURE 3.39. The modified sample exhibits a weak ruthenium-based emission. This suggests that the ruthenium layer is not quenching the emission of the ZnO nanorods, and this suggests that the coverage of the nanorods with the ruthenium complex is quite light. This would explain the relatively low intensity of the ruthenium emission

With regard to the nature of the ZnO emission, the samples exhibit a strong UV emission peak, around 360-380nm. No defect related peaks have been observed in the

500nm region. This suggests that the nanorods are of very good quality. It is clear that the blue emission seen usually around 450nm, is not observed in these samples, when excited at 280nm.

The weakness of the Ru-based emission compared to the ZnO emission merits some comment also. One possibility is that if the ruthenium coverage is incomplete, the ZnO will absorb the 280nm incident beam and re-emit at around 380nm. This emitted radiation may in turn be absorbed by the ruthenium complex and re-emitted as the ruthenium emission at around 640nm. Dual emissions of this sort have been observed in other samples using filters to remove the overtone of the excitation beam (see FIGURE 3.45 below for such a spectrum of sample RU2). However it is still unclear if the ruthenium-based emission is the direct result of absorption of the ZnO 380 nm emission, or absorption of the initial 280nm excitation, and subsequent emission from the ^{3}MLCT state of the ruthenium complex. Our data cannot be used to distinguish at this stage whether the Ru-based emission and the ZnO emission are related as in the former scenario or two, *separate*, unrelated processes as in the latter. A third possibility is that the ruthenium is absorbing the incident light, and an electron is promoted to the LUMO and is then injected into the ZnO nanorods, though based on the discussion below we believe this to be unlikely. In this case, it is unclear what effect this would have on the ZnO emission. Since the ZnO emission of the modified system is comparable to that of the unmodified ZnO nanorods, the absorption of the light by the ruthenium moiety and its subsequent electron injection into the ZnO manifold either has no discernible effect on the ZnO emission or this process is not occurring.

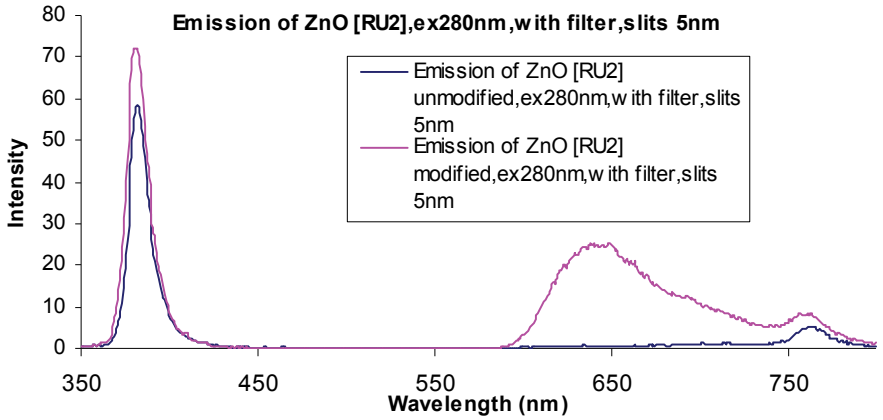

FIGURE 3.45: ZnO [RU2] MODIFIED WITH THE RUTHENIUM COMPLEX, WITH FILTER, EX280NM, SLITS BOTH 5NM.

With regard to the experimental setup, it is possible, exercising a reasonable amount of care, to set up and align the sample with a good deal of reproducibility. This is important in order to continue this work using both new samples and also new metal complexes, and to obtain results that can be reliably compared to the results presented in this chapter. It is equally important that the results obtained for each of the samples in this work can be compared to each other.

In conclusion, the ZnO emission of the modified sample [RU2] does not appear to be quenched by the addition of the ruthenium complex, and it has been established that the ruthenium complex is present. It is concluded that since the ruthenium complex is emitting at 640nm, it is therefore prudent to assume that it is not injecting electrons into the ZnO nanorod substrate. This is undesirable, as it was expected that electron injection would be efficient, using this nanorod based system. However, if the ruthenium emission can be improved or if the peak can be elucidated more clearly when the sample is excited at 280nm, it may be possible to have a dual emitting device with two separate efficient emissions. In addition, if electron injection is desired, it may be possible to achieve this by using a less concentrated solution of the ruthenium complex.

Future work will focus on the reproducibility of both the results presented in this chapter, and on other ZnO/Ru complex systems, involving dinuclear ruthenium polypyridyl complexes, and possibly, Ru-Os dinuclear species. It is anticipated that fluorimetry measurements will again be performed both at room temperature and at temperatures down to 77K. It is also hoped, that using a slightly different cryostat,

measurements may be performed at temperatures as low as 10K. This would be particularly interesting in the case of the ruthenium emission, as very little work has been done thus far with ruthenium complexes on surfaces at temperatures as low as this. ZnO emission at this temperature has been reported for ZnO[27], but not for ZnO modified with ruthenium complexes, and so this may also be a fruitful and worthwhile endeavour. In general, this work is fruitful, especially the low temperature work, because, as was seen in Chapter 1, the investigation of this type of nanorod ZnO-ruthenium system has not dealt extensively with lower temperatures. The work presented in this chapter is a tentative attempt to characterize this type of system using fluorimetry both at room temperature and at lower temperatures. It has been a key aim of the work to obtain reproducible results and the results presented in this chapter are an important step in this direction.

3.7 Bibliography

1 J.Y. Li, X.L. Chen, H. Li, M. He, Z.Y. Qiao, *J. Crystal Growth*, **2001**, *233*, 5-7

2 X. Y. Kong, Z. L. Wang, *Nano Lett.*, **2003**, *3*, 1625-1631

3 L. E. Greene, M. Law, D. H. Tan, M. Montano, J. Goldberger, G. Somorjai, P. Yang, *Nano Lett.*, **2005**, *5*, 1231-1236

4 L. E. Greene, M. Law, J. Goldberger, F. Kim, J. C. Johnson, Y. Zhang, R. J. Saykally, P. Yang, *Angew. Chemie Int. Ed.*, **2003**, *42*, 3031-3034

5 C. W. Blackledge, J. M. Szarko, A. Dupont, G. H. Chan, E. L. Read, S. R. Leone, *J. Nanosci. and Nanotech.*, **2007**, *7*, 3336-3339

6 P. Hari, M. Baumer, W.D. Tennyson, L.A. Bumm, *J. Non Crystall. Solids*, **2008**, *354*, 2843-2848

7 K. Cheng, G. Cheng, S. Wang, L. Li, S. Dai, X. Zhang, B. Zou, Z. Du, *New J. of Physics*, **2007**, *9*, 214/1-214/9

8 W. I. Park, G.-C. Yia, J.-W. Kim, S.-M. Park, *Appl. Phys. Lett.*, **2003**, *82*, 4358-4360

9 J. Song, X. Wang, E. Riedo, Z. L. Wang, *Nano Lett.*, **2005**, *5*, 1954-1958

10 B. Marí, M. Mollar, A. Mechkour, B. Hartiti, M. Perales, J. Cembrero, *Microelec. Journal*, **2004**, *35*, 79-82

11 S. Di Bella, S. Sortino, S. Conoci, S. Petralia, S. Casilli, L. Valli, *Inorg. Chem.*, **2004**, *43*, 5368-5372

12 J.-F. Gohy, B. G. G. Lohmeijer, U. S. Schubert, *Macromolecules*, **2002**, *35*, 4560-4563

13 H. Ma, Tao Dong, F. Wang, W. Zhang, B. Zhou, *Electrochim. Acta*, **2006**, *51*, 4965-4970

14 J. X. He, K. Kobayashi, M. Takahashi, G. Villemure, A. Yamagishi, *Thin Solid Films*, **2001**, *397*, 255-265

15 L. Cheng, J. A. Cox, *Chem. Mater.*, **2002**, *14*, 6-8

16 H. Ma, J. Peng, Y. Chen, Y. Feng, E. Wang, *J. Solid State Chemistry*, **2004**, *177*, 3333-3338
17 Y. F. Hsu, Y. Y. Xi, A. B. Djurišić, W. K. Chan, *Appl. Phys. Lett.*, **2008**, *92*, 113507-1 -113507-3
18 B. J. Chen, X. W. Sun, C. X. Xu, *Ceramics Inter.*, **2004**, *30*, 1725-1729
19 M. Wang, C. H. Ye, Y. Zhang, G. M. Hua, H. X. Wang, M. G. Kong, L. D. Zhang, *J. Crystal Growth*, **2006**, *291*, 334-339
20 O. Taratula, E. Galoppini, D. Wang, D. Chu, Z. Zhang, H. Chen, G. Saraf, Y. Lu, *J. Phys. Chem. B*, **2006**, *110*, 6506-6515
21 Z. L. Wang, *J. Phys. Condens. Materials*, **2004**, *16*, R829-R858
22 Z. L. Wang , *Mater. Today*, June 2004, *7*, 26-33
23 G. E McGuire, Auger Electron Spectroscopy Reference Manual Ed?Transfer Report, Ch4 Ref 1
24 J. F Moulder, W. F. Stickle, P. E. Sobol, K. D. Bomben, Handbook of X-Ray Photoelectron Spectroscopy Ed?Transfer Report, Ch4 Ref 2
25 H. C. Hsu, C. S. Cheng, C. C. Chang, S. Yang, C. S. Chang, W. F. Hsieh, *Nanotechnology*, **2005**, *16*, 297-301
26 K. Keis, J. Lindgren, S-E. Lindquist, A. Hagfeldt, *Langmuir*, **2000**, *16*, 4688-4694
27 B. P. Zhang, N. T. Binh, K. Wakatsuki, Y. Segawa, Y. Kashiwaba, K. Haga, *Nanotechnology*, **2004**, 15, S382-S388
28 S. Campagna, F. Puntoriero, F. Nastasi, G. Bergamini, V. Balzani, *Top. Curr. Chem.*, **2007**, *280*, 117-214
29 L. Wang, N. C. Giles, *J. Appl. Phys.*, **2003**, *94*, 973-978
30 W. I. Park, Y. H. Yun, S. W. Jung, G.-C. Yi, *Appl. Phys. Lett.*, **2003**, *82*, 964-966
31 B. Cao, Y. Li, G. Duan, W. Cai, *Crys. Growth and Design,* **2006**, *6*, 1091-1095
32 J. B. Asbury, Y. Q. Wang, T. Lian, *J. Phys. Chem. B*, **1999**, *103*, 6643-6647
33 T. Shimidzu, T. Iyoda, K. Izaki, *J. Phys. Chem.*, **1985**, *89*, 642-645
34 H. Horiuchi, R. Katoh, K. Hara, M. Yanagida, S. Murata, H. Arakawa, M. Taciya, *J. Phys. Chem. B*, **2003**, *107*, 2570-2574

Chapter 4 Composite Systems Of Single Walled Carbon Nanotubes (SWCNT's) With Metal Complex-Based Polymers

Chapter 4 presents a very different system to that discussed in Chapter 3. The system described in the previous chapter comprised of a solid substrate (Si) on which nanostructures of zinc oxide (ZnO) were grown. This was then modified by a ruthenium polypyridyl complex. In the system presented in this chapter, a ruthenium complex based polymer is used to modify carbon nanotubes. The extent and efficiency of the modification or "exfoliation" is monitored by UV spectroscopy. The results of the modification are presented, and the optimum conditions for the process are discussed. The system was further studied by surface analysis, namely Atomic Force Microscopy (AFM) and these results are also presented and discussed, with particular regard to the morphology of the structures obtained and the density of coverage by the nanotube / Ru polymer composites.

Attempts are made to account for the observations in the UV analysis by looking at the composites on a surface. It is important to note that while surface analysis has been carried out, the focus of the work in this chapter, and Chapter 5, is to examine the exfoliation of Single Walled Nanotubes in a common organic solvent, as the efficient dispersion of nanotubes in solution is one of the primary problems with this type of system, and prevents the carbon nanotubes being easily manipulated and utilised in real world applications.

4.0 Introduction

4.0.1 Introduction to CNT's and polymer composite systems

This chapter and the following chapter present the results obtained in the investigation of a very interesting system. The system in question is a composite material, comprised of carbon nanotubes, exfoliated in an organic solvent with a ruthenium polypyridyl-based polymer. The polymer backbone consists of Poly (4-vinyl pyridine), henceforth referred to as PVP. The general structure of this polymer is shown in FIGURE 4.1, below.

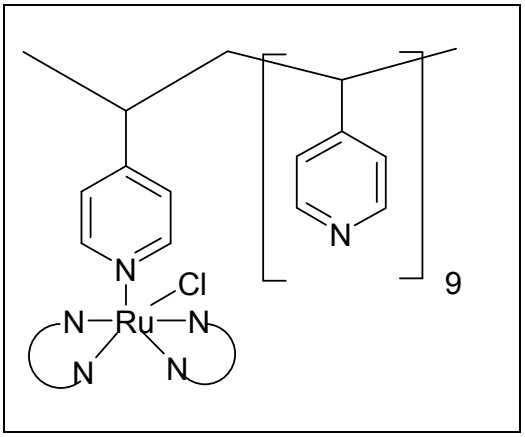

FIGURE 4.1: STRUCTURE OF $[Ru(BPY)_2(PVP)_{10}Cl]Cl$, (**1**) AS USED IN THE WORK DISCUSSED IN THIS CHAPTER AND CHAPTER 5.

This polymer was used to exfoliate the carbon nanotubes in a methanol solution. In this chapter, the nanotubes used were Single Walled Nanotubes, (SWNT's), and will be referred to as SWNT's for the remainder of this Chapter.

SWNT's were first prepared by Iijima *et al*[1], and separately by Bethune et al[2]. Since these first reports in 1993, many other methods of preparation and modification have been discovered and reported[3,12]. One of the significant challenges in manipulating carbon nanotubes with a view to their use in real world applications is the fact that they are not easily soluble in most organic solvents or water. This has led to the intensive research into the development of an efficient and facile exfoliation technique. The exfoliation of Single Walled Nanotubes using polymers such as Poly (4-vinyl pyridine), abbreviated to P4VP, and also ruthenium polypyridyl based polymers has been carried out by various groups[4-6,11]. Yonemura and co workers[4] utilised $Ru(bpy)_3$ – PSS, where

the PSS was poly(sodium 4-styrenesulfonate), to exfoliate Single Walled Nanotubes. These solutions were then deposited on Indium Tin Oxide, and were characterized by AFM. Grossiord *et al*[7,8] have used UV spectroscopy to investigate the exfoliation process of carbon nanotubes using SDS (sodium dodecyl sulphate), as have Jiang and co workers[10]. Sinani and co workers[9] used a PVP variant, poly (N-cetyl-4-vinylpyridinium bromide-co-N-ethyl-4-vinylpyridinium bromide-co-4-vinylpyridine), to solubilize a solution of SWNT's. Berciaud *et al*[19] investigated the UV properties of single walled nanotubes in the absence of polymer or exfoliating agent, and observed the van Hove singularities of the semiconducting nanotubes. From the UV-vis data for the composite systems reported in [7-10] it was observed that increasing the concentration of the nanotubes in the solution resulted in an increase in the absorbance of the solution across the wavelength range. This is also observed in the results obtained for the system investigated in this thesis, and presented in Section 4.1.

The use of ruthenium polypyridyl based polymers in the exfoliation of carbon nanotubes has been rather limited, to the authors knowledge. However, Frehill and co workers[11] used the same ruthenium based polymer in their investigation into the interactions between metallopolymers and carbon nanotubes as has been used in the work to be presented in this chapter, $[Ru(bpy)_2(PVP)_{10}Cl]Cl$. UV-visible spectroscopy was used to investigate the extent of the exfoliation of the nanotubes, and van Hove singularities were observed in the composite material spectra, indicative of the SWNT's, and, importantly, it was also observed that the MLCT transition peak was reduced in the spectra of the composite material, relative to the UV spectra of the ruthenium polymer in the absence of carbon nanotubes. This is also seen in the exfoliation experiments to be presented later in this chapter. Atomic Force Microscopy was also utilized to investigate the morphology of the composite systems on a SiO_2 substrate, with and without washing with water. It was found that washing with water removed much of the free polymer, which was observed as spherical features in the AFM images of the samples that had not been washed. Long nanotube like features were observed in the washed samples.

4.0.1 Aims of Chapter

As has been discussed in the previous section, it is seen that the dissolution of Single Walled Nanotubes using ruthenium polypyridyl-based metallopolymers has not been heavily investigated. Exfoliation is the process where nanotubes become "unbundled" from each other and then are wrapped in the polymer, if it is present, or dissolve in the solvent due to the reduced mass of the separated nanotubes. The work presented in this chapter is an attempt to redress this issue, and to achieve consistent exfoliation results. It is also intended to find the optimum conditions for the exfoliation process, optimum values of concentration of metallopolymer, sonication time, and ratio of metallopolymer to carbon nanotubes. Finally, it was decided to investigate the morphology of deposited films of the composite material formed from the exfoliation of the nanotubes with the metallopolymer. Again, the use of AFM is important, and complements and expands on the absorption data.

4.1 Experimental

The purpose of this work was to find the optimum conditions for the exfoliation of the nanotubes, within a defined concentration range, and ratio of the nanotubes to Ru polymer. Exfoliation is a process where a bundle of nanotubes in solution are "unbundled" and then the polymer, if present wraps around the nanotube, aiding in the dissolution of the nanotubes in the chosen solvent. It is also possible for certain types of nanotubes to be exfoliated in the absence of polymer, however it will be seen in this and the next chapter that while this is possible in some cases, it is less efficient. The process was monitored by UV spectroscopy, as both the nanotubes and the ruthenium polymer both exhibit peaks in this region of the spectrum.

Further to the exfoliation experiments, solutions of exfoliated nanotubes were deposited on solid substrates and investigated by AFM, in order to more fully understand the exfoliation process and the extent to which it occurred. The exfoliation process consisted of the preparation of a 10ml methanol solution of the nanotubes and the ruthenium polymer, both accurately weighed out, and the subsequent sonication and UV analysis of this solution throughout the sonication.

Sonication was generally performed for 6 or 7 hours, using a Hielscher UP50H ultrasonic tip, set at 0.5 Cycles and 40% amplitude. UV measurements were carried out at well defined intervals. The UV solution in every measurement was comprised of 100µL of the experiment solution, diluted with 1000µL of MeOH. Generally the ratio of NT : Ru polymer in the experiments was 0.33:1, 0.5:1, 1:1, 1:2, and 1:3. The volume of methanol used in each exfoliation experiment was 10ml. A full list of the ratios used of *all* types of nanotubes for this chapter and Chapter 5 is given in TABLE 4.1, on the next page.

Amt Ru polymer (mg)	Amt CNT (mg)	Sonication Method	Total Time (mins)
1	1	Sonic Tip	360
N/A	1	Sonic Tip	360
2	1	Sonic Tip	360
3	1	Sonic Tip	360
2.5	1	Sonic Tip	360
1	1	Sonic Tip	480
N/A	1	Sonic Tip	300
1	1	Sonic Tip	480
2.5	1	Sonic Bath	360
1	1	Sonic Bath	360
1	2	Sonic Tip	360
1	2	Sonic Bath	360
1	1	Sonic Tip	360
1	1	Sonic Tip	300
1	2	Sonic Tip	360
N/A	1	SonicTip	300
N/A	1	Sonic Tip	360
1	1	Sonic Tip	360
2	1	Sonic Tip	360
3	1	Sonic Tip	360
3	2	Sonic Tip	360

TABLE 4.1: A LIST OF THE CNT EXFOLIATION EXPERIMENTS CARRIED OUT, SHOWING TYPE OF NT USED, SONICATION TIME AND AMOUNTS OF NT'S AND RUTHENIUM POLYMER USED. EXPERIMENTS ARE DIVIDED INTO TYPE OF NT USED, COLOURED ACCORDING TO THE FOLLOWING SCHEME: MWNT, MWNT-NH_2, SWNT. THESE EXPERIMENTS HAVE ALL BEEN REPEATED.

There are three types of carbon nanotubes used in this work. As mentioned previously, Single Walled Nanotubes are discussed in this chapter, while Chapter 5 deals with both Multi Walled Nanotubes (MWNT's) and amino-functionalized Multi Walled Nanotubes

(MWNT-NH_2). In Section 4.2.1, the exfoliation of the SWNT's in methanol without the ruthenium polymer present is discussed. In Section 4.2.2, the results of the exfoliation process using the ruthenium polymer are presented. In sections 4.2.3 and 4.2.4, the AFM data of the composite system on a SiO_2 surface will be presented. The Si(100) samples prepared for analysis by AFM were first cleaned by sonication in acetone, followed by sonication in methanol. The slides were then immersed in piranha solution overnight. They were removed, washed thoroughly with distilled water, and dried under argon. The composite and polymer solutions were drop cast on to the slides, and allowed to react for 10 minutes. The slides were then washed with distilled water, and dried under an argon atmosphere overnight.

4.2 Results and Discussion

4.2.1 UV Analysis of the Exfoliation of SWNT's in MeOH

In FIGURE 4.2(A), and FIGURE 4.2(B) on the following page, the results of the exfoliation of 1mg of SWNT's in 10ml of MeOH in the absence of ruthenium polymer are shown. In this section, the stabilities of the solutions over a period of one week are also shown. During this time after the original exfoliation, the solution is allowed to stand without sonication. The absorption of the solution is then measured in the same way as it was measured *during* the exfoliation experiment. These stability tests are done for all the samples, and will also be presented for the exfoliation experiments of Multi Walled Nanotubes in Chapter 5. This is important as this stability test has shown interesting results in the case of the SWNT-MeOH solutions. As will be seen in FIGURES 4.2 (A) and (B), the exfoliation appears to be proceeding reasonably well. The intensity of the UV signal is increasing with increased sonication, however, during the experiment it was observed that the solution was not "inking", the nanotubes were merely being dispersed in the solution by the sonication energy. It was observed that the black precipitate settled to the bottom of the sample tube after standing unsonicated for approximately 1 minute. This observation was confirmed by the stability test after 1 week, and this stability test is shown in FIGURE 4.2(C).

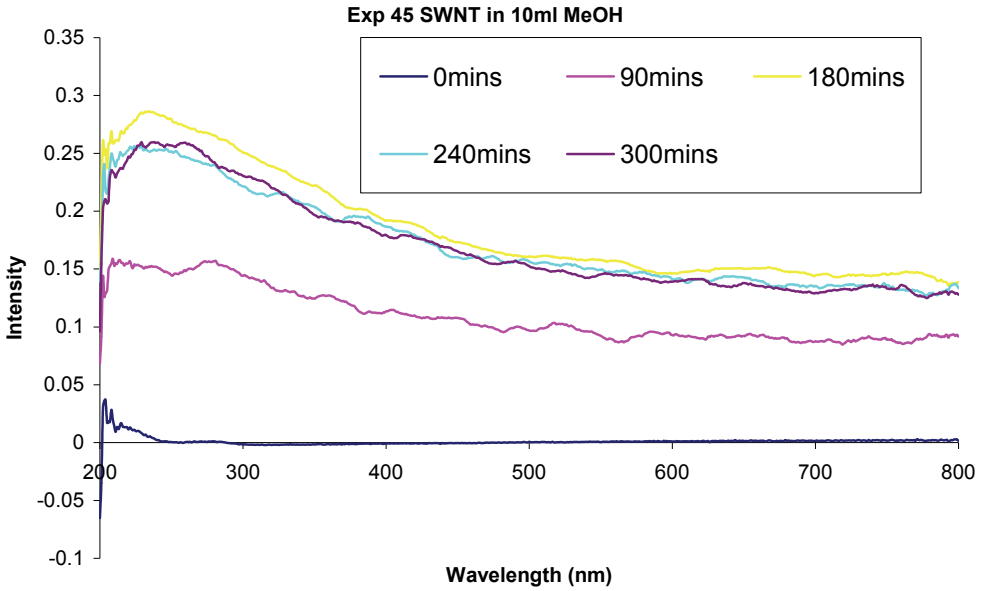

FIGURE 4.2(A): EXP 45, **1MG OF SWNT IN 10ML MEOH**, SONICATED WITH THE SONIC TIP. **UV OF SAMPLE (IN EACH CASE): 100µL OF SOLUTION + 1000µL OF MEOH.**

It should be noted that while the UV's in FIGURE 4.2(A) show the absorbance increasing, the solution itself was observed to be unstable, with the NT's merely dispersed by the sonication, and falling to the bottom of the sample tube shortly after the sonication was stopped each time. This is thought to be from the lack of Ru polymer in the solution, it is well know that SWNT's are extremely difficult to dissolve[15]. The fact that the absorbance increased across the whole wavelength range is interesting, as the main UV features for SWNT's are from the van Hove singularities, usually observed between 600nm and 800nm. These peaks are observed in the spectra in FIGURE 4.2(A), above at around 650nm and 740nm. The peak at approximately 250nm in the spectra is in close agreement with the value reported by Jiang *et al*[10], and by Popov[13], who attributes this band to a π plasmon, which is thought to be a result of the collective excitation of the π electrons in the carbon atom lattice of the nanotubes.

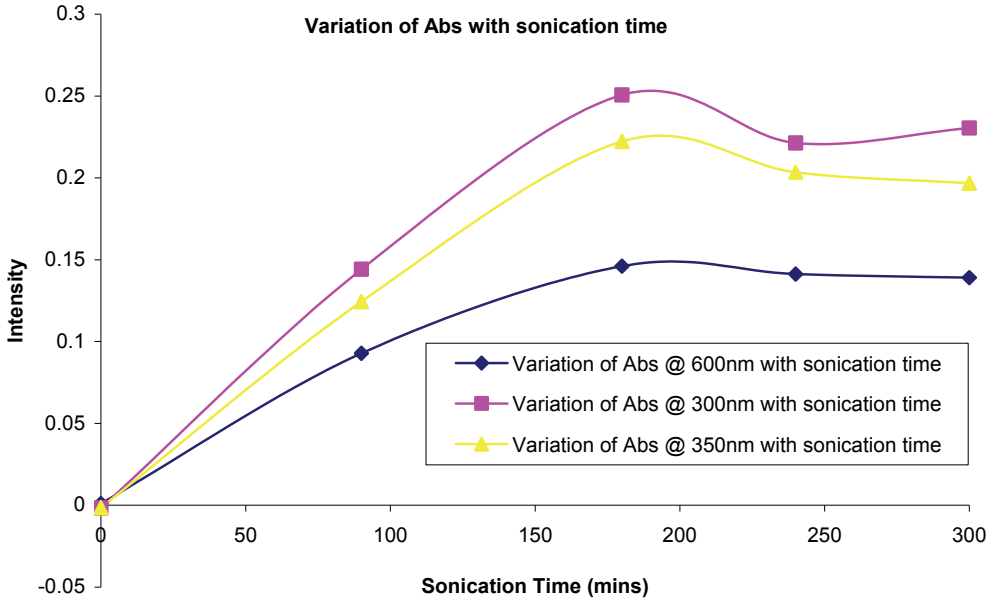

FIGURE 4.2(B): VARIATION OF ABSORBANCE INTENSITY AT 300NM, 350NM, AND 600NM WITH SONICATION TIME FOR EXP 45.

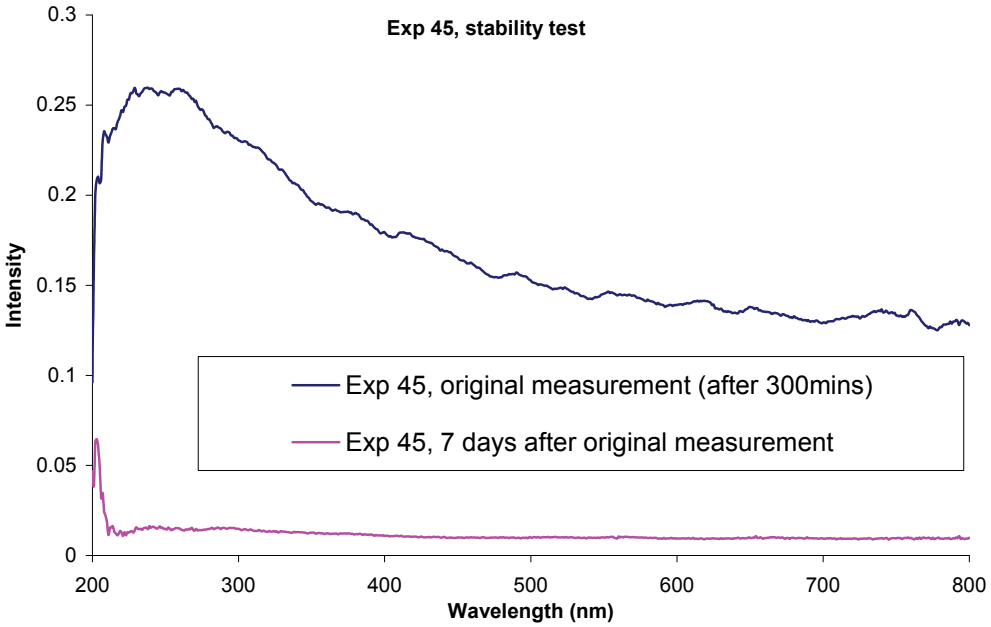

FIGURE 4.2(C): EXP 45 SOLN, COMPARISON OF THE UV SPECTRUM FOR THE ORIGINAL MEASUREMENT (AFTER 300MINS OF SONICATION) WITH THE UV SPECTRUM OF THE SOLN AFTER BEING ALLOWED TO STAND FOR ONE WEEK. **UV OF SAMPLE (IN EACH CASE): 100µL OF SOLUTION + 1000µL OF MEOH.**

As is seen in FIGURE 4.2(C), above, the solution is very unstable over time, and this indicates that no true exfoliation took place. This experiment was repeated and the

results are shown in FIGURE 4.3(A) and FIGURE 4.3(B), and the stability test results are shown in FIGURE 4.3(C).

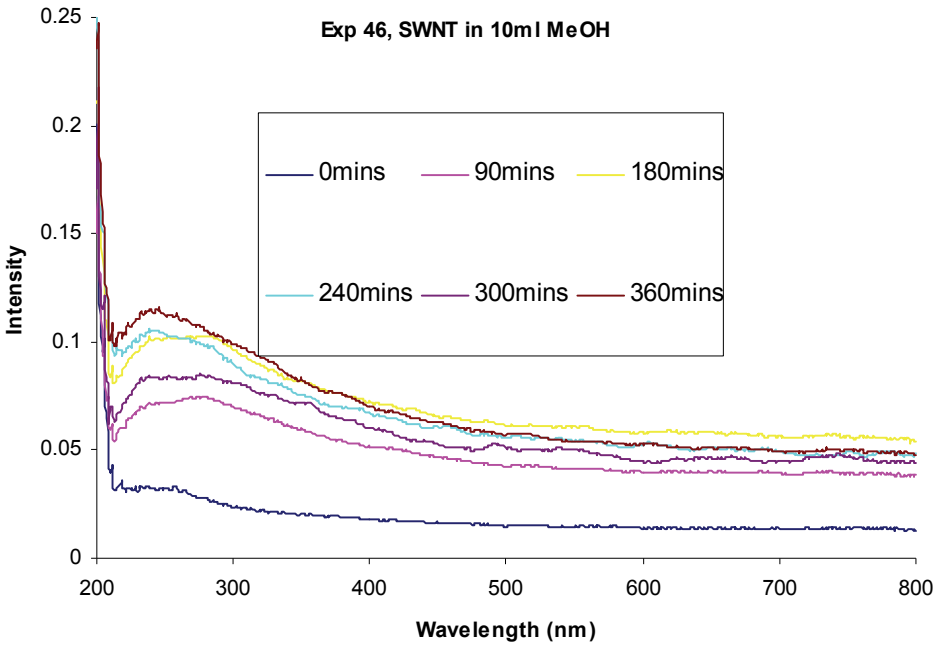

FIGURE 4.3(A): 24 JULY 2007, X255, EXP 46, **SWNT (1MG) IN 10ML MEOH**, WITH NO RUTHENIUM POLYMER PRESENT, SONICATED WITH THE SONIC TIP. **UV OF SAMPLE (IN EACH CASE): 100µL OF SOLUTION + 1000µL OF MEOH**

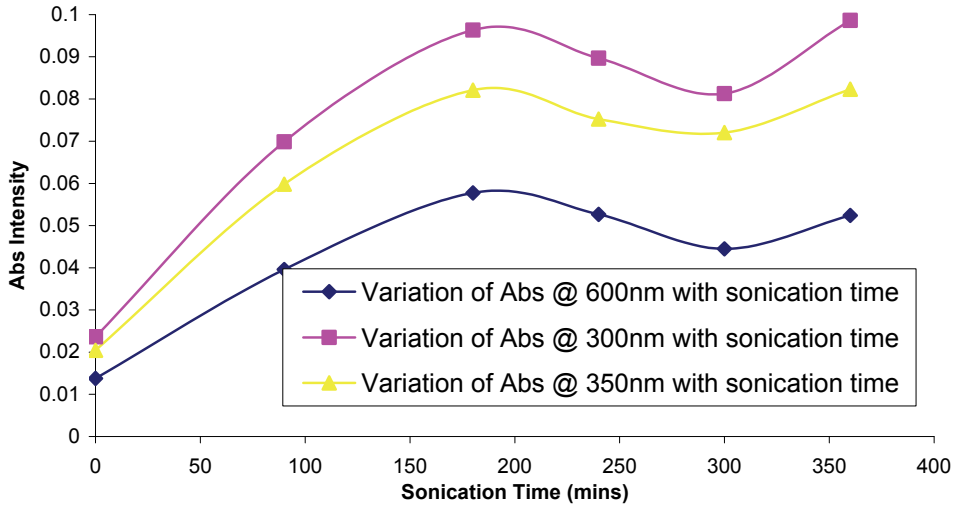

FIGURE 4.3 (B): VARIATION OF ABS INTENSITY @ 300, 350, AND 600NM, WITH SONICATION TIME. IT APPEARS THAT THERE IS NO REAL TREND TO BE SEEN HERE, ALTHOUGH THE TRACES ARE SIMILAR TO THOSE OBSERVED IN FIGURE 4.2(C), ABOVE.

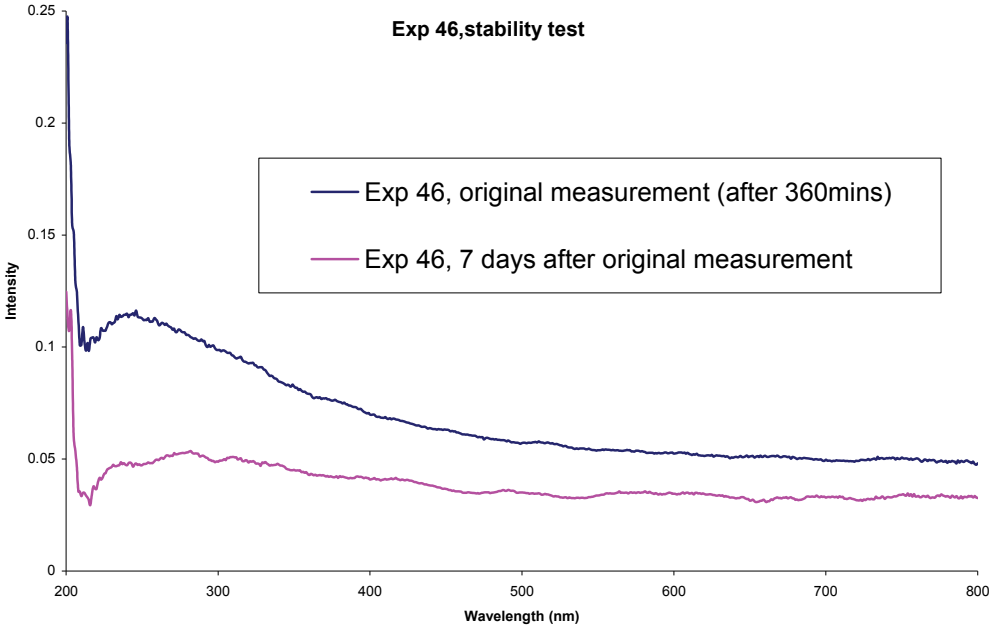

FIGURE 4.3(C): 24/31 JULY 2007, X255, EXP 46 SOLN, COMPARISON OF THE UV SPECTRUM OF THE ORIGINAL MEASUREMENT (AFTER 360MINS OF SONICATION) WITH THE UV SPECTRUM OF THE SOLUTION AFTER BEING ALLOWED TO STAND WITHOUT SONICATION FOR 1 WEEK. **UV OF SAMPLE (IN EACH CASE): 100µL OF SOLUTION + 1000µL OF MEOH**

In FIGURE 4.3(C), above, a significant decrease is seen in the absorbance spectrum of the solution, and this is in agreement with the previous figure (FIGURE 4.2(C), Exp 45). This suggests that the dissolution of SWNT's in MeOH without the presence of an exfoliation agent, such as the ruthenium polymer is not feasible or efficient. This is an interesting result in itself, and it agrees with the generally held assumption that SWNT's are difficult to exfoliate in solution, and it would appear from these results that the process is quite inefficient in the absence of an exfoliating agent such as PVP, SDS and, potentially, the ruthenium polymer (**1**).

4.2.2 SWNT's Exfoliated with $[Ru(bpy)_2(PVP)_{10}Cl]Cl$ in MeOH

It was decided to investigate the exfoliation of SWNT's with the ruthenium polymer, $[Ru(bpy)_2(PVP)_{10}Cl]Cl$ in the same way that the SWNT's were investigated in the previous section. A 1:1 ratio of polymer to nanotubes, by weight, was used first. The results of this experiment are shown in FIGURE 4.4(A), (B) and (C), below and on the next page. This experiment was, as usual, carried out in duplicate, and the results obtained are similar in both experiments.

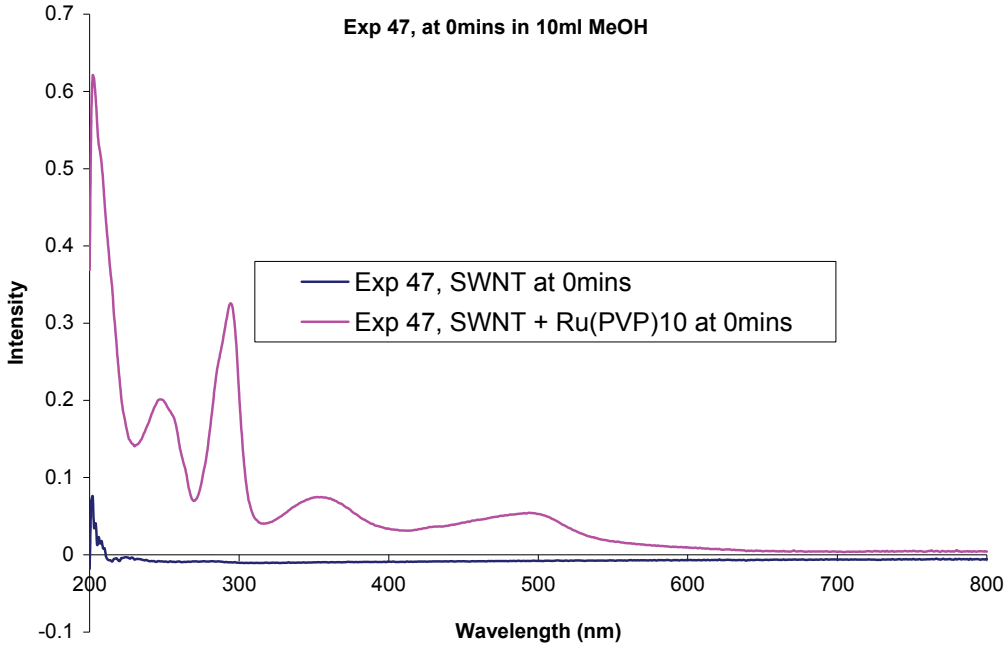

FIGURE 4.4(A): EXP 47, **SWNT (1MG) IN 10ML MEOH** AT 0MINS COMPARED WITH **SWNT (1MG) + [RU(BPY)$_2$(PVP)$_{10}$CL]CL IN 10ML MEOH** AT 0MINS. **UV OF SAMPLE (IN EACH CASE):** 100µL OF SOLUTION + 1000µL OF MEOH.

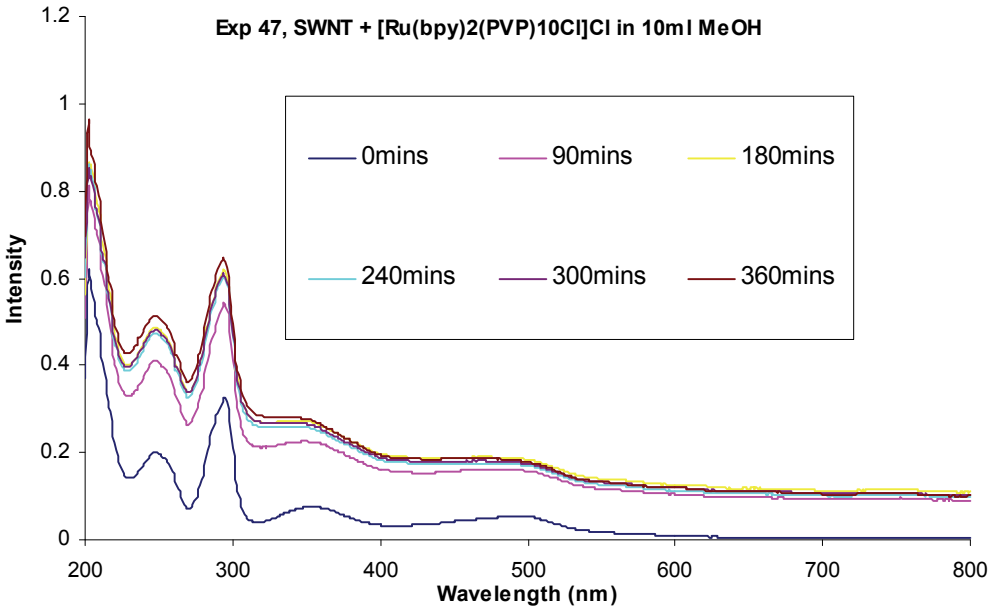

FIGURE 4.4(B):, EXP 47, **SWNT (1MG) + [RU(BPY)$_2$(PVP)$_{10}$CL]CL (1MG) IN 10ML MEOH**, SONICATED WITH THE SONIC TIP.. **UV OF SAMPLE (IN EACH CASE): 100µL OF SOLUTION + 1000µL OF MEOH.**

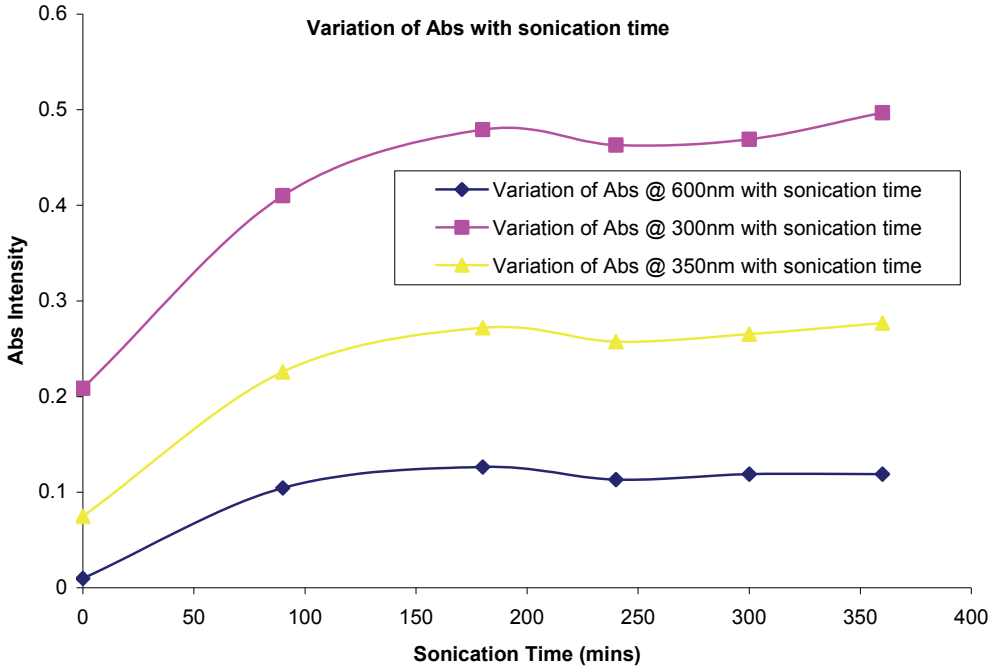

FIGURE 4.4(C): VARIATION OF ABS INTENSITY @ 300, 350, AND 600NM WITH SONICATION TIME.

A number of peaks are seen in the UV spectra in FIGURE 4.4(A). The peak at approximately 250nm is again thought to be the π plasmon process, resulting from the excitation of the carbon nanotubes, and the peaks at around 350nm and 490nm are the Metal to Ligand Transfer (MLCT) transitions in the metallpolymer. The band observed at approximately 290nm is attributed to a Ligand Centred (LC) transition in the bipyridine ligands in the metallopolymer. It is also observed that the intensity of the MLCT peak at 490nm in the composite after sonication is reduced relative to the intensity of the other MLCT peak at 350nm of the composite after sonication, in comparison with these peaks before sonication (0mins trace). This has been reported by Frehill *et al*[11] using the same system. It is thought that this reduction in relative peak intensity is due to a lack of π stacking of ligands in the polymer, and this in turn suggests that the polymer does not interact strongly with the nanotubes. Since there is little interaction between the polymer and the nanotube, it is therefore expected that the UV spectra of the composite material will be reasonably similar to that of the free polymer, since the MLCT's will not be enhanced by the additional π stacking of ligands in the polymer. This would suggest that the polymer does not change its morphology upon

interaction with the nanotubes. The UV data would suggest that some interaction has occurred, and the increase in baseline intensity would suggest that the either larger aggregates are forming in the solution, and therefore increasing the scattered light, or the solution is "inking" and exfoliation is actually occurring, which would result in the dissolution of some of the nanotubes, and therefore the absorbance in the 600nm-800nm region will increase. It is difficult to say for certain whether the exfoliation process is complete, the van Hove singularities are observed as very weak peaks at 655nm and 740nm in the UV traces, they are expected to be observed between 600nm and 800nm. It is possible that there is not enough ruthenium polymer in the solution to adequately exfoliate the nanotubes, and the process that is being observed in this experiment is only a very limited exfoliation. The stability test for this solution (again after the solution was allowed to stand undisturbed for 1 week) is shown in FIGURE 4.4(D), below.

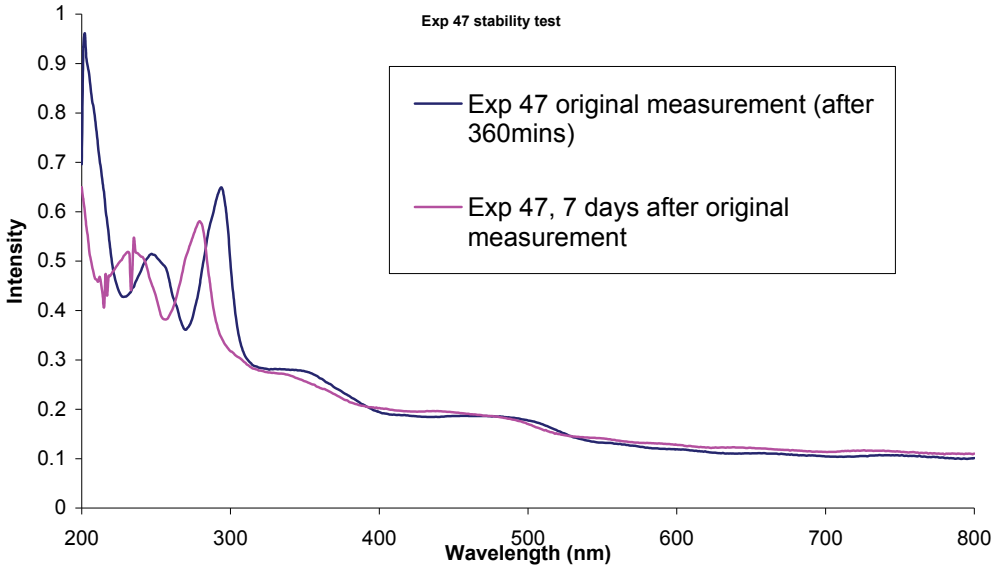

FIGURE 4.4 (D): EXP 47 SOLN, COMPARISON OF UV SPECTRUM OF THE ORIGINAL MEASUREMENT (AFTER 360MINS OF SONICATION) WITH THE UV SPECTRUM OF THE SAME SOLUTION AFTER BEING ALLOWED TO STAND WITHOUT ANY SONICATION FOR 1 WEEK. SOME DRIFTING IN THE WAVELENGTHS IS SEEN, THIS PROBABLY DUE TO INSTRUMENTATION RESPONSE. **UV OF SAMPLE (IN EACH CASE): 100µL OF SOLUTION + 1000µL OF MEOH.**

As is seen in FIGURE 4.4(D), above, some shifting in the wavelength is observed, however this is likely to be instrumental in nature, however it has been reported that SWNT's can sometimes blue shift the spectrum[15]. It is important to note thought that in that work by Blau *et al*[15], it was not a ruthenium based polymer that was employed, rather an organic

conjugated polymer-poly(m-phenylenevinyleneco-2,5-dioctyloxy-p-phenylenevinylene), (PmPV). This should not change the overall effect of the SWNT's blue shifting the spectrum. It has not been seen in every experiment however, and so it is therefore thought to be an instrumentation issue. The van Hove singularities are present after sonication, and are illustrated in FIGURE 4.4(E).

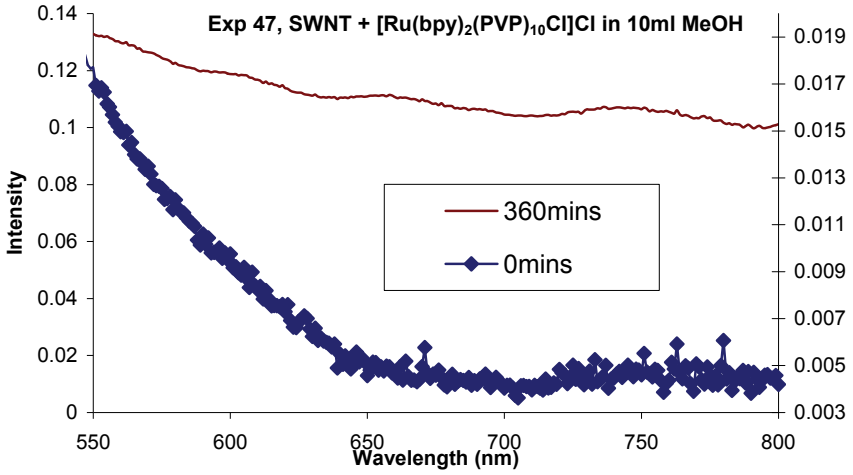

FIGURE 4.4(E): COMPARISON OF 0MIN UV TRACE, (RIGHT AXIS) WITH 360MINS TRACE, (LEFT AXIS), SHOWING VAN HOVE SINGULARITIES AFTER SONICATION.

The amount of ruthenium polymer was increased and the experiment repeated. The results obtained are shown in FIGURE 4.5(A), FIGURE 4.5(B) and FIGURE 4.5(C), below and on the next page.

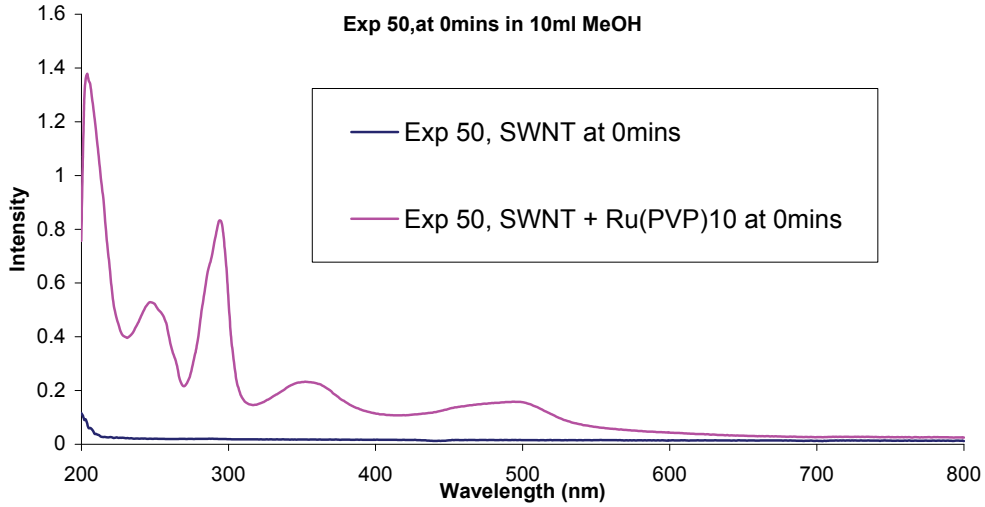

FIGURE 4.5(A): EXP 50, **SWNT (1MG) IN 10ML MEOH** AT 0MINS COMPARED WITH **SWNT (1MG) + [RU(BPY)2(PVP)10CL]CL (2MG) IN 10ML MEOH** AT 0MINS. **UV OF SAMPLE (IN EACH CASE): 100µL OF SOLUTION + 1000µL OF MEOH.**

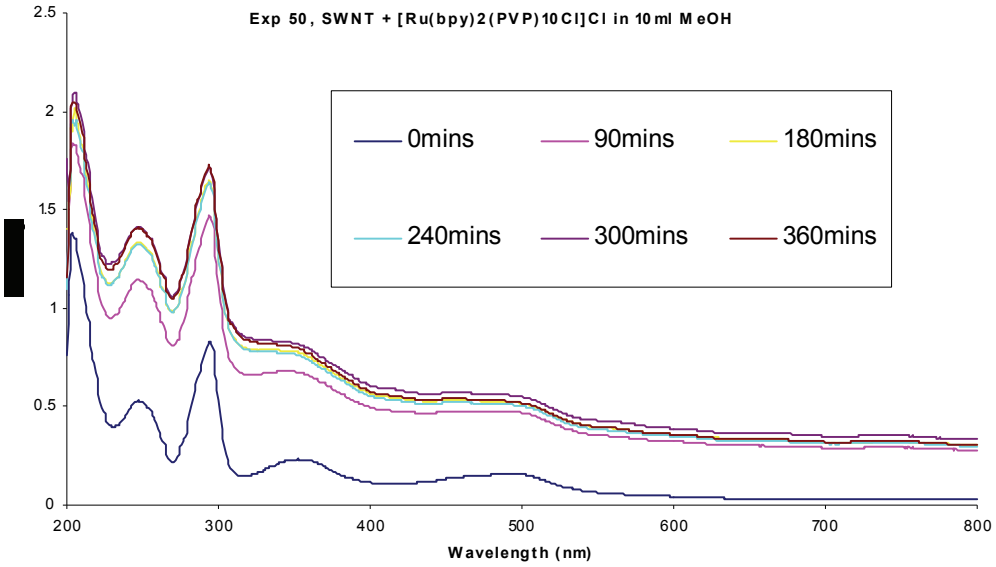

FIGURE 4.5(B): EXP 50, **SWNT (1MG) + [RU(BPY)$_2$(PVP)$_{10}$CL]CL (2MG) IN 10ML MEOH**, SONICATED WITH THE SONIC TIP. **UV SAMPLE (IN EACH CASE): 100µL OF SAMPLE + 1000µL MEOH.**

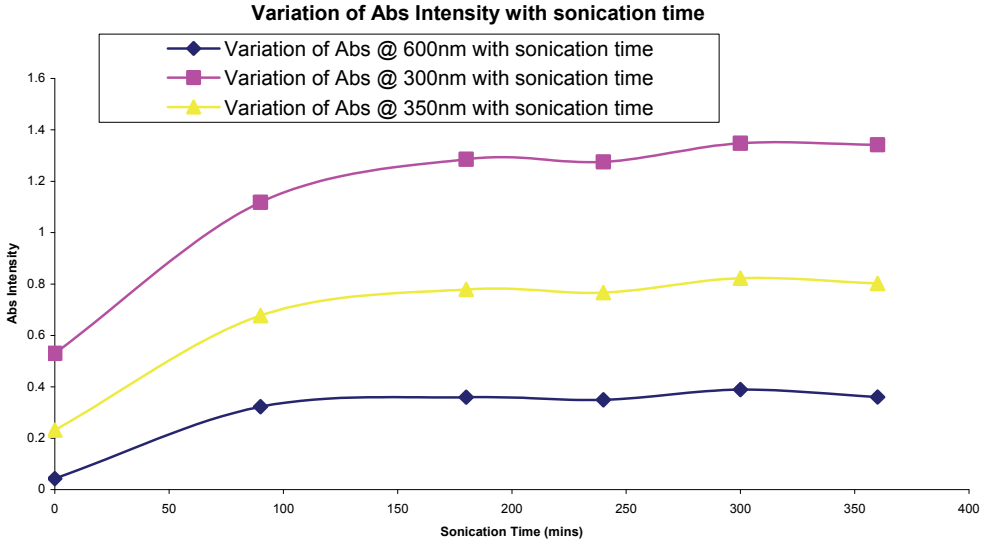

FIGURE 4.5(C): VARIATION OF THE ABS INTENSITY @ 300, 350, AND 600NM WITH SONICATION TIME. IT WOULD APPEAR FROM THIS FIGURE THAT THE EXFOLIATION PROCESS IS COMPLETE.

It would appear from FIGURES 4.5(A), (B) and (C), above that the exfoliation process was completed in the first 180 minutes of sonication. This is similar to the repeat experiment, where the maximum absorbance was achieved in the first 210 minutes. Again, very weak peaks in the absorbance are observed in FIGURE 4.5(B), between 600nm and 800nm.

These are again attributed to the van Hove singularities, characteristic of SWNT's. A close up of the UV traces at 0mins, (before sonication) and after 360 minutes of sonication in the region 550nm-800nm is shown in FIGURE 4.5(D), below.

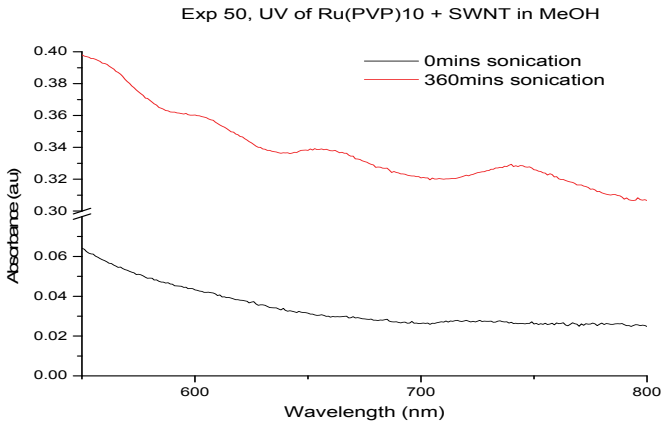

FIGURE 4.5(D): CLOSE UP OF THE "0MINS" AND "360MINS" TRACES IN FIGURE 4.5(B).

In FIGURE 4.5(D), the van Hove singularities are seen in the "360mins" trace, they are very weak, but they are present at approximately 655nm and 738nm, which are very close to the values reported by Frehill *et al* in ref [11]. They are not observed in the "0mins" trace. It is thought that these peaks are the result of the quasi one dimensional nature of the nanotubes, which leads to the electronic density of states to have sharp maxima in their energy profile, called singularities, and the energies of these maxima is predominantly dependant on the diameter of the nanotube itself[18]. Since these features are related to defects or kinks in the density of states within the electronic structure of the nanotubes, it would appear that the modification of the nanotubes with the ruthenium complex does not greatly affect this electronic structure. It is known that the density of states in the context of the electronic structure of a material can be considered to be the number of electrons available for a certain energy interval[14]. In addition, the presence of these features indicates that the sonication process does not damage the nanotubes greatly over the time frame used.

In order to investigate the stability of the solution over a week long period, its absorbance was measured after standing in the dark for a week. This absorbance

spectrum of the solution is seen in FIGURE 4.5(E), on the next page and is compared with the absorbance of the solution after 360mins of sonication.

No shift is seen in the wavelength for the two traces seen in FIGURE 4.5(E), suggesting that the drift that was observed in FIGURE 4.3(D) for the nanotube - only system was the result of instrument response. The absorbance of the solution has not changed appreciably over the week during which it was allowed to stand without sonication. This would indicate that this solution is reasonably stable over this period.

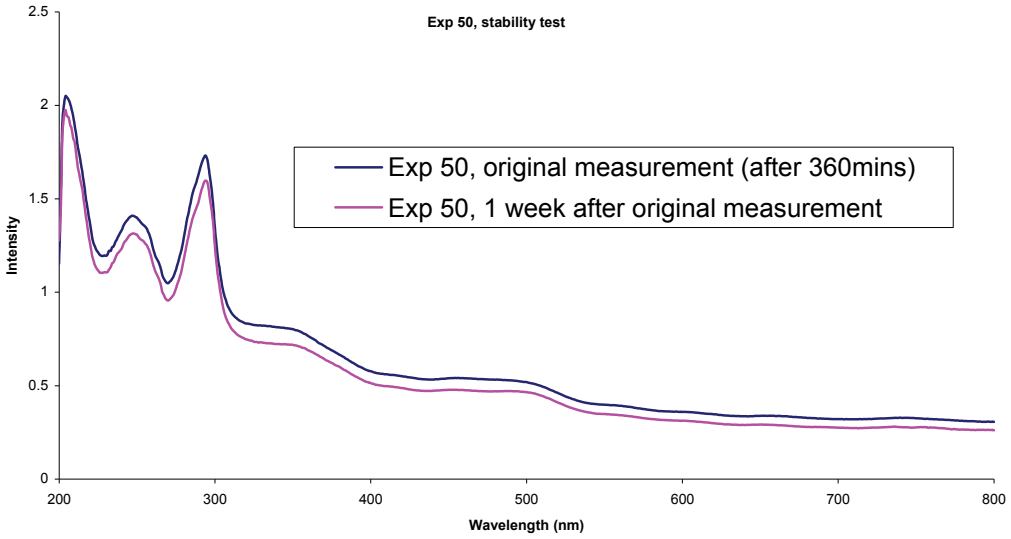

FIGURE 4.5(E): EXP 50 SOLN, COMPARISON OF UV SPECTRUM OF THE ORIGINAL MEASUREMENT (AFTER 360MINS OF SONICATION) WITH THE UV SPECTRUM OF THE SAME SOLUTION AFTER BEING ALLOWED TO STAND WITHOUT ANY SONICATION FOR 1 WEEK. **UV OF SAMPLE (IN EACH CASE): 100µL OF SOLUTION + 1000µL OF MEOH.**

The ruthenium polymer concentration was again increased, while the nanotube concentration was left unchanged. The results obtained for this exfoliation experiment are presented in FIGURES 4.6(A), (B) and (C).

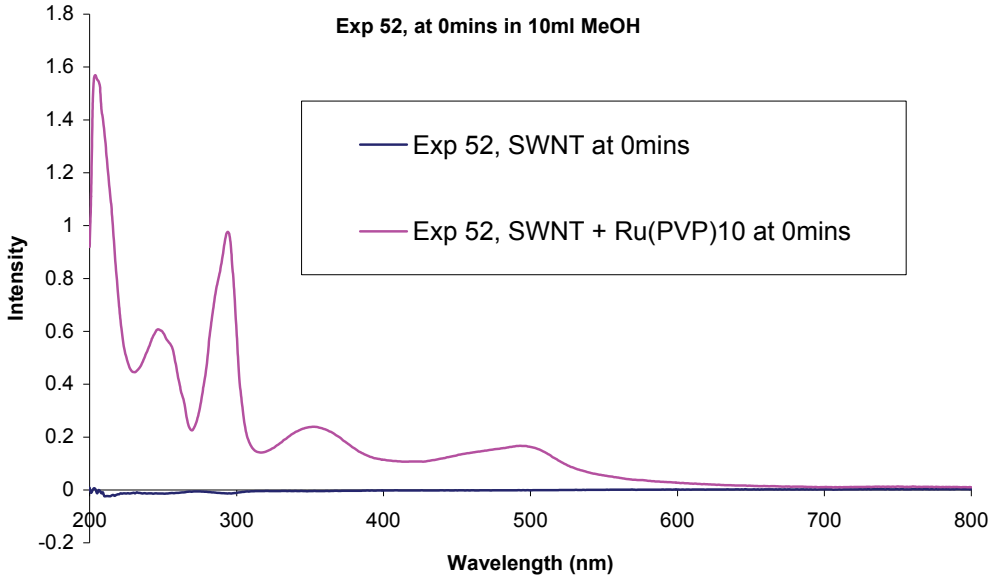

FIGURE 4.6(A): EXP 52, **SWNT (1MG) IN 10ML MEOH** AT 0MINS COMPARED WITH **SWNT (1MG) + [RU(BPY)$_2$(PVP)$_{10}$CL]CL (3MG) IN 10ML MEOH** AT 0MINS. **UV SAMPLE (IN EACH CASE): 100µL OF SOLUTION + 1000µL OF MEOH.**

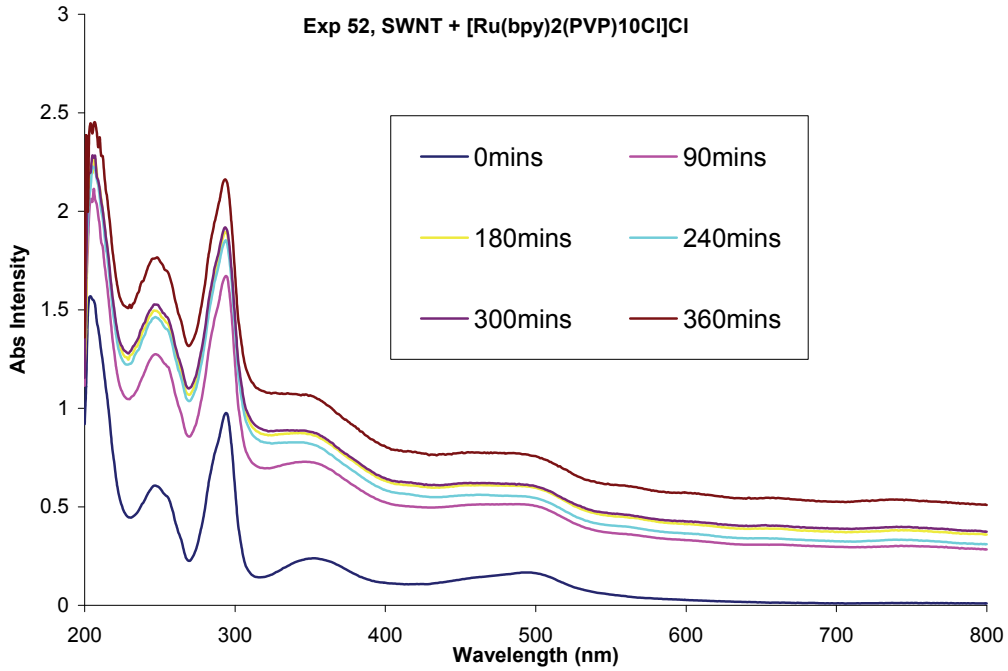

FIGURE4.6(B): EXP 52, **SWNT (1MG) + [RU(BPY)$_2$(PVP)$_{10}$CL]CL (3MG) IN 10ML MEOH**, SONICATED WITH THE SONIC TIP. **UV SAMPLE (IN EACH CASE): 100µL OF SAMPLE + 1000µL MEOH.**

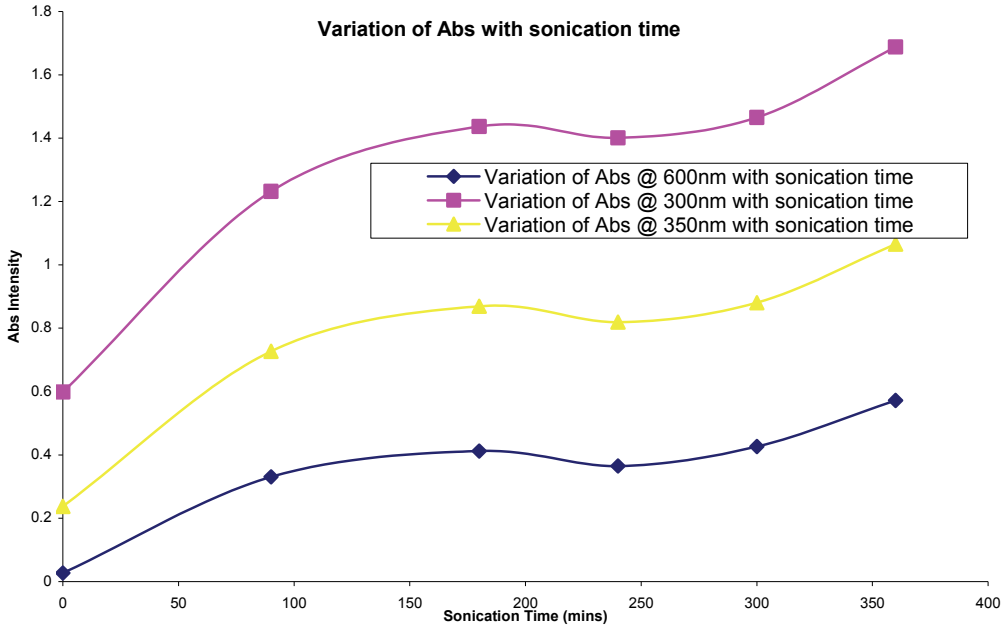

FIGURE 4.6(C): VARIATION OF ABS INTENSITY @ 300, 350, AND 600NM WITH SONICATION TIME. IT IS DIFFICULT TO DETERMINE FROM THIS FIGURE WHETHER THE EXFOLIATION PROCESS IS COMPLETE.

Close inspection of the "360mins" trace in FIGURE 4.6(B) on the previous page in the 550nm – 800nm region shows the van Hove singularities are present again, and that they are not observed in the '0mins" trace. It is difficult to ascertain from FIGURE 4.6(C), above whether the exfoliation process is complete or not. Again, the relative intensities of the MLCT peaks are changed in the final exfoliated solution, relative to the initial solution. The solution is quite stable, as is seen in FIGURE 4.6(D), below. There is approximately a 50% decrease in the absorbance across the wavelength range, and this suggests that perhaps some of the polymer molecules have become detached from the nanotubes. A close inspection of the traces shows that the van Hove bands are not as intense after the solution has been allowed to stand for a week, and this may also indicate a sundering of the composite material. This decrease is also seen in the traces in FIGURE 4.5(E). It was found by Xue *et al*[17] that in the case of a composite system of Multi-Walled Nanotubes and HMSA, Hydrolysed poly(Styrene-co-Maleic Anhydride), the HMSA polymer exists in two forms, the one bound to the nanotubes, and the free form, existing in solution and interacting with the nanotubes by the hydrophobic effect. This is obviously a different system to that investigated in this chapter, but the possibility remains for the free ruthenium polymer to affect the solubility of the nanotubes.

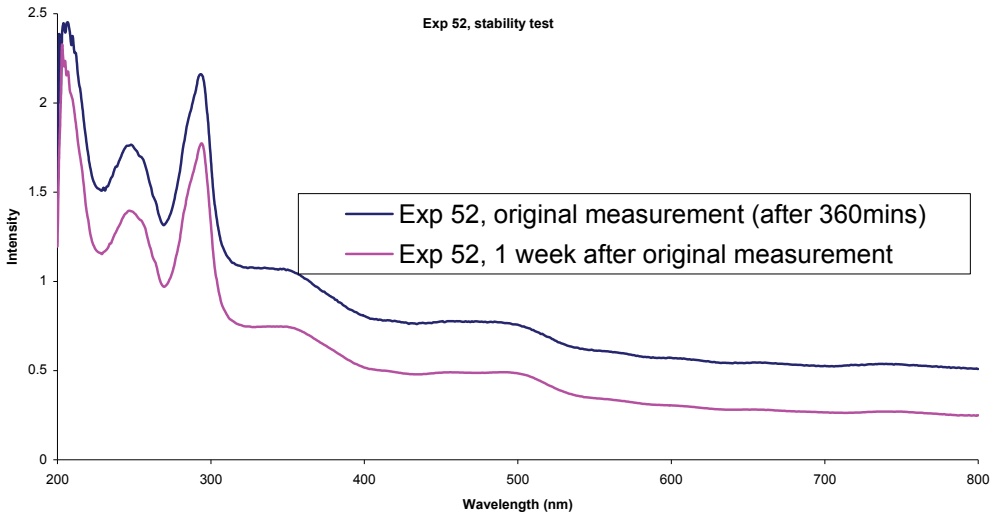

FIGURE 4.6 (D): EXP 52 SOLN, COMPARISON OF UV SPECTRUM OF THE ORIGINAL MEASUREMENT (AFTER 360MINS OF SONICATION) WITH THE UV SPECTRUM OF THE SAME SOLUTION AFTER BEING ALLOWED TO STAND WITHOUT ANY SONICATION FOR 1 WEEK. **UV OF SAMPLE (IN EACH CASE): 100µL OF SOLUTION + 1000µL OF MEOH.**

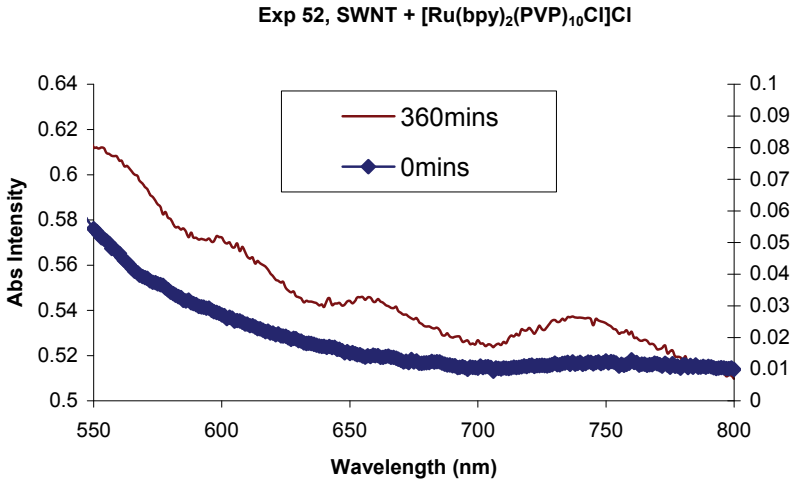

FIGURE 4.6(E): PRESENCE OF VAN HOVE SINGULARITIES (VHS) IN THE UV SPECTRUM AFTER SONICATION.

One thing that must be considered in these results is the presence of the van Hove singularities. It has been reported by Dyke and Tour[16] that the removal of the SDS surfactant from the NT's would result in the van Hove singularities being less distinct, however they would still be present. However the transitions are thought to be lost completely following covalent modification of the NT's with the SDS. This does not appear to be the case, and so would suggest a non-covalent or weakly covalent interaction between the nanotubes and the ruthenium polymer (**1**).

The ruthenium polymer concentration was kept constant at 3mg in 10ml MeOH, while the SWNT concentration was increased to 2mg. The resulting solution was sonicated and the results of this experiment are shown in FIGURES 4.7 (A), (B), and (C). The UV of this solution was measured 1 week after sonication, and this is presented in FIGURE 4.7(D).

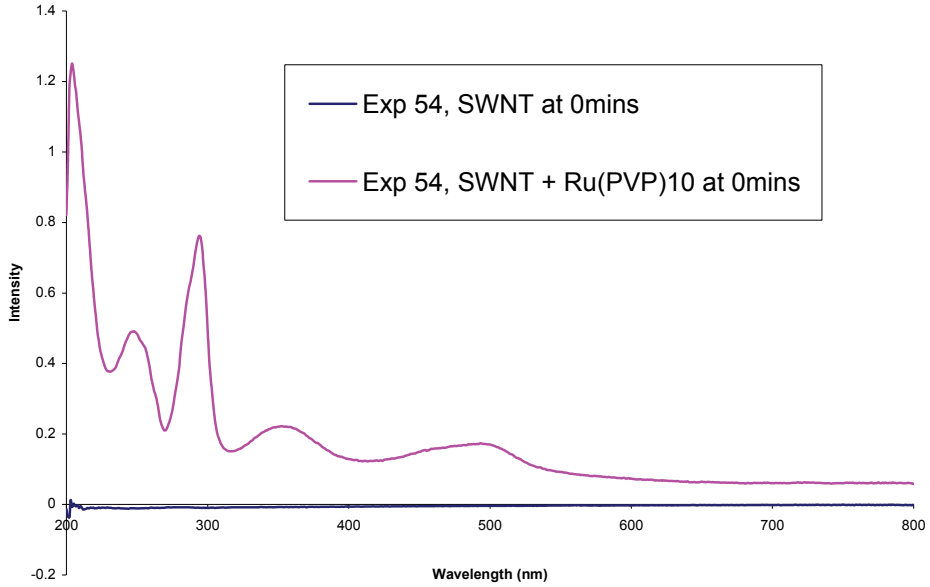

FIGURE 4.7(A): EXP 54, UV OF **SWNT (2MG) IN 10ML MEOH** AT 0MINS COMPARED WITH THE UV OF **SWNT (2MG) + [RU(BPY)$_2$(PVP)$_{10}$CL]CL (3MG) IN 10ML MEOH** AT 0MINS. **UV SAMPLE (IN EACH CASE): 100µL OF SAMPLE + 1000µL OF MEOH.**

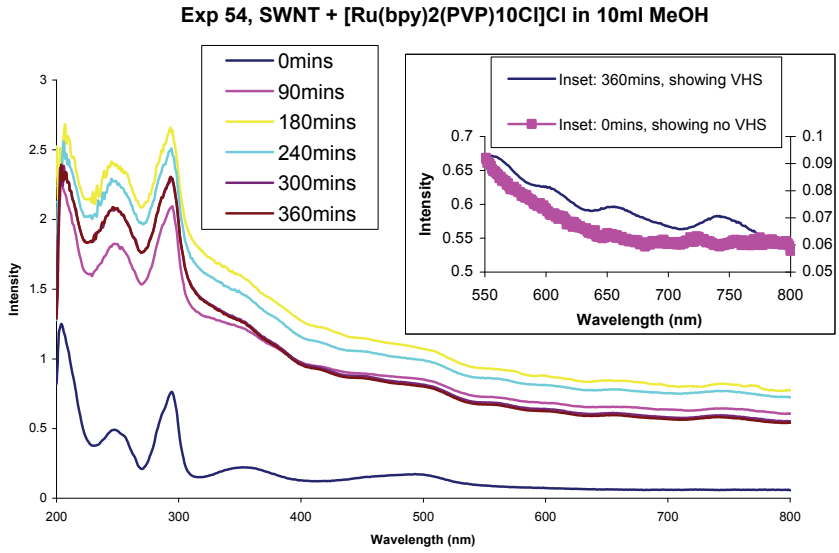

FIGURE 4.7(B): EXP 54, **SWNT (2MG) + [RU(BPY)$_2$(PVP)$_{10}$CL]CL (3MG) IN 10ML MEOH,** SONICATED WITH THE SONIC TIP. **UV SAMPLE (IN EACH CASE): 100µL OF SAMPLE + 1000µL OF MEOH.** INSET SHOWS COMPARISON OF 0MIN TRACE (RIGHT AXIS) WITH 360MIN TRACE (LEFT AXIS), INDICATING PRESENCE OF VHS.

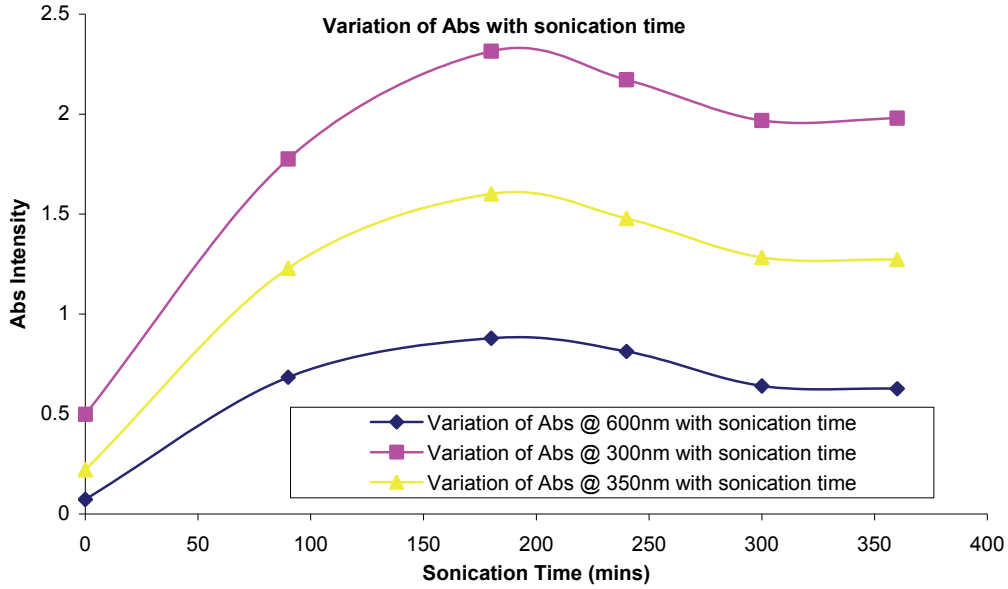

FIGURE 4.7(C): VARIATION IN ABS INTENSITY @ 300NM, 350NM, AND 600NM WITH SONICATION TIME (MINS). IT APPEARS THAT THE EXFOLIATION PROCESS REACHES A MAXIMUM AFTER APPROXIMATELY 3 HRS OF SONICATION TIME.

Comparing FIGURE 4.7(C), above with FIGURE 4.6(C), it appears that the 600nm Abs vs sonication time trace reaches a similar intensity in both cases, however at different sonication times, suggesting that the maximum level of exfoliation has been reached in the solution containing 2mg SWNT's with 2mg of ruthenium polymer. This in turn suggests that adding more ruthenium polymer does not increase the exfoliation. It is also likely that maximum exfoliation has been attained in the solution containing 1mg of SWNT's.

The stability of the solution in Exp 54 was measured, 1 week after the sonication. This is shown in FIGURE 4.7(D) on the next page. The solution seems reasonably stable over this 7 day period. An interesting point to note is that the intensity of the absorbance is higher for the solution after it was allowed to stand for a week, than it was for the original solution, just after sonication. This was unexpected, and may be an instrumentation issue or, potentially, the error may have been in the UV solution used in the measurement. The van Hove singularities are still observed in the solution after 1 week and of a similar intensity to those of the solution immediately after sonication.

The above experiment (Exp 54) was repeated, and reasonable similar results were obtained. These are shown in FIGURES 4.8(A), (B), and (C). Again the 1 week stability test

for the solution is shown in FIGURES 4.8(D) and (E) on the next page and the following pages.

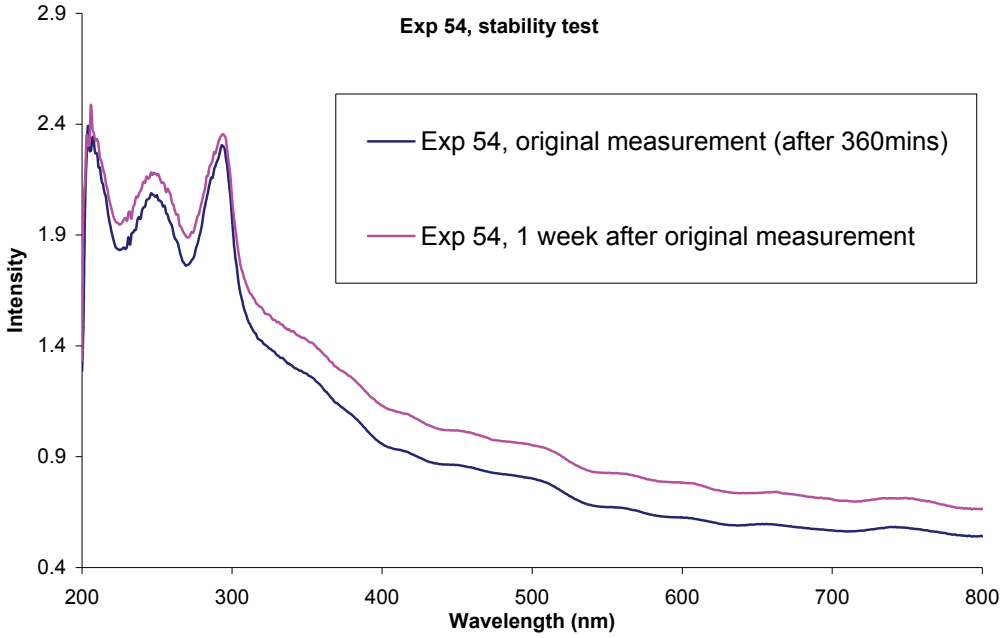

FIGURE 4.7 (D): EXP 54 STABILITY TEST. **UV SAMPLE (IN EACH CASE): 100µL OF SAMPLE + 1000µL OF MEOH.**

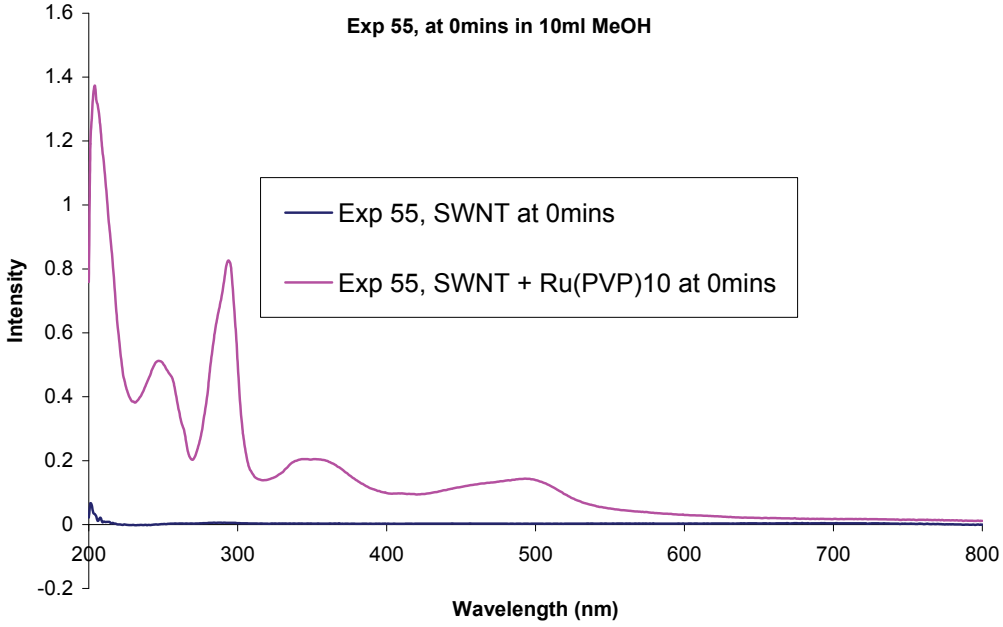

FIGURE 4.8(A): EXP 55, UV OF **SWNT (2MG) IN 10ML MEOH** AT 0MINS COMPARED WITH THE UV OF **SWNT (2MG) + [RU(BPY)$_2$(PVP)$_{10}$CL]CL (3MG) IN 10ML MEOH** AT 0MINS. **UV SAMPLE (IN EACH CASE): 100µL OF SAMPLE + 1000µL OF MEOH.**

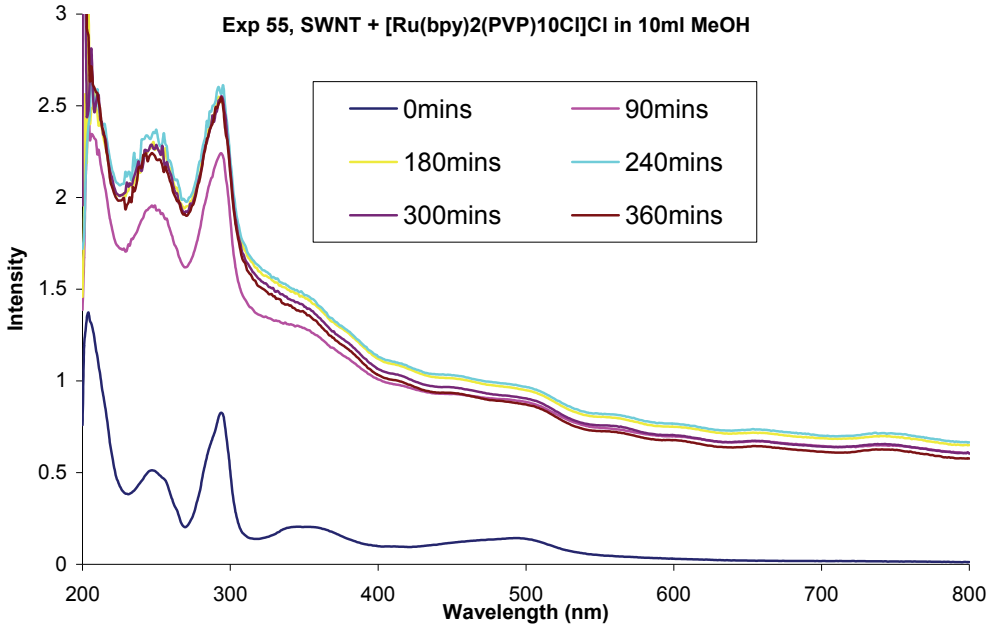

FIGURE 4.8(B): EXP 55, **SWNT (2MG) + [RU(BPY)$_2$(PVP)$_{10}$CL]CL (3MG) IN 10ML MEOH,** SONICATED WITH THE SONIC TIP. **UV SAMPLE (IN EACH CASE): 100µL OF SAMPLE + 1000µL OF MEOH.**

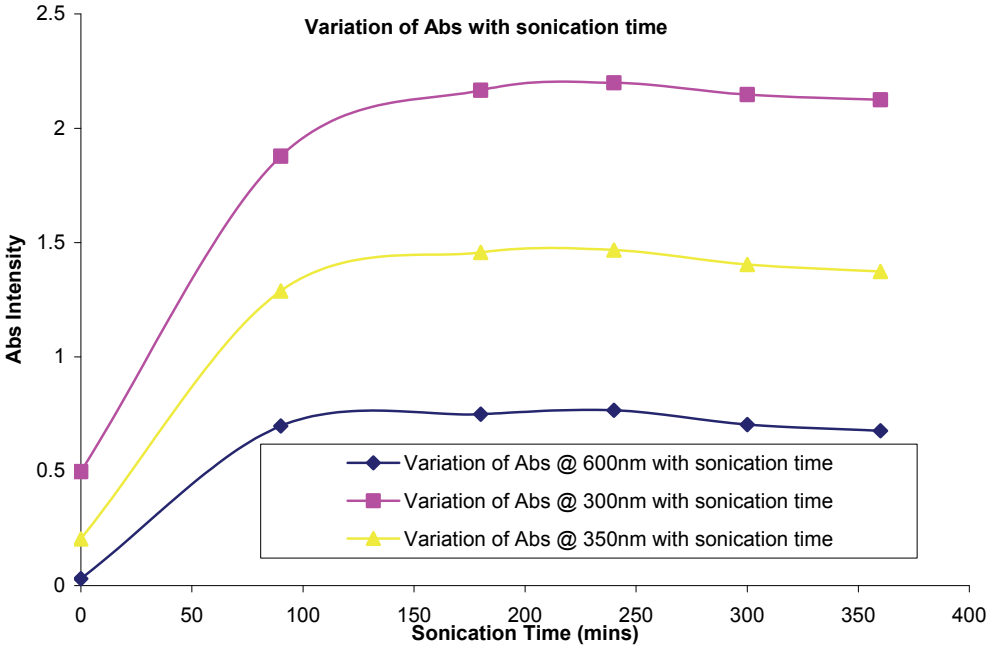

FIGURE 4.8(C): EXP 55, VARIATION OF THE ABS INTENSITY @ 300NM, 350NM AND 600NM WITH SONICATION TIME (MINS). IT APPEARS THAT THE EXFOLIATION PROCESS HAS REACHED A PLATEAU.

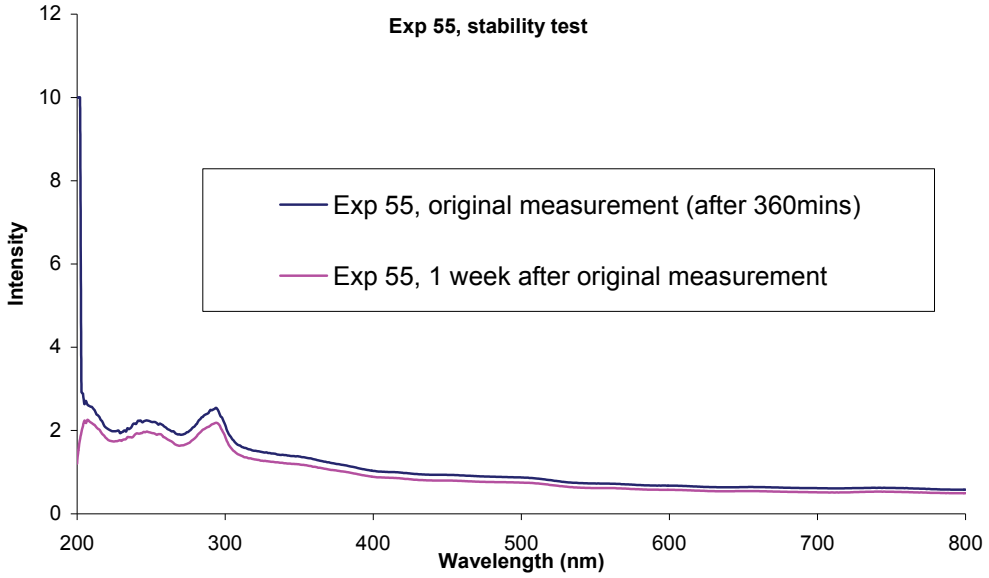

FIGURE 4.8(D): EXP 55, STABILITY TEST. **UV SAMPLE (IN EACH CASE): 100µL OF SAMPLE + 1000µL OF MEOH**

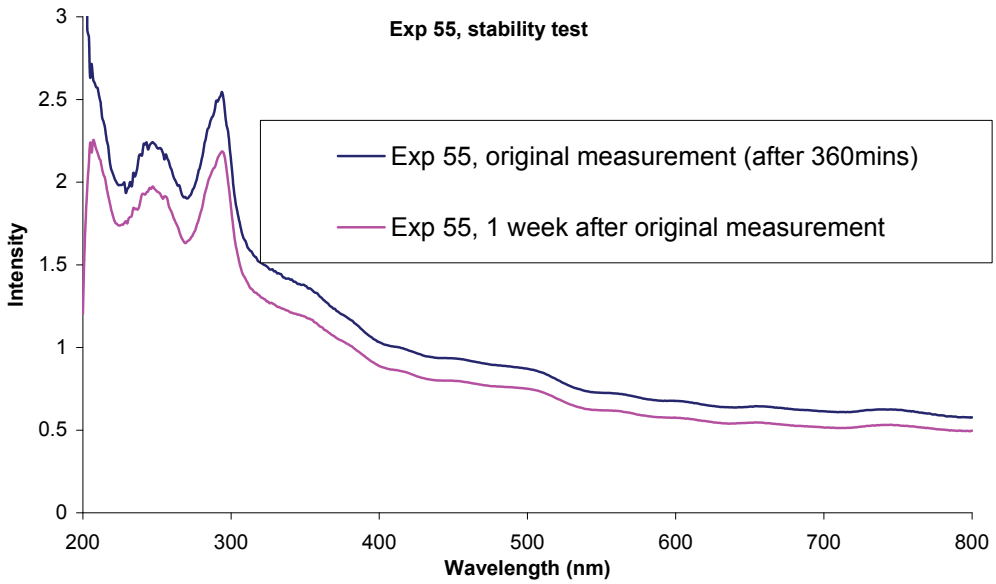

FIGURE 4.8(E): FIGURE 4.8(D) WITH Y-AXIS RANGE SHORTENED. **UV SAMPLE (IN EACH CASE): 100µL OF SAMPLE + 1000µL OF MEOH**

It is seen in FIGURE 4.8(B) that the absorbance at 800nm after 360mins of sonication is very similar to that seen in FIGURE 4.7(B) after the same period of sonication. This indicates a certain degree of consistency in the sonication process and again it indicates that the process is complete at this point in the sonication. It is seen in FIGURE 4.8(C),

above, that the maximum exfoliation is reached after approximately 90 minutes of sonication. Therefore it was decided to investigate this initial 90 minutes more closely. The results of this investigation are presented in FIGURES 4.9(A), (B), and (C).

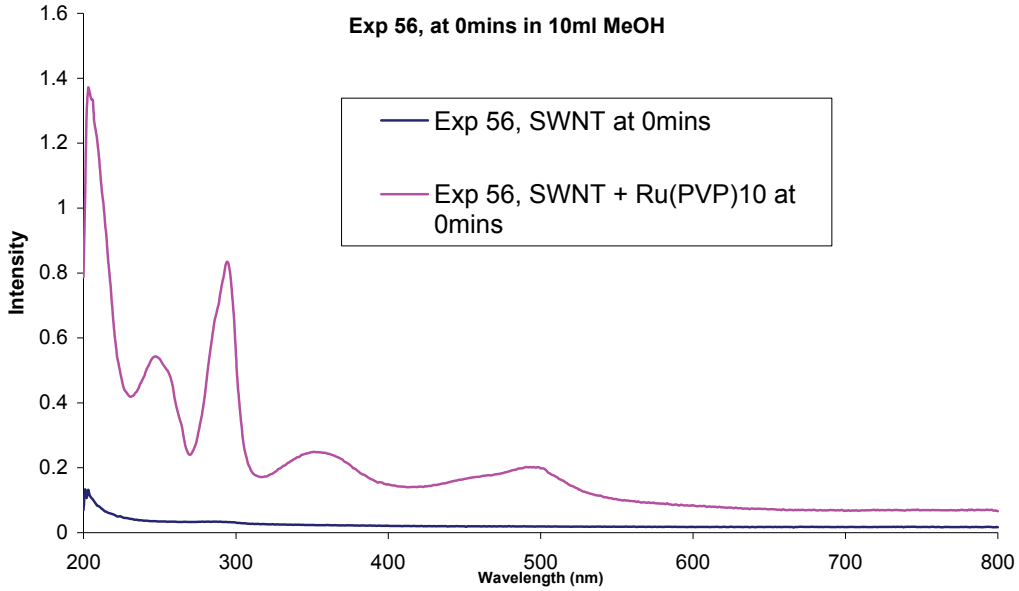

FIGURE 4.9(A): EXP 56, UV OF **SWNT (2MG) IN 10ML MEOH** AT 0MINS COMPARED WITH THE UV OF **SWNT (2MG) + $[Ru(bpy)_2(PVP)_{10}Cl]Cl$ (3MG) IN 10ML MEOH** AT 0MINS. **UV SAMPLE (IN EACH CASE): 100µL OF SAMPLE + 1000µL OF MEOH.**

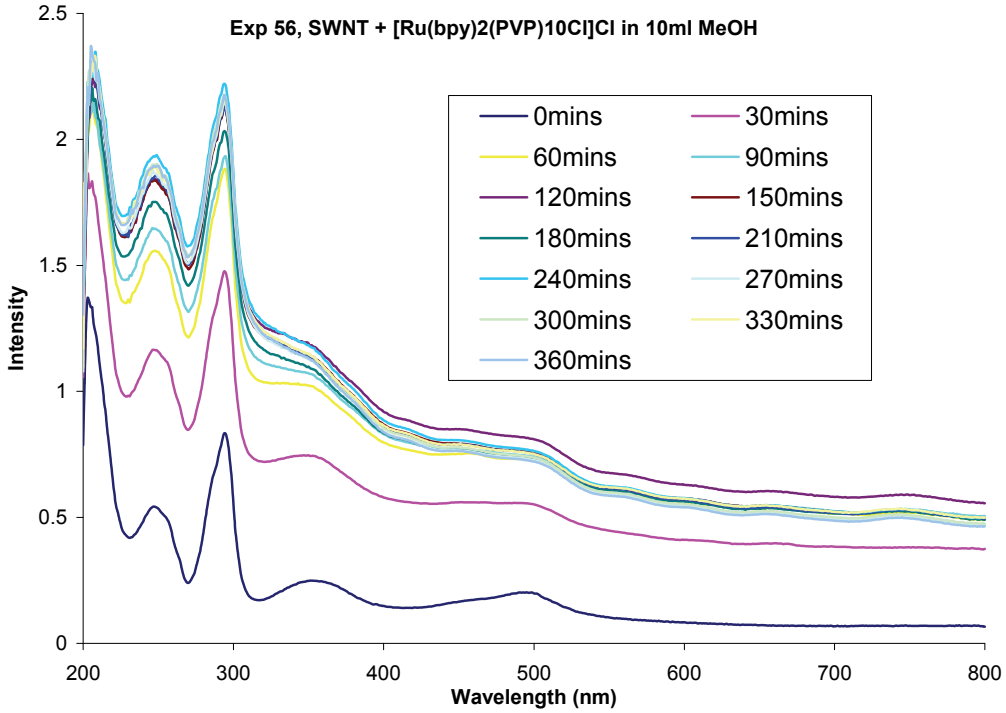

FIGURE 4.9(B): EXP 56, **SWNT (2MG) + $[Ru(bpy)_2(PVP)_{10}Cl]Cl$ (3MG) IN 10ML MEOH,** SONICATED WITH THE SONIC TIP. **UV SAMPLE (IN EACH CASE): 100µL OF SAMPLE + 1000µL OF MEOH.**

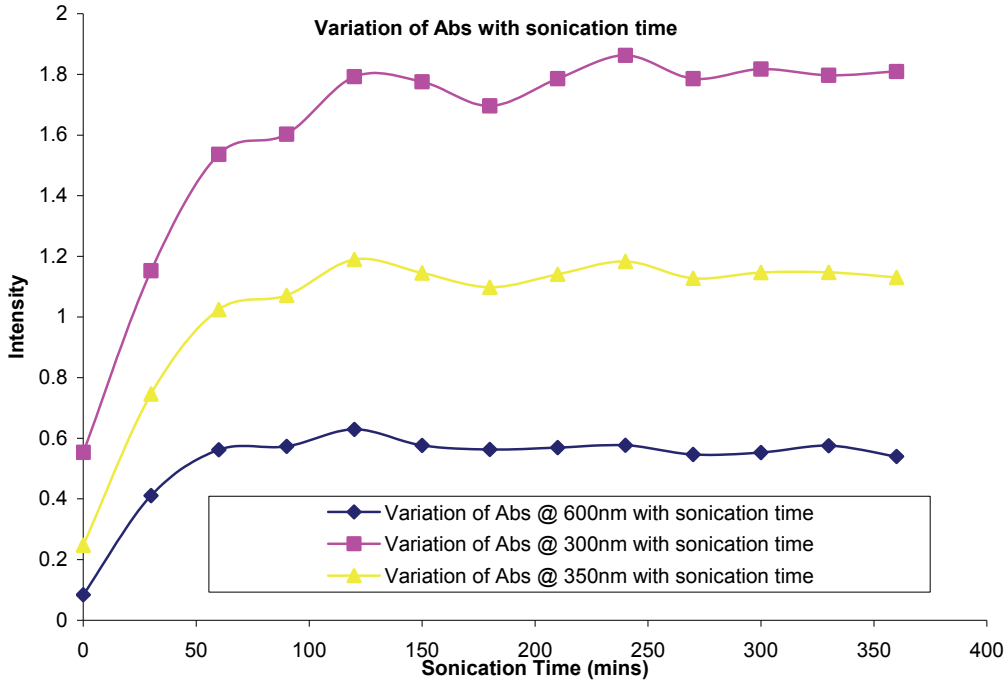

FIGURE 4.9(C): EXP 56, VARIATION OF THE ABS INTENSITY @ 300NM, 350NM AND 600NM WITH SONICATION TIME (MINS).

From FIGURE 4.9(C), above, it is difficult to say whether the process has reached a maximum or not, as there is no clear maximum point. The experiment has been repeated and the results for that experiment are quite similar to these results. It is possible that the maximum lies around the 120 minute point, however there is a similar intensity observed around 240 minutes. It is likely though, that the variations observed in the intensity are not of sufficient magnitude to be meaningful. It is thought that the sonication process in this case is not as effective as it not as continuous as the process used in the previous experiments presented in this chapter. This may be a critical factor in the efficiency of the sonication process, the issue of the sonication being reasonably continous. If this is not the case, then it may be possible that composite formed after a shorter sonication will not be stable enough, and the effect of increased movement of the vessel in which the sonicated solution is placed, in order to carry out a UV measurement, and the effect of increased withdrawals of the UV aliquots (leading to a decreased volume of the parent, sonicated solution), should not be ruled out either. Finally, the shorter sonication times may not allow for sufficient "unbundling" of the carbon

nanotube aggregates present initially in the solution. This would in principle lead to a reduced level of single, well dispersed nanotubes available for exfoliation with the ruthenium polymer. This idea leads to a possible future experiment, where the nanotubes are dispersed initially in the methanol solution, using sonication, *without* the ruthenium polymer, and then after an appropriate time, the ruthenium polymer is added, and this solution is further sonicated.

4.2.3 AFM of SWNT's + Ru Polymer on Si

It was decided to take one of the composite solutions of the SWNT's with the ruthenium polymer and drop cast it on to a silicon slide. AFM was then used to investigate the presence of carbon nanotubes and / or polymer on the surface. A 20µm scan was performed first, to ascertain the extent of the coverage of the nanotubes on the surface. This initial, large scan is shown in FIGURE 4.10, below. Full scan details for all the images are provided in Appendix B.

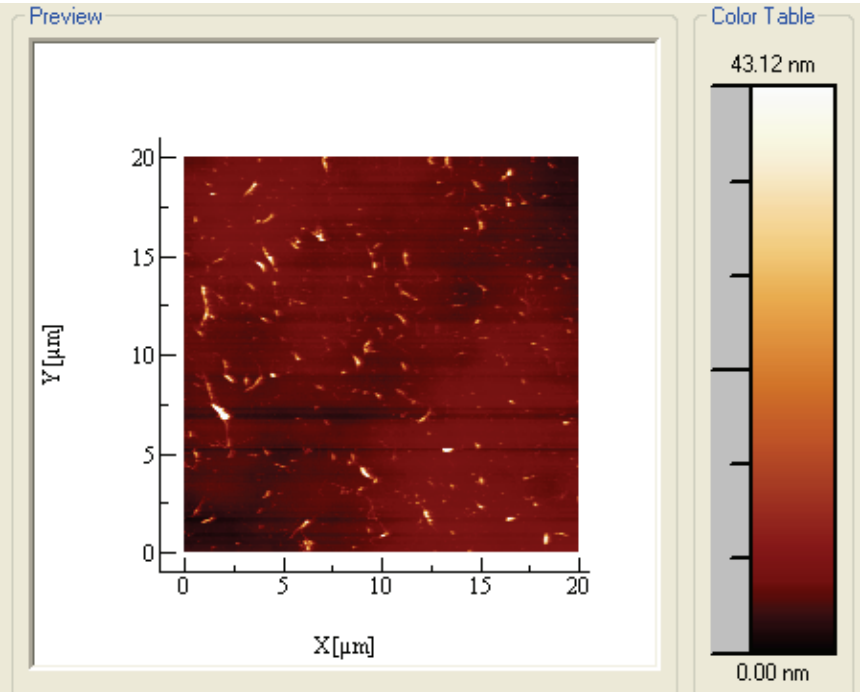

FIGURE 4.10: 20µm X 20µm AFM IMAGE OF SWNT / $[Ru(bpy)_2(PVP)_{10}Cl]Cl$ COMPOSITE DEPOSITED ON Si(100) SUBSTRATE.

The image in FIGURE 4.10 shows a number of nanotube-like features across the surface. It was decided to zoom in on the upper left corner of the image, to investigate the features more fully.

The image in FIGURE 4.11, below shows the features more clearly. It can be concluded that the features resemble carbon nanotubes, however it would appear that they are much wider than expected. It is generally accepted that carbon nanotubes have an aspect ratio of 1000:1, so these features are much larger in diameter than expected. There are two possibilities, the first is that the features observed are bundles of nanotubes, this is not considered to be the case, given the reasonably smooth morphology seen, particularly in FIGURE 4.12(A). The other, more probable reason is that the nanotubes are in fact covered with the ruthenium polymer, an assertion that the UV exfoliation experiments appear to support.

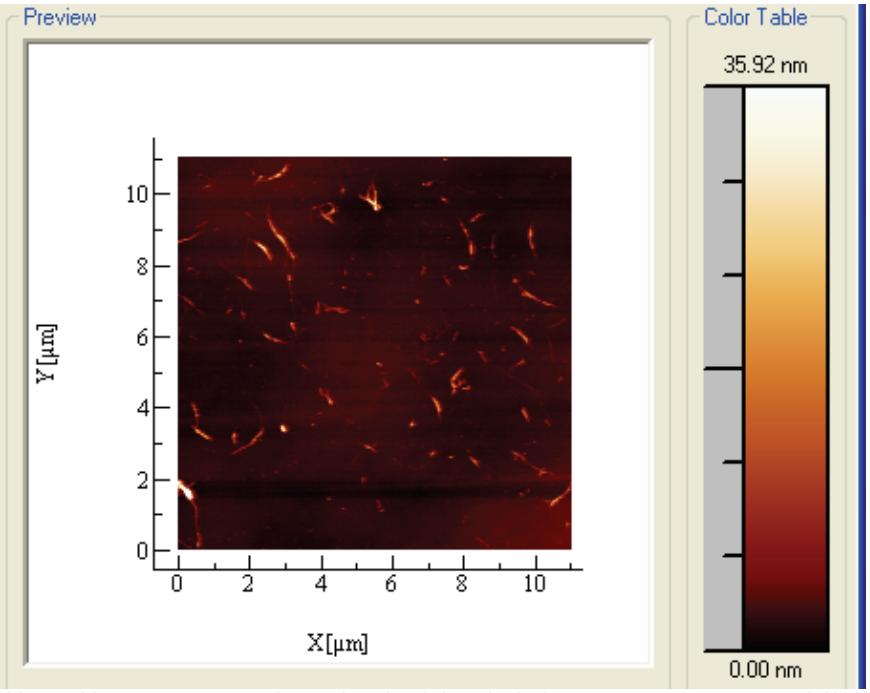

FIGURE 4.11: 11µm X 11µm AFM IMAGE OF SWNT / $[Ru(bpy)_2(PVP)_{10}Cl]Cl$ COMPOSITE DEPOSITED ON Si(100) SUBSTRATE.

FIGURE 4.12, on the next page shows a 3µm zoomed in scan of the upper left portion of the image in FIGURE 4.11, above. It appears to show single nanotubes, or groups of approximately 2 very close together. Upon close examination of the features it can be seen that the nanotubes appear to be thickest in their centres and are thinner towards the

ends, indicating that the polymer tends to bind more to the centre section of the nanotube.

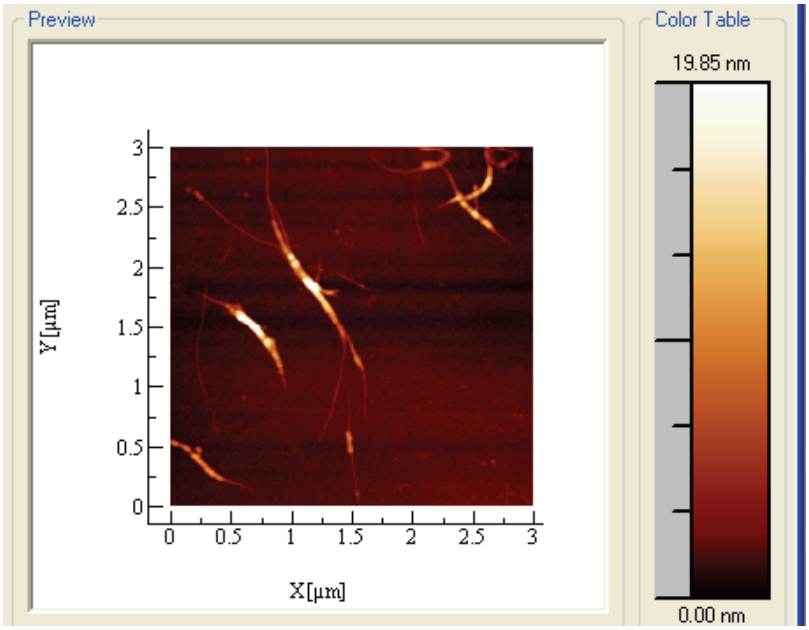

FIGURE 4.12(A): 3µm X 3µm AFM IMAGE OF SWNT / $[Ru(bpy)_2(PVP)_{10}Cl]Cl$ COMPOSITE DEPOSITED ON Si(100) SUBSTRATE.

In order to estimate the diameter of the nanotube, a sectional analysis was carried out on the feature in the above image. The results of this analysis are presented in FIGURE 4.12(B) and FIGURE 4.12(C), below. The green line in FIGURE 4.12(B) shows the section line through the image, while FIGURE 4.12(C) shows the topographical profile along this green line.

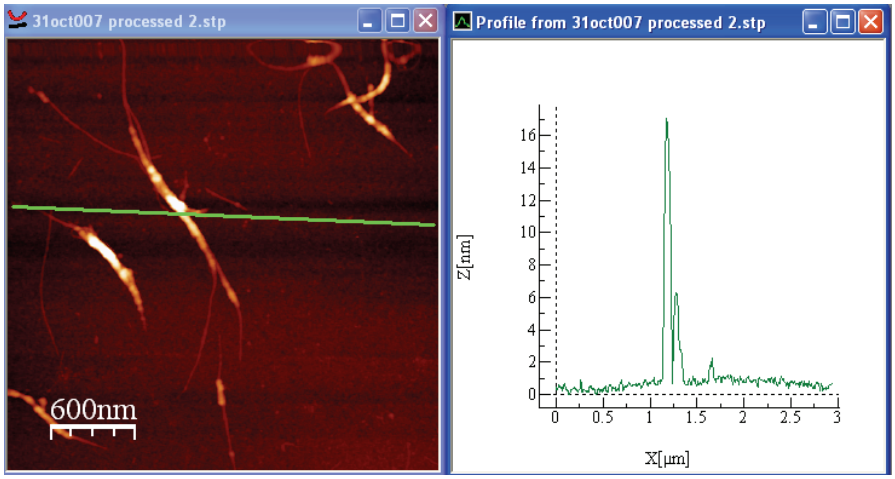

FIGURE 4.12(B), LEFT, SHOWS THE SECTION LINE THROUGH A POSSIBLE CARBON NANOTUBE FEATURE, **(C)**, RIGHT, SHOWS THE PROFILE OF THIS SECTION LINE.

The profile of the image to the left of centre in FIGURE 4.12(C) indicates that the feature has an approximate height of 18nm and a width of around 100nm. This is, as the images themselves suggest, much wider than the expected diameters of single walled carbon nanotubes. Journet *et al*[20], reported the dimensions of a bundle of single walled nanotubes as being between 10-20nm. This is clearly much less than the diameter observed with the sample investigated here. It has been asserted earlier that the larger width is due to a relatively heavy covering of the polymer, and not a result of bundling, and it is thought that the features seen here, with a thicker centre and narrower ends are single nanotubes, and not bundles. This indicates the effectiveness of the exfoliation process.

The tip was disengaged from the surface and another two different areas of the sample were scanned. The results from the second area are shown in FIGURE 4.13-FIGURE4.15, and the images of the third area are shown in FIGURE 4.16-FIGURE 4.18.

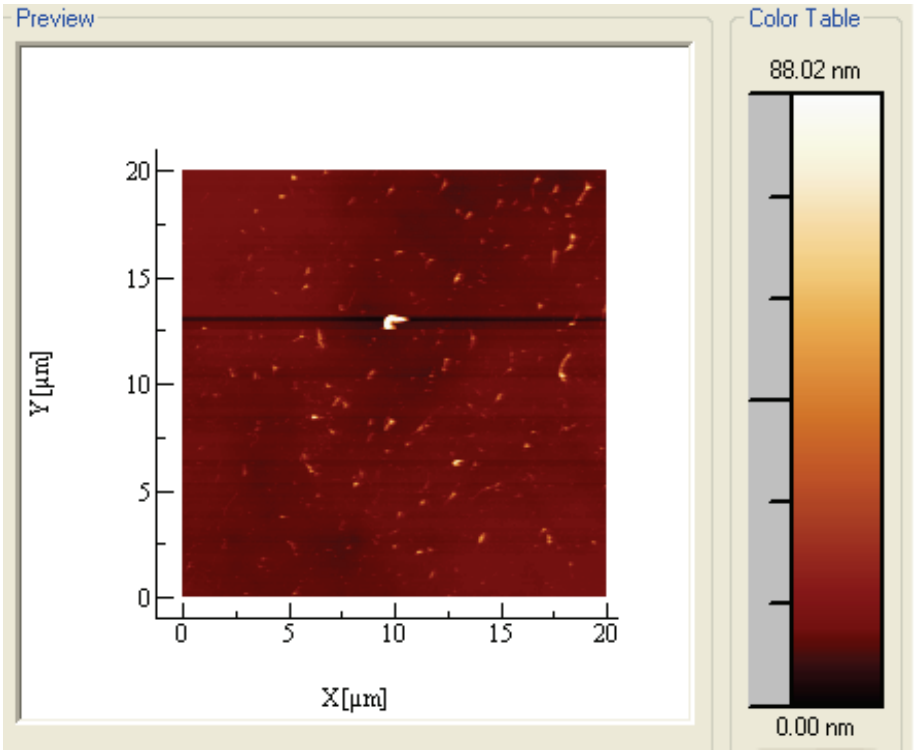

FIGURE 4.13: 20µm X 20µm AFM IMAGE OF SWNT / $[Ru(bpy)_2(PVP)_{10}Cl]Cl$ COMPOSITE DEPOSITED ON Si(100) SUBSTRATE.

FIGURE 4.13 shows the deposited composite on the surface, and again, as in FIGURE 4.10 hints at nanotube-like features. The process of imaging, and zooming in on a promising

area as shown in the previous images in this section was continued. A 9µm scan was performed on the upper right portion of the image in FIGURE 4.13. The resulting image in presented in FIGURE 4.14, below.

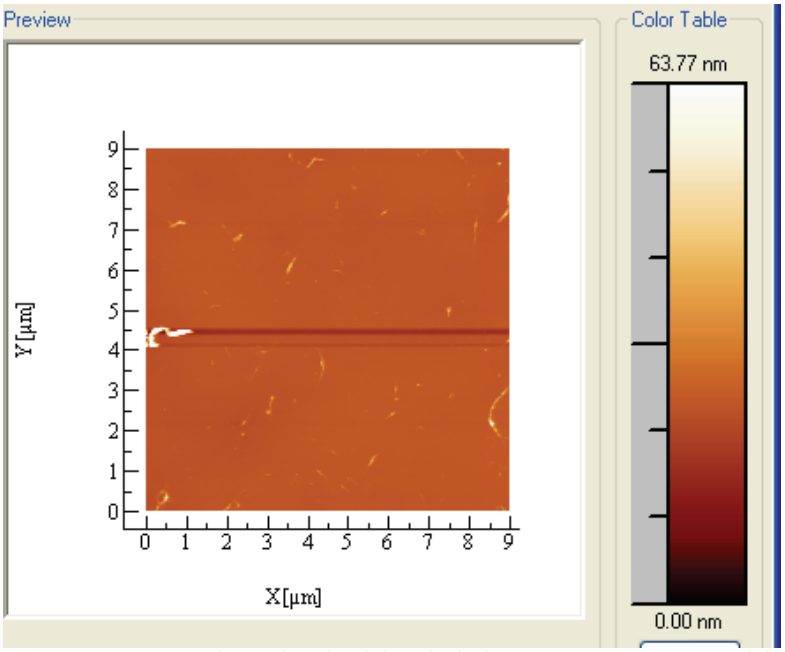

FIGURE 4.14: 9µm X 9µm AFM IMAGE OF SWNT / $[Ru(bpy)_2(PVP)_{10}Cl]Cl$ COMPOSITE DEPOSITED ON Si(100) SUBSTRATE.

The deposition in this area appears to be lighter than in the area shown in FIGURE 4.10-FIGURE 4.12, previously, (see above).

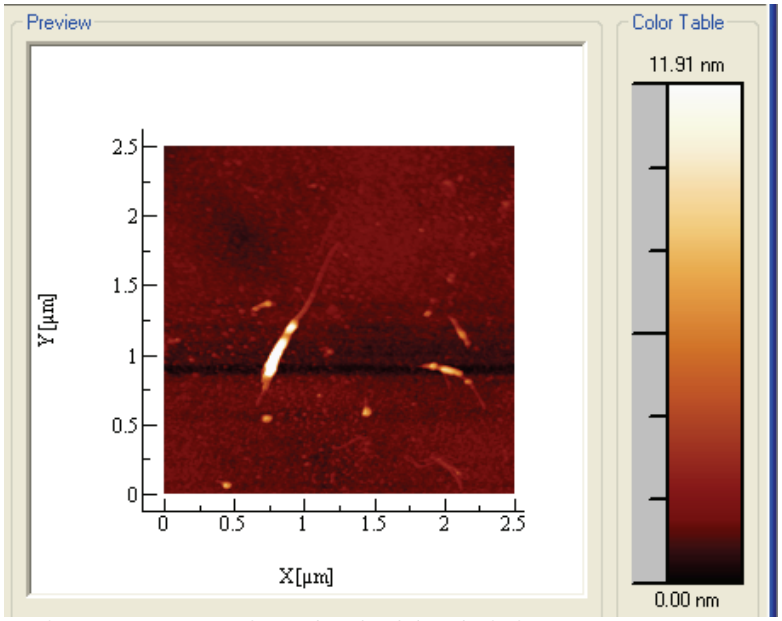

FIGURE 4.15: 2.5µm X 2.5µm AFM IMAGE OF SWNT / $[Ru(bpy)_2(PVP)_{10}Cl]Cl$ COMPOSITE DEPOSITED ON Si(100) SUBSTRATE.

FIGURE 4.15 shows what appears to be a single carbon nanotube, left of the centre of the image, with a polymer coating, again, most prevalent around the centre of the nanotube. The tip was again disengaged and a third area examined. The images obtained from this third area are presented in FIGURE 4.16 - FIGURE 4.18.

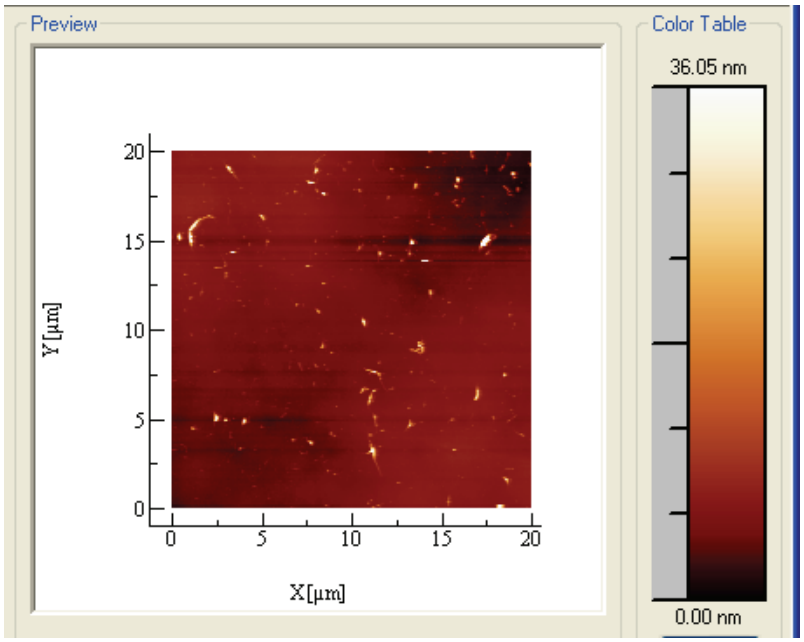

FIGURE 4.16: 20µm X 20µm AFM IMAGE OF SWNT / $[Ru(bpy)_2(PVP)_{10}Cl]Cl$ COMPOSITE DEPOSITED ON Si(100) SUBSTRATE.

FIGURE 4.16 shows a 20µm scan of the third area, again a relatively well dispersed deposition of nanotube-like features is observed. The area just below the centre of the image was then imaged, in an 8µm scan which is presented in FIGURE 4.17, on the next page. In the centre of the image, a number of features are observed and are considered to be carbon nanotubes, modified with polymer.Interestingly, on close inspection of the image, a number of narrower tube like features are seen, in particular one to the left of the centre, coordinates x = 3µm and y = 4µm. This indicates possibly that some of the nanotubes have not been as heavily modified with the ruthenium polymer as others, or potentially, some unmodified carbon nanotubes have been deposited along with the modified ones. This is unexpected, since the unmodified nanotubes should not strictly speaking have been dissolved in the solution. It is possible that they were suspended in

the solution, and were collected in the pipette, and deposited along with the rest of the solution.

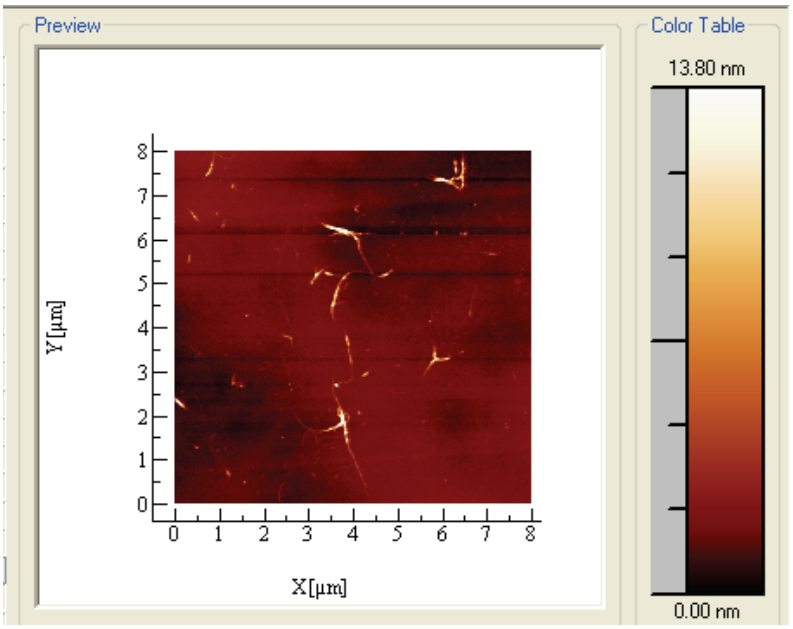

FIGURE 4.17: 8µM X 8µM AFM IMAGE OF SWNT / $[Ru(bpy)_2(PVP)_{10}Cl]Cl$ COMPOSITE DEPOSITED ON Si(100) SUBSTRATE.

The area just above the centre of the image in FIGURE 4.17 was imaged in a 4µm scan, and this is shown in FIGURE 4.18, below. A group of 2-3 nanotubes is observed in the top half of the image, along with single nanotubes in the centre and lower half of the image.

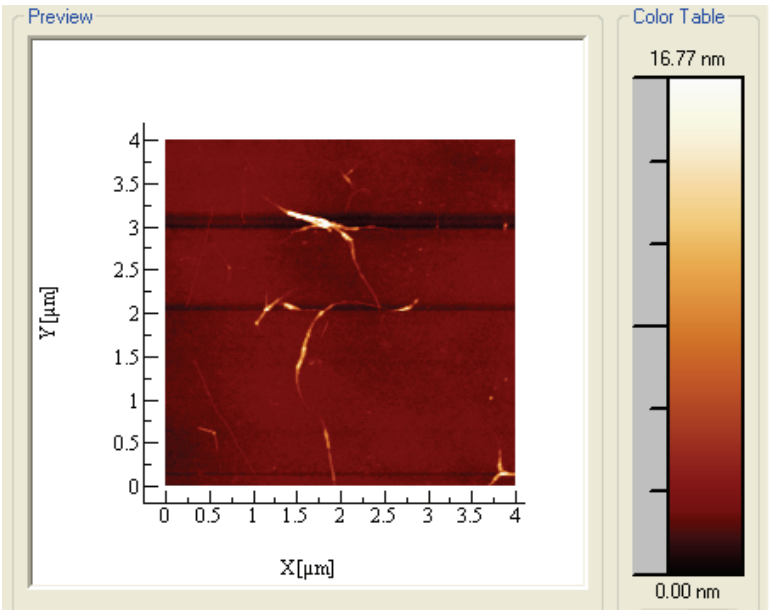

FIGURE 4.18: 4µm X 4µm AFM IMAGE OF SWNT / $[Ru(bpy)_2(PVP)_{10}Cl]Cl$ COMPOSITE DEPOSITED ON Si(100) SUBSTRATE.

This image in FIGURE 4.18 provides an opportunity to compare the dimensions of the larger nanotube features, shown centre and above centre, with the narrower nanotube – like features shown in the bottom left corner of the image. The results of this section analysis comparison are shown in FIGURE 4.19(A), (B), (C), and (D).

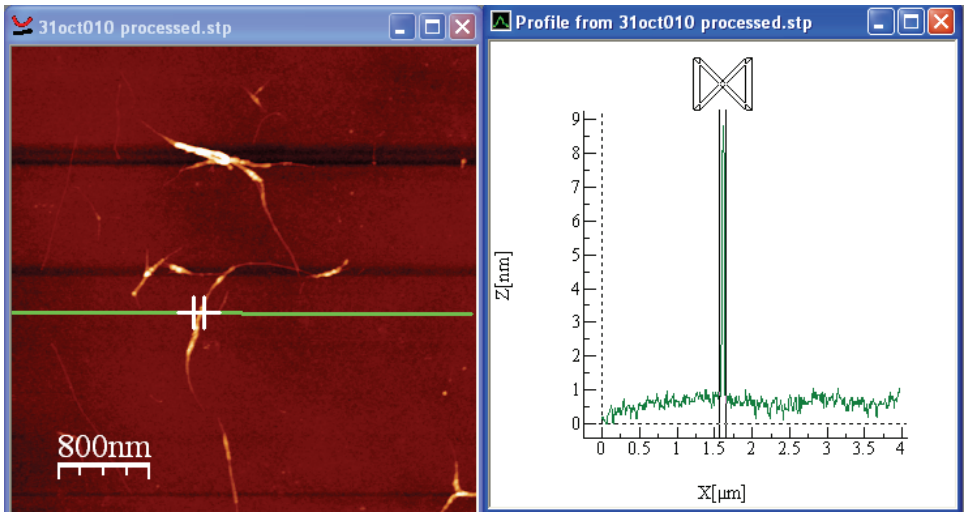

FIGURE 4.19(A), LEFT, SHOWS THE SECTION LINE THROUGH THE LARGER NANOTUBE FEATURE, AND **(B)**, RIGHT, SHOWS THE PROFILE OF THE FEATURE, WITH THE DIAMETER MEASURED. THE DIAMETER WAS ESTIMATED AS 89NM.

The diameter of the feature was estimated by the processing software as being approximately 90nm, again this is much higher than that of the unmodified nanotubes, measured by Journet *et al*[20], as discussed previously. It is also much wider than the diameter of the narrower nanotube like feature observed to the leftt of the centre of the image, the diameter of which was measured in FIGURE 4.19(C), and (D), below as being approximately 50nm.

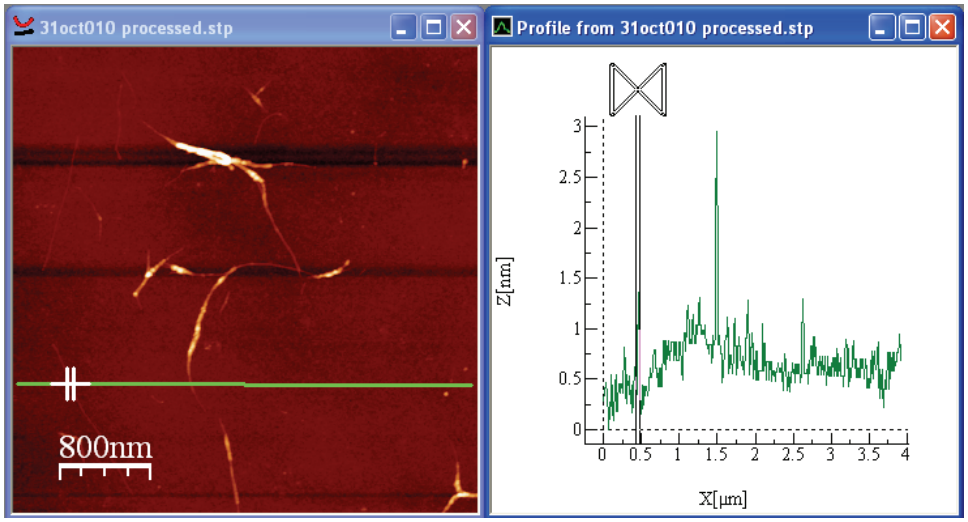

FIGURE 4.19(C), LEFT, SHOWS THE SECTION LINE THROUGH THE SMALLER NANOTUBE FEATURE, AND **(D)**, RIGHT, SHOWS THE PROFILE OF THE FEATURE, WITH THE DIAMETER MEASURED. THE DIAMETER WAS ESTIMATED AS 51NM.

As a final check, a bare silicon surface, cleaned by pirhana solution and left unmodified, i.e. no composite material deposited, was also imaged by AFM. The image obtained shows a relatively featureless surface, which is similar to the "background" of the images already presented. As seen by the colour table in FIGURE 4.20, the height of the surface is between 3-5nm.

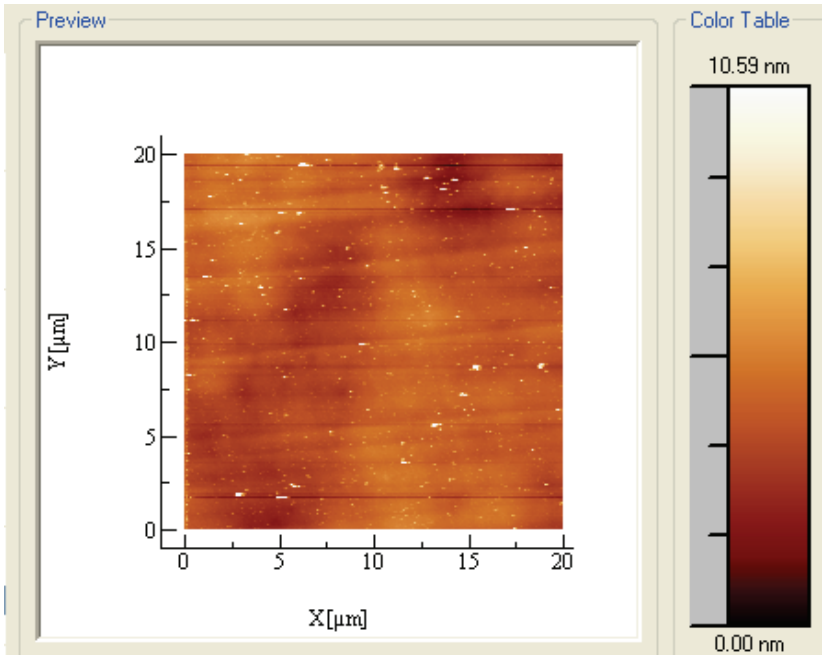

FIGURE 4.20: 20µm X 20µm AFM IMAGE OF A BARE SILICON SURFACE, CLEANED, WITHOUT COMPOSITE DEPOSITED.

4.3 Conclusions and Future Work

A ruthenium polymer has been used to exfoliate single walled carbon nanotubes in a methanol solution. This has been accomplished via the use of sonication, in order to debundle the carbon nanotubes and wrap them in the ruthenium polymer. The observation of van Hove singularities in the UV spectra of the composite solution during sonication is an indication of the occurrence of the exfoliation process, and the increase in intensity of the UV spectra with increasing sonication time, up to a certain length of time, (found to be generally 3-4 hours) is also an indication of the exfoliation process. The nanotubes do not appear to exfoliate upon sonication in the absence of the ruthenium polymer, the nanotubes are dispersed, but this suspension has been found to be unstable over even short timeframes of less than a few minutes in the absence of additional sonication. The nanotubes exfoliated with the polymer were drop cast on to a silicon substrate and analysed by Atomic Force Microscopy. The AFM images obtained appear to show single nanotubes covered in polymer, with very little free polymer present. The free polymer is seen as globular clusters, and these images will be presented in Chapter 5. The coverage of the nanotubes with the polymer is indicated by a marked difference in the diameters of the nanotube features observed, being much greater than bundles of nanotubes reported by other researchers. This is not thought to be an indication of bundling, since the coverage of the polymer is seen to be greatest around the centre portion of the nanotubes, with the nanotubes being narrower at the ends. This would be inconsistent with the idea of the nanotubes being in bundles. The diameters were measured by the AFM processing software, and indicate the average diameter to be around 90-100nm. Narrower nanotube-like features have been observed, and are thought to be either nanotubes modified with a thinner layer of polymer, or possibly unmodified nanotubes. At present, the former is thought to be the more probable.

4.4 Bibiliography

1 S. Iijima, T. Ichihashi, *Nature*, **1993**, *363*, 603-605

2 D. S. Bethune, C. H. Kiang, M. S. de Vries, G. Gorman, R. Savoy, J. Vasquez, R. Bayers, *Nature,* **1993**, *363*, 605-607

3 **(a)** H. Dai, A. Z. Rinzler, P. Nikolaev, A. Thess, D. T. Colbert, R. E. Smalley, *Chem. Phys. Lett.*, **1996**, *260*, 471-475, **(b)** Y. Saito, M. Okuda, T. Koyama, *Surf. Rev. Lett.*, **1996**, *3*, 863-864, **(c)** Y. Saito, K. Kawabata, M. Okuda, *J. Phys. Chem.,* **1995**, *99*, 16076-16079, **(d)** B. C. Satishkumar, A. Govindaraj, R. Sen, C. N. R. Rao, *Chem. Phys. Lett.*, **1998**, *293*, 47-52, **(e)** N. Grobert, *Mater. Today,* Jan/Feb **2007,** 28-35, **(f)** M. L. Terranova, V. Sessa, and M. Rossi, *Chem. Vap. Deposition*, **2006**, *12*, 315-325, **(g)** M. Terrones, A. Jorio, M. Endo, A. M. Rao, Y. A. Kim, T. Hayashi, H. Terrones, J.-C. Charlier, G. Dresselhaus, and M. S. Dresselhaus, *Materials Today,* Oct, **2004,** 22-45, **(h)** M. Terrones, *Annu. Rev. Mat. Res.,* **2003,** *33*, 419-501

4 H. Yonemura, Y. Yamamoto, S. Yamada, *Thin Solid Films*, **2008,** *516*, 2620-2625

5 S. Qin, D. Qin, W. T. Ford, J. E. Herrera, D. E. Resasco, *Macromolecules*, **2004**, *37*, 9963-9967

6 J. H. Rouse, P. T. Lillehei, J. Sanderson, E. J. Siochi, *Chem. Mat*, **2004**, *16*, 3904-3910

7 N. Grossiord, J. Loos, J. Meuldijk, O. Regev, H.E. Miltner, B. Van Mele, C.E. Koning, *Compos. Sci. and Technology*, **2007**, *67*, 778-782

8 N. Grossiord, O. Regev, J. Loos, J. Meuldijk, C. E. Koning, *Anal. Chem.*, **2005**, *77*, 5135-5139

9 V. A. Sinani, M. K. Gheith, A. A. Yaroslavov, A. A. Rakhnyanskaya, K. Sun, A. A. Mamedov, J. P. Wicksted, N. A. Kotov, *J. Am. Chem. Soc.*, **2005**, *127*, 3463-3472

10 L. Jiang, Lian Gao, J. Sun, *J. Colloid and Interface Science*, **2003**, *260*, 89-94

11 F. Frehill, M. in het Panhuis, N. A. Young, W. Henry, J. Hjelm, J. G. Vos, *J. Phys. Chem. B*, **2005**, *109*, 13205-13209

12 D. Tasis, N. Tagmatarchis, A. Bianco, M. Prato, *Chem. Rev.*, **2006**, *106*, 1105-1136

13 V. N. Popov, *Mat. Sci. & Engineering R*, **2004**, *43*, 61-102

14 S. Reich, C. Thomsen, J. Maultzsch, *Carbon Nanotubes - Basic Concepts and Physical Properties*, Wiley VCH, Germany, **2004**

15 B. McCarthy, J. N. Coleman, R. Czerw, A. B. Dalton, M. in het Panhuis, A. Maiti, A. Drury, P. Bernier, J. B. Nagy, B. Lahr, H. J. Byrne, D. L. Carroll, and W. J. Blau, *J. Phys. Chem. B,* **2002** *106* p2210-2216

16 C. A. Dyke, J. M. Tour, *Nano Lett*., **2003** *3,* p1215-1218

17 C.-H. Xue, M.-M. Shi, Q.-X. Yan, Z. Shao, Y. Gao, G. Wu, X.-B. Zhang, Y. Yang, H.-Z. Chen, M. Wang, *Nanotechnology*, **2008**, *19*, 115605-115611

18 M. J. O'Connell, S. M. Bachilo, C. B. Huffman, V. C. Moore, M. S. Strano, E. H. Haroz, K. L. Rialon, P. J. Boul, W. H. Noon, C. Kittrell, J. Ma, R. H. Hauge, R. B. Weisman, R. E. Smalley, *Science*, **2002**, *297*, 593-596

19 S. Berciaud, L. Cognet, P. Poulin, R. B. Weisman, B. Lounis, *Nano Lett.*, **2007**, *7*, 1203-1207

20 C. Journet, W. K. Maser, P. Bernier, A. Loiseau, M. Lamyde la Chapelle, S. Lefrant, P. Deniard, R. Leek, J. E. Fischerk, *Nature*, **1997**, *388*, 756-758

Chapter 5 Composite Systems Of Multi Walled Carbon Nanotubes (MWCNT's) With Metal Complex-Based Polymers

Chapter 5 is a logical continuation of the work presented in Chapter 4, and deals with two other types of carbon nanotubes. Both are multi-walled nanotubes (MWNT's), one type however, has amino functionalities on the walls, and is referred to as MWNT-NH_2, while the other type are unmodified carbon nanotubes, and this type will be referred to from this point as MWNT. The work carried out this system is the same as that which was done for the SWNT's in Chapter 4.

The aim of the work was to investigate if the different types of nanotubes were exfoliated more or less efficiently than the SWNT's, and to find the optimum conditions of exfoliation, for the concentration range studied.

As in Chapter 4, the primary tool for the investigation of the exfoliation process is UV-vis spectroscopy. UV-vis data will be presented and interpreted, and comparisons will be made to similar data reported in the literature, where possible. The work presented in this and the preceding chapter represent a significant step in the understanding of the exfoliation of carbon nanotubes using a ruthenium metallopolymer, a system which, as seen in Chapter 1, has not been as thoroughly investigated as other systems employing "standard", non metal – based polymers, such as P4VP, SDS or PmPV.

5.0 Introduction

The work discussed in this chapter mirrors the work in the previous chapter. It utilizes two different types of nanotubes, and these are compared in terms of ease of exfoliation, both in the presence of the ruthenium polymer and on their own in methanol. Again, various ratios of Ru polymer to nanotubes have been investigated, as described in TABLE 4.1, in the previous chapter. The ruthenium polymer used in this work is the same as that shown in FIGURE 4.1. Since the discovery of Multi-Walled Carbon Nanotubes was reported in 1991 by Iijima[1], this type of system has attracted intense interest, such as electrical properties[2,4], general preparation, purification and morphology[3], spectroscopic properties[5], and use in composite systems with non metal – based polymers[6], metallopolymers and metal complexes[7], much like its sister molecule, the single walled nanotube. Hua *et al*[6(a)] used MWNT's as a filler material in an epoxy resin in order to investigate the electrical and conductivity properties of this nanocomposite material, while Kim and Jo[6(b)] grafted a co-polymer, P3HT/PMMA onto MWNT's. It was found that the PMMA/MWNT composite was well dispersed in chloroform after sonication. This has important implications for the work in this chapter and in chapter 4, since sonication is the method used in this work to exfoliate the nanotubes, and/or to form the composites. Multi Walled Nanotubes have also been modified with amino groups by various research groups[8], and will be denoted in this chapter from this point as MWNT-NH_2. In ref [8(a)], UV data is presented for MWNT-NH_2 dispersed in methanol, and this provides an opportunity to compare the results presented in this chapter for this system with those reported by Shen *et al*[8(a)]. It is important to note that one of the primary UV features for single walled nanotubes, van Hove singularities, do not usually appear in UV spectra of semiconducting MWNT's. This is considered to be due to the intershell coupling, as this is thought to result in non radiative decay via vibrational manifolds due to the nearby metallic nanotubes[9]. They have however been observed experimentally by Brennan and co-workers[9], along with photoluminescence from the van Hove states. Choi *et al*[7(a)] have reported a composite system consisting of MWNT modified with $Ru(bpy)_3^{2+}$ in a sol gel titania and Nafion thin film. Electrochemiluminescence was reported in the system, however no absorbance data was reported. A similar system was

also investigated by Lin and Chen[7(f)]. Frehill and co-workers[7(b)] reported a very similar system to that discussed in this chapter, MWNT-NH_2 covalently modified with a ruthenium complex, ($[Ru(bpy)_2(dcbpy)](PF_6)_2$), shown in FIGURE 3.13. Emission data was reported and wavelength shifts were observed between the ruthenium complex on its own, and the composite Ru complex/MWNT-NH_2 system. Shifts were also observed in the absorbance spectra of the ruthenium complex/NT composite, relative to the parent ruthenium complex. AFM data of this composite system deposited on glass was also reported, and it was observed that "aggregates" of the ruthenium complex served as an interconnect between two or more nanotubes. Lee and Yoo[7(c)] investigated the absorption properties of MWNT's modified with $[Ru(dcbpy)_2(NCS)_2]2H_2O$. Again, this was a covalent modification and it was inferred from the absorption studies that the coverage of ruthenium on the nanotubes was less than full, due to the low concentration of the ruthenium solution used.Tao *et al*[7(d)] used PSS, (polyp-styrenesulfonate) to "wrap" around MWNT's, which were then immobilized in a silane based thin film, and further modified by $[Ru(bpy)_3^{2+}]$. It was reported that this ruthenium complex has a strong interaction with the nanotubes. This is attributed to the strong π-π interaction between the π orbitals of the bipyridine ligands and those of the carbon lattice in the nanotubes. Again, as in the system investigated by Choi *et al*[7(a)], electrochemiluminescence was observed from the ruthenium complex, and the nanotubes were thought to increase the amount of ruthenium complex absorbed in the film, and also played an important role in the conduction properties of the system. It was found that sample preparation, and the amounts of PSS and ruthenium complex used were critical in the standardizing the performance of each device. A very interesting system was described by Hwang and co workers[7(e)], in which a hexameric ruthenium complex was complexed with carboxylate modified MWNT's, via sonication and reflux methods. The ruthenium complex used was $[\{1,3\text{-bis}(2,2':6,2''\text{-terpyridin-4-ylethynyl})\text{-5-tert-butylbenzene}\}_6Ru_6(PF_6)_{12}]$. UV-vis measurements were carried out, but were not reported in this contribution.
AFM was also reported by Jang *et al*[13], on MWNT's, described as "bamboo shaped". The images appear to show nanotube like structures, the diameters of which were estimated to be of the order of 500nm. These results contrast sharply with those obtained by Phang and co workers[11], which found MWNT's modified with PA6 polymer to be

much narrower, estimated to be on average 33nm. These results show the variations in diameters obtained in different systems, employing different polymers.

5.0.1 Aims of Chapter

The aim of the work in this chapter is the same as that in the previous chapter. The system is changed slightly, in that different nanotubes are used, but the investigation of the exfoliation process and the morphology of deposited, exfoliated nanotube/polymer composites on a solid substrate is still the goal of this work. As observed in the introduction to this chapter, there has been little work done dealing with these systems and such investigative methods, as AFM and absorbance spectroscopy of composites. This makes this work somewhat novel, however it also provides little opportunity to compare results with established literature, and therefore it is sometimes difficult to make definitive conclusions, as much is still to be investigated. However, the work in this chapter and in Chapter 4 mark a significant attempt to understand the processes involved and the photophysical properties of these novel nanocomposite materials. The experimental setup and procedures are the same as those discussed in Section 4.1. In some cases but not all, a UV measurement was carried out 7 days after the original experiment to investigate the stability of the solution over time.

5.1 Experimental

The experimental procedures used in this chapter are the same as those used in Chapter 4, and have been discussed in section 4.1.

5.2 Results and Discussion

5.2.1UV Analysis of Exfoliation of Multi Walled Nanotubes in Methanol

It was expected that the absence of ruthenium polymer would mean that less nanotubes would be successfully exfoliated in the methanol solution. Therefore, it was decided to use only 1mg of the MWNT sample in the experiment. The results of the exfoliation process are shown in FIGURES 5.1(A) and (B), on the next page.

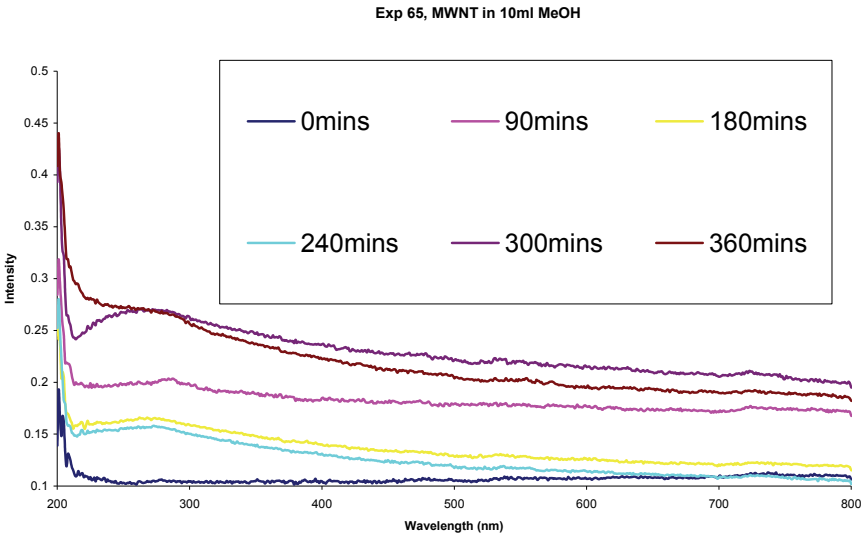

FIGURE 5.1(A): EXP 65, UV OF **MWNT (1MG) IN 10ML MEOH**, 0-360MINS SONICATION. **UV SAMPLE (IN EACH CASE): 100µL OF SAMPLE +1000µL OF MEOH.**

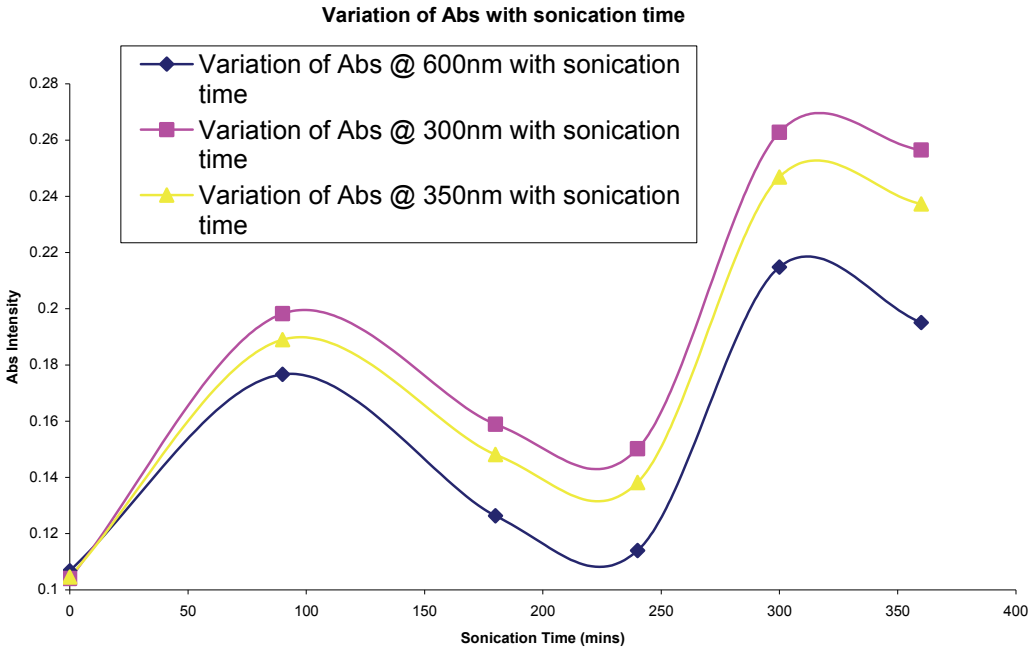

FIGURE 5.1(B): VARIATION OF ABS @300NM, 350NM AND 600NM WITH SONICATION TIME (MINS), 0-360MINS.

The traces do not seem to follow any pattern, and it is likely that the NT's did not dissolve or exfoliate, a conclusion supported by the observation during the experiment that the solution did not "ink", and the NT bundles broke up slightly, but remained at the bottom of the solution, or in the solution as a fine suspension, which may account for the high baseline observed initially. Since this is a difficult result to interpret unambiguously, it was decided to repeat the experiment. The results of this repeated experiment are shown in FIGURES 5.2(A) and (B), below.

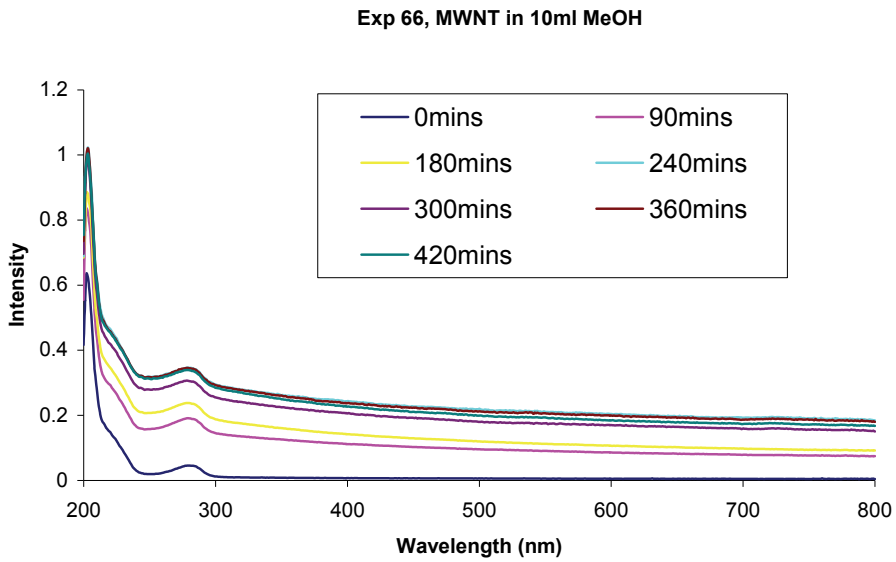

FIGURE 5.2(A): EXP66, UV OF **1MG OF MWNT IN 10ML MEOH**, SONICATED FOR 360MINS. **UV SAMPLE (IN EACH CASE): 100µL OF SAMPLE + 1000µL MEOH.**

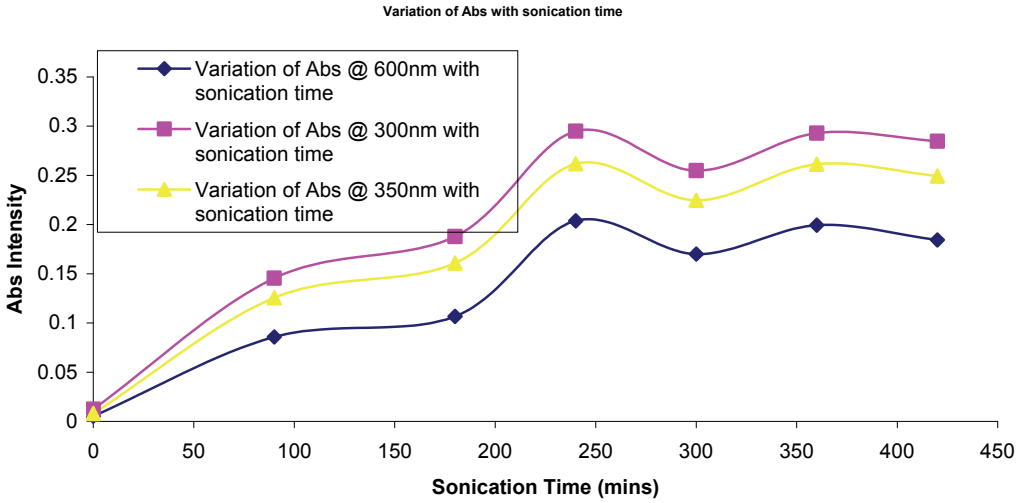

FIGURE 5.2(B): VARIATION OF ABS INTENSITY @ 300NM, 350NM, AND 600NM WITH SONICATION TIME (MINS). IT IS DIFFICULT TO SAY IF THE MAXIMUM IS AT 240MINS, THE SOLUTION APPEARED DARKER IN COLOUR COMPARED WITH THE PREVIOUS EXPERIMENT, (EXP 65), BUT THE ABSORBANCE INTENSITY APPEARS TO BE REASONABLY SIMILAR.

There is no clear plateau in the intensity across the range, and so it is difficult to ascertain the extext of exfoliation. It does appear to be quite difficult to exfoliate the multiwalled nanotubes, in the absence of the ruthenium polymer, however the solution appears to be reasonably stable, as judged by visual inspection, the suspension did not

fall to the bottom to the of the sample tube. It was not clear, however, if inking of the solution occurred.

5.2.2 UV Analysis of Exfoliation of Multi Walled Nanotubes in Methanol Using $[Ru(bpy)_2(PVP)_{10}Cl]Cl$

Further to the experiments in the previous section, the next logical step was to introduce the ruthenium polymer into the system, and as in the experiments discussed in Chapter 4, it was decided to use low concentrations of the polymer initially, and the amount would be varied as appropriate in subsequent experiments. FIGURES 5.3(A-C), below show the results of the exfoliation experiment, with Multi Walled Nanotubes. Once again, the Ru polymer has been denoted as $Ru(PVP)_{10}$.

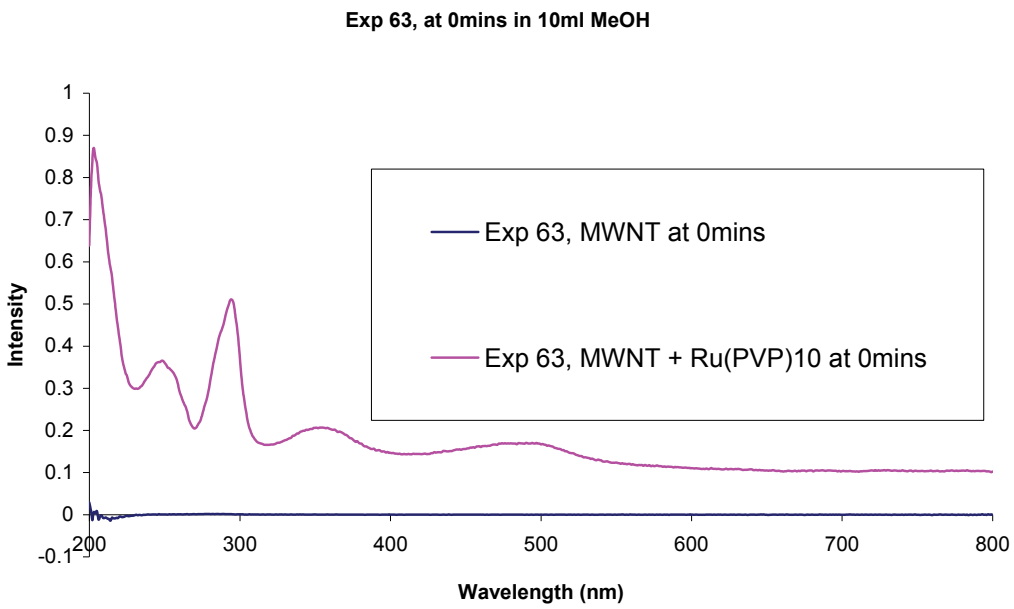

FIGURE 5.3(A): EXP63, UV OF **MWNT (1MG) IN 10ML MEOH** COMPARED WITH UV OF **MWNT (1MG) + $[Ru(bpy)_2(PVP)_{10}Cl]Cl$ (1MG) IN 10ML MEOH**, AT 0MINS. **UV SAMPLE (IN EACH CASE): 100µL SAMPLE + 1000µL MEOH.**

The solution was then sonicated, and the progression of the exfoliation is shown in FIGURE 5.2(B). The inset shows a comparison of the UV of the solution prior to sonication with that of the solution after sonication. It is noted that there are no obvious VHS present, this is somewhat expected, the reasoning for this has been discussed previously by Brennan *et al*[9].

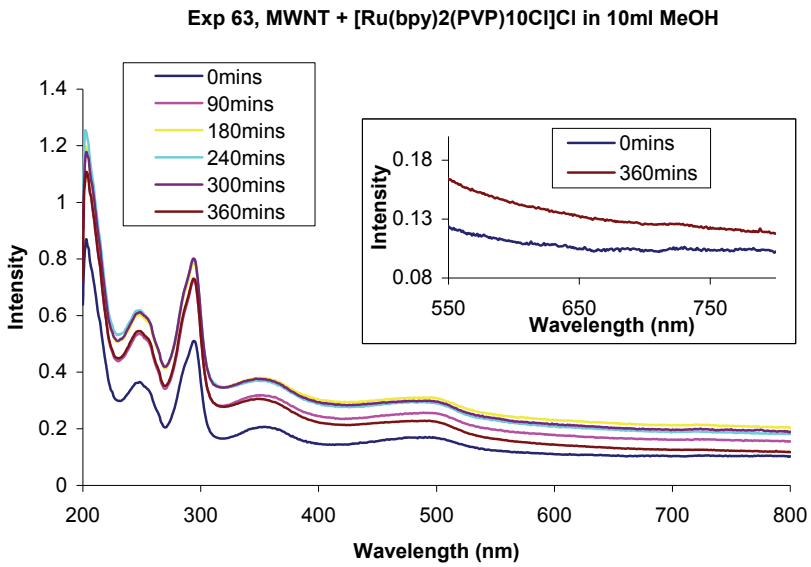

FIGURE 5.3(B): EXP63, UV OF **MWNT (1MG) + [RU(BPY)$_2$(PVP)$_{10}$CL]CL (1MG) IN 10ML MEOH** AT 0-360MINS. **UV SAMPLE (IN EACH CASE): 100µL SAMPLE + 1000µL MEOH.** INSET SHOWS CLOSE UP OF REGION 550NM-800NM.

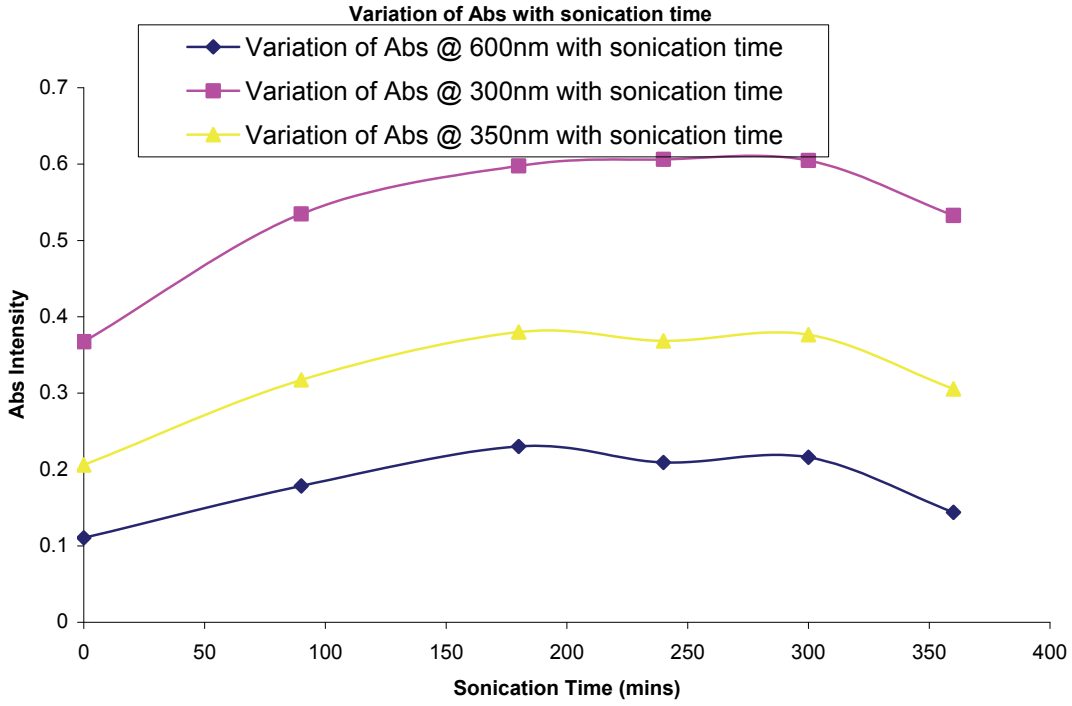

FIGURE 5.3(C): VARIATION OF ABS @ 300NM, 350NM, AND 600NM WITH SONICATION TIME (MINS). THE PROCESS APPEARS TO REACH A PLATEAU AFTER APPROXIMATELY 180MINS-240MINS.

FIGURE 5.3(C), on the previous page shows the variation of the absorbance with sonication time, and appears to show that the process reaches a maximum exfoliation after approximately 3-4 hours. This is a result which will be compared with the exfoliation times of not only other ratios of MWNT's to polymer, but also to other NT-polymer systems utilizing different NT types.

The experiment was repeated, and the results obtained are shown in FIGURES 5.4(A-C), below and on the following page.

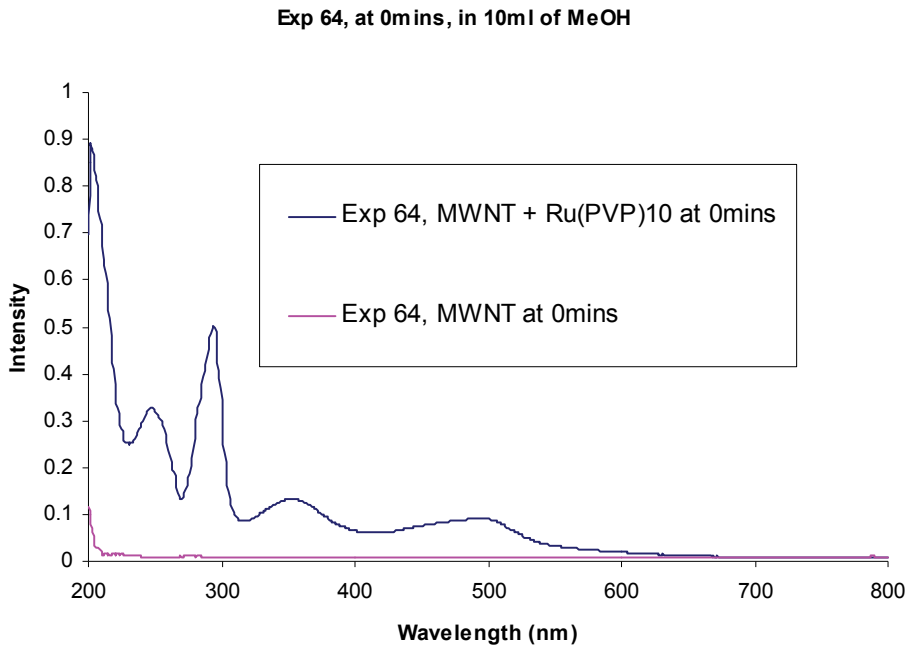

FIGURE 5.4(A): EXP 64, UV OF **MWNT (1MG) IN 10ML MEOH** COMPARED WITH UV OF **MWNT (1MG) + $[Ru(bpy)_2(PVP)_{10}Cl]Cl$ (1MG) IN 10ML MEOH**, AT 0MINS. **UV SAMPLE (IN EACH CASE): 100µL SAMPLE + 1000µL MEOH.**

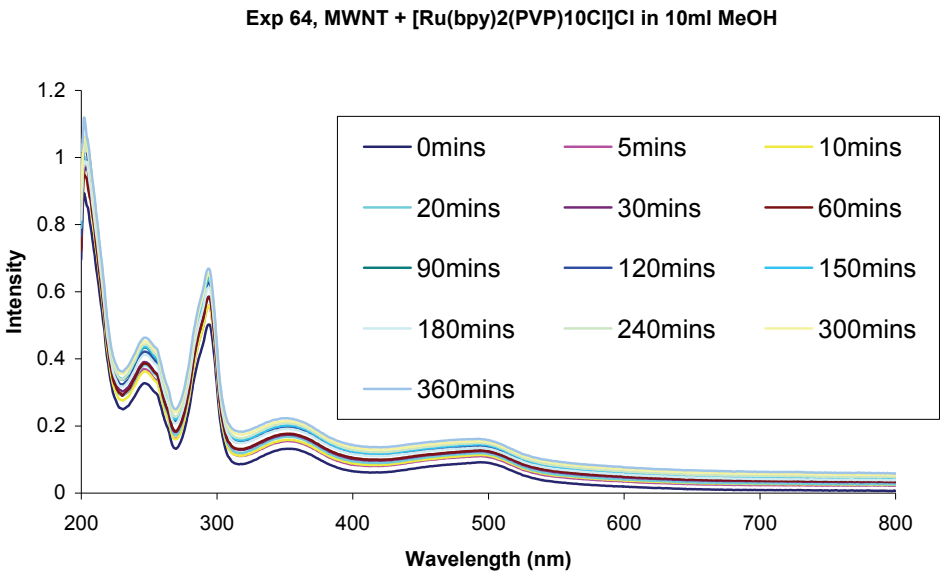

FIGURE 5.4(B): EXP64, UV OF **MWNT (1MG) + [RU(BPY)$_2$(PVP)$_{10}$CL]CL (1MG) IN 10ML MEOH** AT 0-360MINS. **UV SAMPLE (IN EACH CASE): 100µL SAMPLE + 1000µL MEOH.**

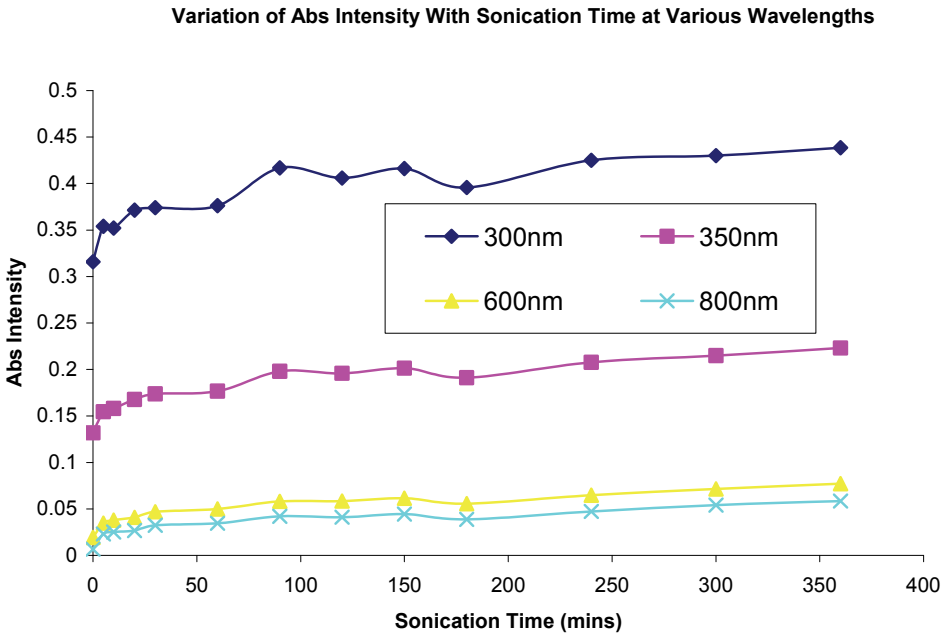

FIGURE 5.4(C): VARIATION OF ABS @ 300NM, 350NM, AND 600NM WITH SONICATION TIME (MINS). IT IS VERY DIFFICULT TO DEFINE WHETHER THE PROCESS HAS PEAKED AT ANY STAGE, OR IF ANY APPRECIABLE EXFOLIATION HAS OCCURRED.

As can be seen in FIGURE 5.4(C), above, it is difficult to establish to what extent exfoliation occurred, as there is only a very small, perhaps even negligible, increase in the absorbance, not only for the four wavelengths chosen, but across the wavelength range as a whole.

FIGURE 5.4(C) is quite similar to FIGURE 5.3(C), and it may be that the frequent interruptions of the sonication process adversely affect the exfoliation, however the difference between the two sets of UV spectra is small in terms of Absorbance changes and intensity.

It was therefore decided to increase the amount of ruthenium polymer in the solution. This was expected to increase the amount of exfoliated nanotubes. The results of this experiment are shown in FIGURES 5.5(A-C), below and on the following page.

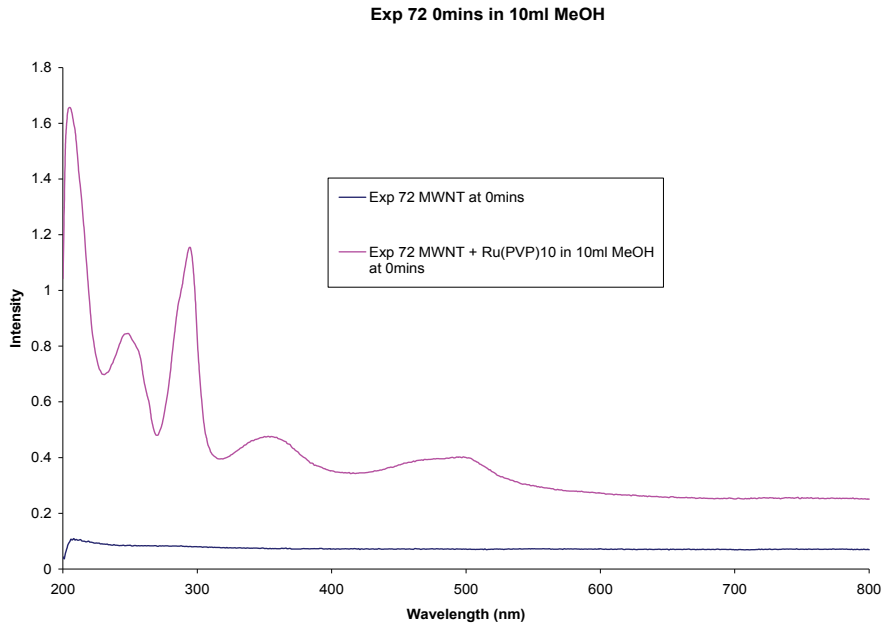

FIGURE 5.5(A): EXP 72, UV OF **MWNT (1MG) IN 10ML MEOH**, COMPARED WITH UV OF **MWNT (1MG) + [RU(BPY)$_2$(PVP)$_{10}$CL]CL (2MG) IN 10ML MEOH**, BOTH AT 0MINS (NO SONICATION). **UV SAMPLE (IN EACH CASE): 100µL SAMPLE + 1000µL MEOH.**

It is observed that the baseline of the initial, 0min trace for the mixture of the ruthenium polymer and the nanotubes is approximately 0.2. This is due either to an instrumentation issue, or may be due to scattering as a result of nanotubes suspended in the solution, after the initial agitation of the solution by the addition of the polymer. FIGURE 5.5(B) shows the progression of the UV spectrum of the exfoliating solution as it was sonicated.

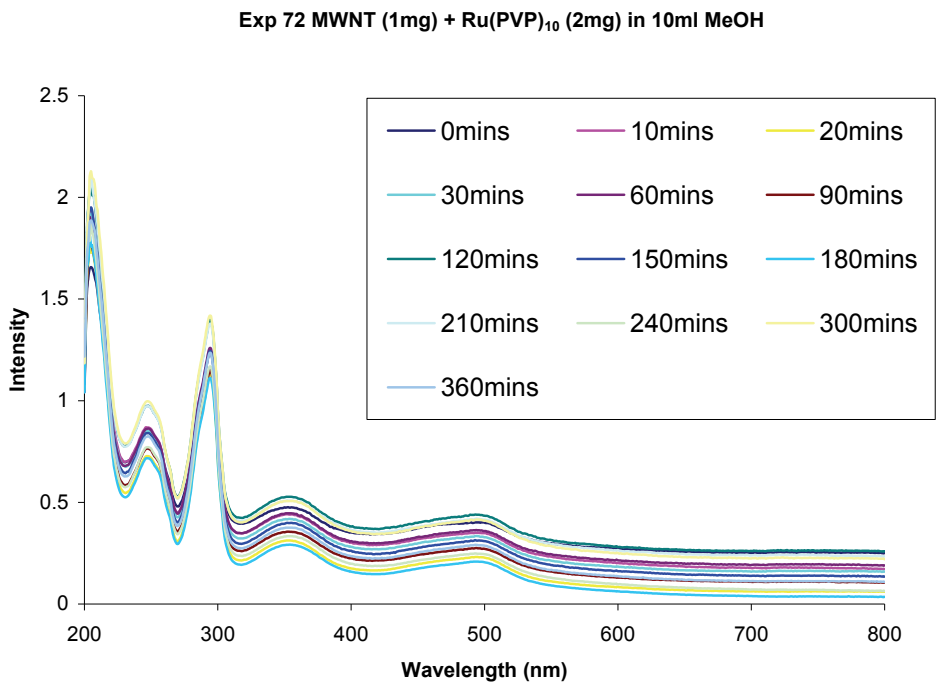

FIGURE 5.5(B): EXP 72, UV OF **MWNT (1MG) + [RU(BPY)$_2$(PVP)$_{10}$CL]CL (2MG) IN 10ML MEOH**, THROUGHOUT 360MINS OF SONICATION WITH SONIC TIP. **UV SAMPLE (IN EACH CASE): 100µL SAMPLE + 1000µL MEOH.**

Again, in FIGURE 5.5(B) it is seen that the VHS seen in SWNT's are not observed in MWNT's. They are not expected, however it can be said that some exfoliation has occurred, given the increase in absorption across the wavelength range. It isclear therefore, that the VHS cannot be used to ascertain the occurrence of exfoliation in the system. Increases in absorption have to be used to determine the occurrence of exfoliation, and this is not as definitive a method as the observance of the van Hove Singularities, as used for the SWNT experiments discussed in the previous chapter. A plot illustration the relationship between sonication time and UV intensity at various wavelengths, at various times is shown in FIGURE 5.5(C), on the next page.

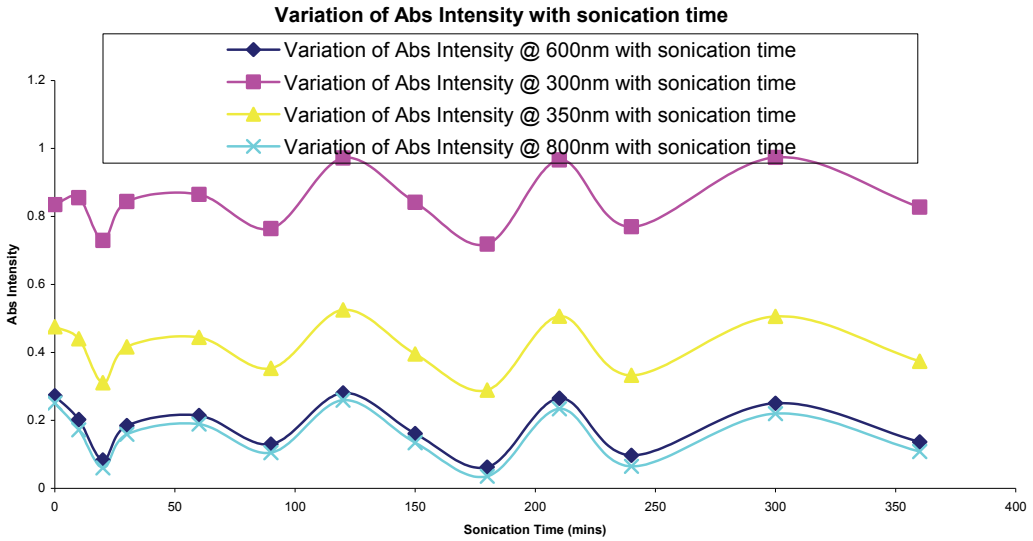

FIGURE 5.5(C): VARIATION PLOT FOR THE ABSORBANCE DATA VS SONICATION TIME AT VARIOUS WAVELENGTHS, IT IS CLEAR THAT NO EXFOLIATION HAS OCCURRED, SINCE THE VALUES FOR 800NM AND 600NM DON'T SEEM TO HAVE INCREASED APPRECIABLY THROUGHOUT THE 360MINS.

It appears from this data that the Multi Walled Nanotubes are quite difficult to exfoliate, since very little change is seen in the absorbance values shown in FIGURE 5.5(C). However, this may be due to the experimental conditions, the frequent stopping of the sonication, in order to perform a UV measurement may have adversely affected the process.Other data for a repeat of this experiment have shown that using longer sonication times, and less UV measurements shows a more consistent picture, with a plateau in the UV intensity occurring after around 3-5hours of sonication.
It was decided to increase the ratio of polymer to MWNT's, and the results obtained from this experiment are shown in FIGURES 5.6(A-C).

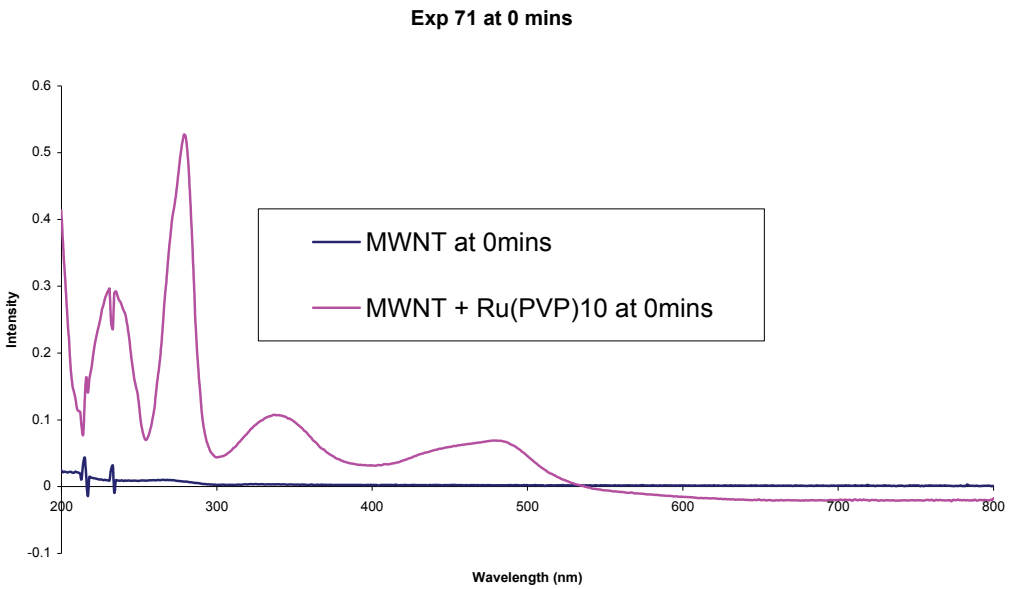

FIGURE 5.6(A): EXP 71, UV OF **1MG OF MWNT IN 10ML MEOH** AT 0MINS, COMPARED WITH UV OF **1MG OF MWNT + 3MG OF [RU(BPY)$_2$(PVP)$_{10}$CL]CL IN 10ML MEOH** AT 0MINS. **UV SOLUTION IN EACH CASE: 100µL OF SAMPLE + 1000µL OF MEOH.**

Again, as in the previous experiments, the carbon nanotube solution at time 0mins, in the absence of polymer shows little or no absorption, consistent with the idea that the nanotubes are not in solution at this stage in the process.

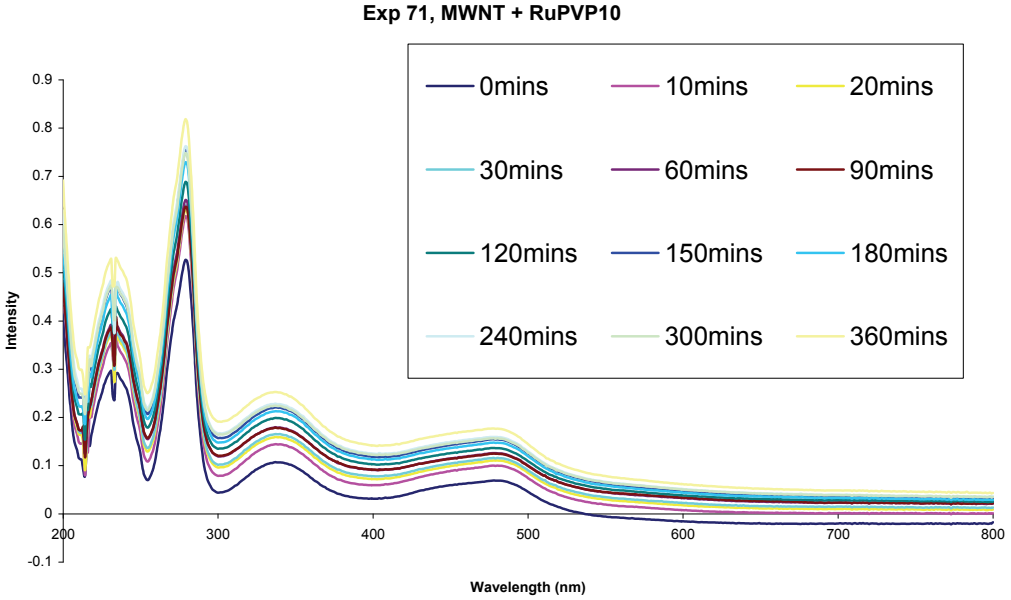

FIGURE 5.6(B): 7 NOVEMBER 2007, EXP 71, UV OF **1MG OF MWNT + 3MG OF [RU(BPY)$_2$(PVP)$_{10}$CL]CL IN 10ML MEOH** DURING 360MINS OF SONICATION. **UV SOLUTION IN EACH CASE: 100µL OF SAMPLE + 1000µL OF MEOH.**

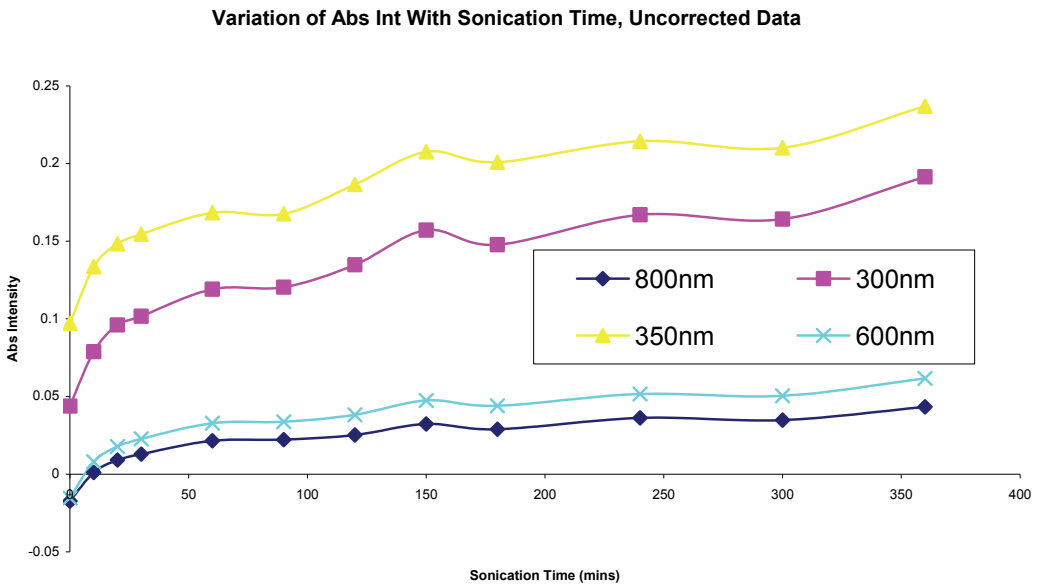

FIGURE 5.6(C): VARIATION OF ABS INTENSITY @ 300, 350, 600 AND 800NM WITH SONICATION TIME.

It appears from FIGURE 5.6(C), above, that the increase in ruthenium polymer has resulted in a better exfoliation than was obtained in FIGURE 5.5(C), however it is not clear if the exfoliation process is complete, given the relatively low intensites observed. The intensities across the various wavelengths plotted are still increasing and therefore it is possible that further sonication of this system would have resulted in more exfoliation. The experiment has been repeated and similar results have been obtained. However, in general, it can be concluded that, at least in methanol, the unfunctionalized multiwalled nanotubes are quite difficult to exfoliate without long, uninterrupted periods of sonication in the presence of the ruthenium polymer.

5.2.3 UV Analysis of Exfoliation of Amino Functionalized Multi Walled Nanotubes in Methanol Without $[Ru(bpy)_2(PVP)_{10}Cl]Cl$

As a comparison to the system discussed in the above section, another type of nanotubes were investigated, these were also MWNT's, however these were functionalized with amino groups. As before, the NT's were exfoliated in Methanol in the absence of the ruthenium polymer. The results of this exfoliation experiment are presented in FIGURES 5.7(A-B), on the following pages.

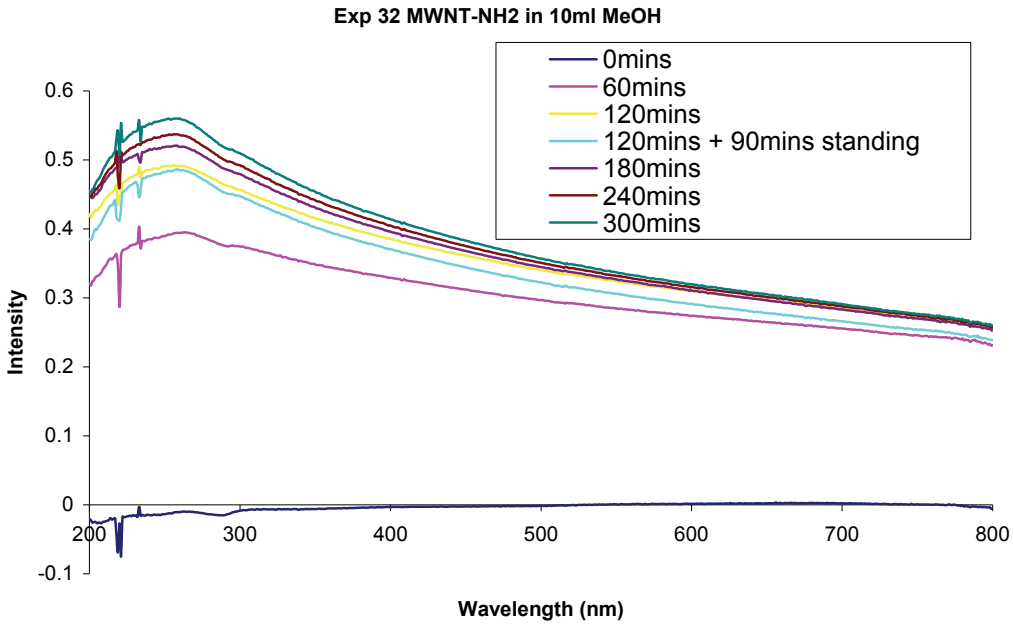

FIGURE 5.7(A): EXP 32, **MWNT-NH_2 (1MG) IN 10ML MEOH**, WITH NO RUTHENIUM POLYMER PRESENT. IT APPEARS THAT AT LEAST SOME OF THE NT'S WERE SOLUBILIZED BY THE SONICATION. **UV SOLUTION IN EACH CASE: 100µL OF SAMPLE + 1000µL OF MEOH.**

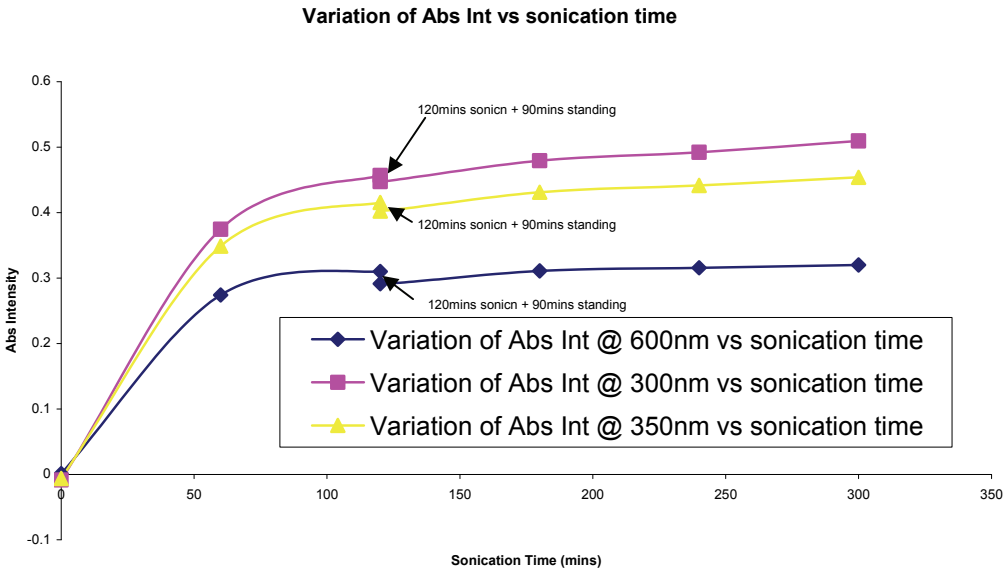

FIGURE 5.7(B): VARIATION OF ABS INT @ 600NM, 300NM AND 350NM WITH INCREASING SONICATION TIME.

In FIGURE 5.7(B), above, it appears that a reasonable increase in the absorbance has occurred and this indicates that exfoliation has occurred, and the fact that no increase is observed after approximately 100 minutes of sonication indicates that a plateau has been

reached in the exfoliation process. The experiment was repeated and an even greater increase in absorbance across the entire wavelength range was observed than was seen in FIGURE 5.7(B). This indicates that the amino-funtionalized MWNT's can be exfoliated in methanol in the absence of the ruthenium polymer. The stability of the solution in the repeat experiment is shown in FIGURE 5.7(C).

FIGURE 5.7(C) shows that the solution is reasonably stable over a period of a few days, and this is in contrast to what was seen for the exfoliation of the MWNT's in methanol. These latter solutions were shown to be unstable after the sonication process. However the amino functionalized MWNT's are reasonably stable in solution and the increase in absorbance with sonication indicates that exfoliation is indeed occurring. There appears to be a shift in the λ_{max} of the main peak in the spectra, at around 270nm, from the spectrum of the original solution, after sonication, and the spectrum of the solution, after standing for 2 days, without any further sonication. This is most likely an instrumentation issue.

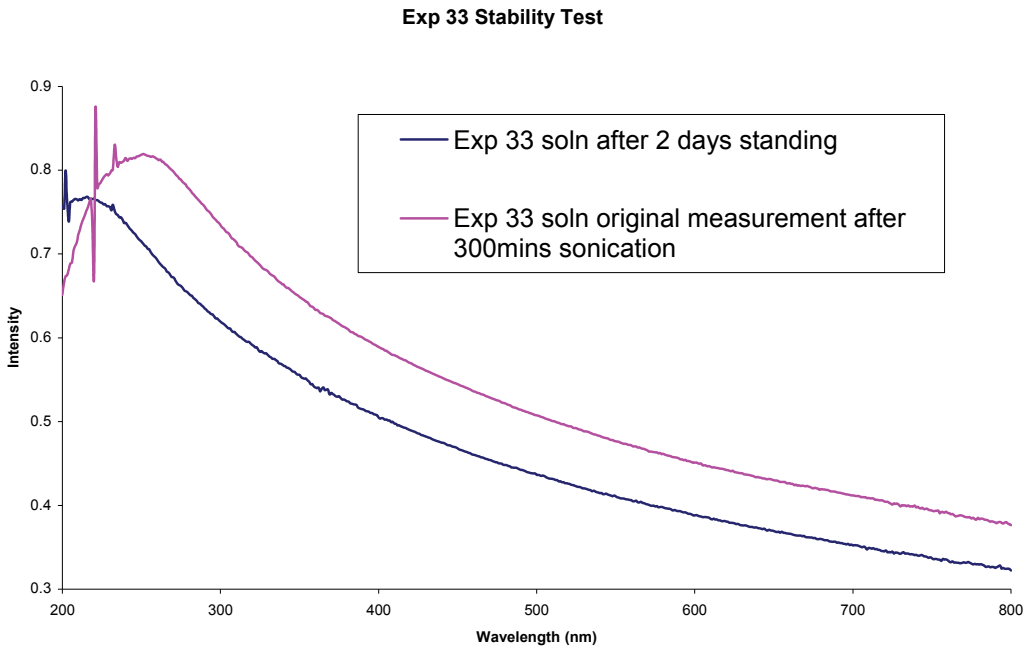

FIGURE 5.7(C): EXP 33 STABILITY TEST, SOLUTION IS THE SAME COMPOSITION AS SHOWN IN FIGURES 5.7(A-B). **UV SAMPLE: 100µL OF SAMPLE + 1000µL OF MEOH.**

The peak seen as the dominant feature in the spectra has been observed for the SWNT's in methanol, without ruthenium polymer, in Chapter 4, and also by Grossiord *et al*[10], for SWNT's. It is seen that the intensity of the UV-vis trace for the sample after standing is slightly higher than that of the trace for the sample immediately after cessation of sonication, this is most likey due to a small error in sample preparation, while aliquots were transferred via autopipette, the possibly remains for suspended nanotubes that may have been incompletely wrapped to be transferred into the cuvette, and cause scattering of the incident light.

5.2.4 UV Analysis of Exfoliation of Amino Functionalized Multi Walled Nanotubes in Methanol Using $[Ru(bpy)_2(PVP)_{10}Cl]Cl$

In addition to the work done on the exfoliation of the MWNT-NH_2 in Methanol, it was decided to add the ruthenium polymer into the system, in order to see whether it improved the exfoliation process or not. As before, with the multiwalled nanotube experiments, it was decided initially to use small amounts of the polymer, and in order to make comparisons between this system and those previous studied in this work, it was decided to initially use the same 1mg : 1mg ratio of NT:Ru polymer. The results of this initial experiment are shown in FIGURES 5.8(A-D).

The UV-vis spectrum of the solution immediately after the addition of the ruthenium polymer to the carbon nanotubes *prior* to sonication is compared with that of the solution containing only the nanotubes, again prior to sonication is presented in FIGURE 5.8(A).

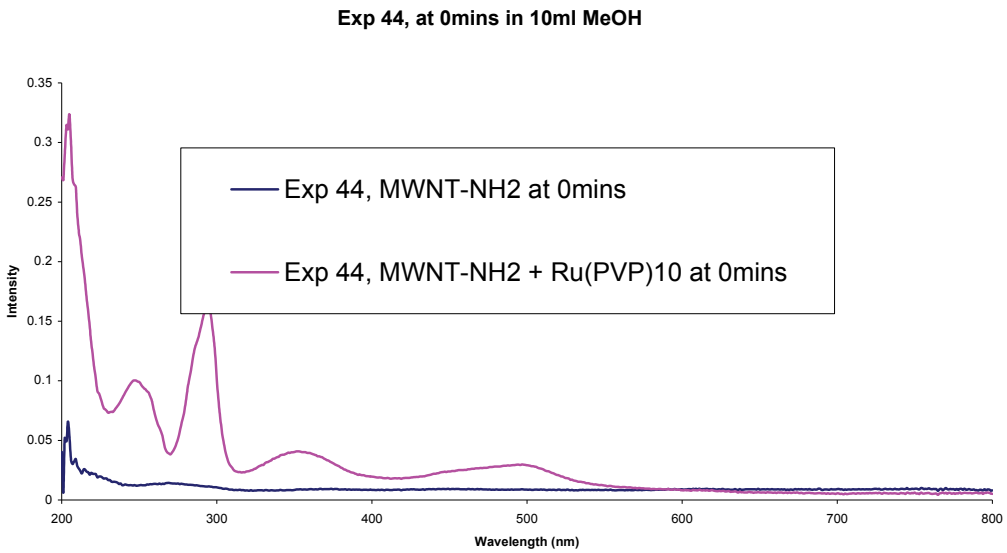

FIGURE 5.8(A): EXP 44, UV OF **1MG MWNT-NH_2 IN 10ML MEOH** AT 0MINS, COMPARED WITH UV OF **1MG SWNT + 1MG OF [RU(BPY)$_2$(PVP)$_{10}$CL]CL IN 10ML MEOH** AT 0MINS. **UV SOLUTION IN EACH CASE: 100µL OF SAMPLE + 1000µL OF MEOH.**

As seen with the ruthenium polymer / MWNT composites, a number of peaks are visible in the UV-vis spectrum of the initial solution. These are all attributed to the ruthenium polymer, indicating that the carbon nanotubes have not been solubilized at this point, prior to sonication. The peak at around 290nm is a Ligand Centred (LC) transition, while the two peaks observed around 350nm and 490nm are both ^{1}MLCT based transitions[7(g)], characteristic of ruthenium complexes. The solution was sonicated and UV measurements taken of the solution at well defined time intervals, and the progression of the exfoliation is shown in FIGURE 5.8(B).

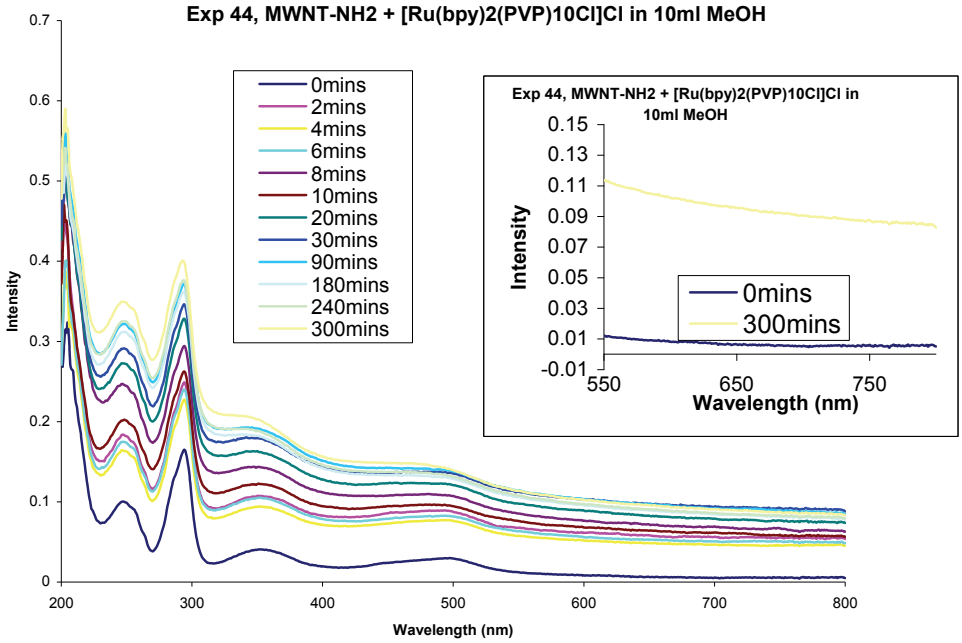

FIGURE 5.8(B): EXP44, **1MG MWNT-NH_2 + 1MG OF [RU(BPY)$_2$(PVP)$_{10}$CL]CL IN 10ML MEOH,** SONICATED WITH OUR OWN SONIC TIP. **UV SAMPLE: 100µL OF SAMPLE + 1000µL OF MEOH.** INSET SHOWS CLOSE UP OF REGION 550NM-800NM

Again, it is seen that the VHS are not visible in the UV-vis spectrum after 300mins, however an increase in absorption is observed after sonication. It is believed that exfoliation has occurred, given the increase, and also the solution had darkened in colour significantly after sonication. This is in contrast to the solutions of MWNT's without ruthenium polymer, and also the experiments using the SWNT's in the absence of the ruthenium polymer, where it is thought that a dispersion only of the nanotubes resulted from the sonication. Further information regarding the extent of the exfoliation is given in FIGURE 5.8(C), where a plateau is seen in the variation of the absorbance intensity with sonication. This indicates that the maximum "allowable" amount of nanotubes have been exfoliated, with this concentration of polymer.

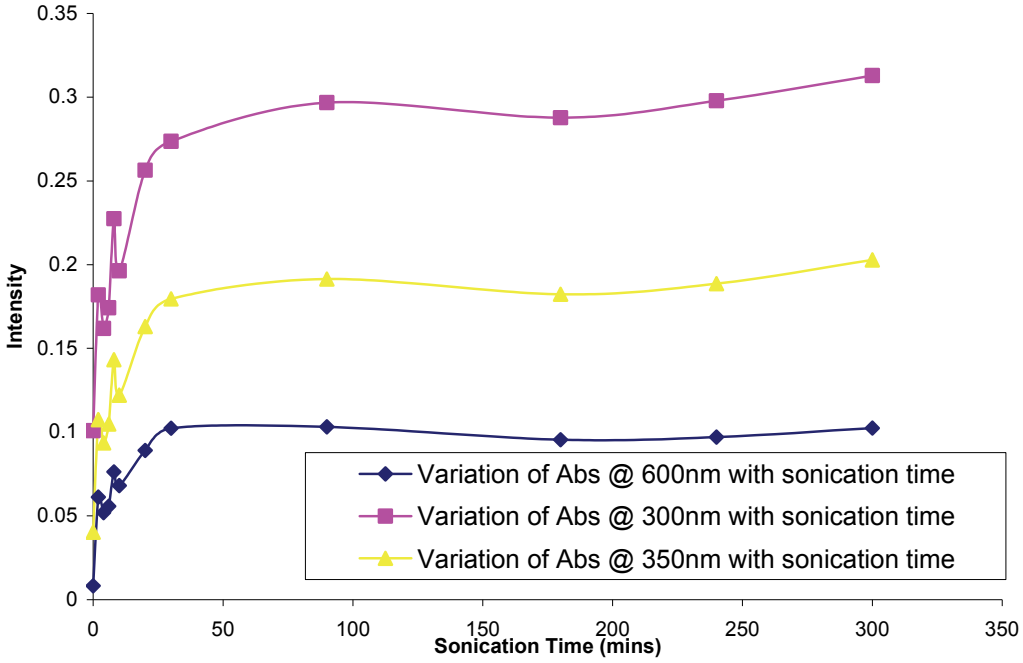

FIGURE 5.8(C): VARIATION OF ABSORBANCE INTENSITY MEASURED AT 600NM, 300NM AND 350NM VS SONICATION TIME.

The peak in intensity appears to occur after a longer period of sonication than expected, it is thought that the regular start-stop of the sonication process at the beginning of the experiment is responsible. Therefore it may be that energy delivered is more important than the time, and that a constant delivery of sonication energy is needed for an efficient exfoliation process. It is seen that the values are less consistent in the first 10mins than they are in the duplicate experiment. This indicates that the constant interruption of the sonication process is adversely affecting the exfoliation. In addition, the increased UV measurements result in more of the parent solution being used, which given the small volume used (10ml) can have an affect on the exfoliation, due to a reduced solvent volume. The stability of the solution over time was also measured and this is shown in the spectra in FIGURE 5.8(D), below.

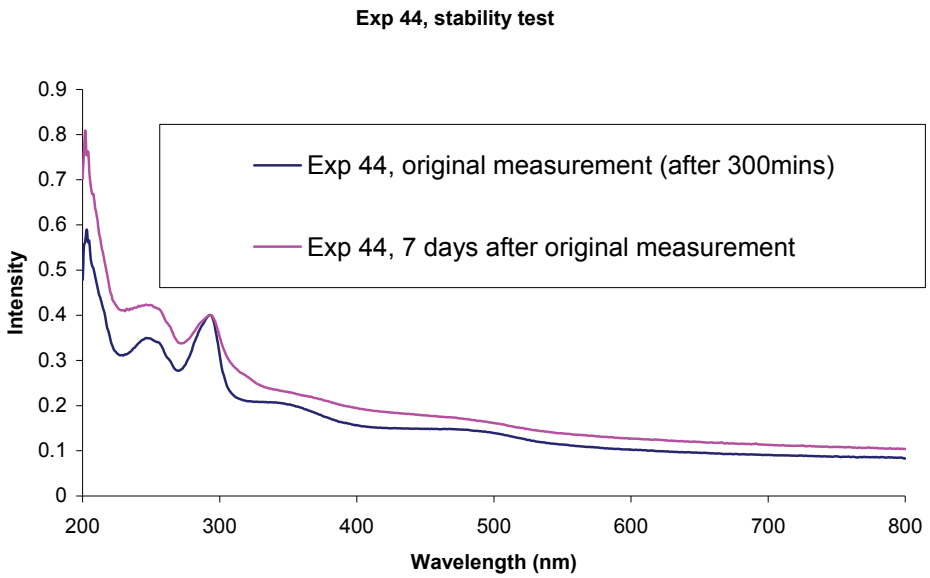

FIGURE 5.8(D): EXP 44 SOLN, COMPARISON OF THE UV SPECTRUM FOR THE ORIGINAL MEASUREMENT (AFTER 300MINS OF SONICATION) WITH THE UV SPECTRUM OF THE SOLN AFTER BEING ALLOWED TO STAND FOR 1 WEEK. **UV SAMPLE: 100µL OF SAMPLE + 1000µL OF MEOH.**

It was decided to increase the polymer concentration first, the aim of this was to try and ensure maximum exfoliation of the nanotubes in the solution. The results of this investigation are shown in FIGURES 5.9(A-C), on the following pages.

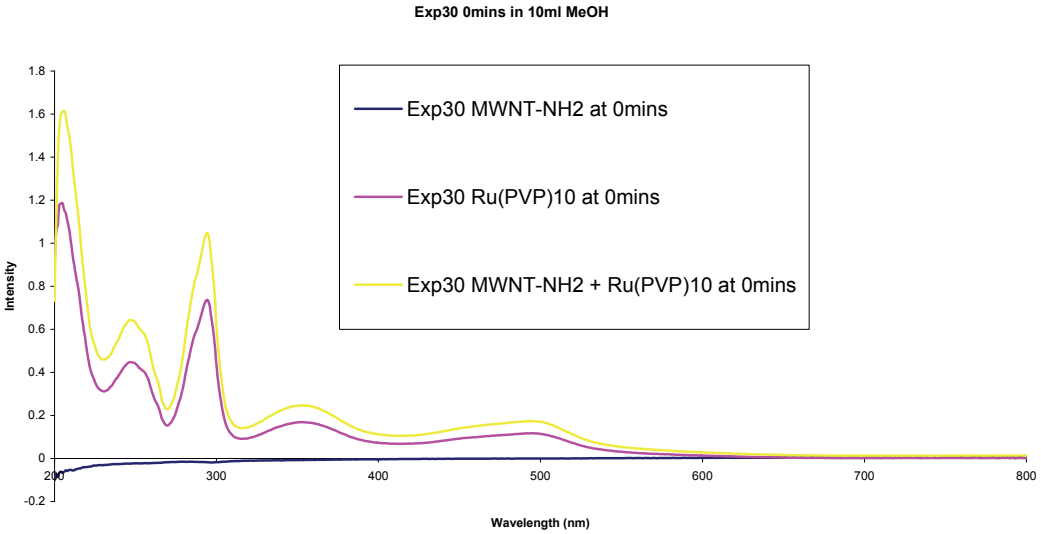

FIGURE 5.9(A): EXP 30, **MWNT-NH_2 (1MG) IN 10ML MEOH**, COMPARED WITH **[RU(BPY)$_2$(PVP)$_{10}$CL]CL (2.5MG) IN 10ML MEOH**, AND **MWNT-NH_2 (1MG) + [RU(BPY)$_2$(PVP)$_{10}$CL]CL (2.5MG) IN 10ML MEOH. UV SAMPLE: 100µL OF SAMPLE + 1000µL OF MEOH.**

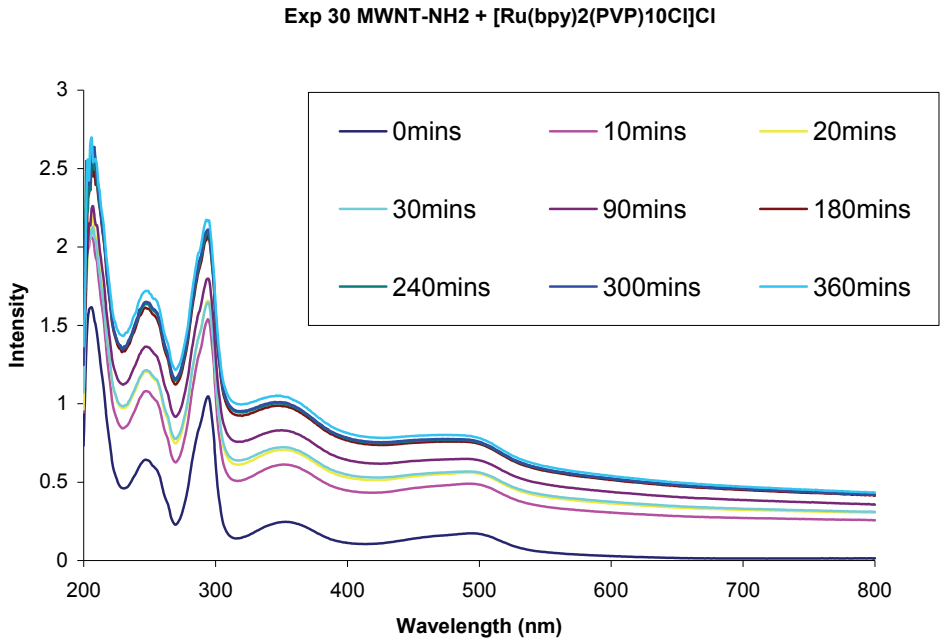

FIGURE 5.9(B): EXP 30, **MWNT-NH_2 (1MG) + [RU(BPY)$_2$(PVP)$_{10}$CL]CL (2.5MG) IN 10ML MEOH,** SONICATED WITH OUR SONIC TIP. **UV OF SAMPLE: 100µL OF SOLUTION + 1000µL MEOH.**

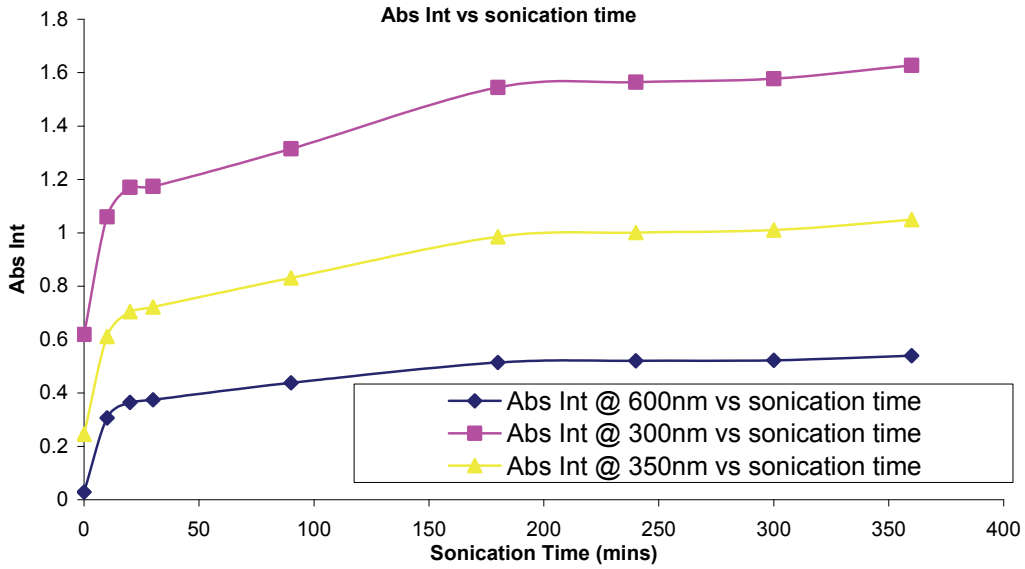

FIGURE 5.9(C): VARIATION IN ABSORBANCE INTENSITY AT 600NM, 300NM, AND 350NM VS INCREASING SONICATION TIME.

It is seen that the intensity of the UV-vis absorption is higher in this experiment (FIGURE 5.9(B)) that in the spectra shown in FIGURE 5.8(B). This is an indication that the exfoliation

has occurred to a greater extent. This is consistent with the fact that a higher polymer concentration was used. The plateau again appears in FIGURE 5.9(C) at around 90mins. The ratio of nanotubes to ruthenium polymer has always been such that the ruthenium polymer has been present in greater amounts by weight, in the 10ml solution of MeOH. In this next experiment, 2mg of MWNT-NH_2 were exfoliated using 1mg of the ruthenium polymer. The results of this experiment are shown in FIGURES 5.10(A-C).

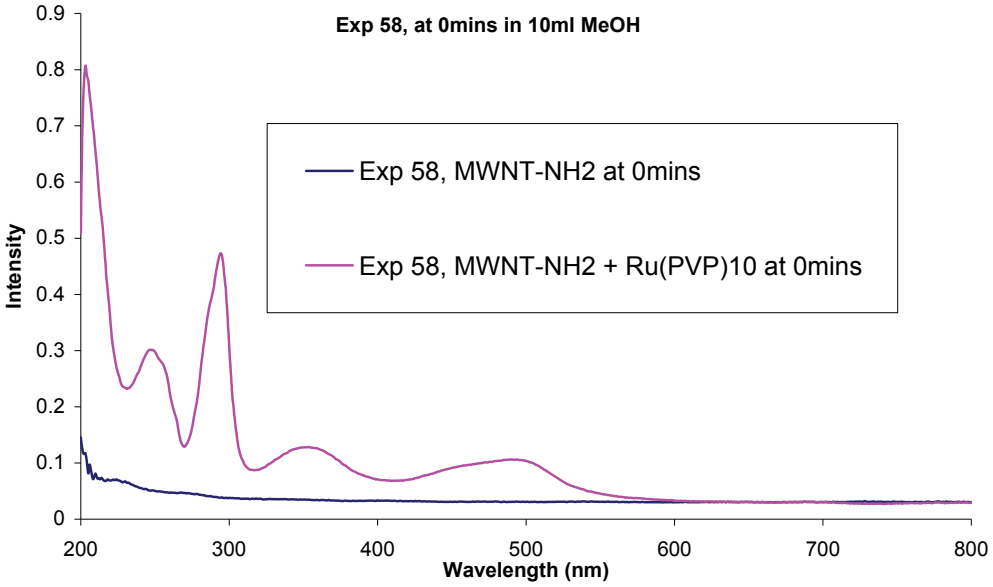

FIGURE 5.10(A): EXP 58, UV OF **MWNT-NH_2 (2MG) IN 10ML MEOH** AT 0MINS, COMPARED WITH UV OF **MWNT-NH_2 (2MG) + [RU(BPY)$_2$(PVP)$_{10}$CL]CL (1MG) IN 10ML MEOH** AT 0MINS. **UV OF SAMPLE: 100µL OF SOLUTION + 1000µL MEOH.**

In FIGURE 5.10(B) it is seen again that the absorption increases with sonication. Another observation which has been observed in other exfoliation experiments using the ruthenium polymer is the change in peak shape, particularly the MLCT at 350nm. This change in peak shape, and change in the relative intensities of the two MLCT peaks has been observed before by Frehill *et al*[7(g)]. The system investigated in that contribution was SWNT-based. A minor difference is seen in the 350nm peak in ref [7(g)] relative to that observed here. The peak seen in the data presented in this chapter shows a more pronounced tail on the high energy bandedge. This may possibly be attributed to the differences in electronic structure between MWNT-NH_2 used in this work and the SWNT's used by Frehill *et al*[7(g)]. In addition, the amino functionalizations will affect the binding between the nanotubes and the polymer. This has been seen in the exfoliation experiments presented in this chapter, and the previous chapter. This would result in a

more pronounced affect on the ruthenium polymer electronic structure, however more detailed investigations would need to be performed to elucidate this affect.

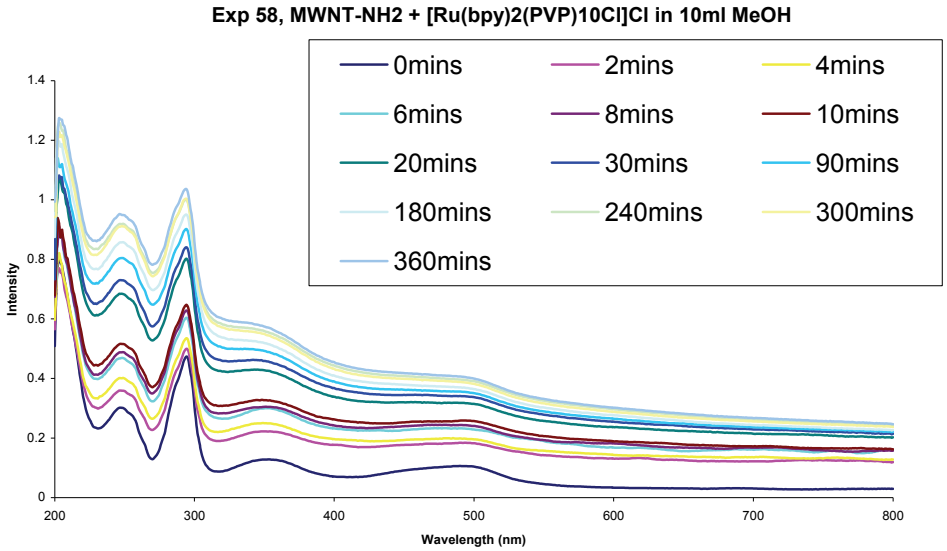

FIGURE 5.10(B): EXP 58, UV OF **MWNT-NH_2 (2MG) + [RU(BPY)$_2$(PVP)$_{10}$CL]CL (1MG) IN 10ML MEOH** THROUGHOUT 360MINS OF SONICATION. **UV SAMPLE (IN EACH CASE): 100µL OF SAMPLE + 1000µL OF MEOH.**

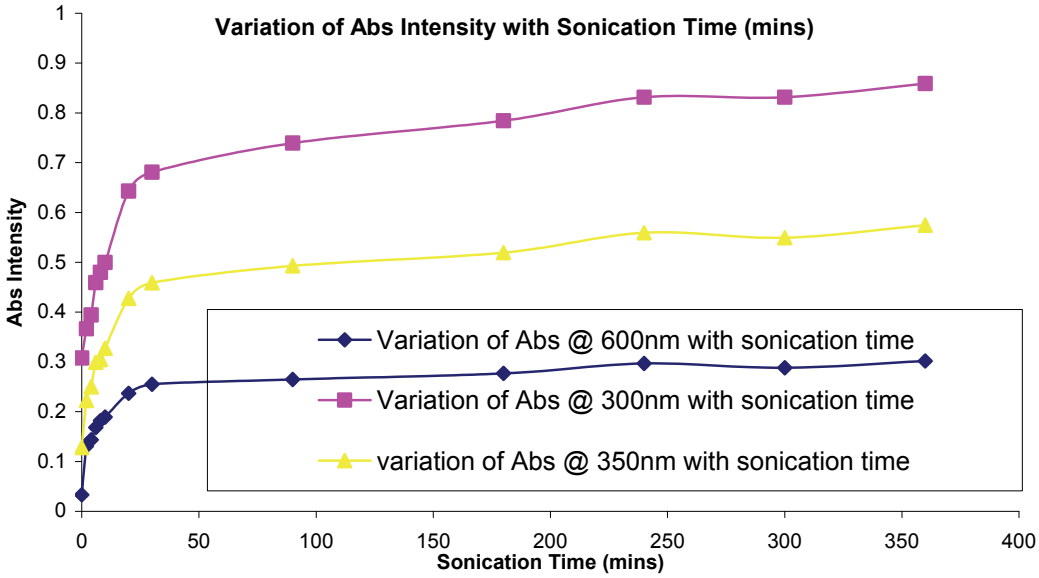

FIGURE 5.10(C): EXP 58 VARIATION IN ABS INTENSITY @ 300, 350, AND 600NM WITH SONICATION TIME (MINS). IT IS DIFFICULT TO SAY WHETHER THE EXFOLIATION PROCESS IS COMPLETE.

It is seen that the intensity of the absorption increases sharply for the first 30mins of sonication, and then more slowly for the remainder of the experiment. This indicates that the exfoliation was not complete after 360mins, which is perhaps to be expected, given the ratio of polymer to nanotubes. This experiment was repeated and the results are shown in FIGURES 5.11(A-C), below and on the next page.

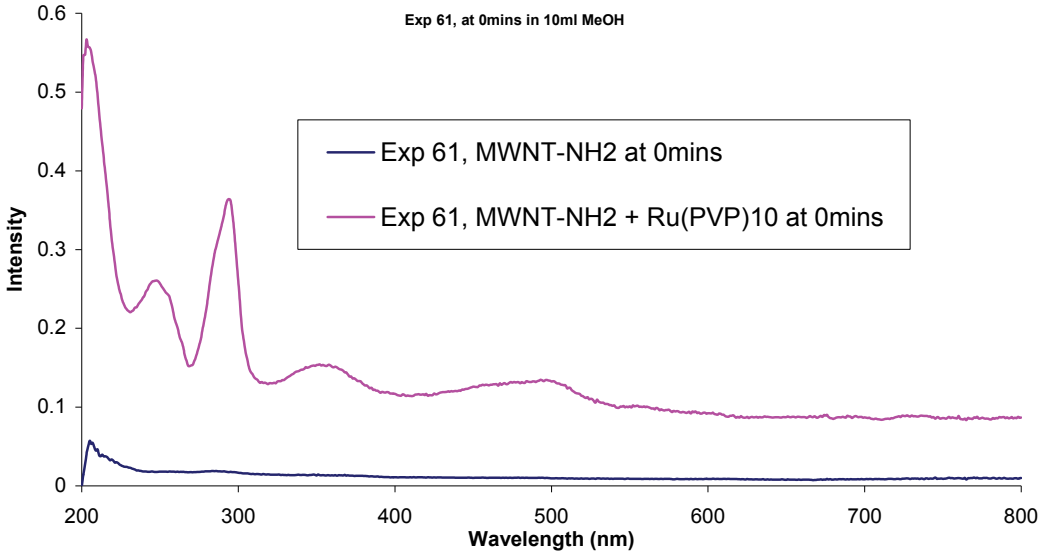

FIGURE 5.11(A): EXP 61, UV OF **MWNT-NH_2 (2MG) IN 10ML MEOH** AT 0MINS, COMPARED WITH UV OF **MWNT-NH_2 (2MG) + [RU(BPY)$_2$(PVP)$_{10}$CL]CL (1MG) IN 10ML MEOH** AT 0MINS. **UV SAMPLE (IN EACH CASE): 100µL OF SAMPLE + 1000µL OF** MEOH.

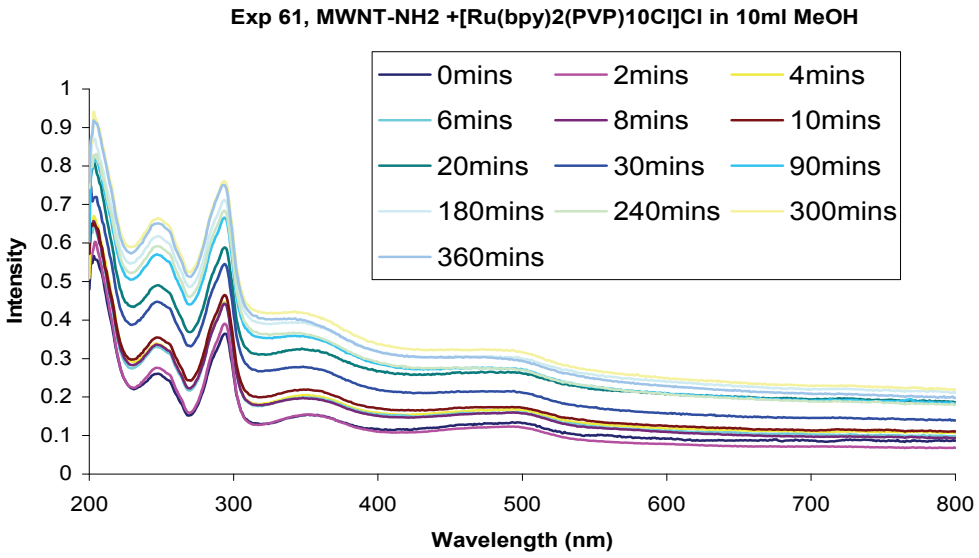

FIGURE 5.11(B): EXP 61, UV OF **MWNT-NH_2 (2MG) + [RU(BPY)$_2$(PVP)$_{10}$CL]CL (1MG) IN 10ML MEOH** THROUGHOUT 360MINS OF SONICATION. **UV SAMPLE (IN EACH CASE): 100µL OF SAMPLE + 1000µL OF MEOH.**

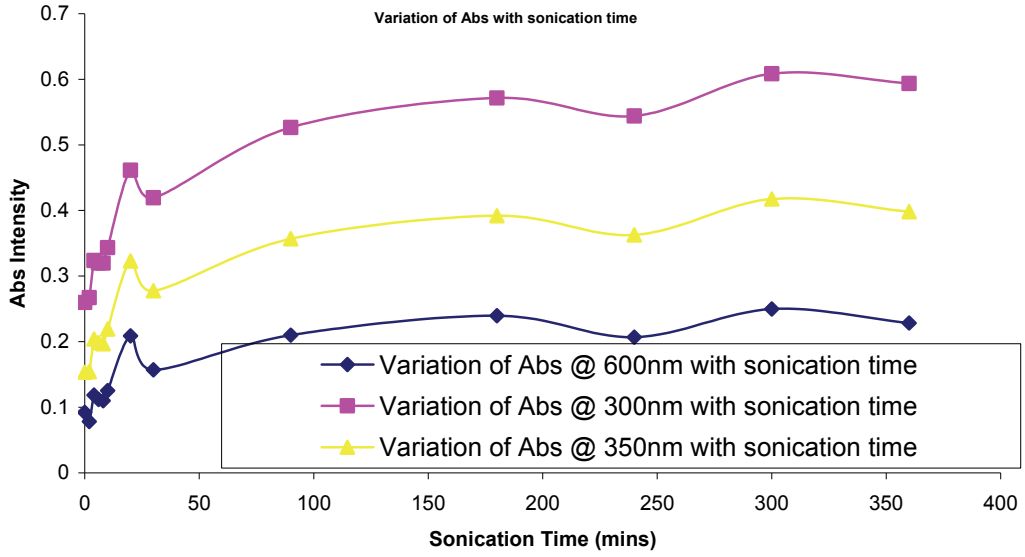

FIGURE 5.11(C): EXP 61, VARIATION OF THE ABSORBANCE INTENSITY @ 300NM, 350NM AND 600NM WITH SONICATION TIME (MINS).

Again, the increase in absorption is sharp for the first 30-60mins, and after this point it is seen to be a more gradual increase. Again, no obvious plateau is observed. In conclusion, it appears that the amino functionalized nanotubes are more easily exfoliated in polymer, than in the absence of the polymer, and are also more easily exfoliated than the unfunctionalized multiwalled nanotubes. The maximum absorption observed is similar to that seen in Figure 5.10(B), indicating that exfoliation still occurs, but the amount of nanotubes exfoliated in a NT : Polymer ratio of 2:1 is similar to that for the 1:1 solution.

5.2.5 Surface Analysis of System

As in the previous chapter, it was decided to deposit a solution of the composite material, prepared and monitored as discussed in the previous section, on a silicon (100) substrate. The preparation of the silicon substrate and the deposition procedure are exactly as detailed in the experimental section of Chapter 4. The images which are presented in this section are of the composite material of the *amino-functionalized*

multiwall nanotubes, wrapped in the ruthenium polymer. The solution used to drop cast onto the silicon was a mix of 1mg of the nanotubes and 2mg of the ruthenium polymer, in 10ml MeOH.

5.2.5.1 Si(100) substrate with MWNT-NH_2/[$Ru(bpy)_2(PVP)_{10}Cl$]Cl composite

The method of image acquisition was the same as for the AFM images presented in Chapter 4, the scanning of a large (20µm X 20µm) scan area, then zooming in on areas of interest. The solution drop cast onto the silicon surface was 2-3drops, taken from the parent solution of 2mg of ruthenium polymer, 1mg of MWNT-NH_2, in 10ml MeOH.

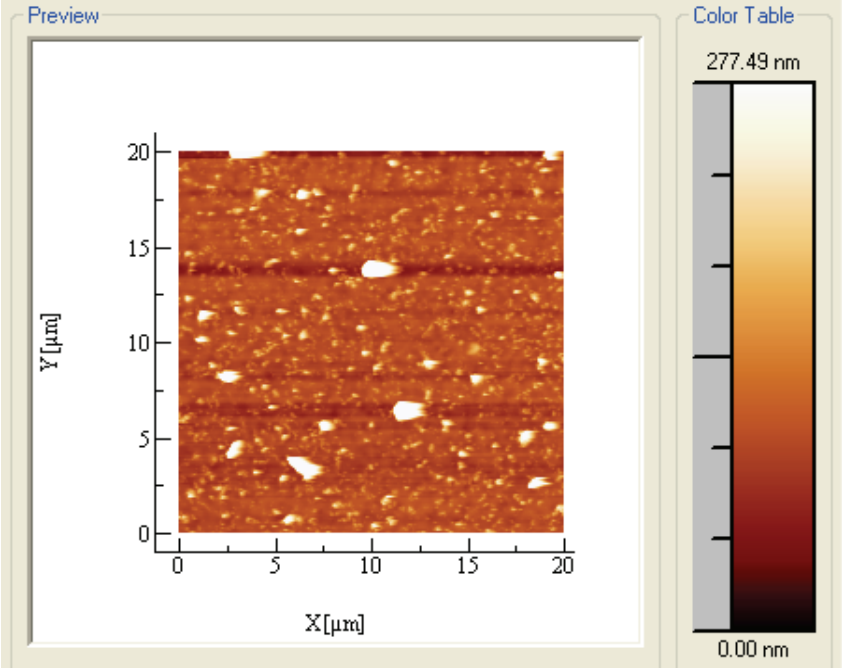

FIGURE 5.12: 20µm X 20µm AFM SCAN OF THE CNT / RU POLYMER COMPOSITE SOLUTION DROP CAST ON TO A Si(100) SLIDE.

The image shown in FIGURE 5.12 shows a dispersion of nanotube-like features, along with some large globular features, (above and below the centre of the image). A smaller scan was performed and this is shown in FIGURE 5.13, on the next page.

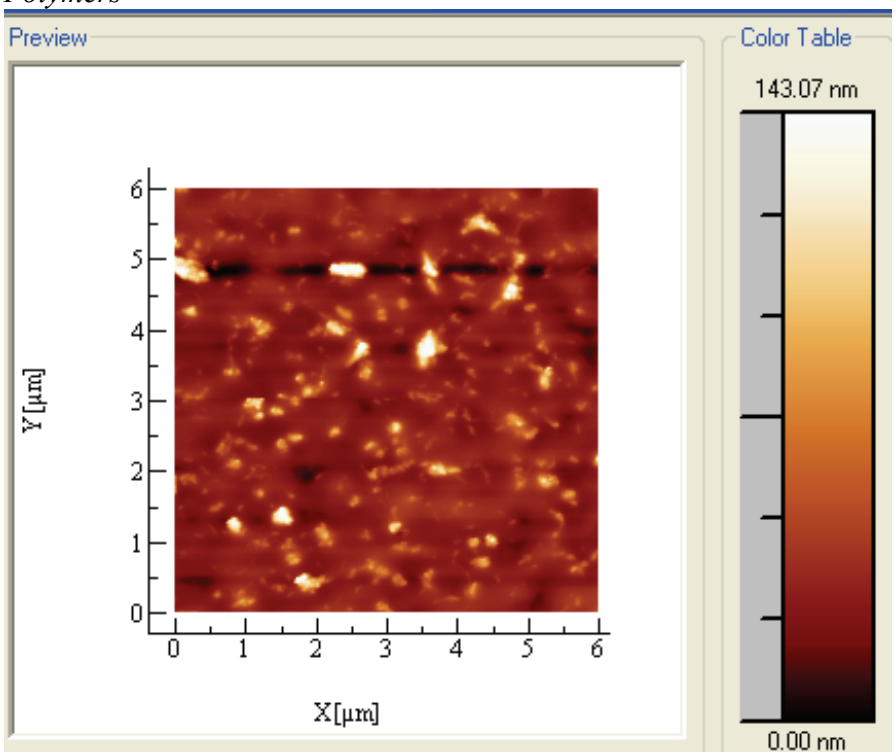

FIGURE 5.13: 6µm x 6µm AFM SCAN.

A greater number of nanotube features are seen in the images presented here, than were seen in the AFM images presented in Chapter 4. This supports the data found in the UV measurements, that the amino functionalized MWNT's are more easily exfoliated than the SWNT's. In addition to the nanotube features in FIGURE 5.13, the larger globular features are attributed to small (2-5) nanotubes enclosed in a clump of polymer, this appears to be what is shown in the phase image shown in FIGURE 5.14(B), taken from the height data in FIGURE 5.14(A), on the next page. This feature is in the centre of the image.

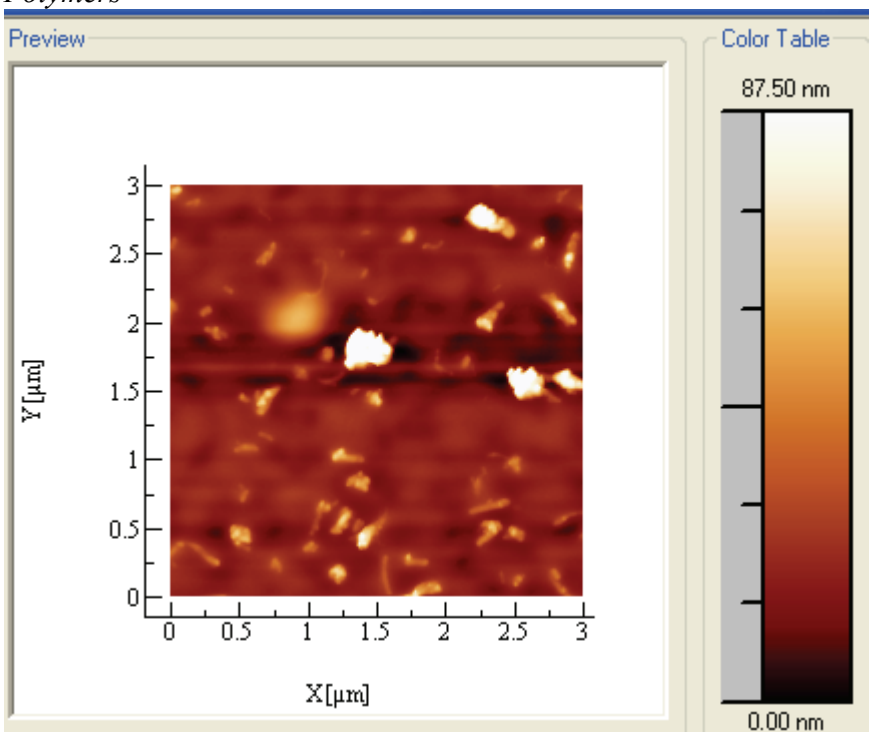

FIGURE 5.14(A): 3µm X 3µm AFM SCAN OF THE SURFACE, SHOWING WHAT APPEAR TO BE NANOTUBE-LIKE FEATURES.

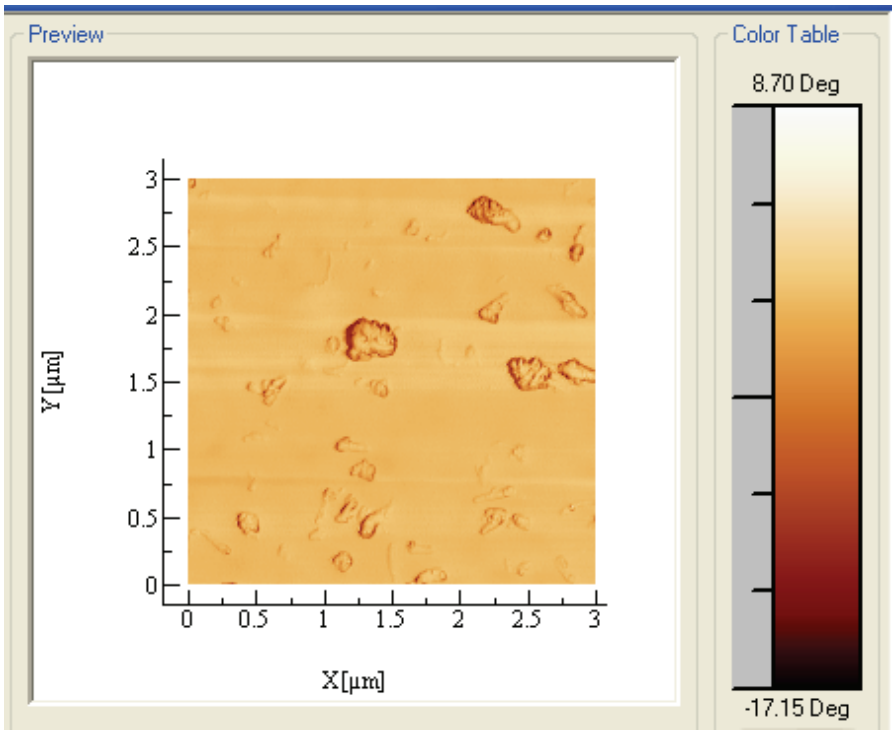

FIGURE 5.14(B): 3µm X 3µm AFM PHASE IMAGE OF SWNT / $[Ru(bpy)_2(PVP)_{10}Cl]Cl$ COMPOSITE DEPOSITED ON Si(100) SUBSTRATE.

The next image (FIGURE 5.15(A)) was obtained by zooming in on the image in FIGURE 5.14(A), above.

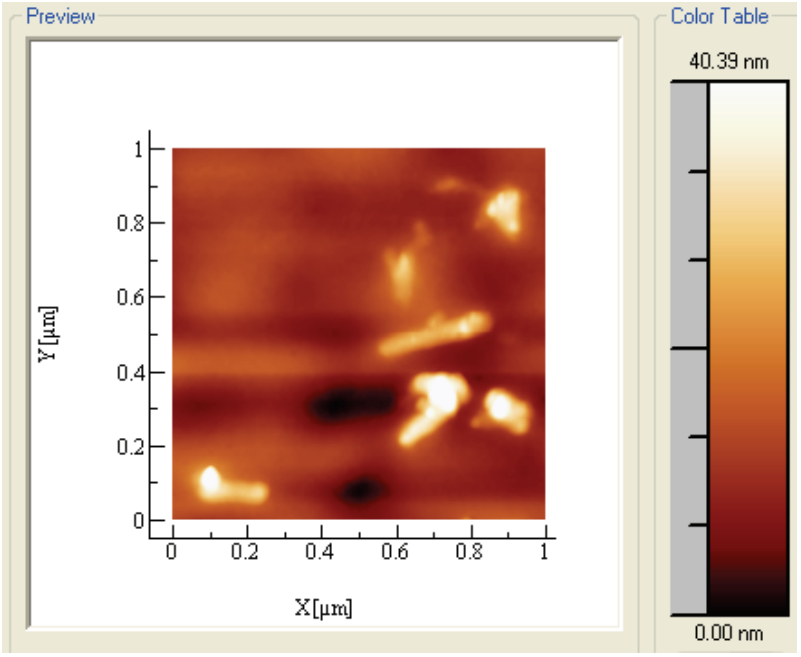

FIGURE 5.15(A): 3µm X 3µm AFM SCAN OF THE SURFACE, SHOWING WHAT APPEAR TO BE NANOTUBE-LIKE FEATURES.

A possible group of nanotubes covered in a clump of polymer is seen to the right bottom corner of the image. This is suggested by the fact that it is a higher feature than the others, from the height scale and the data in FIGURE 5.15(C), it appears to be 30nm-40nm high. The dimensions of the feature to the right of the centre of the image in FIGURE 5.15(A) were estimated using the processing software. The results of the analysis are shown in FIGURE 5.15(B) and FIGURE 5.15(C), below. The diameter of the feature is estimated to be of the order of 100nm. This is consistent with the values obtained for the SWNT/polymer system in Chapter 4. It indicates that quite a thick layer of polymer is present on the nanotubes, since the diameters of MWNT's are 20nm according to Brennan *et al*[9]. It is not thought that the amino groups would affect this value greatly.

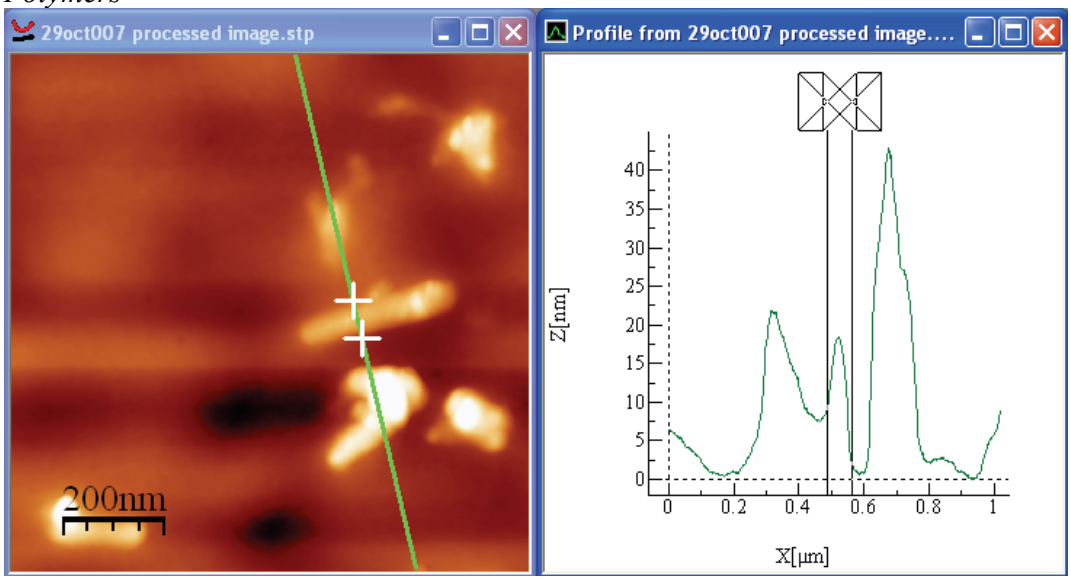

FIGURE 5.15: (B), LEFT, SHOWS THE SECTION TAKEN OF THE IMAGE (GREEN LINE), AND THE POINTS WHERE THE MEASUREMENT IS MADE ARE SHOWN BY WHITE "X" MARKS, WHILE **(C)**, RIGHT, INDICATES THAT THE WIDTH (X-AXIS) IS SLIGHTLY LESS THAN 100NM.

5.2.5.2 Si(100) substrate with $[Ru(bpy)_2(PVP)_{10}Cl]Cl$ polymer

In order to see what the ruthenium polymer solution without nanotubes would look like on the surface, two solutions of different concentrations of the ruthenium polymer were prepared and deposited onto silicon subtrates, in the same way as the composite solutions were. The two concentrations of polymer were 2mg/10ml MeOH, as in the composite material solution, and 25mg/5ml MeOH, a concentration used by Frehill *et al*[7(g)]. This allows a comparison to be made with the images reported in ref [7(g)], and also with the images reported here. The images of the polymer depositions are shon in FIGURE 5.16 and FIGURE 5.17.

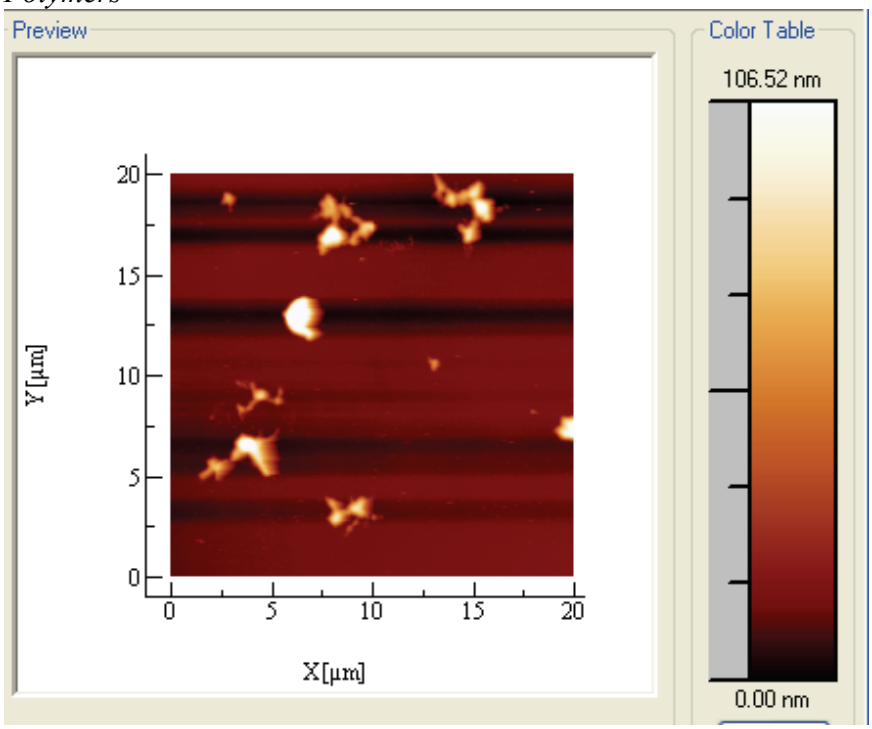

FIGURE 5.16: 20µm X 20µm AFM IMAGE OF THE RUTHENIUM POLYMER (2MG IN 10ML PARENT SOLUTION) DEPOSITED ON Si(100) SUBSTRATE.

In FIGURE 5.16, globular features are seen on the surface, these are believed to be aggregations of polymer. These were reported by Frehill *et al*[7(g)], however the polymer concentration used in that contribution was much higher, however, it is concluded that the features seen in the previous section are of modified nanotubes. There are some aggregations of polymer present on the surface, along with the modified nanotubes. These polymer features were not observed in the Single Walled Nanotube based composites discussed in Chapter 4. This is due to the fact that more polymer is required to exfoliate the SWNT', and there is little "free" polymer left in the solution, post-exfoliation. The amino-functionalized nanotubes, however, have been easily exfoliated and therefore the possibility exists for the presence of "free" polymer.

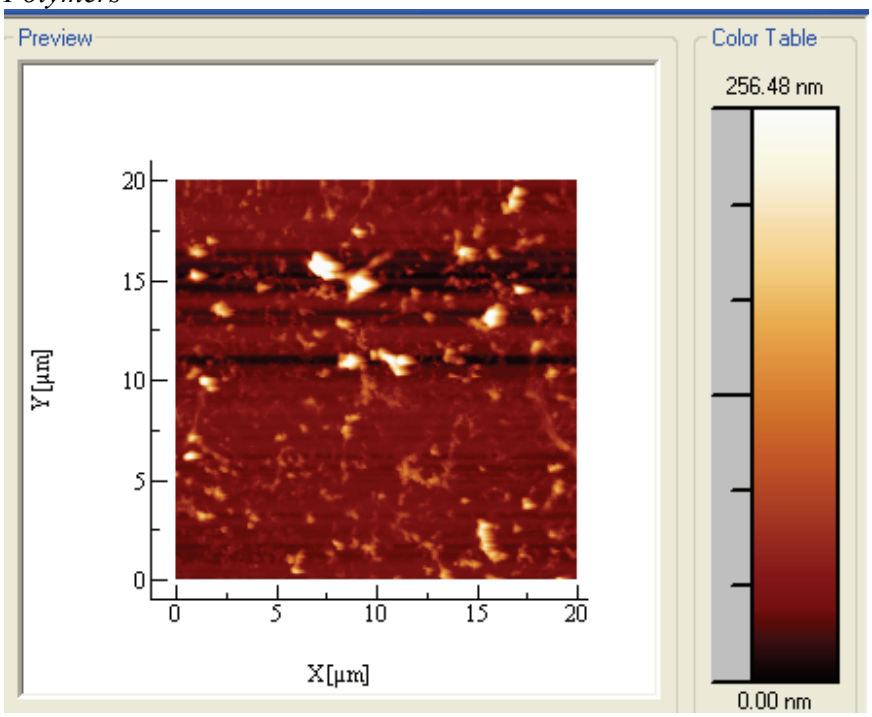

FIGURE 5.17: 20µm X 20µm AFM IMAGE OF THE RUTHENIUM POLYMER (25MG IN 5ML PARENT SOLUTION) DEPOSITED ON Si(100) SUBSTRATE.

It is seen in FIGURE 5.17 above, that the more concentrated polymer solution results in much greater number of globular features, in the same scan size. A number of scans were performed on both polymer-only samples, and the images shown here are representative of the respective samples.

5.3 Conclusions

It has been found that the unfunctionalized multiwalled nanotubes appear to be more diificult to exfoliate in methanol, with the polymer concentrations used in the experiments. The most probable reason for this is a poor interaction between the nanotubes and the polymer. This is not the case for the amino functionalized multiwalled nanotubes, which were quite easily exfoliated, even in the absence of the ruthenium polymer. The AFM images appear to support the conclusion that the amino functionalized nanotubes have a high affinity for the polymer as they show what are thought to be polymer aggregates on the surface, surrounding the nanotubes. This may explain the ease of exfoliation. The dimensions of the nanotube features were estimated to be in the region of 100nm, larger than values reported for composite MWNT based

systems such as by Phang *et al*[11](~33nm), but comparable to the system investigated by Sinani et al[12] (~100-200nm). Of the three types of carbon nanotubes investigated, SWNT, MWNT and MWNT-NH_2, it appears that the latter are the most easily exfoliated, with the SWNT's being the next most facile. It has also been shown that the exfoliation process can be monitored in-situ by UV-vis spectroscopy, and that AFM can provide further evidence of the extent of the exfoliation.

5.4 Bibliography

1 S. Iijima, *Nature*, **1991**, *354*, 56-58

2 J. C. Charlier, J. P. Issi, *Appl. Phys. A – Mat. Sci. & Processing*, **1998**, *67*, 79-87

3 **(a)** S. – H. Su, W. - T. Chiang, C. - C. Lin, M. Yokoyama, *Physica E*, **2008**, *40*, 2322-2326, **(b)** R. Andrews, D. Jacques, D. Qian, T. Rantell, *Acc. Chem. Res.*, **2002**, *35*, 1008-1017

4 N. Hamada, S. Sawada, A. Oshiyama, *Phys. Rev. Lett.* **1992**, *68*, 1579-1581

5 A. Rubio, *Appl. Phys. A*, **1999**, *68*, 275-282

6 **(a)** N. Hua, Z. Masuda, G. Yamamoto, H. Fukunaga, T. Hashida, J. Qiu, *Comp. Part A*, **2008**, *39*, 893-903, **(b)** K. H. Kim, W. H. Jo, *Comp. Sci. & Tech*. **2008**, *68*, 2120-2124, **(c)** S. Li, Y. Qin, J. Shi, Z.-X. Guo, Y. Li, D. Zhu, *Chem. Mat.*, **2005**, *17*, 130-135

7 **(a)** H. N. Choi, J.-Y. Lee, Y.-K. Lyu, W.-Y. Lee, *Anal. Chim. Acta.*, **2006**, *565*, 48-55, **(b)** F. Frehill, J. G. Vos, S. Benrezzak, A. A. Koós, Z. Kónya, M. G. Rüther, W. J. Blau, A, Fonseca, J. B. Nagy, L. P. Biró , A. I. Minett, M. in het Panhuis, *J. Am. Chem. Soc.*, **2002**, *124*, 13694-13695, **(c)** T. Y. Lee, J.-B. Yoo, *Diamond & Related Mater.*, **2005**, *14*, 1888-1890, **(d)** Y. Tao, Z.-J. Lin, X.-M. Chen, X. Chen, X.-R. Wang, *Anal. Chim. Acta*, **2007**, *594*, 169-174, **(e)** S.-H. Hwang, C. N. Moorefield, L. Dai, G. R. Newkome, *Chem. Mat.*, **2006**, *18*, 4019-4024, **(f)** Z. Lin, G. Chen, *Talanta*, **2006**, *70*, 111-115, **(g)** F. Frehill, M. in het Panhuis, N. A. Young, W. Henry, J. Hjelm, J. G. Vos, *J. Phys. Chem. B.*, **2005**, *109*, 13205-13209

8 **(a)** J. Shen, W. Huang, L. Wu, Y. Hu, M. Ye, *Mat. Sci. & Eng. A.*, **2007**, *464*, 151-156, **(b)** J. Shen, W. Huang, L. Wu, Y. Hu, M. Ye, *Comp. Part A.*, **2007**, *38*, 1331-1336, **(c)** X. Chen, J. Wang, M. Lin,W. Zhong, T. Feng, X. Chen, J. Chen, F. Xue, *Mat. Sci. & Eng. A.*, **2008**, *492*, 236-242

9 M. E. Brennan, J. N. Coleman, A. Drury, B. Lahr, T. Kobayashi, W. J. Blau, *Optics Lett.*, **2003**, *28*, 266-268

10 N. Grossiord, O. Regev, J. Loos, J. Meuldijk, C. E. Koning, *Anal. Chem.*, **2005**, *77*, 5135-5139

11 I. Y. Phang, T. Liu, W.-D. Zhang, H. Schönherr, G. J. Vansco, *Euro. Poly. J.*, **2007**, *43*, 4136-4142

12 V. A. Sinani, M. K. Gheith, A. A. Yaroslavov, A. A. Rakhnyanskaya, K. Sun, A. A. Mamedov, J. P. Wicksted, N. A. Kotov, *J. Am. Chem. Soc.*, **2005**, *127*, 3463-3472

13 J. W. Jang, C. E. Lee, T. J. Lee, C. J. Lee, S. J. Noh, *Solid State Comm.,* **2003**, *127*, 29-32

Chapter 6: Excited State Photophysics Of Ruthenium Polypyridyl Complexes

Chapter 6 presents photophysics measurements made on a variety of Ruthenium Polypyridyl – type complexes. These measurements are of two broad types, emission spectroscopy, and Time Correlated Single Photon Counting (TCSPC). The latter receives particular emphasis in this chapter. These measurements were performed in various solvents, and at both room temperature. The aim of these experiments was to provide an insight into the photophysical pathways of the ruthenium complexes studied and in particular measure the lifetime of the excited state.

6.0 Introduction

The investigation of the excited state properties of ruthenium complexes is of considerable interest, and has led to the preparation and characterization of an extremely diverse range of ruthenium complexes.[1-2, 3,4,5,6,8,9,10] Much of the basics of ruthenium photophysics have been discussed in Chapter 1. The introduction which follows discusses some of the photophysical investigations reported on complexes that are structurally analogous to those investigated in the following of the present chapter [Type I complexes, (see FIGURE 6.8)].

O' Donoghue and co-workers[1] prepared a series of ruthenium bis(phenanthroline) complexes with a substituted diphenylquinoxaline ligand and found that methylation of this ligand resulted in increased luminescence lifetimes in aqueous solution. This is attributed to the methyl groups on the quinoxaline ligand interfering with the hydrogen bonding from the solvent, thus reducing the solvent related quenching. An example of the structure of the complexes and ligands studied is shown in FIGURE 6.1. It is seen that the ligands reported in this contribution such as dppz and tppz are the same as the ligands in the Type I complexes.

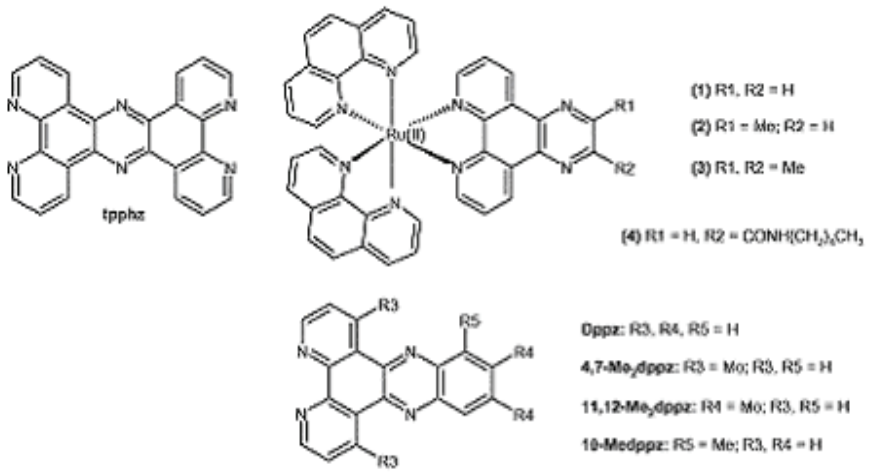

FIGURE 6.1: STRUCTURES OF COMPLEXES INVESTIGATED BY O' DONOGHUE *et al.* ADAPTED FROM REF [1].

Recently, a review article by Browne and McGarvey[2] addressed the photophysics of ruthenium bis(bipyridyl) complexes of the form $[Ru(bpy)_2dppz]^{2+}$. In this important contribution, the authors noted that in the case of $[Ru(bpy)_2dppz]^{2+}$, the excited state was found to be located on the phenazine part of the dppz ligand[3,4], and not on the bpy ligands. The phenazine based absorbance peak is observed around 357nm in the complex and at 359nm for the free ligand.

In addition, ruthenium polypyridyl complexes coordinated to a dppz ligand such as $[Ru(bpy)_2(11\text{-bromo-dppz})]^{2+}$ has been prepared and investigated by Lundin and co-workers[10(a)], Coates *et al*[10(b),10(c)]. Lundin[10(a)]observed the metal-to-ligand-charge transfer (MLCT) absorbance peak for $[Ru(bpy)_2(11\text{-bromo-dppz})]^{2+}$ (FIGURE 6.2) at 441nm, and reported the ligand-based $\pi \rightarrow \pi^*$ transitions at 284nm, 364nm, and 375nm. The emission λ_{max} was observed around 652nm. Coates *et al*[10(b)] utilized transient resonance Raman spectroscopy (TRRS) to investigate dppz type complexes, and reported a dppz-based excited state for the bis (phenanthroline) analogue, $[Ru(phen)_2dppz]^{2+}$ in aqueous media, an also for $[Ru(bpy)_2dppz]^{2+}$ in ref [10(c)]. The phen-based complex was previously[13] found to possess negligible luminescence in aqueous media and was thought to decay via a non-radiative process, with the weak luminescence process having a lifetime on the picosecond scale[10(b)].

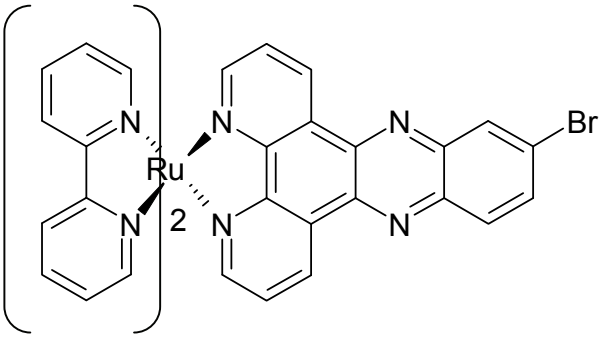

FIGURE 6.2: STRUCTURE OF $[Ru(bpy)_2(11\text{-bromo-dppz})]^{2+}$ INVESTIGATED IN REF [10(A)].

Rau *et al*[5] synthesised a range of ruthenium complexes with substituted bpy ligands and bibenzimidazole ligands. The mononuclear complexes were reported to have similar lifetimes to each other, in the order of tens of ns, while the substituents on the bpy ligands, which appeared to lead to increased electron density at the metal centre, were

not found to affect the photophysics greatly. A pair of stereoisomeric dinuclear complexes were found to exhibit very similar lifetimes, which is tentatively explained as being to due to the fact that the bpy ligands act as the luminophore. One of the mononuclear complexes reported in this contribution is shown in FIGURE 6.3, below.

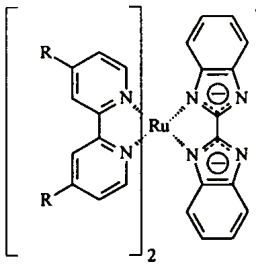

FIGURE 6.3: TYPE OF STRUCTURE INVESTIGATED BY RAU *et al* IN REF [5].

Of particular relevance to the investigation of the Type I complexes are the contributions by Rau *et al*[6] and Schäfer *et al*[7]. In these reports, both dinuclear and mononuclear ruthenium complexes were investigated for catalytic activity. These were in most cases ruthenium tris bpy type compounds, two of the bpy ligands being modified with t-butyl groups, and the third modified with a phenazine moiety, which in turn was bound to the bpy ligand of another ruthenium centre, or a platinum centre, as is illustrated in FIGURE 6.4, below[6].

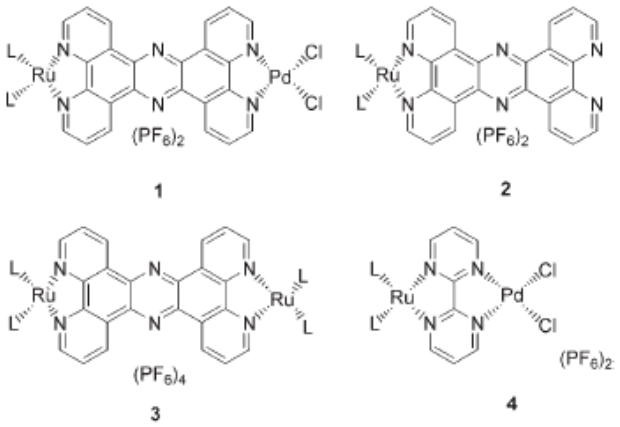

FIGURE 6.4: STRUCTURES OF THE COMPLEXES USED BY RAU *et al*, TAKEN FROM REF [6].

Lifetime values were reported ranging from 27ns for (**1**) to 150ns for (**2**), a biexponential decay (27/130ns) for (**3**), in aerated acetonitrile (compound numbers taken from FIGURE 6.4, above). The values were not discussed in ref [6], however in the report by Schäfer *et al*[7], interpretations of the reported results were offered. The lifetime measurements were performed in DCM and ACN, and the values indicated a strong dependency on the solvent chosen. In addition, it was found that the aryl substituents on the uncomplexed end of the phenazine ligand increased the lifetime of the excited state, possibly through steric hindrance and/or disruption of the hydrogen bonding from the solvent, effects which have also been reported by O Donoghue *et al*[1].

Brennaman *et al*[17] has studied the photophysical properties of $[Ru(bpy)_2dppz]^{2+}$ and has found that the excited state is located on the dppz ligand, and more specifically, the bpy portion of the dppz was identified as the excited state location. This is in close agreement with the findings of other groups[2-4].

The Rau group has also investigated ruthenium complexes bearing a tetra-substituted 1,10-phenanthroline ligand.[8, 9] The addition of the bromo substituents on the phenanthroline ligand was observed to have significantly lowered the electron density of the metal centre. Lifetime values were not reported in this contribution, however, it was anticipated that the lifetimes would be short, given the findings in ref [9]. Bromination of the phenanthroline ligand was found to decrease the lifetime of the excited state (111ns, compared to 200ns for the unbrominated phenanthroline complex).

Dose and Wilson[18] reported the synthesis and photophysical characterization (UV-vis and emission) of heteroleptic ruthenium polypyridyl complexes amongst which, $[Ru(bpy)_2(2,9\text{-}Me_2phen)](PF_6)_2$ is relevant here. No lifetime data were presented, however the absorbance λ_{max} of the complex was found to be 450nm for the MLCT, while the emission λ_{max} was observed around 600nm, indicating that the excited state is indeed bpy based, and not based on the phenanthroline ligand.

Huang *et al*[19] has also reported the synthesis and characterization of heteroleptic ruthenium polypyridyl complexes with phenanthroline and bipyridine ligands. Absorption data were presented, showing characteristic Ru(II) polypyridyl MLCT's around 450nm. A representative complex is shown in FIGURE 6.5. It is seen that the complex in FIGURE 6.5 can be considered to be a structural derivative of **9**, a Type II

complex investigated in this thesis. Therefore, the work presented by Huang *et al*[19] is a useful reference work for the interpretation of the results obtained for **9**. The R group for **9** is an ethynyl phenyl moiety, while a methoxy phenyl comprises the R group for the complex in FIGURE 6.5.

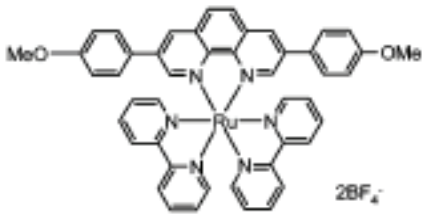

FIGURE 6.5: STRUCTURE OF ONE OF THE COMPLEXES REPORTED BY HUANG *et al*. TAKEN FROM REF [19].

Recently[20], Browne and co-workers reported the investigation of two different complexes, $[Ru(bpy)_x(ph_2phen)_{3-x}]^{2+}$, where x = 0–3 and ph_2phen is 4,7-diphenyl-1,10-phenanthroline, and $[Ru(bpy)_2(dcbpy^{2-})]$, where H_2dcbpy is a 4,4'-dicarboxy-2,2'-bipyridyl ligand. It was found that by replacing the bpy ligands of the complexes with di-phenyl phenanthroline (dpp), the emission was red shifted, an expected result due to the lower lying MLCT π^* states of the dpp ligand. It was also found that increasing substitution of the bpy ligands with dpp resulted in longer lifetimes at room temperature in deaerated ACN.

Sun *et al*[21] investigated a series of complexes which are structurally analogous to complex **2** in this chapter, with a triazine moiety in place of the phenanthroline/quinoxaline macrocyclic moiety in **2**. It was found that methylation of the bpy ligands in the 4,4' positions lead to a reduction in the excited state lifetime, while the lifetimes of the complex with the bpy ligands were slightly shorter than that of the complex with phenanthroline ligands, as found also by Browne *et al*[20]. One of the complexes studied in this contribution[21] is shown in FIGURE 6.6, below.

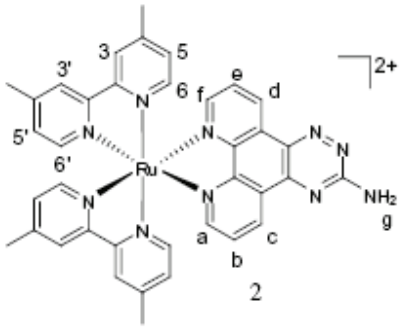

FIGURE 6.6: STRUCTURE OF THE COMPLEX WITH METHYLATED BPY LIGANDS, TAKEN FROM REF [21].

Bouskila *et al*[22] also investigated ruthenium complexes with a mixture of phenanthroline and bpy ligands. Photophysical data in ethanol at both room temperature and 77 K were reported. It was found that the lifetime for the Ru(II) tris-phenanthroline complex was much shorter, (50%), than Ru(II) tris bpy exhibited in ethanol. However, at 77 K, this situation changes dramatically, with the tris phenanthroline complex now exhibiting a lifetime twice that of the tris bpy. The fluorescence data suggests the excited state lies on the bpy ligands.

Tzalis and Tor[23] reported the synthesis of a complex similar to both complexes studied here (**9**) and also a complex reported by Huang *et al*[19], a ruthenium complex with an aryl-ethyne phenanthroline ligand. The structure of the ligand is shown in FIGURE 6.7 below.

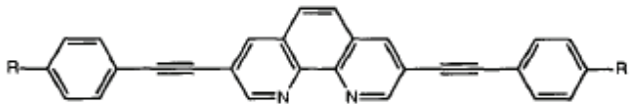

FIGURE 6.7: STRUCTURE OF LIGAND USED BY TZALIS, TAKEN FROM REF [23].

The R group is either a methoxy group, a tolyl group or a H atom. The absorbance data at room temperature in acetonitrile were reported for the three complexes synthesized, and the MLCT in each case was found to be red-shifted relative to the standard $[Ru(phen)_3](PF_6)_2$ complex, indicating the substituents can be used to lower the energy of the phenanthroline ligand, most likely as a result of increased delocalization of the excited state over a larger π^* network.

Another contribution by Rau *et al*[24] reported the use of a hetero-dinuclear complex analogous to complex **4** discussed later in this chapter. This complex reported in ref [24] can be used as a photocatalyst, combining a light harvesting centre and catalytic centre. This report serves to illustrate one of many potential uses for such ruthenium polypyridyl complexes, and also illustrates the need to fully understand their excited state properties.

Rau and co-workers[25] also reported the synthesis and characterization of complex **5**, seen in FIGURE 6.17, and discussed later in this chapter, as a Type II complex. Photophysical data in deaerated ACN were presented, a lifetime of approximately 1.4μs was reported, with MLCT bands present in the emission spectra at around 610nm, indicating a bpy based excited state. This complex will be used as a standard complex.

6.0.1 Aims of Chapter

The work presented in this chapter was carried out in order to determine the excited state lifetimes and spectroscopic properties of ruthenium polypyridyl complexes of two main types, Type I and Type II. These complexes were investigated as part of a collaborative project between the Prof. J. G. Vos group in Dublin City University, Ireland, and the group of Prof. S. Rau, Jena, Germany. Type I embraces the primary complexes that are potential photocatalysts with a light harvesting moiety and a catalytic centre. In order to investigate their photocatalytic potential, an understanding of their photophysics was required. This forms the primary aim of this work. The Type II complexes are reference compounds for the Type I complexes. The structures of the Type II complexes investigated here are shown in FIGURE 6.8, and FIGURE 6.17. In addition to determining the excited state lifetimes of the complexes, attempts were made to understand the values obtained, and to account for the UV-vis and emission spectra obtained for the samples.

6.1 Experimental

All complexes investigated were synthesized by and received from the group of Prof. Sven Rau, Jena, Germany. All samples were used as received, with no further

purification. All measurements were performed in air. The absorbance of each sample was measured first, followed by steady state emission (fluorescence) measurements to establish the emission λ_{max} of the sample.

Preparation of sample solutions was carried out in the absence of ambient light, and solutions were wrapped in aluminium foil and carefully sealed to avoid exposure to light, and evaporation. Samples were always prepared fresh, immediately prior to the measurements. $[Ru(bpy)_3]^{2+}$ in aerated ACN was used as a standard for the lifetime measurements, as this has a well established value in this solvent, of approximately 160ns.

6.1.1 Instrumentation and Materials

The excited state lifetime measurements were performed on an Edinburgh Instruments Single Photon Counter, using an nF900 Nanosecond Flash Lamp. The apparatus used in the lifetime and steady state spectroscopy experiments (Absorbance and Emission) have been discussed in Chapter 2. Room temperature measurements were performed in aerated acetonitrile (ACN), dichloromethane (DCM), and H_2O. All solvents used were spectroscopic grade, and were used as received. The error in the lifetime values is ±10%.

6.2 Results and Discussion

The results presented in this chapter pertain to lifetime measurements performed on ruthenium complexes possessing different ligand combinations. The measurements were carried out in aerated acetonitrile, and at room temperature, unless stated otherwise. The results have been divided into 2 main sections, depending on the structure of the complex presented. In each section the results are presented as a table, with Sample I.D., lifetime value and χ^2 value. Typical decay profiles and residual plots for the samples are also presented in each section. Other residual plots can be found in Appendix C.

6.2.1 Type I Complexes

The structures of the Type I complexes investigated are shown in FIGURE 6.8. It is seen that they all possess two bpy type ligands, and a third modified phenanthroline ligand. The third ligand has an extended aromatic π bond structure. One of the complexes is dinuclear, with one ruthenium centre, and a palladium (Pd) metal centre. The next section presents the spectroscopic and photophysical data obtained for these complexes.

Sample I.D	Structure Of Complex	Sample I.D.	Structure Of Complex
1	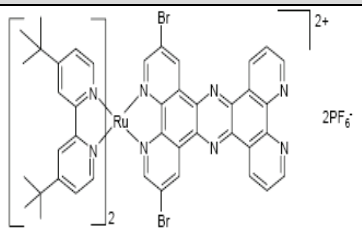	2	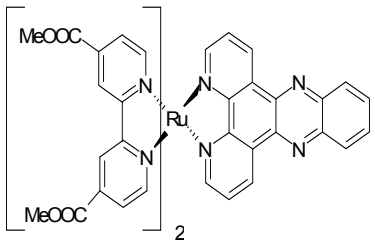
3	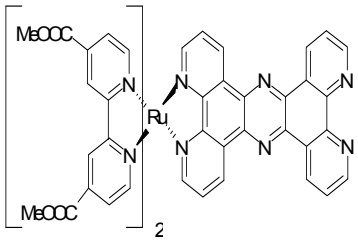	4	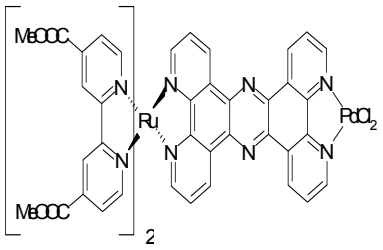

FIGURE 6.8: TYPE I COMPLEXES.

6.2.1.1 Type 1 Complexes, Spectroscopy and Photophysics

The spectroscopic and photophysical data obtained for the Type I ruthenium complexes in aerated acetonitrile are displayed in TABLE 6.1, while TABLE 6.2 shows the data obtained for **2**-**4** in water. The results shown in both tables are absorbance data, emission data, followed by the lifetime value, τ, and the reduced Chi squared value, (χ^2) which is an indication of the closeness of the calculated fit to the experimental decay data.

Sample I.D.	Abs (nm) (ACN)	Emission λ_{max} (nm) (ACN)	Lamp Parameters	τ(ns) in ACN / χ^2
1	246, 282, 440,	661	40kHz, 6.5kV, 1.1bar	226 / 1.000
2	306, 353, 469(19500)	650	40kHz, 3.5kV, 0.3bar	470 / 1.049
3	306, 460 (24800)	650	40kHz, 3.5kV, 0.3bar	447 / 0.998
4	280, 297, 463 (24800)	650	40kHz, 3.5kV, 0.3bar	466 / 1.01

TABLE 6.1: SPECTROSCOPIC AND PHOTOPHYSICAL DATA FOR TYPE I COMPLEXES.

Sample I.D.	Abs (nm)	Emission λ_{max} (nm)	Lamp Parameters	τ (ns)	Prefactors (%)	χ^2
2	280, 307, 357, 470	641	-	-	N/A	-
3	280, 304, 369, 467	650	20kHz, 3.5kV, 0.3bar	532	100	1.05
4	280, 304, 369, 467	640	20kHz, 3.5kV, 0.3bar	532, 111	72, 28	1.037

TABLE 6.2: SPECTROSCOPIC AND PHOTOPHYSICAL DATA FOR 2-4 IN H_2O, ROOM TEMPERATURE.

FIGURE 6.9 shows the UV spectra for the complexes in aerated ACN. FIGURE 6.10 shows the emission spectra for the complexes, while in FIGURE 6.11, the decay profile for 2 in aerated ACN is presented.

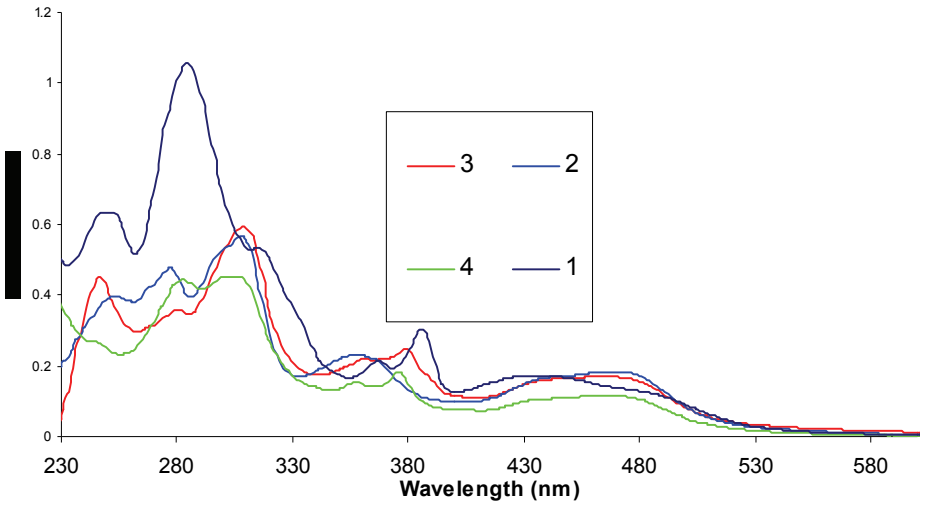

FIGURE 6.9: UV-VIS SPECTRA OF TYPE I COMPLEXES IN AERATED ACN.

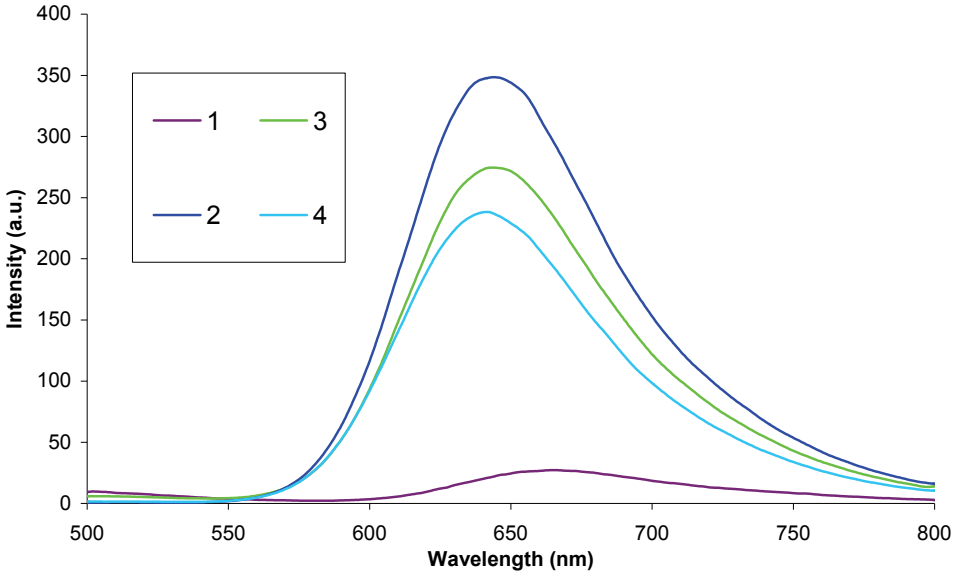

FIGURE 6.10: EMISSION SPECTRA FOR TYPE I COMPLEXES IN AERATED ACN, ROOM TEMPERATURE. EX SLIT = EM SLIT =10nm.

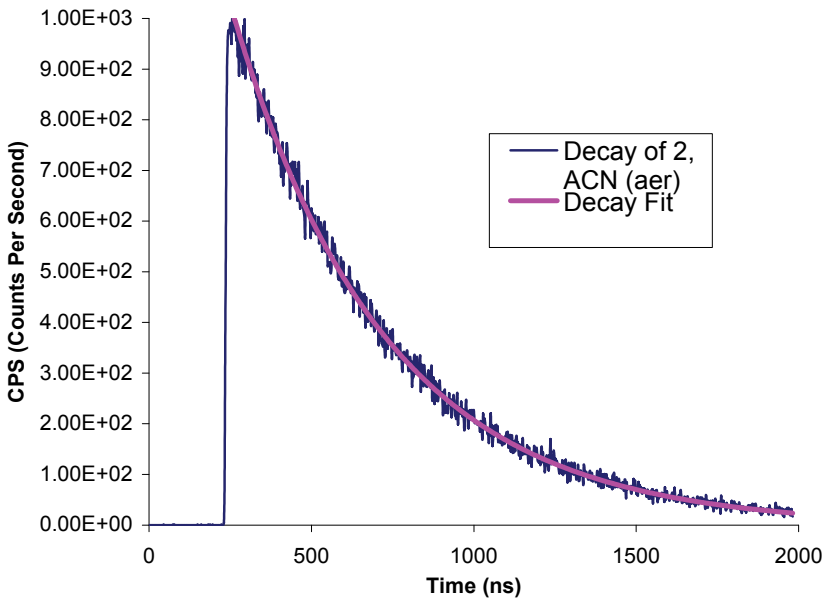

FIGURE 6.11(A): DECAY OF **2** IN AERATED ACN, ROOM TEMPERATURE. LIFETIME WAS ESTIMATED TO BE AROUND 470NS, CHI^2= 1.049.

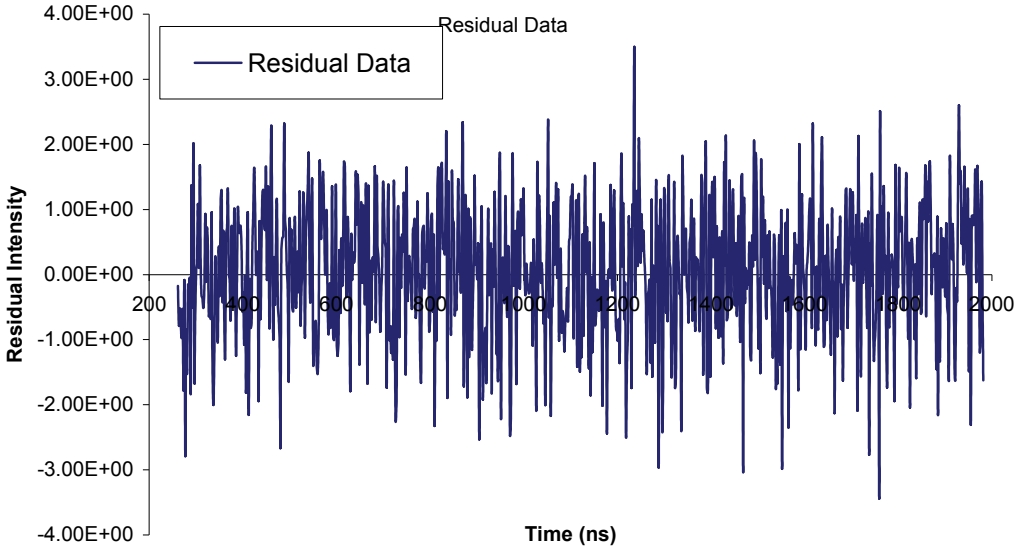

FIGURE 6.11(B): RESIDUAL DATA FOR DECAY OF **2** IN AERATED ACN

The UV-vis and fluorescence spectra for **2**-**4** in H_2O are presented in FIGURE 6.12 and FIGURE 6.13 respectively. FIGURE 6.14(A) shows the decay profile for **3**, while FIGURE 6.14(B) shows the decay for **4**, fitted with a biexponential fit, while FIGURE 6.14(C) shows the decay and monoexponential fit for **4**. The residual data for the biexponential fit is shown in FIGURE 6.14(D), while that for the monoexponential fit is presented in FIGURE 6.14(E).

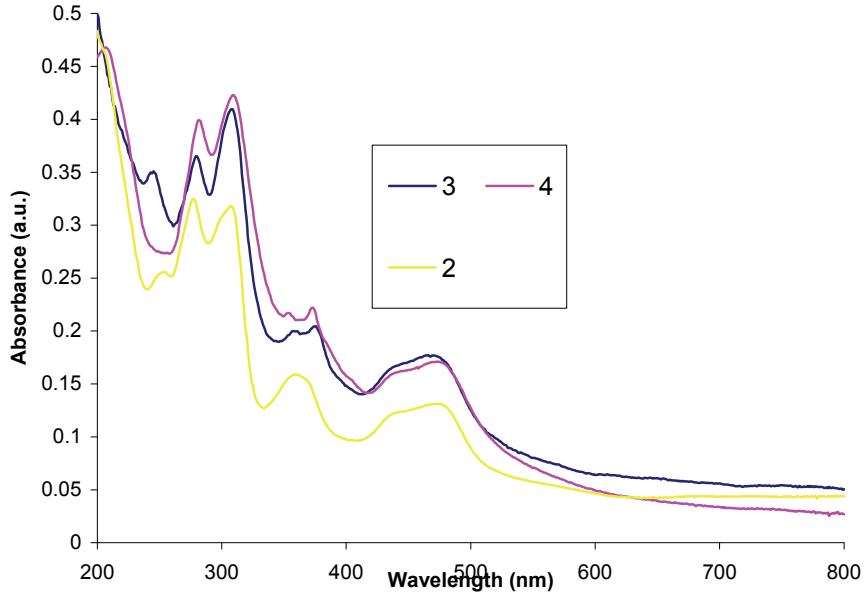

FIGURE 6.12: UV SPECTRA OF COMPLEXES **2**-**4** IN H_2O.

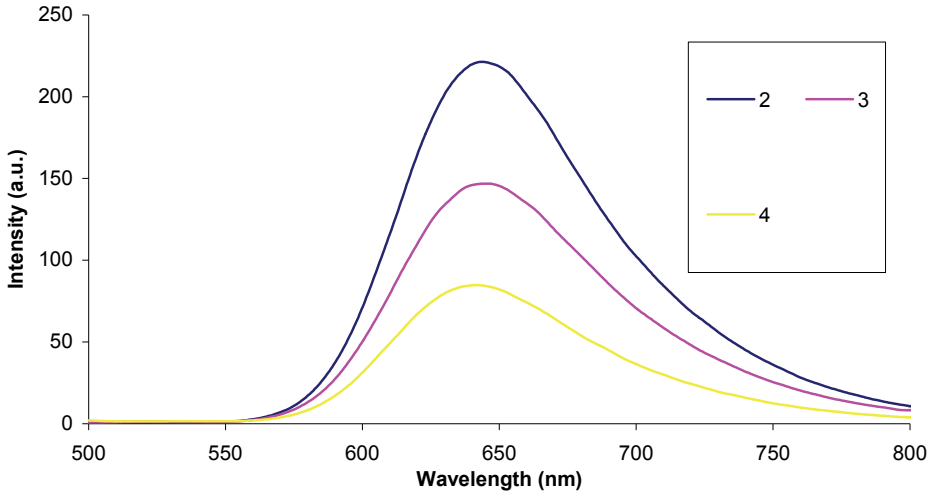

FIGURE 6.13: EMISSION SPECTRA OF COMPLEXES **2**-**4** IN H_2O.

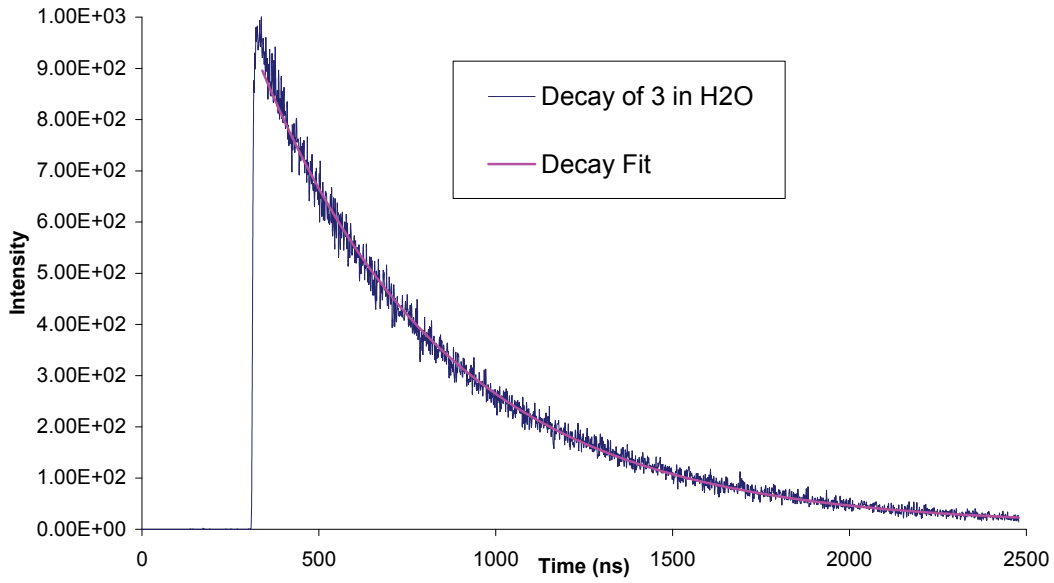

FIGURE 6.14(A): DECAY OF **3** IN H_2O, LAMP SETTINGS USED WERE: 20KHZ, 3.5KV, AND 0.3BAR.

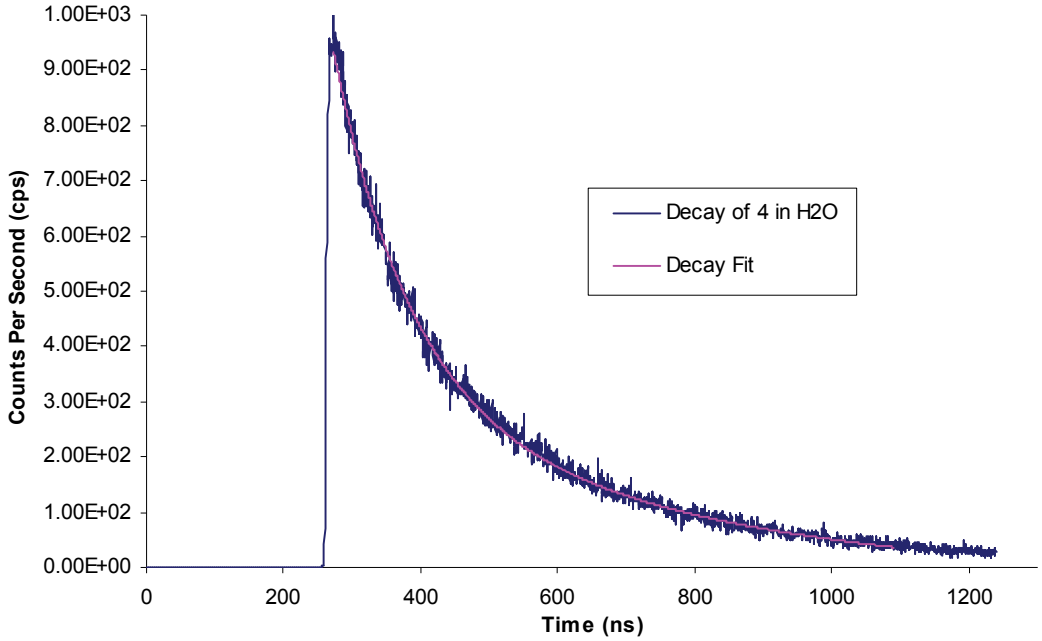

FIGURE 6.14(B): LIFETIME DECAY OF **4** IN H_2O, RT, FITTED TO A BIEXPONENTIAL FIT.

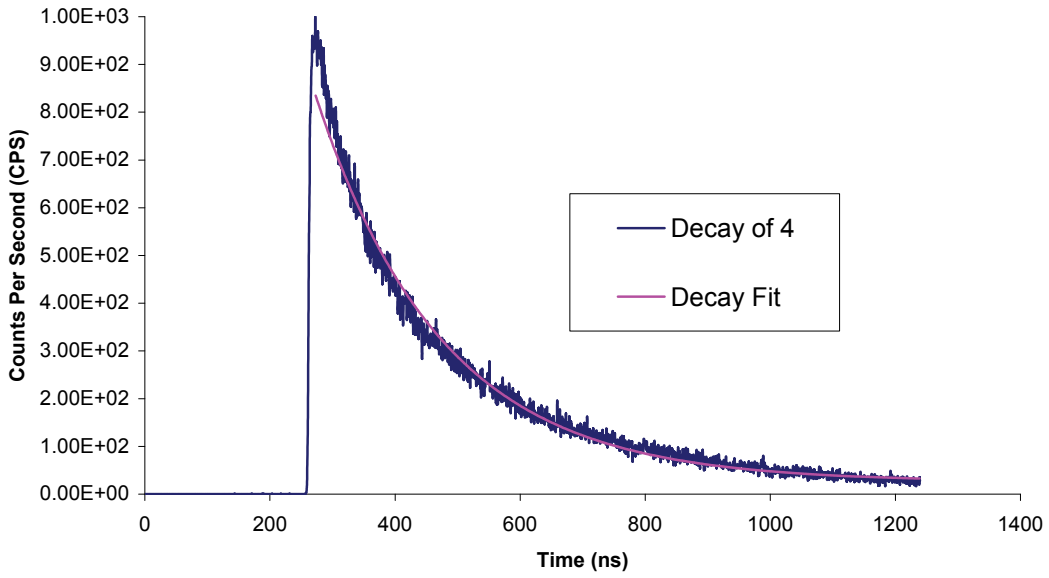

FIGURE 6.14(C): LIFETIME DECAY OF **4** IN H_2O, RT, FITTED TO A MONOEXPONENTIAL FIT. LAMP SETTINGS WERE 0.3 BAR, 3.5KV, AND 20KHZ.

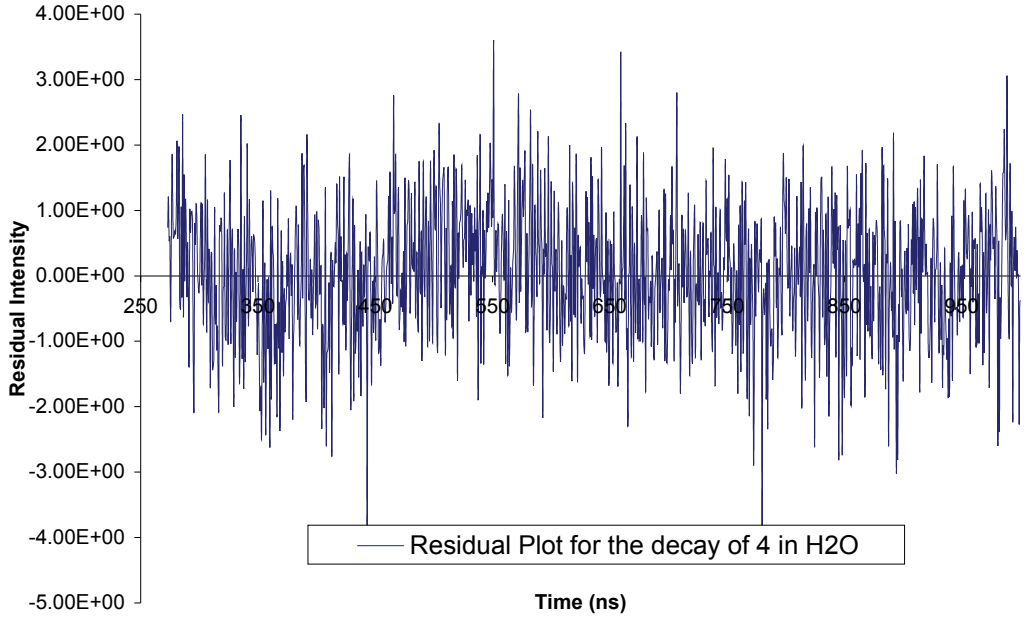

FIGURE 6.14(D): RESIDUAL DATA FOR DECAY OF **4** IN H_2O, USING A BI-EXPONENTIAL FIT. X-AXIS RANGE IS 250ns-1000ns.

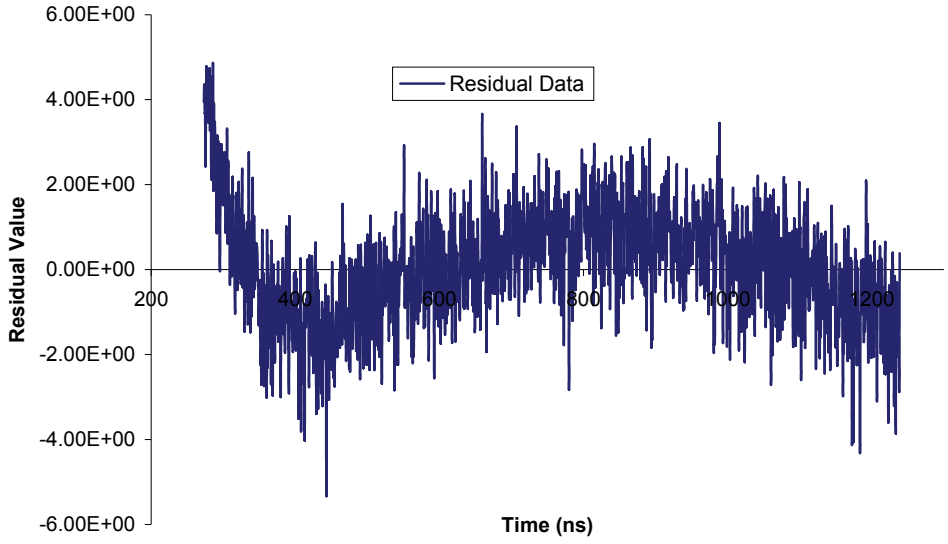

FIGURE 6.14(E): RESIDUAL DATA FOR DECAY OF **4** IN H_2O, USING A MONOEXPONENTIAL FIT.

Examination of the spectra in FIGURE 6.9 shows that all complexes **1**-**4** exhibited characteristic bands around the 450nm region, assigned to the an electron transfer from a metallic orbital to a ligand orbital (d→π* , MLCT process),[15] seen for most ruthenium polypyridyl complexes. In the UV region of the spectrum, strong ligand based π→π* transitions are also observed, as expected.[6,15] Upon excitation of the complexes into the

MLCT band, emission spectra were obtained (FIGURE 6.10). All complexes were found to be emissive, with λ_{max} values around 650-660nm. The intensity values are based on arbitrary units, and the absorbance of the complexes at the wavelength of excitation must be taken into account to give an indication of the relative emission intensities from complex to complex. The lifetimes for all four complexes can be analysed using a single exponential decay model, as seen in FIGURE 6.11. All complexes exhibit lifetimes in the hundreds of ns. In each case, as seen in TABLE 6.1, the reduced Chi (χ) squared values are all very close to 1.1, indicating a close fit to the experimental data.

Complexes **2**-**4** were also measured in water. FIGURE 6.12 shows the absorbance spectra of **2**, **3** and **4**, in H_2O and it is readily seen that they are very similar to each other. Characteristic LC peaks are seen at around 280nm, 300nm and 370nm, the latter is weak and indistinct, attributed to the phenazine based ligand, and is in agreement with published values[3]. The MLCT is observed around 470nm in each case. The emission spectra (FIGURE 6.13) were obtained by exciting at the wavelength of the MLCT transition, and show that the three complexes are emissive in water at room temperature, with λ_{max} values of 641nm for **2**, 650nm for **3**, and 640nm for **4**.

A red shift of 18nm is observed for **4** relative to the Ru-dppz-Pd complex reported by Rau *et al*[6], most likely due to the presence of the methoxy ester substituents on the bpy ligands. It was found that the emission of **1** was red shifted by a value of 11nm, relative to complexes **2**-**4**. This is attributed to the fact that the excited state for this complex is on the tppz ligand, and not on the higher energy t-butyl bpy ligands, which has been seen for $[Ru(bpy)_2tppz]^{2+}$, see for example, ref [14]. This is further supported by the very weak emission and the significantly shorter lifetime for complex **1** which was found to be ~50% shorter than the lifetimes exhibited by complexes **2**-**4**. Complex **1** however, was found to possess a longer lifetime than that reported by Rau *et al*[6], for $[Ru(tbbpy)_2(tppzBr_2)]^{2+}$, a structural analogue of **1**, (226ns *vs* 154ns). This is most likely due to the electron withdrawing effect of the bromine substituents on the tppz ligand and the acceleration of triplet excited state decay due to the heavy atom effect imparted by bromide. The most interesting result is that obtained for complex **4**. It was found to have a long lived (466ns) excited state, thought to be based on the bpy ligands, and not on the tppz moiety as illustrated in FIGURE 6.15. Rau *et al*[6] reported the lifetime of an analogue

of **4**, $[Ru(tbbpy)_2(tppz)\text{-}PdCl_2]^{2+}$, where tbbpy is 4,4'-di-t-butyl-2,2'-bipyridine. The lifetime for this complex was much shorter (~27ns) than that observed for **4**, (466ns). This is most likely due to the excited state for **4** being on the bpy ligands, which are lower in energy, due to the methoxy ester substituents, and not on the tppz ligand. Wacholtz *et al*[31] showed the lowest emitting energy level state in $[Ru(dmbpy)_2(decbpy)]^{2+}$, where decbpy=4,4' dethoxy ester- 2,2'-bipyridine, and dmbpy= 4,4'-dimethyl-2,2'-bipyridine, was from the bpy bearing the ethoxy ester groups, while Lundin *et al*[10(a)] showed that for $[Ru(bpy)_2dppz]^{2+}$, the excited state lies on the dppz ligand, consistent with the results found here for **1**. This is an important result, as it provides a very clear example of the role of substituents on the tuning of the excited state properties of the complex.

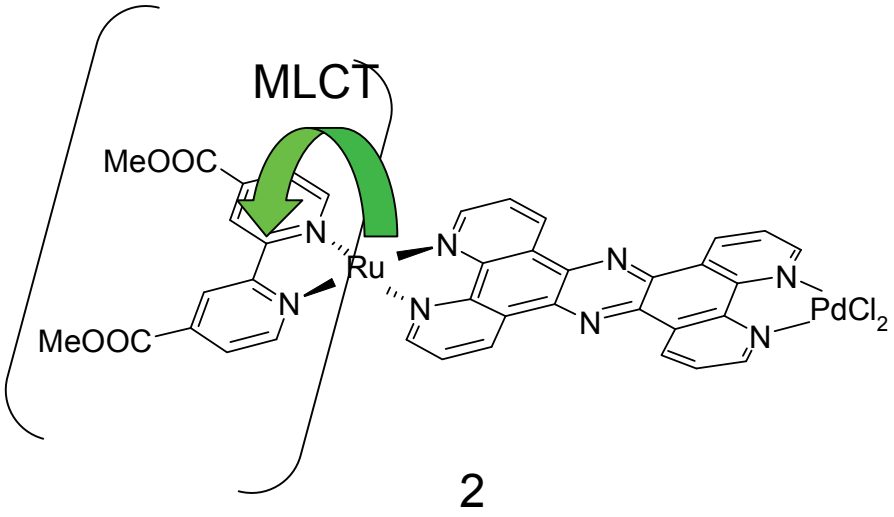

FIGURE 6.15: SCHEMATIC REPRESENTATION OF THE FORMATION AND LOCATION OF THE EXCITED STATE IN COMPLEX **4** IN ACETONITRILE.

In summation, the excited state of the complexes in acetonitrile can be visualized in the following schemes, SCHEME 6.1, SCHEME 6.2 and SCHEME 6.3, using the paradigm complex $[Ru(bpy)_3]^{2+}$ as a basis. Further evidence for the absence of the quenching effect by the Pd centre is given by the fact that the lifetime and emission of **4** is almost identical to both **2** and **3**, neither of which possess the Pd moiety. Komatsuzaki *et al*[14] suggests that the in the case of $[Ru(bpy)_2dppz]^{2+}$ or $[Ru(bpy)_2tppz]^{2+}$ the dppz is more susceptible to solvent interaction than the more sterically hindered tppz, and this results in longer

lifetimes for tppz ligand based complexes than for complexes bearing a dppz ligand (580ns vs 30ns). Since no such disparity is seen in the lifetimes of **2**-**4**, this suggests that the excited state is on the bpy ligands. This is in itself an important result, since it appears that the modification of the bipyridine ligands with methoxy ester groups in the 4 and 4' positions leads to a significant difference in the photophysical behaviour of the complex, relative to that exhibited by complex **1**, where the 4 and 4' positions on the bpy ligands are occupied by *t*-butyl groups.

With regard to the results obtained in H_2O, the emission values of λ_{max} ranging between 640nm and 650nm suggest bpy-based excited states in the cases of **2**, **3** and **4** , as also found for these complexes in acetonitrile. These values are similar to those reported by Schwalbe *et al*[27]. The emission values were found to be somewhat independent of solvent, as values of 650nm were also observed for these complexes in ACN. However the lifetime values of complexes **3** and **4** in H_2O are of particular interest. The decay for **3** was modeled using a single exponential decay which yielded a value of ~530ns. However, a bi-exponential decay was required to fit the decay data for **4** in this case, yielding lifetime values of ~530ns and 110ns (FIGURE 6.14(B)). The prefactors for these lifetimes were calculated as 72% and 28% for the 530ns and 110ns decays, respectively. There are at least three possible explanations for this process. The first, and most probable, is the result of partial or complete hydrolysis of the methoxy esters on the bpy ligands. Since the excited state is thought to be located on these ligands, any change to the methoxy groups would be expected to result in a change to the lifetime of the complex.

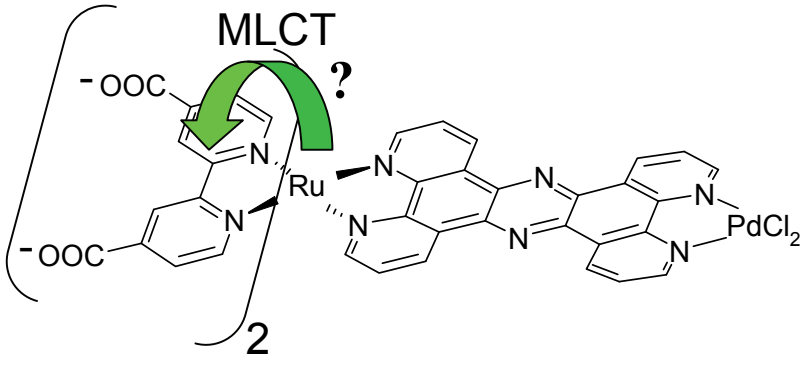

FIGURE 6.16: ILLUSTRATION OF THE FORMATION OF A POSSIBLE EXCITED STATE AFTER HYDROLYSIS OF THE METHOXY ESTERS.

A second factor to be considered is the possible existence of an impurity within the sample. This is unlikely to be the case, since this shorter process was not observed for this sample in acetonitrile. The third possible explanation for this unexpected result is related to the presence of the Pd centre. However, this is considered unlikely to effect the lifetime, given the similarities between it and complex **3**. A complex was reported in ref [6], with a second ruthenium centre in place of the palladium centre ([Ru(4,4'-di-t-butyl-2,2'-bpy)$_2$-tppz-Ru(4,4'-di-t-butyl-bpy)$_2$]$^{4+}$, labeled as "3" in FIGURE 6.4, exhibited a biexponential decay, with one of the decays (130ns) agreeing closely with the shorter decay exhibited by the ruthenium - palladium complex, **4**, (110ns). This data discounts the possibility of the Pd centre being the reason for the biexponential decay. An attempt was made to model the decay data for **4** with a monoexponential fit, (FIGURE 6.14(C) and FIGURE 6.14(E)), however this yielded values of τ = 201ns and χ^2 = 1.83. There was some structure observed in the residual data, which was not observed in the residual data for the bi-exponential fit in FIGURE 6.14(D). From this observation, and the high χ^2 value obtained for the mono-exponential fit, it was concluded that the monoexponential fit is not appropriate in this case. At this stage, it is not certain where the excited state lies, however it is thought to be most likely located on the bpy ligands, as illustrated in FIGURE 6.16 (*vide supra*).

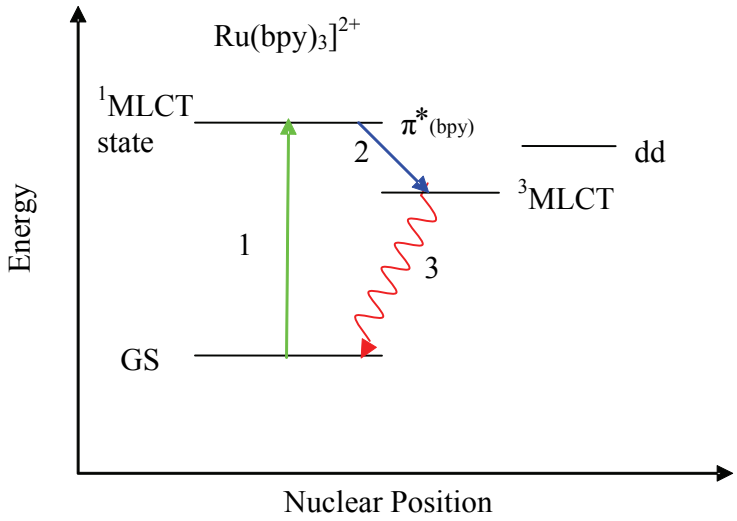

SCHEME 6.1: SCHEMATIC REPRESTATION OF THE ENERGY LEVELS IN [RU(BPY)$_3$]$^{2+}$, SHOWING EXCITATION (1), INTERSYSTEM CROSSING (2) AND RADIATIVE DECAY (3) PROCESSES.

The energy levels of the $[Ru(bpy)_3]^{2+}$ complex can be simplified to those for the metal centre, the T_{2g} levels which are considered to be the ground state of the complex, represented as "GS", and the π^* levels of the ligands. In the case of heteroleptic complexes, such as those investigated in this work, the situation becomes more complex, with π^*_L levels possible for each different type of ligand. This leads to the two different possible π^*_L levels shown in SCHEME 6.2 and SCHEME 6.3 for the Type I complexes. In the complexes presented here, the levels have been assigned the appropriate energy *relative* to each other, based on previous reports in the literature discussed in the introduction to this chapter, and the spectroscopic data presented here. From this assignment, the likely location of the excited state can be deduced.

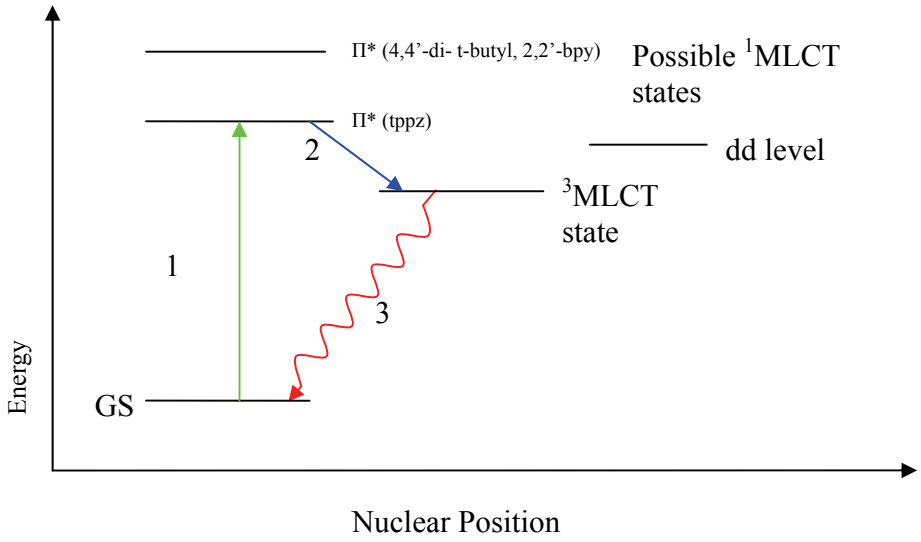

SCHEME 6.2: SCHEMATIC REPRESTATION OF THE ENERGY LEVELS IN COMPLEX **1**, SHOWING EXCITATION (1), INTERSYSTEM CROSSING (2) (SINGLET→TRIPLET) AND RADIATIVE DECAY (3) PROCESSES.

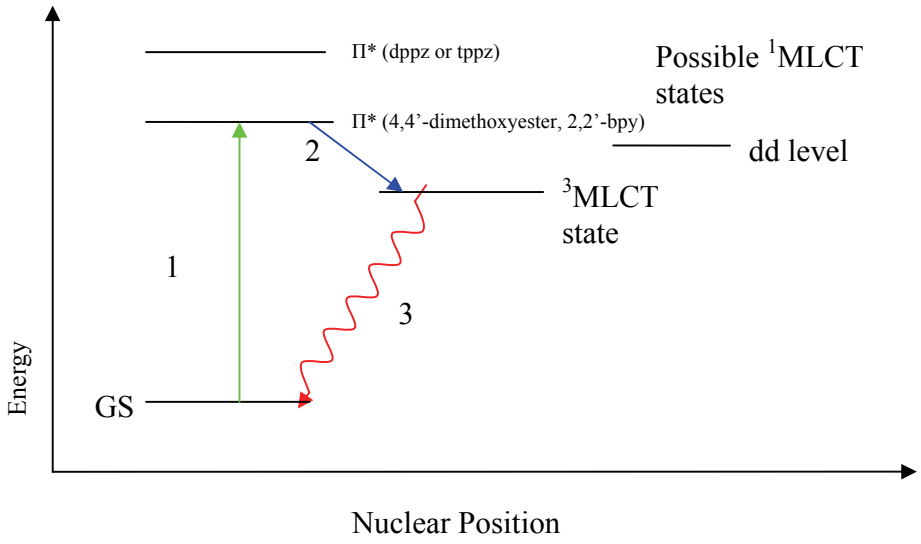

SCHEME 6.3: SCHEMATIC REPRESTATION OF THE ENERGY LEVELS IN COMPLEXES **2-4**, SHOWING EXCITATION (1), INTERSYSTEM CROSSING (SINGLET→TRIPLET) (2), AND RADIATIVE DECAY (3) PROCESSES.

6.2.2 Type II Complexes

As discussed previously in this chapter, the Type II complexes serve as reference compounds for the Type I complexes. The Type II complexes possess one of two main types of structures, $[Ru(4,4'\text{-}R_2\text{-}bpy)_3]^{2+}$ where R= t-butyl or a cyano group, or a $[Ru(4,4'\text{-}R_2bpy)_2LL]^{2+}$ structure, where the LL is a phenanthroline based ligand, and R= COOMe or a *t*-butyl group. The structures of the Type II complexes are shown in FIGURE 6.17, below. The spectroscopic data will then be presented for solutions in aerated ACN and DCM, and 4:5 PCN:BuCN for the measurements performed at 77 K. All measurements were performed at room temperature, unless otherwise stated. Different lamp settings were used from sample to sample for the lifetime measurements. This was necessary in order to obtain a meaningful decay. The lamp settings used for each sample are listed in the tables of spectroscopic data.

Sample I.D	Structure Of Complex	Sample I.D.	Structure Of Complex
5	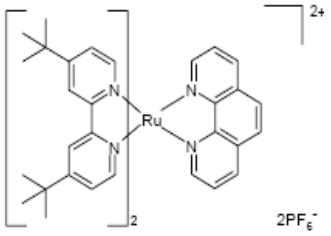	6	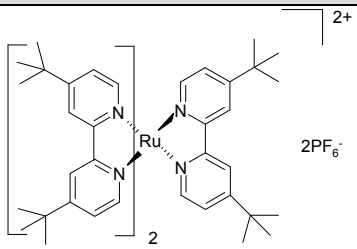
7	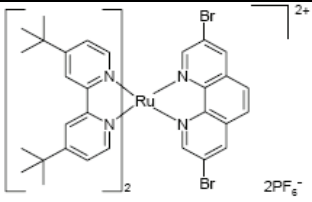	8	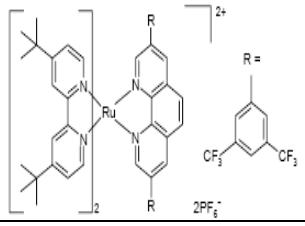
9	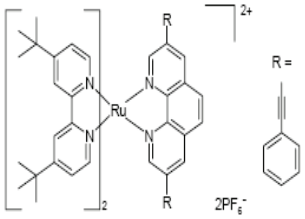	10	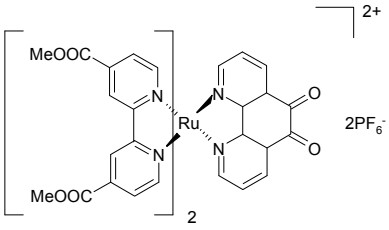
11	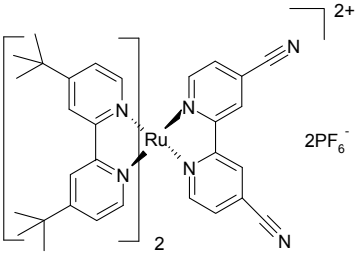		

FIGURE 6.17: STRUCTURES OF TYPE II COMPLEXES.

6.2.2.1 Type II Complexes, Room Temperature

A summary of the spectroscopic and photophysical data for the Type II complexes is presented in TABLE 6.3. All values in TABLE 6.3 were obtained at room temperature, however, some lifetimes were obtained using the normal pressure lamp settings (6.5kV, 40kHz, 1.1bar), and some were obtained using the lower pressure settings of (3.5kV, 20kHz, 0.3bar)

Sample I.D.	Abs in ACN (nm)	Emission λ_{max} (nm) (ACN)	Lamp Parameters	τ(ns) in ACN / χ^2
5	264, 285, 450	614	40kHz, 6.5kV, 1.1bar	103/1.077
6	287, 322, 456	620	40kHz, 6.5kV, 1.1bar	105/1.081
7	242, 278, 430	648	40kHz, 6.5kV, 1.1bar	169/1.033
8	282, 320(s), 436	668	40kHz, 6.5kV, 1.1bar	205/1.01
9	284, 359,432, 490(s)	682	40kHz, 6.5kV, 1.1bar	232/1.016
10	304, 454	650	40kHz, 3.5kV, 0.3bar	456/1.052
11	287, 404, 506	743	40kHz, 6.5kV, 1.1bar	134

TABLE 6.3: SPECTROSCOPIC AND PHOTOPHYSICAL DATA FOR TYPE II COMPLEXES IN AERATED ACN.

The absorption and emission spectra of these Type II complexes in aerated acetonitrile (ACN) are shown in FIGURE 6.18(A) and (B) and FIGURE 6.19(A) and (B), respectively. A representative decay of one of the samples, complex **10** in aerated ACN, is shown in FIGURE 6.20.

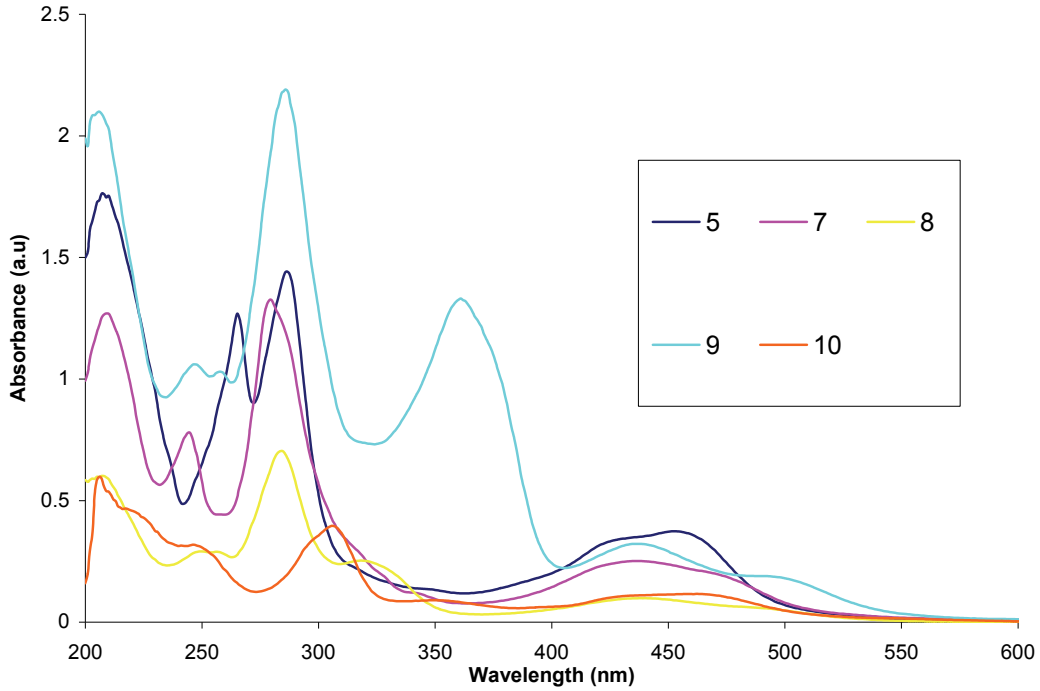

FIGURE 6.18(A): ABSORPTION SPECTRA FOR SOME OF THE TYPE II COMPLEXES, IN AERATED ACN.

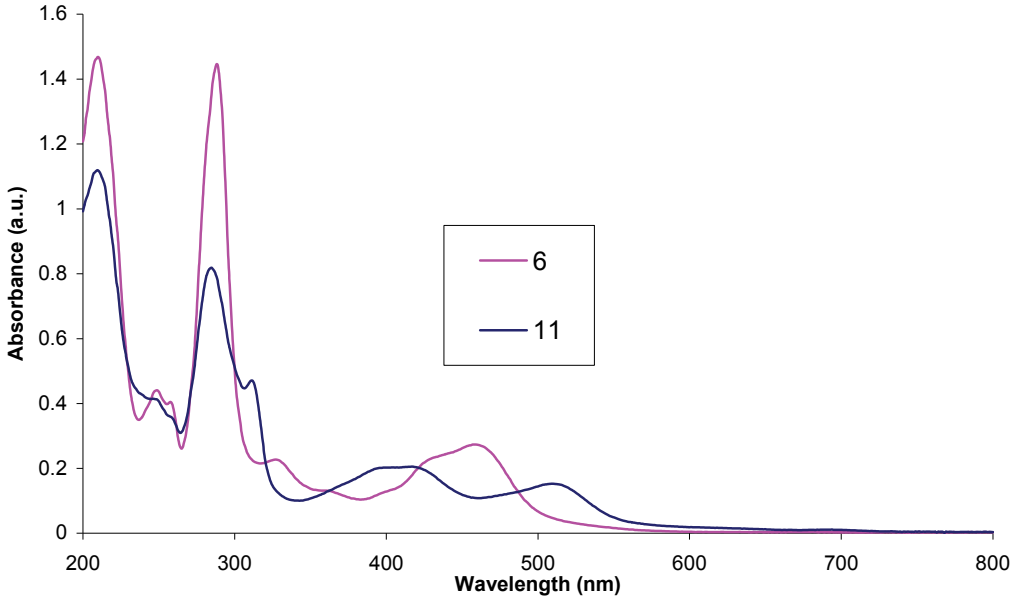

FIGURE 6.18(B): ABSORPTION SPECTRA FOR TYPE II COMPLEXES **6** AND **11**, IN AERATED ACN.

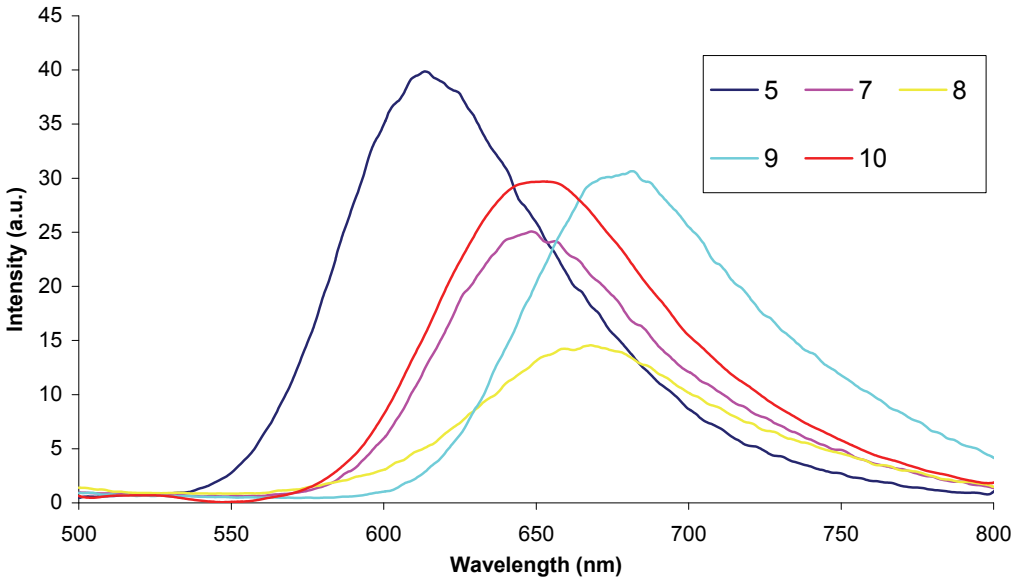

FIGURE 6.19(A): EMISSION SPECTRA FOR THE TYPE II COMPLEXES DISCUSSED IN THIS SECTION, IN AERATED ACN.

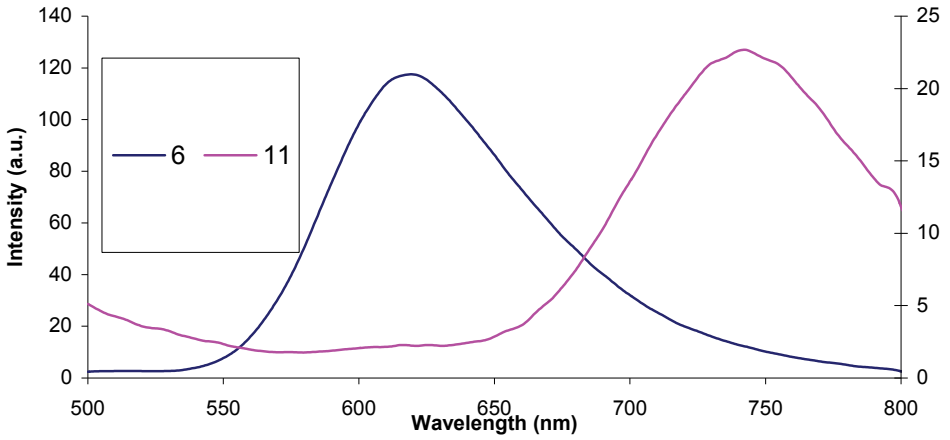

FIGURE 6.19(B): EMISSION OF **6** AND **11** IN AERATED ACN. EMISSION INTENSITY OF **11** IS PLOTTED ON RIGHT HAND AXIS.

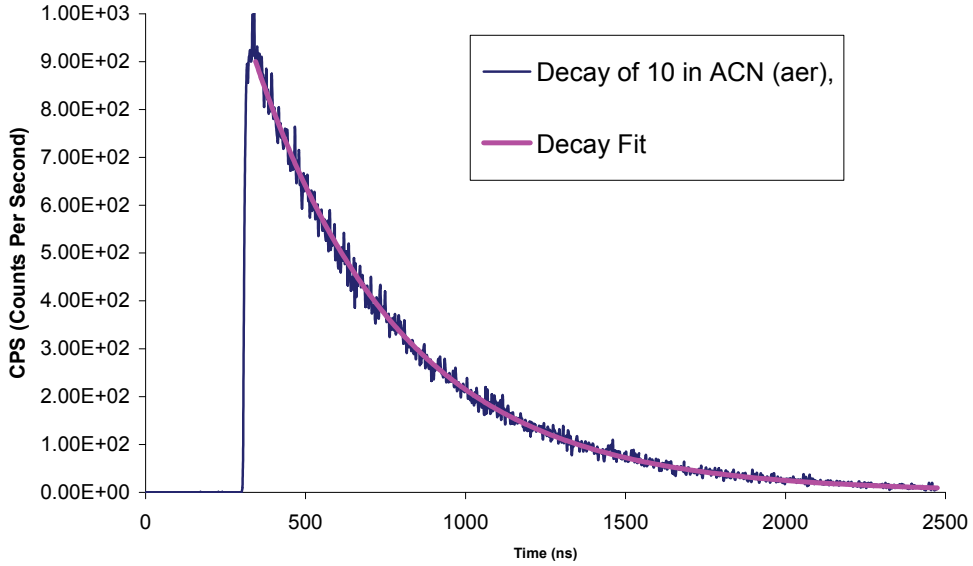

FIGURE 6.20: DECAY OF **10** IN AERATED ACN, LAMP SETTINGS USED WERE 40KHZ, 3.5KV AND 0.3BAR. LIFETIME ESTIMATED TO BE AROUND 456NS, x^2= 1.052

FIGURE 6.18 shows the absorbance traces for the Type II complexes in aerated ACN. All complexes exhibit absorption features in the region of 430nm-470nm, indicative of an MLCT process, which is expected for ruthenium complexes.[11,15,16] LC transitions are observed around 260nm-300nm, due to $\pi \rightarrow \pi^*$ transitions in the complexes. Complex **9** exhibits a strong peak at around 359nm, and this can be attributed to the substituted phenanthroline ligand. This result is in agreement with values reported by Tzalis *et al*[23],

of 354nm for the free ligand and 356nm for the tris complex. In addition, two peaks are observed for **9** in the MLCT region, at 432nm and 490nm. The first is likely attributed to the Ru → bpy ligands MLCT process, while the lower energy band is thought to be due to the Ru → phenanthroline MLCT transition. Analysis of the emission spectra for the complexes shows that all complexes exhibit a ^{3}MLCT based emission[15]. The emission peaks for **5**, **7**, **8**, and **10** are difficult to identify, since the λ_{max} values are somewhat red-shifted relative to **5**, and cannot be attributed conclusively to either the ttbpy or the phenanthroline based ligand on the basis of this data. It is seen that **8** is red-shifted to 668nm, relative to **5**, possibly due to the additional conjugation of the modified phenanthroline ligand, and **9** is red-shifted 68nm, relative to **5** due to the possibility for increased delocalization of the excited state on the heavily conjugated modified phenanthroline ligand. The emission observed for the tris complex **6**, has a λ_{max} value of 620nm, similar to that reported previously (614nm-see ref [27]) and can be attributed to the MLCT transition involving the 4,4'-t-butyl, 2,2'-bpy ligand. The largest red-shift observed relative to **5** is the emission for **11** which is significantly red-shifted to 743nm, indicating a dicyano-bpy based excited state, as illustrated in SCHEME 6.4, below.

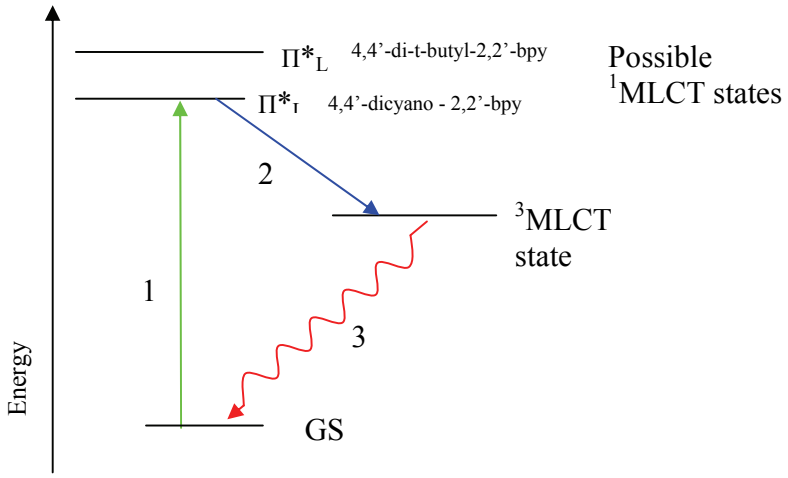

SCHEME 6.4: SCHEMATIC REPRESTATION OF THE ENERGY LEVELS IN COMPLEXES **6** AND **11**, SHOWING EXCITATION (1), AND RADIATIVE DECAY (2) PROCESSES. LIGAND ENERGY LEVELS ARE OFFSET FOR CLARITY AND INTERSYSTEM CROSSING (SINGLET → TRIPLET) HAS BEEN SHOWN WITH A BLUE ARROW.

The emission of **11** is considerably weaker than that of the tris complex **6**, and also appears at lower energy (750nm or 1.653eV) relative to most ruthenium polypyridyl

complexes[15]. The shift appears to be somewhat independent of solvent, as a similar situation is observed for the complexes in aerated DCM, shown in FIGURE 6.21.

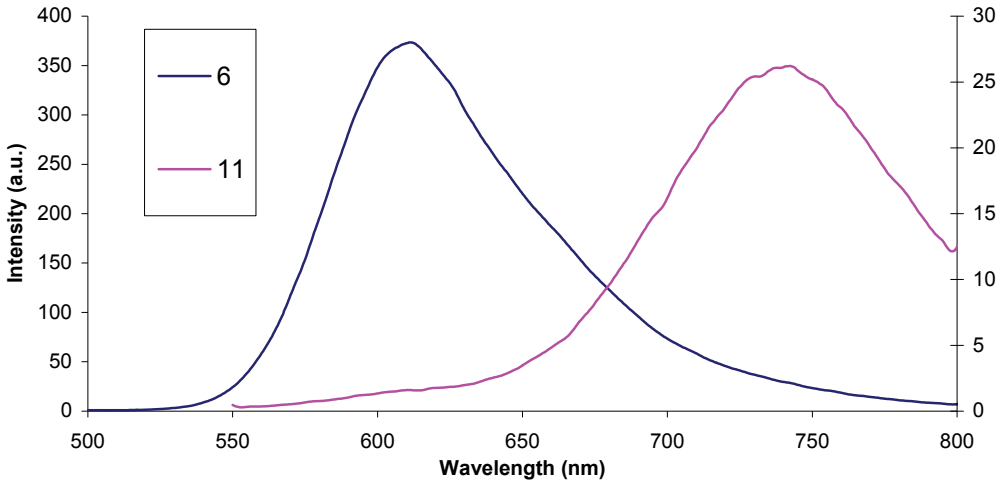

FIGURE 6.21: EMISSION SPECTRA OF **6** AND **11** IN AERATED DCM, ROOM TEMPERATURE. EMISSION INTENSITYFOR **11** IS PLOTTED ON THE RIGHT HAND AXIS.

All complexes exhibit monoexponential lifetimes of the order of hundreds of ns in DCM, with **5**, **6** and **11** all having similar (~200ns) values. This indicates that the bpy ligand is the site where the excited state of complex **5** most likely resides. In ACN, **5** and **7** exhibit lifetimes of 100ns and 170ns respectively, similar to what is found for $[Ru(bpy)_3]^{2+}$ (160-170ns). This indicates once again an excited state most likely located on one of the bpy ligands and not on the phenanthroline. However, for **8** and **9**, the lifetimes are longer, and the possible involvement of a phenanthroline based excited state cannot be ruled out.[32] For example, the value for **10** was found to be twice as long (456ns) as the values for **5** and **7**, indicating an excited state localized on phenanthroline ligand, in agreement with the observations of Browne *et al*[20]. It is also seen that the phenanthroline based Type II complexes exhibited shorter lifetimes in aerated ACN, than the Type I complexes. This is a result of the presence of the methoxy ester groups in the Type I complexes **2**, **3** and **4**. Representative decays in ACN are shown in FIGURE 6.22, and FIGURE 6.23.

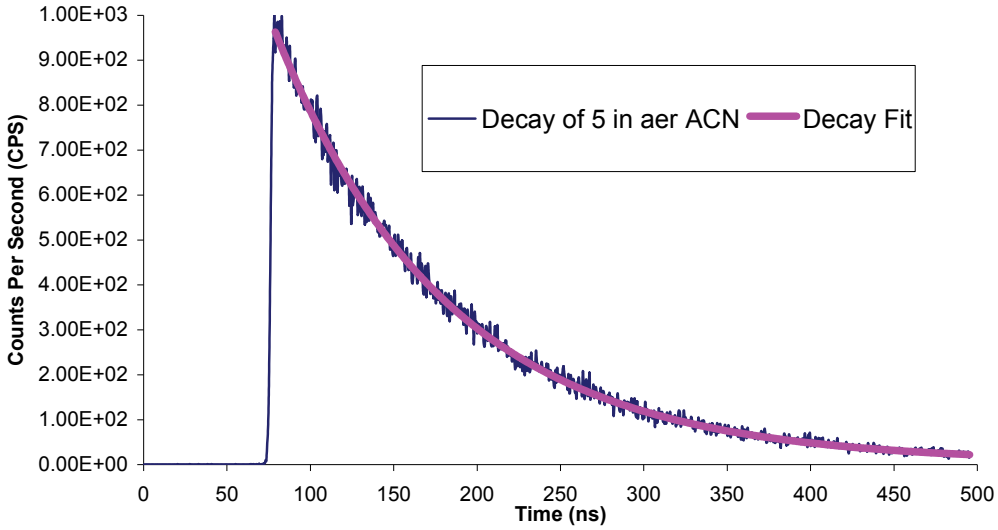

FIGURE 6.22(A): DECAY OF **5** IN AERATED ACN, ROOM TEMPERATURE. LIFETIME WAS ESTIMATED TO BE AROUND 100ns.

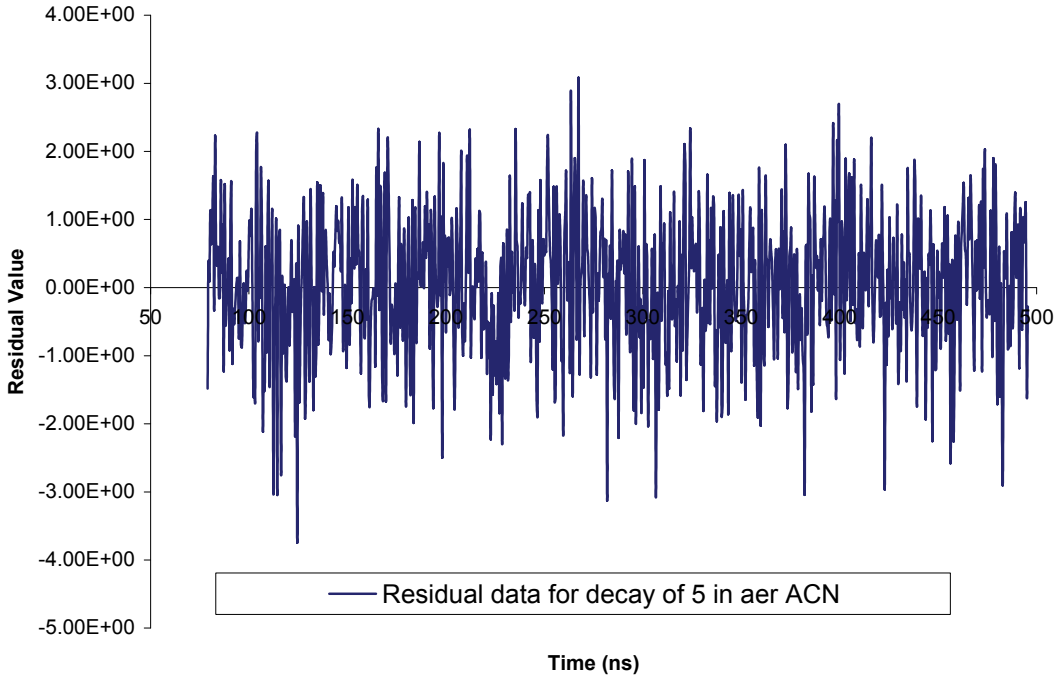

FIGURE 6.22(B): RESIDUAL DATA FOR DECAY OF **5** IN AERATED ACN, ROOM TEMPERATURE.

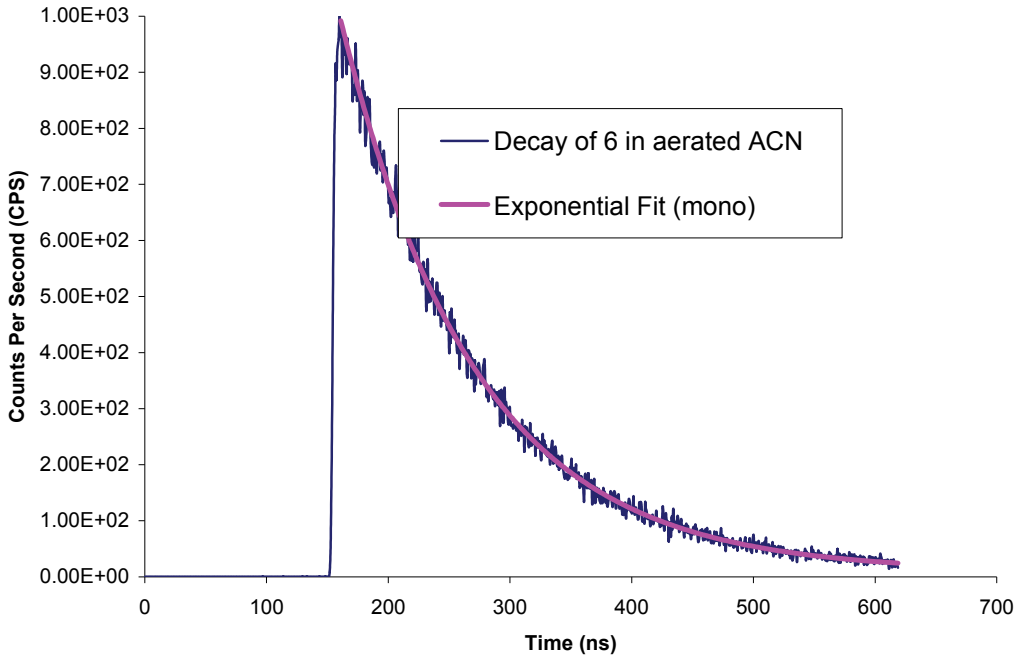

FIGURE 6.23(A): DECAY OF **6** IN AERATED ACN, ROOM TEMP, NORMAL PRESSURE SETTINGS (1.1BAR, 40KHZ, 6.5KV). LIFETIME IS ESTIMATED TO BE AROUND 100ns.

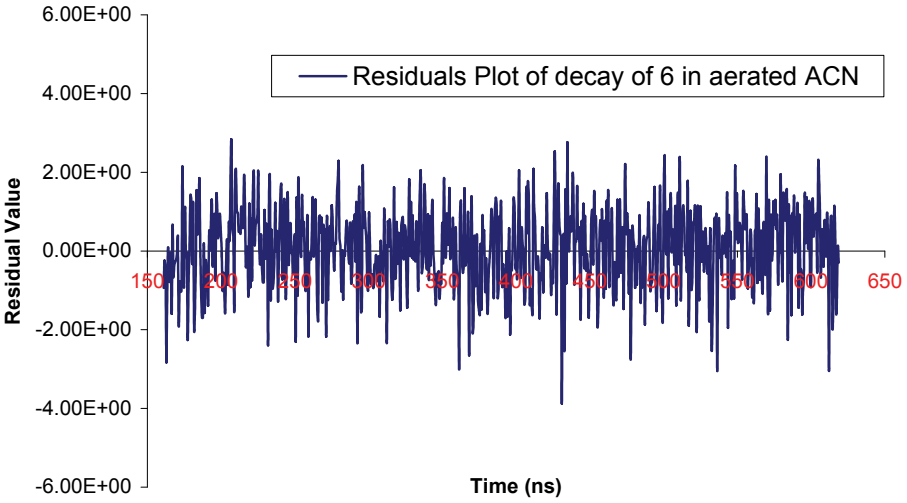

FIGURE 6.23(B): RESIDUAL DATA FOR DECAY OF **6** IN AERATED ACN, ROOM TEMP.

Based on the data presented here, it is not possible to unambiguously assign the location of the excited for all of these complexes. This is primarily due to the heteroleptic nature of the complexes investigated. Other techniques such as electrochemistry and resonance Raman spectroscopy could be used to further elucidate the nature and location of the

excited state, particularly in the cases where the emission data suggests a ^{3}MLCT of mixed phenanthroline/bipyridine character.

6.3 Conclusion

The photophysics of various ruthenium polypyridyl complexes has been investigated, with UV-vis absorption and luminescence spectroscopy, and time correlated single photon counting. An important feature of the complexes studied is that all, with the exception of **6**, are heteroleptic in nature, with 2,2'-bipyridine and or 1,10-phenanthroline based ligands. This results in most cases in at least two possible locations for the excited state of the complex. In order to completely and unambiguously identify the location of the excited state, it would be necessary to further investigate the systems using resonance Raman spectroscopy, and/or electrochemical studies. An attempt has been made to identify the site of localization of the excited state, at least in the sense of whether it is bpy based, or based on the third ligand. In the case of the structural similar phenanthroline ligands, this is made more difficult. Measurements have been carried out in different solvents for some complexes, to give an idea of the level of solvent dependency of the complex, which can in turn be used in some cases to locate the excited state.

Excited state lifetimes have been calculated for the samples, in various solvents, at room temperature. The values and decay data obtained suggest that, as far as Type I complexes are concerned, the excited state is based on one of the methoxy ester modified bpy ligands, and not on the dppz or tppz ligands, with the exception of 1. In the case of the Type II complexes, the situation is less clear with the emission and lifetime data inferring that the excited state is of mixed bpy/phenanthroline character. Of particular note is the lifetime result for **4**, where a significantly longer lifetime was observed than for the analogous complex reported previously by Rau *et al*[6]. This evidences the potentially significant effects of modifying ligands in metal complexes, which can change both the location of the excited state, and the photophysical behaviour of the complex. It is this feature of metal complexes, amongst others, that has driven the

research over the last number of decades, and has lead to many of the applications of transition metal complexes, such as catalysis, solar cells, biosensors, and provided significant impetus to the synthesis and investigation of the photophysical properties of new ruthenium complexes.

6.4 Bibliography

1 K. O'Donoghue, J. C. Penedo, J. M. Kelly, P. E. Kruger, *Dalton Trans.*, **2005**, 1123-1128

2 W. R. Browne, J. J. McGarvey, *Coord. Chem. Rev.*, **2006**, *250*, 1696-1709

3 J. Fees, W. Kaim, M. Moscherosch, W. Matheis, J. Klima, M. Krejcik, S. Zalis, *Inorg. Chem.*, **1993**, *32*, 166-174

4 J. R. Schoonover, W. D. Bates, T. J. Meyer, *Inorg. Chem.*, **1995**, *34*, 6421-6422

5 S. Rau, M. Ruben, T. Büttner, C. Temme, S. Dautz, H. Görls, M. Rudolph, D. Walther, A. Brodkorb, M. Duati, C. O'Connor, J. G. Vos, *J. Chem. Soc., Dalton Trans.*, **2000**, 3649-3657

6 S. Rau, B. Schäfer, D. Gleich, E. Anders, M. Rudolph, M. Friedrich, H. Görls, W. Henry, J. G. Vos, *Angew. Chem. Int. Ed.*, **2006**, *45*, 6215-6218

7 B. Schäfer, H. Görls, M. Presselt, M. Schmitt, Jürgen Popp, W. Henry, J. G. Vos, S. Rau, *Dalton Trans.*, **2006**, 2225-2231

8 S. Rau, R. Fischer, M. Jäger, B. Schäfer, S. Meyer, G. Kreisel, H. Görls, M. Rudolf, W. Henry, J. G. Vos, *Eur. J. Inorg. Chem.*, **2004**, *22*, 2001-2003

9 B. Schäfer, H. Görls, S. Meyer, W. Henry, J. G. Vos, S. Rau, *Eur. J. Inorg. Chem.*, **2007**, *25*, 4056-4063

10 **(a)** N. J. Lundin, P. J. Walsh, S. L. Howell, J.J. McGarvey, A. G. Blackman, K. C. Gordon, *Inorg. Chem.*, **2005**, *44*, 3551-3560, **(b)** C. G. Coates, P. Callaghan, J. J. McGarvey, J. M. Kelly, L. Jacquet, A. Kirsch-De Mesmaeker, *J. Mol. Structure*, **2001**, *598*, 15-25, **(c)** C. G. Coates, L. Jacquet, J. J. McGarvey, S. E. J. Bell, A. H. R. Al-Obaidi, J. M. Kelly, *J. Am. Chem. Soc.*, **1997**, *119*, 7130-7136

11 A. Juris, V. Balzani, F. Barigelletti, S. Campagna, P. Belser, A. von Zelewsky, *Coord. Chem. Rev.*, **1988**, *84*, 85-277

12 B. Durham, J. V. Caspar, J. K. Nagle, T. J. Meyer, *J. Am. Chem. Soc.*, **1982**, *104*, 4803-4810

13 E. J. C. Olson, D. Hu, A. Hörmann, A. M. Jonkman, M. R. Arkin, E. D. A. Stemp, J. K. Barton, P. F. Barbara, *J. Am. Chem. Soc.*, **1997**, *119*, 11458-11467

14 N. Komatsuzaki, R. Katoh, Y. Himeda, H. Sugihara, H. Arakawa, K. Kasuga, *Dalton Trans.*, **2000**, 3053-3054

15 S. Campagna, F. Puntoriero, F. Nastasi, G. Bergamini, V. Balzani, *Topics Curr. Chem.*, **2007**, *280*, 117-214

16 K. Kalyanasundaram, Photochemistry of Polypyridine and Porphyrin Complexes, Academic Press, London, **1996**.

17 M. K. Brennaman, T. J. Meyer, J. M. Papanikolas, *J. Phys. Chem. A.*, **2004**, *108*, 9938-9944

18 E. V. Dose, L. J. Wilson, *Inorg. Chem.*, **1978**, *17*, 2660-2666
19 W. Huang, G. Masuda, S. Maeda, H. Tanaka, T. Hino, T. Ogawa, *Inorg. Chem.*, **2008**, *47*, 468-480
20 W. R. Browne, P. Passaniti, M. T. Gandolfi, R. Ballardini, W. Henry, A. Guckian, N. O'Boyle, J. J. McGarvey, J. G. Vos, *Inorg. Chim. Acta*, **2007**, *360*, 1183-1190
21 B. Sun, J. Chu, Y. Chen, F. Gao, L.-N. Ji, H. Chao, *J. Mol. Structure*, **2008**, *890*, 203-208
22 A. Bouskila, B. Drahi, E. Amouyal, I. Sasaki, A. Gaudemer, *J. Photochem. Photobio. A. Chem.*, **2004**, *163*, 381-388
23 D. Tzalis, Y. Tor, *Tetrahed. Lett.*, **1995**, *36*, 6017-6020
24 S. Rau, D. Walther, J. G. Vos, *Dalton Trans.*, **2007**, 915-919
25 S. Rau, B. Schäfer, A. Grüßing, S. Schebesta, K. Lamm, J. Vieth, H. Görls, D. Walther, M. Rudolph, U. W. Grummt, E. Birkner, *Inorg. Chim. Acta*, **2004**, *357*, 4496-4503
26 S. V. Litke, T. V. Mezentseva, G. N. Lyalin, A. Y. Ershov, *Optics & Spectros.*, **2003**, *95*, 980-987
27 M. Schwalbe, B. Schäfer, H. Görls, S. Rau, S. Tschierlei, M. Schmitt, J. Popp, G. Vaughan, W. Henry, J. G. Vos, *Eur. J. Inorg. Chem.*, **2008**, *21*, 3310–3319
28 B. Gholamkhass, K. Koike, N. Negishi, H. Hori, T. Sano, K. Takeuchi, *Inorg. Chem.*, **2003**, *42*, 2919-2932
29 N. Onozawa-Komatsuzaki, O. Kitao, M. Yanagida, Y. Himeda, H. Sugihara, K. Kasuga, *New J. Chem.*, **2006**, *30*, 689-697
30 S. Losse, H. Görls, R. Groarke, J. G. Vos, Sven Rau, *Eur. J. Inorg. Chem.*, **2008**, 4448-4452
31 W. F. Wacholtz, R. A. Auerbach, R. H. Schmehl, *Inorg. Chem.*, **1986**, *25*, 227-234
32 H. P. Hughes, D. Martin, S. Bell, J. J. McGarvey, J. G. Vos, *Inorg. Chem.*, **1993**, *32*, 4402-4408

Chapter 7: Conclusions and Future Work

Chapter 7 presents an overall summary of the work presented in this thesis and the general conclusions drawn from the results obtained. An overview of potential future work is given, in order to build on the results already obtained.

7.0 Conclusions

This work has focused on the modification of well defined ZnO nanostructures on a solid surface with a photoactive ruthenium complex, and the analysis of this hybrid system with surface probing techniques such as SEM and AFM, in addition to photoluminescence measurements at low and room temperatures. This was done in order to investigate the effect of the ruthenium complex on the photophysics of the ZnO nanostructures, as well as to ascertain the topology of the composite system. In addition, a ruthenium polymer has been used to solubilize or exfoliate carbon nanotubes in an organic solvent, and AFM has been used to investigate the extent of the exfoliation process, along with in-situ UV measurements of the exfoliating solution. Finally, the excited state lifetimes of a range of ruthenium complexes were measured and interpreted.

Chapter 3 investigated the modification of ZnO nanorods with $[Ru(bpy)_2(dcbpy)](PF_6)_2$. It was found via photoluminescence measurements that electron injection into the ZnO nanorods from the ruthenium complex, did not occur. This has been attributed to the concentration of the ruthenium complex being too high, resulting in sensitization of only the surface layer of the ruthenium complex, and therefore preventing an excited electron from permeating through to the ZnO nanorods. This view is supported by the observation of a ruthenium based emission, however, since it is difficult to anticipate how intense this signal should be, it is not possible to rule out the electron injection process completely. However, it is thought, based on the results obtained, to be unlikely. The possibly of a high surface coverage of the ruthenium complex is also indicated by the AFM images presented, which show a significant difference in the diameter of the ZnO nanorods upon modification with the ruthenium complex. The ZnO emission does not vary appreciably upon modification, however, the Auger spectra indicate the presence of the ruthenium complex, and an absence of the ZnO signal. The SEM images of modified nanorods show a marked difference in the morphology compared with the unmodified nanorods, again suggesting a significant coverage of the ruthenium complex on the surfaces of the nanorods. The AFM data presented shows that, while it is difficult

to image arrays of nanotubes, the nanotubes can be imaged when they are not well aligned, as is the case with the samples investigated.

Chapter 4 involved the use of UV spectroscopy as a facile, in-situ method of investigating the process of exfoliating Single Walled Carbon Nanotubes (SWNT's) in methanol, using a ruthenium poly(vinyl pyridine) based polymer, as well as in the absence of the polymer. With the polymer present, as the sonication time was increased, the intensity of the spectra increased across the wavelength range, being especially apparent in the 550nm-800nm portion of the range. In this area, as the intensity increased, van Hove singularity peaks were observed, and these are characteristic of SWNT's. This indicated that the nanotubes were being solubilized, since they were not visible in the spectra prior to sonication. Further evidence of the effectiveness of the exfoliation process is provided by the AFM images obtained of the solution drop cast onto a silicon (100) substrate. These images appear to show single nanotubes, and also groups of in general, less than 10 nanotubes. The diameters of the nanotube features were estimated by the processing software, and were found to be much higher (~90nm) than those expected for single walled nanotubes without a polymer coating. In the absence of the ruthenium polymer, the SWNT's appeared initially to be exfoliated, however, upon the cessation of the sonication process, the nanotubes would fall to the bottom of the sample tube, indicating only a temporary suspension of the nanotubes in solution.

Chapter 5 paralleled the work in Chapter 4, dealing with Multi Walled Carbon Nanotubes (MWNT's) and amino-functionalized MWNT's exfoliated in methanol, with and without the ruthenium polymer. It was found that exfoliation of the multiwalled nanotubes was not possible without the ruthenium polymer, the UV traces did not show a clear increase in intensity over time. It was found that the amino-functionalized nanotubes were slightly easier to exfoliate. The stability of these composite solutions after the cessation of the soncation process was better than that exhibited by the SWNT's. This is expected, since it is generally thought that SWNT's are more difficult to exfoliate than their multiwalled counterparts. In the presence of the ruthenium

polymer, the exfoliation process was found to be more facile. The AFM images obtained of the MWNT /Ru polymer composite show nanotube features on the surface, and these, like the SWNT's, were found to be much wider (~100nm) than bare multiwalled nanotubes are thought to be. Two solutions of differing concentrations of the ruthenium polymer only (no nanotubes) were also drop cast on to silicon slides, and investigated by AFM. It was found that the AFM images of the more concentrated solution showed more globular features than those of the less concentrated solution. This is to be expected, and while not many globular clusters were observed in the less concentrated solution, it can be concluded that the nanotubes observed in both the images in this chapter and in chapter 4 show modified nanotubes, since very few globular features are observed in the nanotube/polymer AFM images. This is also supported by the fact that the less concentrated polymer solution had the same concentration of polymer as that used in both the SWNT and MWNT solutions deposited on to the silicon substrates.

Chapter 6 presented the excited state lifetimes of a number of ruthenium complexes, with different complements of ligands, some phenanthroline-based and some bipyridine – based. The complexes were in general heteroleptic, therefore while it was not possible to precisely assign the locations of the excited states using Time Correlated Single Photon Counting (TC-SPC), attempts were made to assign the excited state to *either* the bpy ligands, or the other ligand.

7.1 Future Work

During the course of the work presented in this thesis, a number of potential areas for future work have been found, some leading on from the work already completed, and other, newer avenues of research. The potential areas for future work are discussed in this section.

7.1.1 Chapter 3

In order to investigate more thoroughly, the effect of the concentration of the ruthenium dye on the photophysics, a range of dye solutions of varying concentration (1μM – 1mM) could be prepared and deposited on the ZnO nanorods. The ZnO and ruthenium based photoluminescences of these samples could be measured, again at room and low temperatures. Upon observation of the quenching of the ruthenium – based emission, it would then be possible to assume that electron injection is occurring. It would then be useful to use other ruthenium polypyridyl complexes to investigate the effects of a dinuclear ruthenium complex, for example, on the electron injection process.

7.1.2 Chapter 4 and Chapter 5

The exfoliation of multiwalled and single walled nanotubes in methanol using the ruthenium polymer was found to be a relatively facile and efficient process. Potential future work would involve the use of analogues of this ruthenium polymer, with different PVP loadings. Another potential avenue of research would be to use the osmium polymers, since these are more difficult to synthesise and purity, this work would provide both a synthetic challenge and also a potential advantage over the ruthenium polymers, as the osmium polymers are thought to be less photolabile, due to the higher $10D_q$ value of osmium complexes, relative to ruthenium complexes. The preparation of composite solutions of varying concentrations of both polymer and nanotubes and the analysis of these solutions using AFM would also be an interesting project.

7.1.3 Chapter 6

Future work in the investigation of the excited states of the ruthenium complexes would utilize Resonance Raman Spectroscopy to fully elucidate the nature and locations of the excited states. Other ruthenium complexes could, of course be investigated by TC-SPC. Quantum yield measurements could be carried out on the more emissive complexes.